Arnold Gucsik

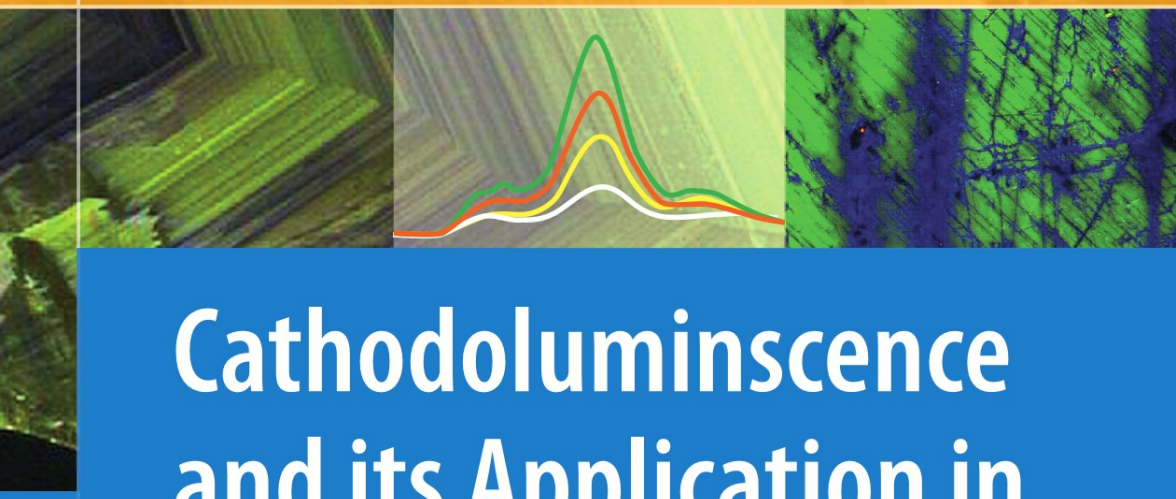

Cathodoluminscence and its Application in the Planetary Sciences

Springer

Cathodoluminescence and its Application in the Planetary Sciences

Arnold Gucsik (Ed.)

Cathodoluminescence and its Application in the Planetary Sciences

Springer

Dr. Arnold Gucsik
MPI für Chemie
Abt. Geochemie
55020 Mainz
Germany

ISBN: 978-3-540-87528-4 e-ISBN: 978-3-540-87529-1

Library of Congress Control Number: 2008935011

Cover design: deblik, Berlin

Printed on acid-free paper

9 8 7 6 5 4 3 2 1

springer.com

This book has been dedicated to my family (my mother: Eszter; wife: Zsuzsanna, and my children: Bence, Reka, Akos) and Prof. Dr. Christian Koeberl (University of Vienna, Austria), Prof. Kiyotaka Ninagawa (Okayama University of Science, Japan) and Dr. Ulrich Ott (Max Planck Institute for Chemistry, Germany)

Preface

In the broad sense the subject of this book belongs to the Physics of Minerals and Planetary Sciences, namely to the cathodoluminescence spectroscopy and microscopy. This technique enables us to receive new data, which contribute greatly to our fundamental knowledge of planets and may be practically used as an *in-situ* Planetary Cathodoluminescence Spectroscopy for the planetary exploration robotic missions in the near future.

This book is addressed to graduate students, professors and scientists in physics, microbiology, chemistry, earth and planetary sciences, materials science and engineering. It discusses cathodoluminescence microscopy and spectroscopy of planetary materials such as shock-metamorphosed rocks and minerals from terrestrial impact structures as well as Lunar and Martian samples.

The book should be divided into seven chapters. The first chapter contains the basic definitions of cathodoluminescence. Its application in the geosciences is also shortly described. The second chapter describes fundamentals of shock metamorphism as a leading geological process on surface of the planetary bodies. The following chapter deals with a cathodoluminescence microcharacterization of shock metamorphic rocks from terrestrial impact craters. The fourth chapter gives an overview of the impact diamonds and their CL properties. The fifth chapter provides details on the Lunar samples and their mineralogical and geological consequences. The sixth chapter describes the potential of CL instrumentation on the in-situ analysis of the Martian sediments. The last chapter contains a systematic CL study of Mn carbonates, which can aid to understand about the ancient life forms of Earth or Mars.

The editor of this book is highly appreciated because this book represents a fruitful international collaboration between scientists from Canada, France, Germany, Hungary, Italy, Japan, and Switzerland.

Contents

Contributors

Bernadett Bajnóczi, Institute for Geochemical Research, Hungarian Academy of Sciences, H-1112, Budapest, Budaörsi str. 45, Hungary,
e-mail: bajnoczy@geochem.hu

Vincent Barbin, GEGENAA, EA 3795, Université de Reims Champagne-Ardenne, France, e-mail: vincent.barbin@univ-reims.fr

Paul Gille, CNRS LPCE, Laboratoire de Physique et Chimie de l'Environnement, Orléans, France, e-mail; Paul.Gille@cnrs-orleans.fr

Thomas Götte, Institute for Geological Sciences, University of Bern, Baltzerstrasse 1+3, CH-3012 Bern, Switzerland, e-mail: thomas.goette@geo.unibe.ch

Jens Götze, TU Bergakademie Freiberg, Institute of Mineralogy, Brennhausgasse 14, D-09596 Freiberg, Germany, e-mail: goetze@mineral.tu-freiberg.de

Arnold Gucsik, Max Planck Institute für Chemie, Abteilung Geochemie, Joh.-J.-Becherweg 24., Mainz, D-55128, Germany,
e-mail: gucsik@mpch-mainz.mpg.de

Ulf Kempe, TU Bergakademie Freiberg, Institute of Mineralogy, Brennhausgasse 14, D-09596 Freiberg, Germany, e-mail: goetze@mineral.tu-freiberg.de

Richard Leveille, Canadian Space Agency, St-Hubert, Québec, Canada,
e-mail: Richard.Leveille@space.gc.ca

Márta Polgári, Institute for Geochemical Research, Hungarian Academy of Sciences, H-1112, Budapest, Budaörsi str. 45, Hungary, e-mail: polgari@geochem.hu

Giovanni Pratesi, Dipartimento di Scienze della Terra , Università di Firenze, Via G. La Pira 4, 50121 Firenze, Italy; Museo di Scienze Planetarie, Provincia di Prato, Via Galcianese 20/H, 59100 Prato, Italy, e-mail: Giovanni@unifi.it

Claire Ramboz, CNRS ISTO, Institut des Sciences de la Terre, Université d'Orléans, OSUC, France, e-mail: cramboz@cnrs-orleans.fr

Karl Ramseyer, Univ. Bern, Institute of Geological Sciences, Baltzerstrasse 1+3, 3012 Bern, Switzerland, e-mail:ramseyer@geo.unibe.ch

Kazue Tazaki, Department of Earth Sciences, Faculty of Science, Kanazawa University, Kakuma, Kanazawa, Ishikawa 920-1192, Japan,
e-mail: kazuet@kenroku.kanazawa-u.ac.jp

Laurent Thirkell, CNRS LPCE, Laboratoire de Physique et Chimie de l'Environnement, Orléans, France,
e-mail: thirkell@cnrs-orleans.fr

Roger Thomas, CNRS LPCE, Laboratoire de Physique et Chimie de l'Environnement, Orléans, France, e-mail: Roger.Thomas@univ-orleans.fr

Tamás Vigh, Mangán Ltd. Úrkút, H-8409, Hungary, e-mail: manganvigh@vnet.hu

Hiroaki Watanabe, Department of Earth Sciences, Faculty of Science, Kanazawa University, Kakuma, Kanazawa, Ishikawa 920-1192, Japan,
e-mail: watanabe@kenroku.kanazawa-u.ac.jp

Chapter 1
Physical Principles of Cathodoluminescence (CL) and its Applications in Geosciences

Jens Götze and Ulf Kempe

1.1 Introduction

Luminescence spectroscopy has been developed into standard analytical techniques in different fields of science and technology. In geosciences, cathodoluminescence (CL) is widely used for mineralogical and petrological investigations. CL is an excellent method to supplement observations by optical polarizing microscopy and other conventional analytical methods such as X-ray diffraction (XRD), microprobe analysis, or scanning electron microscopy (SEM).

Distinct CL properties of certain minerals such as elements (diamond), sulphides (sphalerite), oxides (periclase, corundum, cassiterite), halides (fluorite, halite), sulphates (anhydrite), wolframates (scheelite), phosphates (apatite), carbonates (calcite, dolomite, magnesite) or silicates (feldspar, quartz, zeolites, kaolinite, zircon) allow rapid identification of the different mineral constituents and their distribution within rocks using CL microscopy. This is of special interest if samples contain small inclusions, consist of fine-grained material, and/or of minerals with similar optical or crystallographic properties. Small grains of accessory phases can often rapidly be recognized if displaying bright CL, even in cases where only one extremely small grain appears in the whole sector viewed. CL microscopy alone provides at least a clear differentiation of different phases even in samples with high contents of non-crystalline components or extremely heterogeneous material.

Another point of interest is that the CL of mineral phases (e.g., quartz, feldspar, zircon, apatite, fluorite, etc.) is often highly variable depending on the composition and some specific conditions during formation (e.g., Ramseyer and Mullis 1990; Morozov et al. 1996; Götze et al. 2000, Kempe et al. 1991, 1999, 2000; Götze et al. 2001; Gorobets and Rogojine 2002; Kempe and Götze 2002). The knowledge of the typomorphic luminescence characteristics of minerals can be used to reconstruct the processes of mineral formation, alteration and diagenesis. For instance, the diversity of CL colours in detrital quartz of sediments (e.g. quartz sands) provides a basis for provenance studies in geology (e.g., Zinkernagel 1978; Götze

Jens Götze (✉)
TU Bergakademie Freiberg, Institute of Mineralogy, Brennhausgasse 14, D-09596 Freiberg, Germany
e-mail: goetze@mineral.tu-freiberg.de

A. Gucsik (ed.), *Cathodoluminescence and its Application in the Planetary Sciences*,

and Zimmerle 2000; Richter et al. 2001). Furthermore, the sequence of crystallization can be ascertained and detrital or newly formed authigenic components can easily be distinguished as well as secondary alterations revealed (e.g. Richter et al. 2001). Furthermore, CL is an outstanding method to study radiation damage in minerals due to radioactive decay (e.g., Meunier et al. 1990; Owen 1988; Kempe et al. 2000).

The close relationship between crystal-chemical properties and CL characteristics of minerals is the basis of detailed studies on internal textures, zonal growth and distribution of trace elements within solid phases. The specifics of CL allow revealing of such internal textures, which are not discernible using conventional microscopy. The results can provide information about the conditions during crystal growth, defect density, incorporation of certain trace elements, the inheritance of relic cores of older crystals, etc. The detected heterogeneities or zones can subsequently be investigated very effectively by additional analytical methods with high spatial resolution such as microprobe, PIXE, laser ablation ICP-MS or SHRIMP for microchemical analysis or detailed isotope studies (e.g., Habermann et al. 1998, 1999, 2000b; Götze et al. 1999a–d; Pagel et al. 2000; Blanc et al. 2000; Kempe et al. 1999, 2000, 2002).

Additional information about the crystal structure and trace-element distribution can be obtained by luminescence spectroscopy. The detection of luminescence spectra in combination with other techniques such as ESR allows the determination of the nature of impurity ions, molecules and other centres in solids as well as the valence of the ions, their coordination and their local symmetries (e.g., Mariano and Ring 1975; Gaft et al. 1997, 2000a, b, 2001, 2002; Mikhail et al. 1999; Pagel et al. 2000; Blanc et al. 2000; Kempe et al. 2002).

As the luminescence process is the result of multiple interactions within the crystal lattice, spectral information is not limited to the emission of light. A brief introduction to the fundamental physical principles of luminescence will therefore be given to provide a better understanding of the different luminescence mechanisms and how they may influence the spectral information.

1.2 Physical Basics of Luminescence

1.2.1 Principle Processes of Luminescence Production

Luminescence (luminescence glow) is a common phenomenon in solids that results from an emissive transition in anions, molecules, or a crystal from an excited electronic state to a ground or other state with lesser energy (Marfunin 1979). According to the different lifetime of luminescence emission it can be differentiated between *fluorescence* with a lifetime of $< 10^{-8}$ s after excitation and *phosphorescence*, where the emission occurs later than 10^{-8} s after excitation.

Although it is rather difficult to describe the whole luminescence phenomenon in detail, a unique property of luminescence is the transformation of diverse kinds

of energy into visible light. In general it is possible to distinguish the following main processes: (1) absorption of excitation energy and stimulation of the system into an excited state, (2) transformation and/or transfer of the excitation energy, and (3) emission of light and relaxation of the system to a non-excited state (Marfunin 1995). The last two stages are mainly depending on crystallo-chemical factors such as the types and structures of anions, molecules, and lattices as well as of specific luminescence centres, whereas the first stage is also strongly influenced by the mode of excitation.

According to the mode of excitation several types of luminescence can be distinguished: photo-, cathode-, thermo-, electro-, chemo-, bio-, tribo-, crystallo-, and X-ray luminescence. Cathodoluminescence is one of the various processes, which are created during irradiation of a solid surface with an electron beam (Fig. 1.1).

The penetration depth of electrons and accordingly, the excitation depth from a crystal depend on the energy of the electrons and are commonly in the range of 2-8 μm (Fig. 1.2a). However, energy transfer may occur in a crystal provided by the lattice, anion groups, or interaction of neighbouring lattice defects, and then the emission site may be far away from the site of excitation (Remond et al. 2000; Kempe et al. 2000; cf. Fig. 1.2b). The CL intensity is, in general, proportional to the acceleration voltage and current density, but the power level used is limited by the destruction of the specimen or of specific defects including luminescence centres under electron bombardment.

There are different models to explain the various processes during luminescence production. The luminescence processes can be described based on a scheme of the energy levels in a crystal by using the band theory and the ligand field theory. In insulators and semiconductors a band gap (forbidden zone) exists between the valence band and the conduction band, whereas conductors show overlapping valence and conduction bands (Fig. 1.3). Additional energy levels in the forbidden zone between valence band and conduction band can be occupied due to the existence

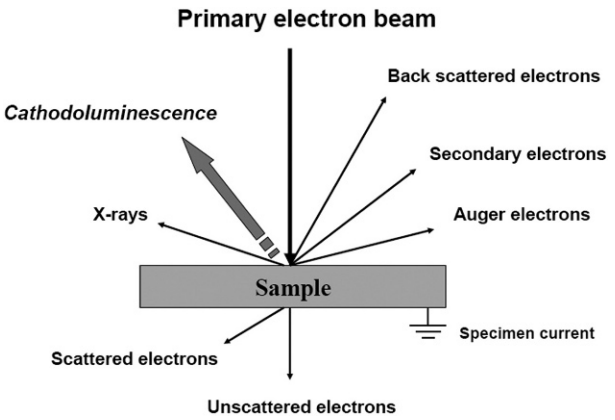

Fig. 1.1 Schematic illustration of interactions of an electron beam with a solid surface (modified after Yacobi and Holt 1990)

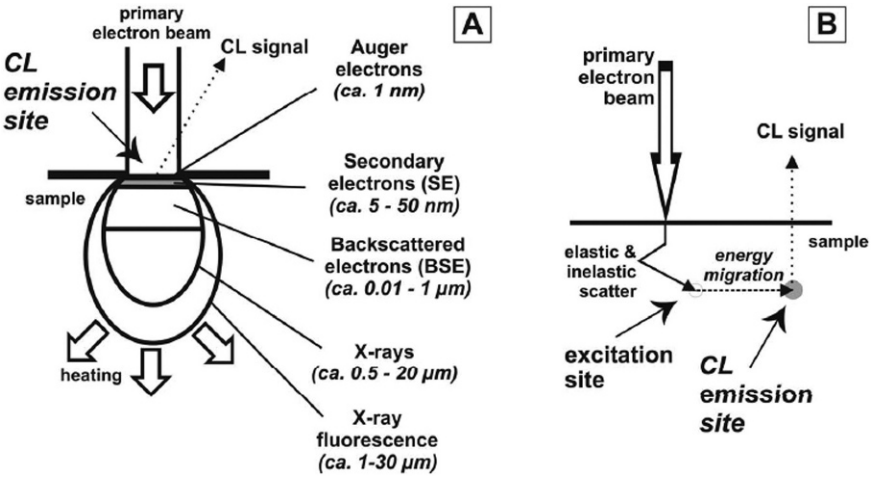

Fig. 1.2 Interaction of an electron beam with a solid showing the resulting signals in dependence on the penetration depth of electrons **A** – direct excitation of cathodoluminescence by secondary electrons yields escape depths of tenth of nm or less; **B** – energy migration causes significant separation of excitation and emission site (eg in samples of silicates, phosphates, molybdates and wolframates)

of luminescence centres (impurity ions, lattice defects) (Fig. 1.4). These luminescence centres are defect centres in crystals, which can be related to pure lattice defects (e.g. vacancies or other electron-hole centres) or to incorporated impurities of foreign ions or atoms. They can be classified by their electronic structure into (Marfunin 1979):

(1) transition metal ions (e.g., Mn^{2+}, Cr^{3+}, Fe^{3+}),
(2) rare earth elements ($REE^{2+/3+}$),
(3) actinides (particularly uranyl ions UO_2^{2+}),

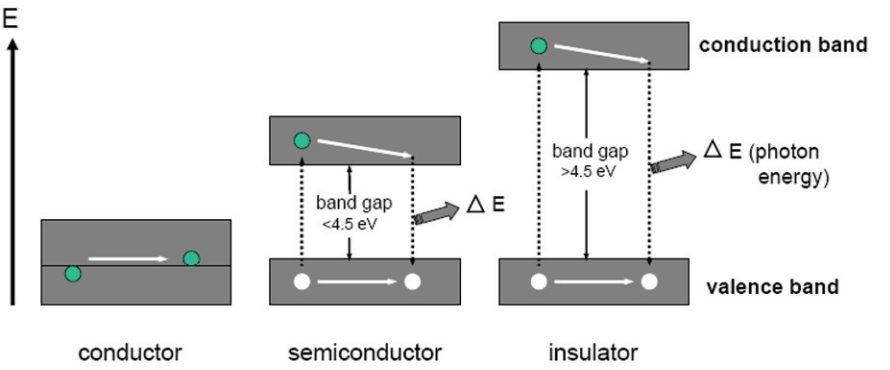

Fig. 1.3 Schematic energy levels in a band scheme for different crystal types: (**a**) conductor with overlapping valence and conduction band, (**b**) semiconductor with small interband

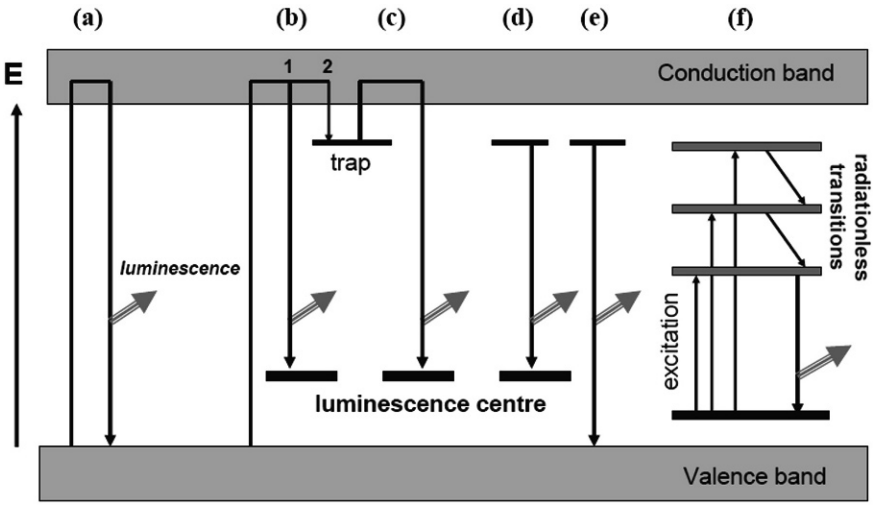

Fig. 1.4 Processes of charge transfer and luminescence production in insulator crystals (modified after Krbetschek et al. 1998) (**a**) Excitation of an electron by high-energy particles or photons from the valence band to the conduction band and transition back to the valence band (*intrinsic luminescence*); (**b**) Excitation of electrons and recombination with an activator and resulting luminescence emission of a photon with energy $h \cdot \gamma$ (1) or trapping of the electron (2); (**c**) a trapped electron can be stimulated either thermally or optically to the conduction band and recombine with an activator (eg, thermoluminescence); a direct transition of the electron to the recombination centre (**d**) or to the valence band (**e**) is also possible; (**f**) excitation of several energy levels by absorption of photons and resulting radiation-less and emissive transitions (luminescence emission), respectively

(4) heavy metals (mercury-like ions such as Pb^{2+}),
(5) electron-hole centres (molecular ions S_2^-, O_2^-, F-centres, etc.).

Other defects such as dislocations and clusters may also take part in the luminescence production process.

The occurrence of luminescence can be described in terms of three elementary processes: excitation (absorption), emission, and radiation-less transitions. When exciting the crystal with various kinds of energy, a system with non-filled orbitals pass from the ground state to an excited state, which is attended by the appearance of an absorption band in the optical spectrum (i.e. excitation/absorption). The luminescence system can return from the excited state to the ground state by emissive transitions or through radiation-less transitions (e.g., absorption or emission of lattice vibrations = phonons). In the case of emissive transition, the wavelength of the emitted light (photon energy) depends on the energy difference between the excited state and the ground state.

In the case of electron transitions between the valence and conduction band, the energy reflects the band gap energy and the luminescence is called *intrinsic luminescence* in sensus stricto. If defects related to impurity atoms/ions (activators) are involved in the luminescence process it is called *extrinsic luminescence* and the energy (wavelength) of the emitted luminescence can be related to the type of the

impurity defect. Electron-hole centres without changes in the general crystal chemistry (including vacancies etc.) may be regarded as "intrinsic" defects and the related luminescence also called "intrinsic" in sensus lato. Quite often, the glow of luminescent insulator crystals and minerals is due to transitions within the limits of the ion activator levels without participation of energy bands (e.g., Cr^{3+} in Al_2O_3 with an interband distance of 7.4 eV). Band transition in these crystals only occurs during excitation with high-energy radiations such as X-rays or electrons.

1.2.2 Crystal Field Theory and Luminescence Spectra

For the interpretation of luminescence spectra, the interactions of luminescence centres with other constituents in the surrounding crystal lattice have to be taken into consideration. The crystal field theory describes the origin and consequences of interactions of the surroundings on the orbital energy levels of a given ion (Burns 1993). In the case of a strong interaction between the ion and the lattice, the diagram of levels defining the absorption/excitation spectra will not sufficient for exact description of the luminescence process. Beside the three basic processes excitation (absorption), emission and non-radiative transitions, one has to consider as an additional fact the interaction of the activator ion with the surrounding lattice (ligands). These interactions lead to a change in the local symmetry of the activator ion under the influence of the crystal field. Furthermore, changes in the symmetry result in a splitting of the electron energy levels of the activator ion (Fig. 1.5). Excitation

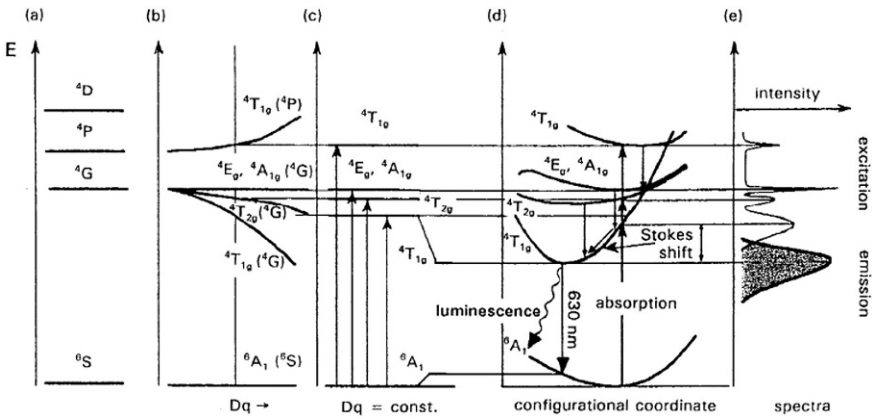

Fig. 1.5 The sensitivity of the electronic states of the Mn^{2+} ion in octahedral coordination to changes in the intensity of the crystal field splitting Dq and representation in a configurational coordinate diagram (modified after Medlin 1968 and Marfunin 1979). (**a**) States as defined by group theory at zero crystal field intensity (**b**) Effect of increasing crystal field strength; some states are independent of Dq, others shift up or down in energy (**c**) Energy states for fixed Mn^{2+}-O distance in calcite (**d**) Configurational coordinate diagram showing changes in state energy with variations in Mn^{2+}-O distance The centre of the ground state ($^6A_1$) is nominally the equilibrium distance (**e**) Excitation and emission spectra, Stokes' shift and the effect of curvature on spectral band width

of the ion and subsequent emission are separated by a time interval in which the surrounding ligands shift to a new equilibrium position with a new distance to the excited luminescent ion. During this process, some of the excitation energy is transferred to the crystal lattice resulting in a shift (Stokes shift) of the emission band in relation to the corresponding absorption band towards longer wavelengths (i.e. to lower energies).

The process of excitation and emission of an individual luminescence centre can thus be described using a configurational coordinate diagram (Fig. 1.6). This scheme shows the potential energy curves of the absorbing centre as a function of the relative distance R of the nucleus to the equilibrium position (electron in the ground state with vibrational level $n = 0$). Due to the excitation energy E_a, the electron is promoted from the ground state to a higher vibrational state of the excited state. The position and width of the absorption band are determined by the central position of the ground state and the shape of the potential curve (Fig. 1.6).

Since the electron transitions are faster ($\Delta t \sim 10^{-16}$s) than lattice relaxation ($\Delta t \sim 10^{-13}$s), the transition occurs as a (nearly) "vertical" transition (Franck-Condon principle). After absorption, the system relaxes at first into the lowest level of the excited state $m = 0$ accompanied by emission of phonons, and then the electron returns into the ground level (luminescent emission with energy E_e). The wavelength and width of the emission band are dependent on the potential curve of the excited state. The energy difference between absorption and emission is called the Stokes shift. The horizontal displacement ΔR is the cause of line broadening. The larger the value of ΔR, the broader are the absorption and the emission band. The displacement is temperature dependent and hence the radiation-less return to

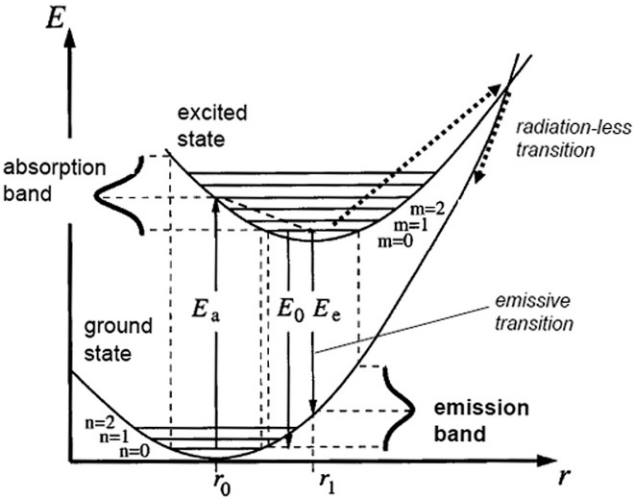

Fig. 1.6 Configurational coordinate diagram for transitions according to the Franck-Condon principle with related absorption and emission spectra, respectively (modified after Yacobi and Holt 1990); radiation-less transitions are possible via the point of intersection of the potential curves (eg at higher temperatures)

the ground state via the point of intersection of the potential curves becomes more important at higher temperatures (i.e. leads to the effect of "thermal quenching" of luminescence at higher temperatures).

The activator-ligand distances in the different states and the slopes of the energy levels depend on the extent of the crystal field interaction (expressed as crystal field splitting parameter $\Delta = 10Dq$). The stronger the interaction of the activator ion with the lattice, the greater are the Stokes shift and the width of the emission line. Factors influencing values of Δ or $10Dq$ are the type of cation, the type of ligand, the interatomic distance, pressure, temperature, and the symmetry of the ligand environment (Burns 1993). Accordingly, the luminescence of a given ion may strongly depend upon its position in the crystal and on the crystal field. The following general conclusions can be drawn from the facts mentioned above for the characteristics of luminescence spectra:

1. If the electronic energy levels responsible for much of the absorption and emission of photons are not involved in bonding to nearby atoms, the influence of the crystal field is weak and results only in a small splitting of the energy levels. Accordingly, the resulting luminescence emission is characterized by narrow emission lines without a significant Stokes shift. This is the case for most of the trivalent ions of the REEs, where the electron transitions within the 4f orbitals are shielded from the influence of the crystal field by the electron shells of the 5s and 6p orbitals. Accordingly, the emission spectra are specific for each REE^{3+} ion, relatively independent on the crystal structure of the host crystal (Fig. 1.7). The same effect may be found for ions of other elements with similar electronic structure.

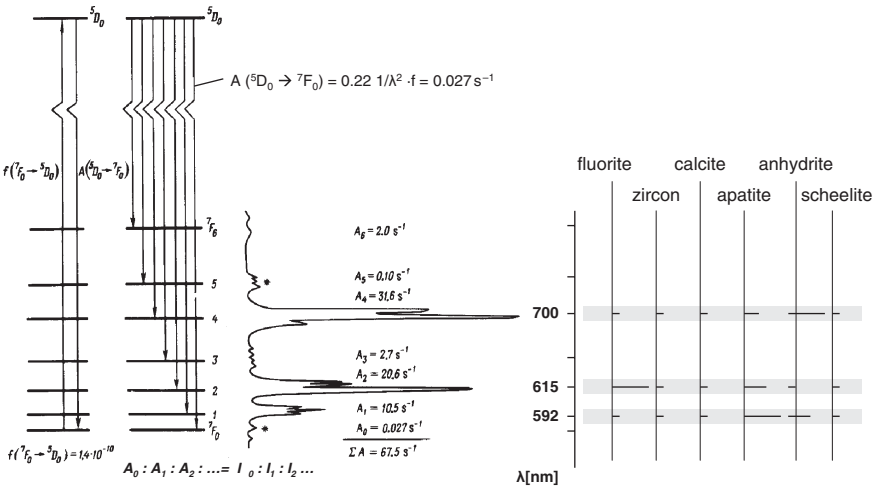

Fig. 1.7 Energy levels diagram and emission spectrum of Eu^{3+} in $Eu_2(SO_4)_3 \cdot 8H_2O$ (modified after Marfunin 1979); f - oscillator strength (effectiveness of excitation); A - probability of emission transitions The spectrum shows narrow emission lines, which are specific of the activator ion Eu^{3+}. On the right, the positions and relative intensities of Eu^{3+} emission lines in certain minerals are shown (data from Blanc et al. 2000)

2. If the electron transitions take place in energy levels which are influenced by the local crystal field, luminescence emission spectra show relatively broad bands (Fig. 1.8). Because of the dependence of the Stokes shift on the strength of the local crystal field (field parameter *Dq*), the wavelength of the luminescence emission of each activator element varies from mineral to mineral and is specific for the crystal structure of the host crystal. Hence, one type of ions can produce a great variety of luminescence spectra. For examples, Mn^{2+} is an activator ion with partially filled 3d orbitals in the outer shell which can be influenced by the crystal field. Tetrahedrally coordinated Mn^{2+} gives a green-yellow emission, whereas the emission from octahedrally coordinated Mn^{2+} is in the orange-red range. This effect can be observed for the Mn^{2+} activated luminescence in carbonates, which show shifting emission maxima (and with that visible luminescence colours) in dependence on the crystal type (Fig. 1.8). Shifts of the luminescence emission bands can also be observed in mixed crystals in dependence on the chemical composition. These effects are detectable, for instance, in the solid solutions of the plagioclases (Fig. 1.9). The red luminescence emission, which is

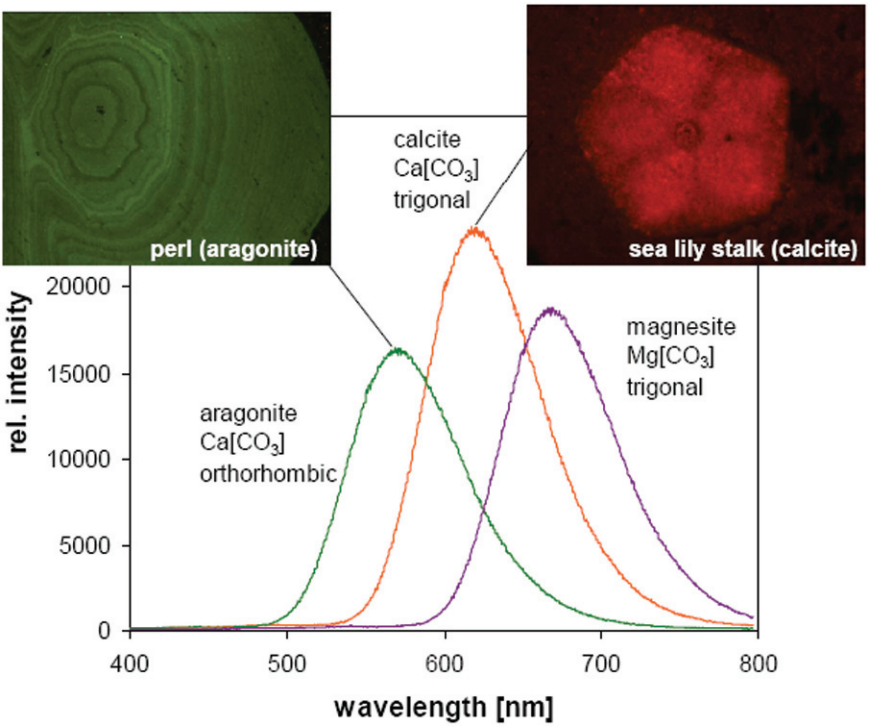

Fig. 1.8 CL emission spectra of Mn^{2+} in different carbonate minerals showing a typical broad band and a shift of the emission maxima in dependence on the structure (crystal field) of the host crystal The carbonate minerals differ in structure (trigonal or orthorhombic) and chemical composition, respectively, which both influence the local crystal field of the Mn^{2+} centre Accordingly, the CL emission spectra are specific of the host crystal

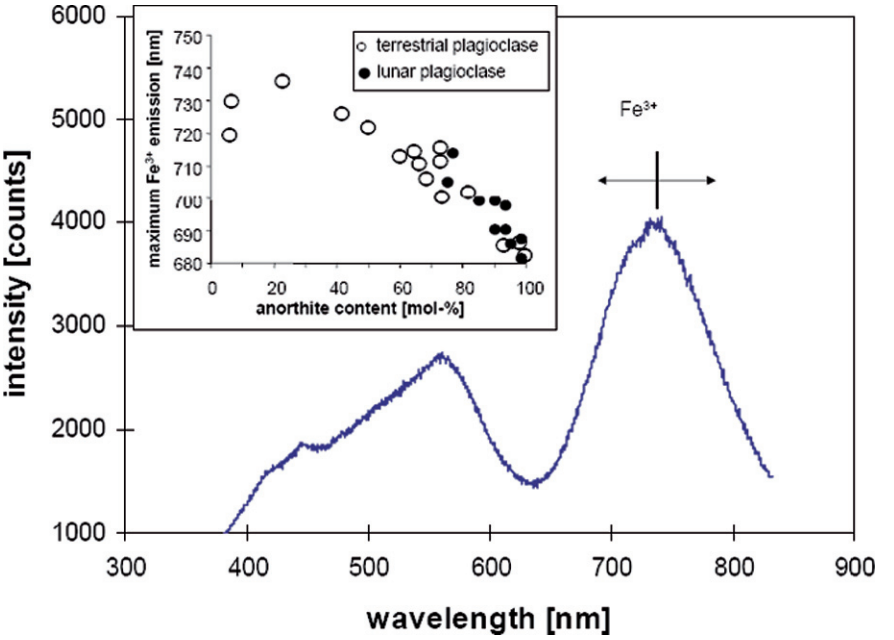

Fig. 1.9 The spectral position of the Fe^{3+}-activated CL emission band in plagioclases of terrestrial (*empty circles*) and lunar (*black circles*) origin in relation to the anorthite content (modified after Krbetschek et al. 2002)

explained by Fe^{3+} lattice defects, shifts between ~680 and 750 nm with varying feldspar composition. The observed effects can be explained by the influence of the structural state of the feldspar and the site occupancy of the trivalent iron (Krbetschek et al. 2002). Similar effects were also detected in alkali feldspars with varying Na-K composition (Finch and Klein 1999; Brooks et al. 2002).

1.2.3 Effects of Sensitizing and Quenching

Natural samples commonly contain a great variety of different luminescent and non-luminescent centres and an interaction between two or more activators present in a crystal can take place resulting in changes in their luminescence spectra and intensities due to transfer of excitation energy from one centre to another. These processes may result in sensitizing or quenching of the luminescence emission and have particularly to be considered in quantitative measurements or when some emissions are strongly enhanced or quenched completely.

Sensitized luminescence is the luminescence of ions excited as a result of the energy transfer from other ions excited by absorption of incident energy. The energy transfer from the sensitizer to the activator can be accomplished in several ways (Marfunin 1979): (1) emission-reabsorption ("cascade" luminescence),

(2) radiation-less resonance, (3) radiation-less nonresonance. Typical sensitizer ions are (i) ions with intensive absorption bands in the UV region (e.g., Tl^{+}, Cu^{+}, Pb^{2+}, Ge^{4+}) for sensitization of Mn^{2+}, (ii) ions of transition metals (e.g., Cr^{3+}, Mn^{2+}) for sensitization of REE^{3+}, (iii) REE^{2+}, REE^{3+} or uranyl ions ($UO_2{}^{2+}$) for sensitization of trivalent ions of REE (Marfunin 1979).

Quenching (luminescence decay) is another phenomenon which can result from transfer of the excitation energy. Various types of quenching can be distinguished such as (i) concentration quenching (self quenching) at high concentration levels, (ii) quenching by ions with intense charge transfer bands, (iii) quenching due to lattice defects or (iv) thermal quenching.

The decay of luminescence intensity due to high activator concentration is called *concentration quenching* (self quenching) and can be explained by interactions between ions of the same kind which are more effective at high activator concentrations (Fig. 1.10).

Some ions such as Fe^{3+}, Fe^{2+}, Co^{2+}, and Ni^{3+} have broad and intense charge transfer bands in the absorption spectrum, quenching the glow of all activators whose emission bands are overlapped by it. The *quenching by ions with intense charge transfer bands* influences especially the visible and near UV region, whereas luminescence emissions in the IR region are more or less unaffected. Because of this effect, the luminescence intensity is often not only a result of the activator content but of the ratio of activator and quencher ions (see also the example of apatite given below).

Quenching due to lattice defects can occur at high concentration levels of electron-hole centres if the crystal structure is damaged by mechanical processes, radiation, growth defects, impurities, etc. These lattice defects can create new

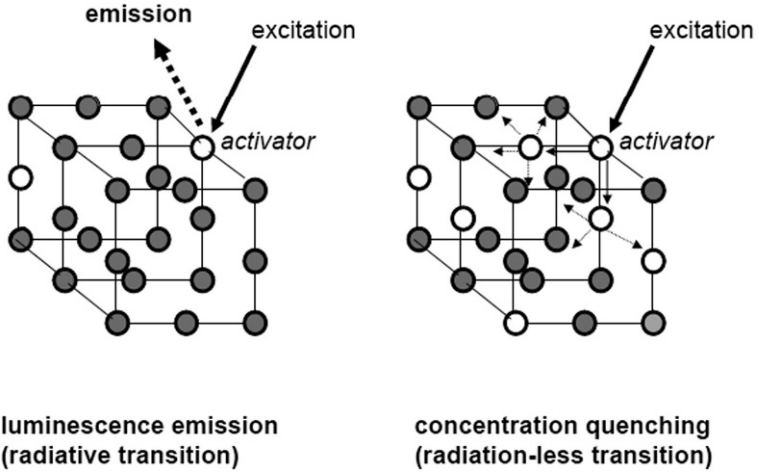

Fig. 1.10 Effect of concentration quenching (self quenching) due to high activator concentration (**a**) Excitation and luminescence in a crystal with low activator concentration (**b**) In the case of high activator concentrations some of the excitation energy is quantitatively transferred to other activator ions with resulting quenching of the luminescence emission of the ion

energy levels between the conduction band and the valence band resulting in absorption of the excitation energy, radiation-less energy transfer or emission at lower frequencies.

Another process which can lower the luminescence intensity is *thermal quenching*, which may occur at elevated temperatures. During irradiation of a sample with high-energy particles (e.g., electrons, ions), parts of the energy can be transformed into heat. This energy or external heating of a sample may rise electrons from lower levels of the excited state to the point of intersect of the energy curves (compare Fig. 1.6) and influences the energy transfer processes. The electrons do not return to the ground state by emissive transitions, but via the point of intersect resulting in radiation-less transitions.

1.3 Practical Aspects of CL Microscopy and Spectroscopy

1.3.1 Instrumentation, Sample Preparation and Documentation of CL Spectra and Images

CL can be observed on a wide variety of analytical instruments using electron beams for excitation. On one hand, there is a group of CL detectors working with high spatial resolution in combination with scanning electron microscopes or microprobes. On the other hand, different combinations of CL detectors with light microscopes have been performed providing "true colour" luminescence images. The electron guns of these CL microscopes may be operated as "cold cathode", i.e. the discharge takes place between the cathode and anode in an ionized gas, or as "hot cathode", i.e. the electrons are emitted from a heated filament or other cathode type. The characteristics and advantages of these different techniques are discussed in more details by Götze and Kempe (2008). Special equipments were developed for the simultaneous analysis of petrographic samples with CL and energy-dispersive X-ray spectroscopy (Vortisch et al. 2003) or the investigation of macro samples (Marshall 2004).

The sample preparation for CL investigations mainly depends on the type of the sample and the type of the CL equipment (Fig. 1.11). Polished thin sections are commonly used in all types of CL equipments, whereas polished sections as well as polished sample pieces can only be analysed in equipments, where the electron beam and signal detection are arranged in reflection geometry. In some types of "hot-cathode" CL microscopes, transparency of the sample is necessary, since excitation and signal detection are provided from opposite sites. Special sample preparation was developed for the combination of CL with fluid inclusion studies, which allows investigation of both features on the same sample piece. Furthermore, pressed tablets with smooth sample surfaces can be used, if the sample consists of very fine-grained material (e.g. clay minerals; Götze et al. 2002). In some cases, the use of grain preparates for CL studies in sediments was also discussed (Marshall 1988).

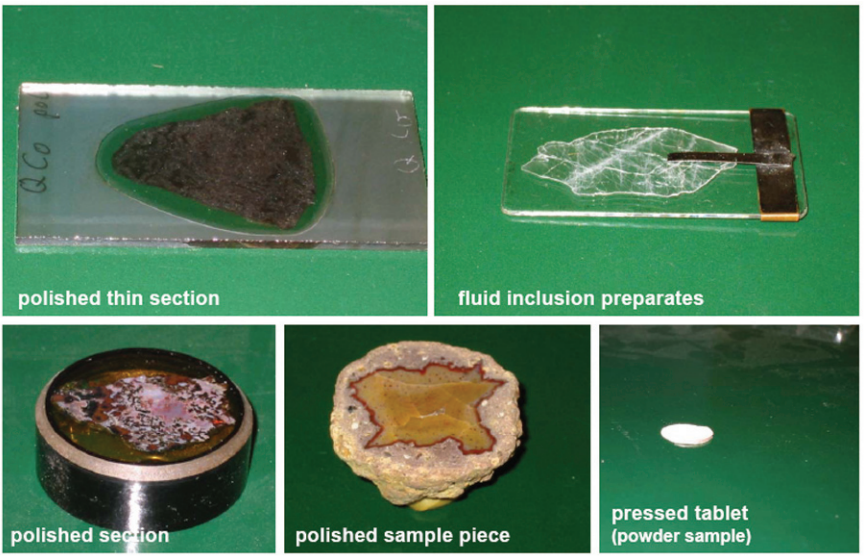

Fig. 1.11 Sample types commonly used for CL microscopy and spectroscopy using OM- and SEM-CL equipments

As mentioned before, the basic processes of CL involve the excitation of an electron to a state of higher energy followed by the emission of a photon with energies in the UV, visible or IR wavelength ranges when the electron returns to a state of lower energy. The advantages of CL over UV excited photoluminescence are much higher luminescence intensities due to a much greater energy density in electron excitation, which makes CL applicable to a greater variety of minerals and synthetic materials. On the other hand, excitation in CL is not energy-specific in contrast to most applied photoluminescence techniques (Gaft et al. 2005). Modern laser techniques with tuneable laser systems provide signal intensities comparable to those of CL.

Modern CL equipments can detect the optical signal of luminescence visually or by spectral measurements. CL can reveal microtextures and variations in the chemical composition of solids which cannot be detected with other analytical methods (Fig. 1.12a).

Recent developments allow to capture luminescence images “on-line” during CL operations by means of an adaptable digital video-camera. This configuration allows the acquisition of digital signals from the video camera and the processing of high-contrast colour patterns produced by CL as real colour images, and in combination with computer-aided image analysis the quantification of different mineral phases (Evans et al. 1994; Götze and Magnus 1997). Alternatively, CL spectra with high local resolution down to about 1 µm can be obtained using digital triple-grating spectrographs with CCD detectors attached to the CL equipments by mirror optics or light fibre-guides. In these configurations, different defects and trace element impurities, their valence and structural position can be detected with high spatial resolution (Fig. 1.12b).

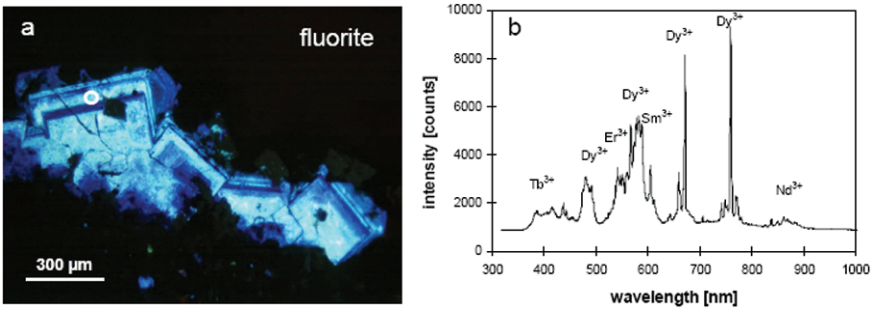

Fig. 1.12 (**a**) Volcanic fluorite crystal from Chemnitz, Germany with strong oscillatory growth zoning that is only visible under CL (**b**) The CL spectrum of a distinct greenish-blue zone (*circle in* **a**) reveals the dominant activation of the luminescence by Sm^{3+} and Dy^{3+} ions

1.3.2 Interpretation of the CL Signals

As shown above, the intensity of the CL signals is influenced by a number of factors including those of experimental conditions (analytical factors) and others deriving from the sample characteristics. The analytical factors include sample preparation (sample surface, thickness, etc.), sample coating (quality, thickness, material), factors deriving from the specifics of the equipment used, and all analytical conditions (acceleration voltage, beam current, beam size, beam mode, vacuum, temperature, etc.). For quantitative measurements and comparison of the results it is therefore necessary to work under standardized conditions. The sample-related factors are all those arising from the properties of the crystal or crystal area under investigation. Some examples for the complex interplay of several sample-related factors are given below.

The emission intensity (I_e) of luminescence is described by the equation $I_e = N_m \cdot h \cdot U_{mn} \cdot A_{mn}$ where N_m is the number of ions in an excited level *m* determined by the effectiveness of excitation, i.e. by the absorption coefficient (oscillatory strength), $h \cdot \upsilon_{mn}$ is the energy of electron transition from the excited level m to energy level n, and A_{mn} is the probability of emissive transition. Accordingly, the number of activators should generally correlate with the luminescence intensity. Various trace elements in different minerals were investigated to quantify their contents by use of quantitative luminescence spectroscopy (e.g., Habermann et al. 1998, 1999, 2000a; Götze et al. 2000; Häger and Dung 2003).

First promising results were published to relate the manganese content in carbonates with the intensity of the Mn^{2+} activated emission band (e.g., El Ali et al. 1993; Habermann et al. 1998; Götte and Richter 2004). Habermann et al. (1998) proposed a linear correlation between the Mn^{2+} activated spectral CL intensity and the Mn content in calcite in the range of 100 ppb up to 2000 ppm. Götte and Richter (2004) showed that there is a correlation of the Mn content in different carbonate minerals and the perceived CL intensity (Fig. 1.13). However, natural minerals commonly contain a great variety of different centres, which result in complex emission spectra

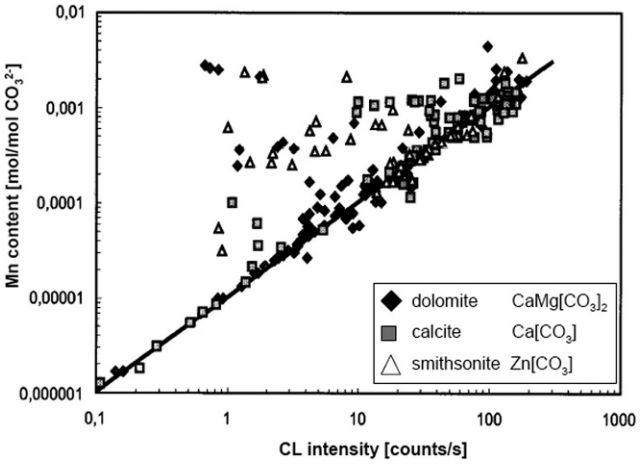

Fig. 1.13 Correlation of the intensity of the Mn^{2+}-activated CL emission band and the Mn content in different trigonal carbonate minerals (modified after Götte and Richter 2004) Deviations from the linear correlation (decreased luminescence intensity) may be explained by effects of concentration quenching (self-quenching) and quenching effects due to elevated contents of iron

that are often difficult to interpret. Therefore, it is very difficult to correlate the visible bulk CL intensity (especially in panchromatic SEM images) directly with the concentration of a specific activator, since the visible signal may be the result of several overlapping emission bands from different activators. Additionally, the interaction of activators, sensitizers and quenchers as well as the specific analytical conditions may influence the CL signal.

In some cases, the luminescence of certain activators can be prevented by a strong luminescence emission of another activator. In apatite crystals with high amounts of Mn^{2+}, the CL emission of certain rare earth elements may be hidden although the contents of REE are in the range of several tenth of ppm (Kempe and Götze 2002). The sensitivity of different types of luminescence centres to activation energy and life-time of the excited state is especially used in other luminescence types (e.g. time-resolved laser-induced luminescence) to differentiate between different defect centres (e.g. Gaft et al. 2005). Emission spectra of laser-induced time-resolved luminescence could reveal luminescence emissions of Eu^{2+} in the presence of manganese (Fig. 1.14). However, the Eu^{2+}-activated luminescence is only detectable within a very short delay time (40 ns). Already 50 µs after excitation, only the strong Mn^{2+} activated luminescence is detectable. In principle, similar time-resolved luminescence investigations may be also undertaken with CL equipments.

The intensity of CL activated by certain trace elements in minerals is influenced by several additional factors. For instance, apatite crystals with very high concentrations of manganese (ca. >2 wt-% MnO) show strong effects of self-quenching resulting in decreasing luminescence intensities, even in areas with very low concentrations of other trace elements including iron (Fig. 1.15). In other cases, the luminescence intensity is not only dependent on the manganese concentration,

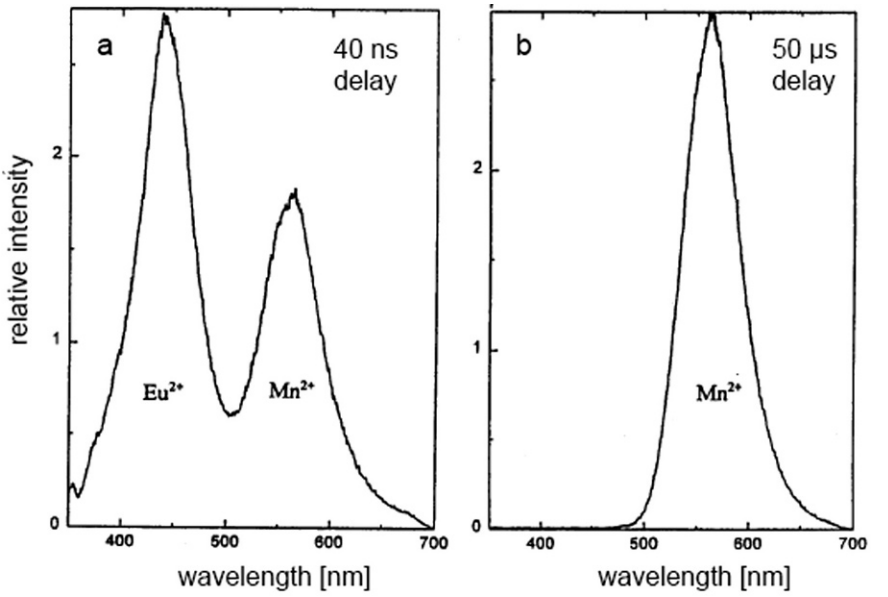

Fig. 1.14 Emission spectra of laser-induced time-resolved luminescence (excitation wavelength 337 nm) taken from the same sample of an apatite crystal from Ehrenfriedersdorf, Germany Eu^{2+}-activated luminescence is only detectable with very short delay time (**a** - 40 ns) whereas after 50 µs delay time only Mn^{2+} luminescence is detectable (**b**)

but also on the content of iron as an effective luminescence quencher. Accordingly, the luminescence intensity in some strongly zoned apatite crystals is not correlated with the manganese content but with the Mn/Fe ratio in the different zones (Fig. 1.16).

An additional factor, which has to be considered in CL measurements using a stationary beam, is irradiation time. Because of the different life-time of the excited state of luminescence centres and the instability of some types of centres during electron irradiation, the luminescence spectra can change dramatically in dependence on irradiation time. This is due to several interactions of the electron beam with the crystal leading to heating of the sample (thermal quenching), destruction of luminescence centres, and conversion of precursor centres into luminescence active ones, and the formation of new defect centres. Figure 1.17 shows the effect of thermal quenching due to heating during electron irradiation of an apatite crystal.

Effects of transformation of defect centres can especially be observed in crystals with CL related to the presence of electron-hole centres. Such materials often show transient luminescence properties. One example is quartz where some of these effects can be observed in the several cases. The irradiation of hydrothermal quartz with an electron beam results in the conversion of diamagnetic precursor centres of the type $[AlO_4/M^+]^0$ into paramagnetic $[AlO_4]^0$ centres, which is associated with the loss of the luminescence emission in the blue spectral range around 400

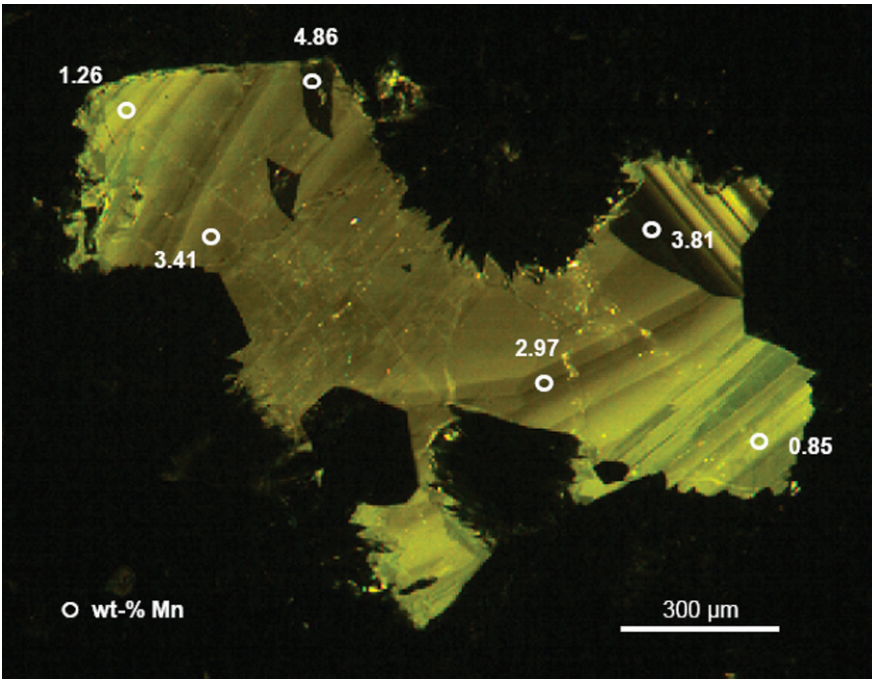

Fig. 1.15 CL image of an apatite crystal from Vysoky Kamen (Czech Republic) demonstrating the effect of self-quenching of the Mn^{2+}-activated CL at high concentrations Areas with Mn contents greater then 2 wt-% show a progressively decreasing CL intensity (modified after Kempe and Götze 2002)

nm. At the same time, the interaction with the electron beam may convert precursors (e.g., Si-OH silanol groups) into luminescence active centres of the type of non-bridging oxygen-hole centres (NBOHC). Such a conversion results in an increase of the CL emission band in the red part of the visible spectrum at 650 nm (Fig. 1.18).

All these examples illustrate that the interpretation of CL images and spectra has to be done carefully under consideration of all analytical and sample-related factors which may influence the luminescence properties of the investigated material.

1.4 Conclusions

Cathodoluminescence (CL) imaging and spectroscopy are luminescence techniques with the most widespread application in geosciences. During the last years, a wealth of investigations was performed on geomaterials to visualise growth textures and other internal textures that are not discernable with other analytical techniques, to use the information coming from CL studies for the reconstruction of processes of

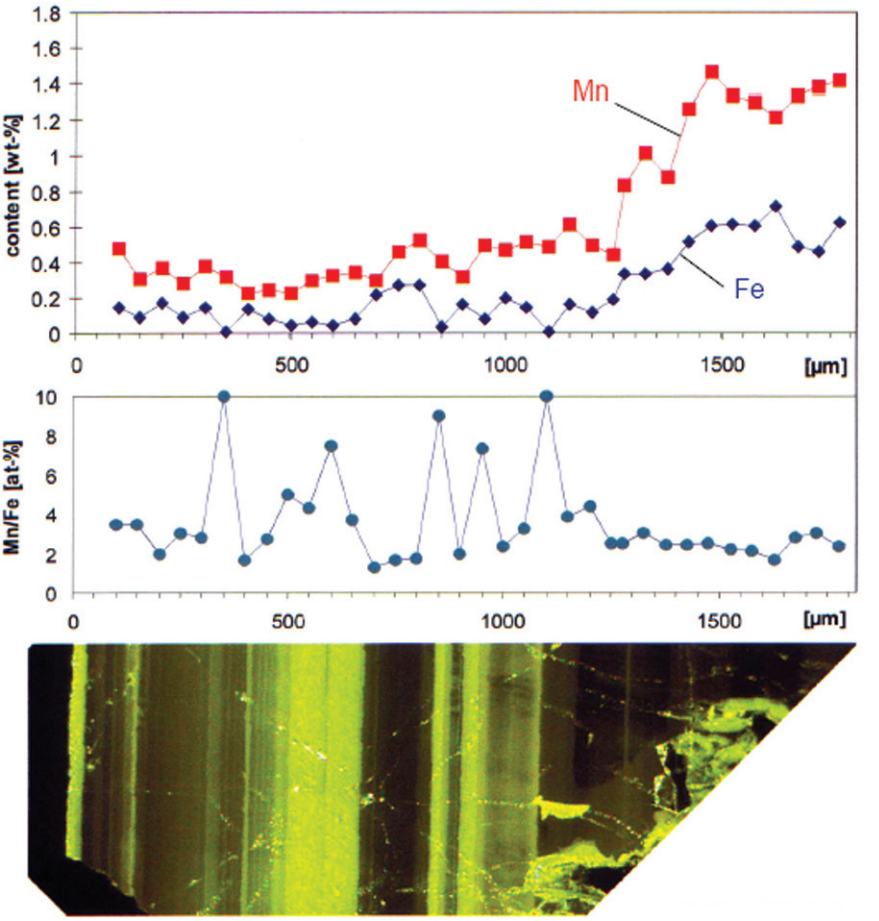

Fig. 1.16 Correlation of the CL intensity with the contents of Mn and Fe respectively, as well as with the Mn/Fe ratio in a strongly zoned apatite crystal from Ehrenfriedersdorf, Germany showing the influence of activator (Mn^{2+}) and quencher (Fe^{2+}) on the resulting luminescence intensity (modified after Kempe and Götze 2002)

mineral formation and alteration, to provide information about the real structure of minerals and materials, and to proof the presence and type of lattice incorporation of several trace elements.

In the present paper, the principal physical backgrounds of luminescence processes were given, which are necessary for the understanding of the luminescence phenomena. Several analytical and sample-related factors are discussed, which influence the luminescence signal. These factors are of fundamental importance for the interpretation of CL images as well as of CL spectra. The presented data illustrate that, although the principle processes in solids leading to luminescence are known, various specifics and interactions may significantly complicate the interpretation, especially in natural solids with complex, a priori unknown

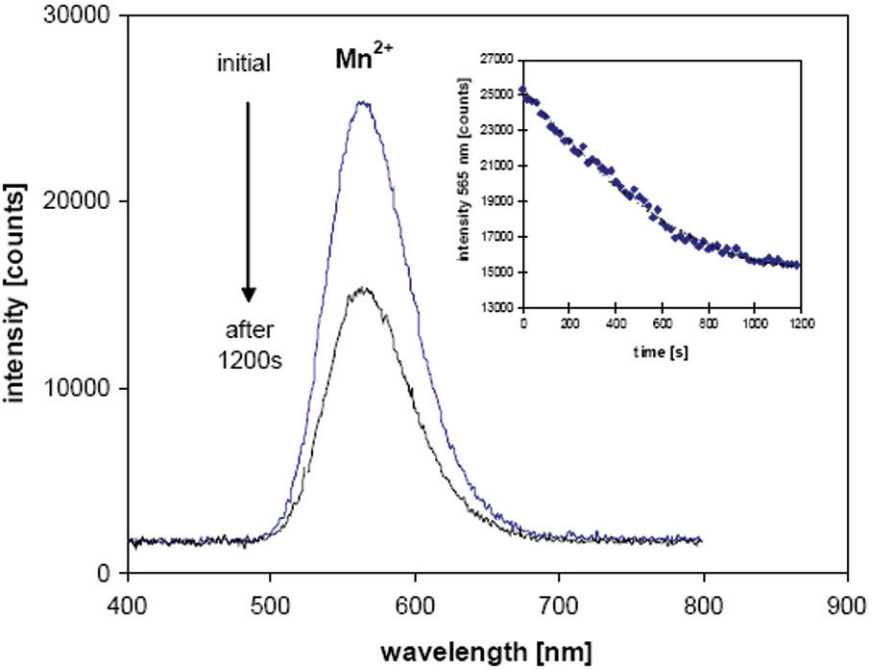

Fig. 1.17 Intensity of the Mn^{2+} emission band in an apatite crystal from Ehrenfriedersdorf, Germany in dependence of irradiation time. The observed decrease of luminescence intensity is probably related to effects of thermal quenching (modified after Kempe and Götze 2002)

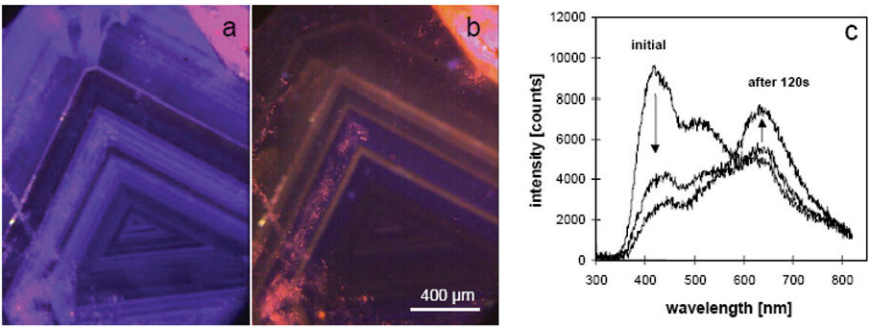

Fig. 1.18 Transient CL (left: images, right: spectra) of hydrothermal quartz (c) During electron irradiation, the transient blue CL (~400 nm) decreases dramatically, whereas the emission band in the red around 650 nm increases The result is a change of the visible CL colouration from initially blue (**a**) to reddish-brown (**b**)

chemical composition. Effects such as sensitizing, quenching or transient luminescence behaviour have to be considered for the interpretation of the data. In general, best results are achieved when luminescence studies are performed under standardized conditions and combined with other analytical, especially spectroscopic techniques with high sensitivity and high spatial resolution.

References

Blanc P, Baumer A, Cesbron F, Ohnenstetter D, Panczer G, Remond G (2000) Systematic cathodoluminescence spectral analysis of synthetic doped minerals: anhydrite, apatite, calcite, fluorite, scheelite and zircon. In: Pagel, M, Barbin, V, Blanc, P, Ohnenstetter, D (eds) Cathodoluminescence in geosciences Springer Verlag, Berlin Heidelberg New York, pp. 127–160

Brooks RJ, Finch AA, Hole DE, Townsend PD, Wu Z (2002) The red to near-infrared luminescence in alkali feldspar. Contrib Mineral Petrol 143:484–494

Burns RG (1993) Mineralogical applications of crystal field theory. 2nd ed., Cambridge University Press, Cambridge, 551 p

El Ali A, Barbin G, Cervelle B, Ramseyer K, Bouroulec J (1993) Mn^{2+}-activated luminescence in dolomite, calcite and magnesite: quantitative determination of manganese and site distribution by EPR and CL spectroscopy. Chem Geol 104:189–202

Evans J, Hogg AJC, Hopkins MS, Howarth RJ (1994) Quantification of quartz cements using combined SEM, CL, and image analysis. J Sediment Res A64:334–338

Finch, AA, Klein J (1999) The causes and petrological significance of cathodoluminescence emissions from alkali feldspars. Contrib Mineral Petrol 135:234–243

Gaft M, Reisfeld R, Panczer G, Shoval S, Champagnon B, Boulon G (1997) Eu^{3+} luminescence in high-symmetry sites of natural apatite. J Lum 72–74:572–574

Gaft M, Panczer G, Reisfeld R, Shinno I, Champagnon B, Boulon G (2000a) Laser-induced Eu^{3+} luminescence in zircon $ZrSiO_4$. J Lum 87–89:1032–1035

Gaft M, Boulon G, Panczer G, Guyot Y, Reisfeld R, Votyakov S, Bulka G (2000b) Unexpected luminescence of Cr^{5+} and Cr^{3+} ions in $ZrSiO_4$ zircon crystals. J Lum 87–89:1118–1121

Gaft M, Panczer G, Reisfeld R, Uspensky E (2001) Laser-induced time-resolved luminescence as a tool for rare-earth element identification in minerals. Phys Chem Minerals 28:347–363

Gaft M, Seigel H, Panczer G, Reisfeld R (2002) Laser-induced time-resolved luminescence spectroscopy of Pb^{2+} in minerals. Eur J Mineral 14:1041–1048

Gaft M, Reisfeld R, Panczer G (2005) Luminescence spectroscopy of minerals and materials. Springer-Verlag Berlin, Heidelberg, 356pp

Gorobets BS, Rogojine AA (2002) Luminescent spectra of minerals. RPC VIMS, Moscow, 300p

Götte T, Richter DK (2004) Quantitative high-resolution cathodoluminescence spectroscopy of smithsonite. Mineral Mag 68:199–207

Götze J, Magnus M (1997) Quantitative determination of mineral abundance in geological samples using combined cathodoluminescence microscopy and image analysis. Eur J Mineral 9:1207–1215

Götze J, Zimmerle W (2000) Quartz and silica as guide to provenance in sediments and sedimentary rocks. Contributions to Sedimentary Petrology 21, Schweizerbart'sche Verlagsbuchhandlung, Nägele and Obermiller, Stuttgart, 91p

Götze J, Kempe U (2008) A comparison of optical microscope (OM) and scanning electron microscope (SEM) based cathodoluminescence (CL) imaging and spectroscopy applied to geosciences. Mineral Mag (submitted)

Götze J, Habermann D, Neuser RD, Richter DK (1999a) High-resolution spectrometric analysis of REE-activated cathodoluminescence (CL) in feldspar minerals. Chem Geol 153:81–91

Götze J, Kempe U, Habermann D, Nasdala L, Neuser RD, Richter DK (1999b) High-resolution cathodoluminescence combined with SHRIMP ion probe measurements of detrital zircons. Mineral Mag 63:179–187

Götze J, Plötze M, Fuchs H, Habermann D (1999c) Defect structure and luminescence behaviour of agate - results of electron paramagnetic resonance (EPR) and cathodoluminescence (CL) studies. Mineral Mag 63:149–163

Götze J, Habermann D, Kempe U, Neuser RD, Richter DK (1999d) Cathodoluminescence microscopy and spectroscopy of plagioclases from lunar soil (Luna20, Luna 24). Am Mineral 84:1027–1032

Götze J, Krbetschek MR, Habermann D, Wolf D (2000) High-resolution cathodoluminescence studies of feldspar minerals. In: Pagel, M, Barbin, V, Blanc, P, Ohnenstetter, D (eds)

(2000) Cathodoluminescence in geosciences. Springer Verlag, Berlin Heidelberg New York, pp. 245–270

Götze J, Plötze M, Habermann D (2001) Origin, spectral characteristics and practical applications of the cathodoluminescence (CL) of quartz: a review. Mineral Petrol 71:225–250

Götze J, Plötze M, Götte T, Neuser RD, Richter DK (2002) Cathodoluminescence (CL) and Electron Paramagnetic Resonance (EPR) studies of clay minerals. Mineral Petrol 76:195–212

Habermann D, Neuser R, Richter DK (1998) Low limit of Mn^{2+}-activated cathodoluminescence of calcite: state of the art. Sed Geol 116:13–24

Habermann D, Meijer J, Neuser RD, Richter DK, Rolfs C, Stephan A (1999) Micro-PIXE and quantitative cathodoluminescence spectroscopy: Combined high resolution trace element analyses in minerals. Nucl Instr Methods Phys Res B 150:470–477

Habermann D, Neuser RD, Richter DK (2000a) Quantitative high resolution spectral analysis of Mn^{2+} in sedimentary calcite. In: Pagel, M, Barbin, V, Blanc, P, Ohnenstetter, D (eds) Cathodoluminescence in geosciences. Springer Verlag, Berlin Heidelberg New York, pp. 5331–5358

Habermann D, Götte T, Meijer J, Stephan A, Richter DK, Niklas JR (2000b) High resolution rare-earth elements analyses of natural apatite and its application in geo-sciences: Combined micro-PIXE, quantitative CL spectroscopy and electron spin resonance analyses. Nucl Instr Methods Phys Res B 161–163:846–851

Häger T, Dung PT (2003) Quantitative laser-induced photoluminescence and cathodoluminescence spectroscopy of natural and synthetic rubies. In: Hofmeister, W, Quang, VX, Dao, NQ, Nghi, T (eds) Geo- and material sciences on gem-minerals of Vietnam Proc 2nd Int workshop Hanoi, pp. 122–128

Kempe U, Götze J (2002) Cathodoluminescence (CL) behaviour and crystal chemistry of apatite from rare-metal deposits. Mineral Mag 66:135–156

Kempe U, Trinkler M, Wolf D (1991) Yttrium und die Seltenerdfotolumineszenz natürlicher Scheelite. Chem Erde 51:275–289

Kempe U, Götze J, Dandar S, Habermann D (1999) Magmatic and metasomatic processes during formation of the Nb-Zr-REE deposits from Khaldzan Buregte (Mongolian Altai): Indications from a combined CL - SEM study. Mineral Mag 63:165–177

Kempe U, Gruner T, Nasdala L, Wolf D (2000) Relevance of cathodoluminescence for the interpretation of U-Pb zircon ages, with an example of an application to a study of zircons from the Saxonian Granulite Complex, Germany. In: Pagel, M, Barbin, V, Blanc, P, Ohnenstetter, D (eds) (2000) Cathodoluminescence in geosciences. Springer Verlag, Berlin, Heidelberg, New York, pp 425–456

Kempe U, Plötze M, Brachmann A, Böttcher R (2002) Stabilisation of divalent rare earth elements in natural fluorite. Mineral Petrol 76:213–234

Krbetschek MR, Götze J, Dietrich A, Trautmann T (1998) Spectral information from minerals relevant for luminescence dating. Radiat Meas 27:695–748

Krbetschek MR, Götze J, Irmer G, Rieser U, Trautmann T (2002) The red luminescence emission of feldspar and its wavelength dependence on K, Na, Ca – composition Mineral Petrol 76:167–177

Marfunin AS (1979) Spectroscopy, luminescence and radiation centres in minerals. Springer-Verlag, Berlin, 352p

Marfunin AS (1995) Advanced Mineralogy Vol 2 – Methods and instrumentations: Results and recent developments. Springer-Verlag, Berlin, Heidelberg, New York

Mariano AN, Ring PJ (1975) Europium-activated cathodoluminescence in minerals. Geochim Cosmochim Acta 39:649–660

Marshall DJ (1988) Cathodoluminescence of geological materials. Unwin-Hyman, Boston, 146 p

Marshall DJ (2004) Macrophotography of cathodoluminescence of mineral specimens. 32nd International Geological Congress, Florece, Italy, Abstracts, 576

Medlin WL (1968) The nature of traps and emission centers in thermoluminescent rock materials. In: McDougall, DJ (ed) Thermoluminescence of geological materials. Academic Press, New York, pp 193–223

Meunier JD, Sellier E, Pagel M (1990) Radiation-damage rims in quartz from uranium-bearing sandstones. J Sed Petrol 60:53–58

Mikhail P, Hulliger J, Ramseyer K (1999) Cathodoluminescence and photoluminescence of Sm^{n+} (n=2,3) in oxide environments. Solid State Commun 112:483–488

Morozov M, Trinkler M, Plötze M, Kempe U (1996) Spectroscopic studies on fluorites from Li-F and alkaline granitic systems in Central Kazakhstan. In: Shatov V, et al (eds) Granite-related ore deposits of Central Kazakhstan and adjacent areas. GLAGOL Publ House, St Petersburg, pp 359–369

Owen MR (1988) Radiation-damage halos in quartz. Geology 16:529–532

Pagel M, Barbin V, Blanc P, Ohnenstetter D (eds) (2000) Cathodoluminescence in geosciences. Springer Verlag, Berlin, Heidelberg, New York, 514p

Ramseyer K, Mullis J (1990) Factors influencing short-lived blue cathodoluminescence of alpha-quartz. Am Mineral 75:791–800

Remond G, Phillips MR, Roques-Carmes C (2000) Importance of instrumental and experimental factors on the interpretation of cathodoluminescence data from wide band gap materials. In: Pagel M, Barbin V, Blanc P, Ohnenstetter D (eds) (2000) Cathodoluminescence in geosciences. Springer Verlag, Berlin, Heidelberg, New York, pp 59–126

Richter DK, Götte Th, Götze J, Neuser RD (2001) Progress in application of cathodoluminescence (CL) in sedimentary geology. Mineral Petrol 79:127–166

Vortisch W, Harding D, Morgan J (2003) Petrographic analysis using cathodoluminescence microscopy with simultaneous energy-dispersive X-ray spectroscopy. Mineral Petrol 79:193–202

Yacobi C, Holt DB (1990) Cathodoluminescence microscopy of inorganic solids. Plenum, New York, 292 p

Zinkernagel U (1978) Cathodoluminescence of quartz and its application to sandstone petrology. Contr Sed 8:69 p

Chapter 2
Shock Metamorphism of Terrestrial Impact Structures and its Application in the Earth and Planetary Sciences

Arnold Gucsik

2.1 Introduction

Shock metamorphism is the sum of irreversible chemical, mineralogical and physical changes in the target materials that occur during the hypervelocity impact event (Melosh 1989). The following chapters have been summarized from reviews by French and Short (1968); Sharpton and Grieve (1990); Stöffler and Langenhorst (1994); Grieve et al. (1996); Koeberl (1997) and French (1998).

When an extraterrestrial projectile (comet or asteroid) hits target rocks of a planetary surface, geologic materials are subjected to shock pressures above their Hugoniot Elastic Limit (HEL), which is on the order of 5-10 Gigapascals (GPa) (Sharpton and Grieve 1990). Shock metamorphism provides evidence for conditions associated with impact cratering (e.g., French and Short 1968; Stöffler and Langenhorst 1994; Grieve et al. 1996; Koeberl 1997; French 1998, Deutsch 1998 and references therein) including the high pressures, temperatures, and strain rates ($10^6 - 10^8$ s^{-1}), which lead to as characteristic structural and phase changes in minerals. Figure 2.1 shows that endogenic metamorphism of crustal rocks does not exceed temperatures of 1200°C and pressures of 2 GPa, except static pressure, which affects specific deep-seated rocks, as for example eclogites (Koeberl 1997).

Large impact events differ in many ways from endogenic processes such as volcanic explosions, earthquakes, and plate tectonics (French 1998):

- There have been no historical records or examples of large meteorite impacts.
- The impact energy is limited only by the mass and velocity of the projectile and concentrated within a fraction of time compared to the hundreds or thousands of years through volcanism, earthquakes, tectonic processes, and heat flow.
- The energy is released in an impact event shattering, deforming, melting, and even vaporising large volumes of target rock in a fraction of seconds.
- Large impact events cause biological extinctions, because their impact energy is released near the surface and directly into the biosphere.

Arnold Gucsik (✉)
Max Planck Institut für Chemie, Abteilung Geochemie, Joh.-J.-Becherweg 27. Universitätcampus, D-55128 Mainz, Germany
e-mail: gucsik@mpch-mainz.mpg.de

A. Gucsik (ed.), *Cathodoluminescence and its Application in the Planetary Sciences*,

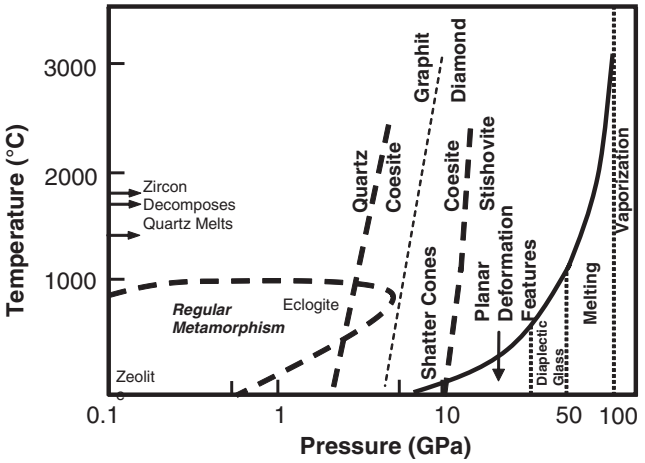

Fig. 2.1 Conditions of endogenic metamorphism and shock metamorphism in the pressure-temperature fields. This comparison diagram exhibits the onset pressures of various irreversible structural changes in the rocks due to shock metamorphism and the relationship between pressure and post-shock temperature for shock metamorphism of granitic rocks (modified after Koeberl 1997; his Fig. 2.2))

- Unique deformation effects occurred as changes in minerals such as mineral deformations and melting under the extreme high pressure and temperature (e.g., the shock pressure may be than 60 GPa and post-shock temperature may be 2000°C).

2.2 Impact Cratering Mechanics

The impact cratering process is commonly divided into the contact and compression, excavation, and modification stages (Gault et al. 1968; Melosh 1989 1992,). During the compression stage, structural modifications and phase changes occurred in the target rocks. The morphology of a crater is developed in the excavation and modification stages.

2.2.1 Contact and Compression Stage

During the contact and compression stage, the projectile or impacting object first hits the planet's surface (the target) and transfers its energy and momentum to the underlying rocks. The projectile traveling at a few kilometers per second produces large specific kinetic energy ($E = 1/2mv^2$, m = mass, v = velocity) (Melosh 1992). For instance, a stony meteorite of only 6 m diameter, colliding with the Earth at 20

km/s, releases as much energy [8.3×10^{23} Joules (J) or 20,000 tons (20 kT) of TNT] as an atomic bomb (French 1998). This stage lasts only a bit longer than the time required for the impacting object to travel its own diameter,

$$t_{cc} = L/v_i, \tag{2.1}$$

where t_{cc} is the duration of contact and compression, L the projectile diameter, and v_i the impact velocity.

The shock wave in the projectile reaches its back (or top) surface in contact and compression stage. Simultaneously, the pressure is released as the surface of the compressed projectile expands upward (wave of pressure relief propagates back downward toward the projectile-target interface). During the irreversible compression process, the projectile has been compressed to high pressure (hundreds of gigapascals) producing liquid or gaseous state due to heat deposited in the projectile (Melosh 1992).

Very high velocity jets of highly shocked material are formed, where strongly compressed material is close to a free surface. The jet velocity depends on the angle between the converging surface of the projectile and the target, but may exceed the impact velocity by factors as large as five (Melosh 1992).

2.2.1.1 Hugoniot Elastic Limit (HEL)

The projectile hits the target, generating strong shock waves, which leads to compression of the target rocks at pressures far above a material parameter called the Hugoniot elastic limit (Melosh 1989). The Hugoniot Elastic Limit (HEL) describes the maximum stress in an elastic wave that a material can be subjected to without permanent deformation (Melosh 1989). The value of the HEL is about $5-10$ GPa for most minerals and whole rocks. The only known natural process that generates these high shock pressures exceeding the HELs is hypervelocity impact. The strength of the shock waves can be demonstrated or measured from the Hugoniot equations, relating quantities in front of the shock wave (subscript 0) to quantities behind the shock wave (Melosh 1989)

$$\rho(U-\mu_p) = \rho_0 U \tag{2.2}$$

$$P - P_0 = \rho_0 \mu_p U \tag{2.3}$$

$$E - E_0 = 1/2(P+P_0)(1/\rho_0 - 1/\rho) \tag{2.4}$$

where P is pressure, ρ density, μ_p particle velocity after the shock, U the shock velocity, and E energy per unit mass. These three equations are equivalent to the conservation of mass, momentum, and energy, respectively, across the shock front. The Hugoniot equations must be supplemented by a fourth equation, the equation of state, that relates the pressure to the density and internal energy in each material,

$$P = P(\rho, E) \tag{2.5}$$

Alternatively, a relation between shock velocity and particle velocity may be specified,

$$U = U(\mu_p) \tag{2.6}$$

As this relation is frequently linear, it often provides the most convenient equation of state in impact processes. Thus, we can write:

$$U = c + S\mu_p \tag{2.7}$$

where c and S are empirical constants. These equations can be used to compute the maximum pressure, particle velocity, shock velocity, etc. in an impact (Melosh 1992). A Hugoniot equation of state curve is a shock wave equation of state data, which are plotted on a P-V plane (Fig. 2.2). It defines the locus of all shock states achievable in any material by shock waves of variable intensity, e.g., by various impact velocities of a projectile (Melosh 1989; Koeberl 1997).

Temperatures in the shocked states can be determined by integrating the following equation because of the internal energy, which is related to temperature and volume through an equation of state (Martinez et al. 1995; Martinez and Agrinier 1998):

$$\frac{dT}{dV} = T\left[\frac{\gamma}{V}\right] + \left[\frac{dP}{dV}(V_0 - V) + (P_0 - P)\right]\frac{1}{2C_v} \tag{2.8}$$

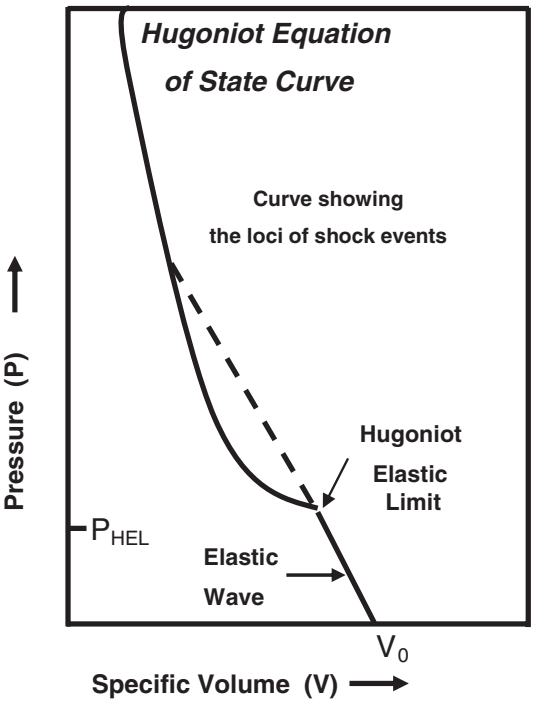

Fig. 2.2 The Hugoniot equation state curve does not represent a continuum of states as in thermodynamic diagrams, but the loci of individual shock compression events. The yielding of the material at the Hugoniot Elastic Limit is indicated (modified after Koeberl 1997; his Fig. 2.1)

where V_0 and P_0 are initial volume and pressure.

Models of specific heat C_v and Grüneisen parameters γ (which are quantities that are relatively constant by the product of three times the coefficient of linear expansion divided by the product the compressibility with the specific heat per unit volume) at high temperature and compression are therefore required for calculating shock temperatures (Melosh 1989; Martinez and Agrinier 1998).

Post-shock temperatures in the material can be related to temperatures in the shocked state using

$$\frac{dT}{dV} = -T\left[\frac{\gamma}{V}\right] \tag{2.9}$$

which is the adiabatic part of the Hugoniot equation and represents the adiabatic decompression from the shock state to the final zero-pressure state (Melosh 1989; Martinez and Agrinier 1998).

2.2.2 Excavation Stage

The expanding shock waves open the actual impact crater during the excavation stage (Melosh 1989; Grieve 1991). The transient cavity is a freshly opened bowl-shaped crater and surrounded by an ejecta curtain that develops is several orders of magnitude larger than the diameter of the projectile.

At the high pressures and post-shock temperatures the rocks may melt or even vaporise upon release. The lower pressures cause pervasive fracturing and planar deformation elements in individual crystals and produce characteristic cone-in-cone fractures called shatter cones. The target material strength and gravity become important near the end of excavation. This stage ends much longer than the contact and compression stage, requiring seconds or minutes to reach completion, depending upon the several factors as follows: crater size, direction of the impact, impact velocities, presence of a water table or layers of different strength, rock structure, joints, or initial topography in the target (Melosh 1992).

2.2.3 Modification Stage

The modification stage begins when the transient crater collapses under gravity, and elastic rebound of the underlying, compressed rock layers may also play a role. It was suggested from volume conservation that the crater collapse appears almost immediately after formation of the transient crater, which produces an increase of the original diameter of the crater by about 15%. During modification, loose debris slides down the steep interior walls of small craters, pooling on the floor of the final bowl-shaped depression (Melosh 1992). The normal geologic processes of gradation, isostatic adjustment, infilling by lavas, sediments, etc. on geologic time scales may eventually result in obscuration or even total obliteration of the crater (Melosh 1992).

2.3 Types of Terrestrial Impact Craters

The Earth Impact Database is a resource that has been assembled since 1985 by researchers at the Geological Survey of Canada (a division of Natural Resources, Canada). It has now been transferred to the Planetary and Space Science Centre at the University of New Brunswick, Department of Geology. Here, 175 impact structures (2008) were registered on the webpage: www.unb.ca/passc/ImpactDatabase/. These confirmed terrestrial impact craters (Fig. 2.3) have two basic morphological forms: simple and complex. The two forms differ only in the diameter range at which the transition from one form to another takes place. On the Earth, simple craters occur up to a diameter of 4 km in crystalline and 2 km in sedimentary target rocks (Dence 1972). Terrestrial craters with a diameter greater than 4 km show a complex form. Depending on their size, complex craters may be further subdivided into peak ring crater and multiring basins.

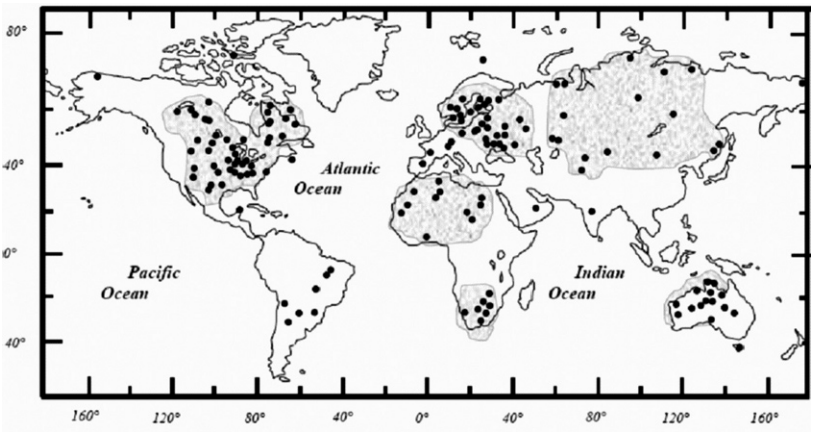

Fig. 2.3 Distribution of currently (2008) known impact structures, which are concentrated mainly to the cratonic areas (as indicated by grey regions) of continents (data from www.unb.ca/passc/Impact Database)

2.3.1 Simple Craters

Simple craters are the smallest impact structures and occur as bowl-shaped depressions (French 1998). These craters can be characterized by a structurally upraised and fractured rim area (e.g., Barringer Crater, Arizona, USA) (Fig. 2.4). The sizes of these craters are up to 2 km (sedimentary target rocks) to about 4 km in diameter (crystalline target rocks) on Earth, depending on the strength of the target rocks (Dence 1972; Melosh 1992). The interior of the crater has a smoothly sloping parabolic profile and its rim-to-floor depth is about one-fifth of its rim-to-rim diameter. The surrounding plain is blanketed with a mixture of ejecta (proximal ejecta)

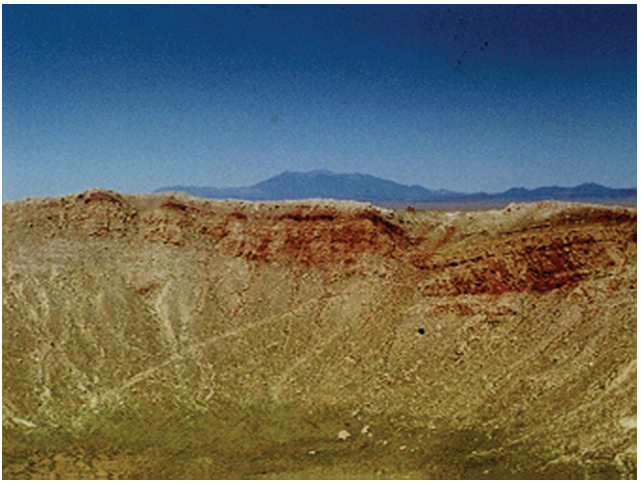

Fig. 2.4 A young, well-known and well-preserved simple impact crater (1.2 km in diameter): Barringer Meteor Crater (Arizona, USA). This crater was formed about 50.000 years ago, when an iron meteorite approximately 30 m across struck the horizontal sediments of northern Arizona's Colorado Plateau. The photo, looking northwest, shows the uplifted rim (photo by author)

and debris scoured from the pre-existing surface for a distance of about one crater diameter from the rim (Melosh 1992). The floor of simple craters is underlain by a lens of broken rock, breccia, which slid down the inner walls of the crater shortly following excavation. This breccia typically includes representatives from all the formations intersected by the crater and may contain layers of melted or highly shocked rocks.

2.3.2 Complex Craters

The complex craters have flat interior floors or internal rings instead of central peaks and formed with diameters larger than 4 km on Earth (depending on the target lithology). These craters are believed to have formed by collapse of an initially bowl-shaped transient crater, and because of this more complicated structure they are known as complex craters (Melosh 1992). The floors of complex craters are covered by melted and highly shocked debris. The surfaces of the terrace blocks tilt outward into the crater walls, and melt pools are also common in the depressions thus formed. The central peaks consist of material that is pushed upward from the deepest levels excavated by the crater. Complex craters are generally shallower than simple craters of equal size and their depth increases slowly with increasing crater diameter. Rim height also increases rather slowly with increasing diameter because much of the original rim slides into the crater bowl as the wall collapses (Melosh 1992). The amount of structural uplift (SU) at complex craters can be measured, where the subsurface stratigraphy is known. The relationship is:

$$SU = 0.06D^{1.1} \quad (2.10)$$

where SU is the amount of stratigraphic uplift undergone by the deepest lithology now exposed at the surface in the center and D is the diameter of the crater (Grieve 1991). The uplifted area may consist of parts of the upper crust at the larger complex craters (e.g., Siljan, SU = 4km; Manicouagan, SU = 9.5km). The ejecta blankets of complex craters show some similarities to those of simple craters. However, the hummocky texture characteristics of simple craters is replaced by more radial troughs and ridges as size increases (Melosh 1992).

2.4 Geology: Lithological Indicators of Impact Structures

An impact event is a surface process that produces circular, shallow, rootless structures in contrast to volcanic processes (French 1998). The lithological indicators for an impact structure may be a layer of fragmental breccia, which is found as crater filling or overlying a possibly raised, partially brecciated, and up- or over-turned rim (Koeberl 1997).

2.4.1 Breccia Types at Impact Structures

The impact-derived breccias contain shocked minerals, impact melts, and impact glasses in an impact crater (Stöffler and Langenhorst 1994; Koeberl 1997). The monomict and polymict breccias that formed during impact processes could be divided into three main types: (1) cataclastic (fragmental breccias), (2) suevitic (fragmental with a melt fragment component) breccias (Fig. 2.5a,b), or (3) impact melt (melt breccia - i.e., melt in the matrix with a clastic component) breccias. The

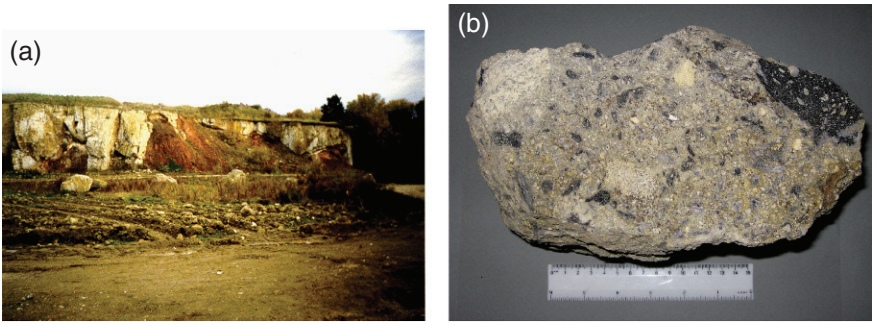

Fig. 2.5 (**a**) Aumühle quarry of suevite, which is located in the northwest of the Ries impact structure (Germany). This image shows a dark Jurassic clay and red clay and sandstones of the Keuperian. (**b**) Suevite: the elongated, grey parts of suevite are impact glasses (photos by author)

breccias can be allochthonous or autochthonous. Additionally, the basement rocks contain dikes of injected or locally formed fragmental or pseudotachylitic breccias (Reimold 1995). Whether all these breccia types are actually present at an impact crater depends on factors including the size of the crater, the composition of the target area (e.g., Kieffer and Simonds 1980), and the level of erosion (see; Horz 1982; Grieve 1987, and references therein).

2.4.2 Complete Melting

The target rocks undergo complete (bulk) melting to form impact melts at pressures in excess of about 60 GPa. The resulting melts are deposited as splash-form glass particles and "bombs" in suevitic breccias or as coherent impact melt body. The presence of inclusions of minerals, such as lechatelierite (monomineralic quartz melt that forms from pure quartz at temperatures at 1700°C), or baddeleyite (thermal decomposition product of zircon forming at a temperature of at least 1680°C), is associated with very high temperatures. Lechatelierite as a good indicator of meteorite impact origin is not found in any other natural rock, except in fulgurites, which form by fusion of soil or sand when lightning hits the ground (Stöffler and Langenhorst 1994; and references therein).

2.4.2.1 Impact Glasses

Impact glasses are more commonly found at relatively young impact craters rather than at old impact structures, because glass is not stable over geological times. Such impact-derived glasses have chemical and isotopic compositions that are similar to those of the target rocks. The similarities in chemical and isotopic composition between impactites and crater target rocks have been employed in several source crater investigations (e.g., Blum et al. 1993; Meisel et al. 1995). Impact glasses have much lower water contents (about 0.001-0.05 wt%) than volcanic or other natural glasses (Koeberl 1992). These impact melts and glasses are useful for the dating of an impact structure using K-Ar, ^{40} Ar$-^{39}$Ar, fission track, Rb-Sr, Sm-Nd, or U-Th-Pb isotope age-dating methods (Montanari and Koeberl 2000). The age that should be obtained for an impact event is different from that of volcanism because impact melts or glasses give a unique (local), much younger age as compared to the target rocks, which are usually old crustal rocks.

2.4.2.2 Tektites and Microtektites

The centimeter-sized tektites as chemically homogeneous glasses have been ejected from a few terrestrial impact structures and spread over thousands of kilometers. They found on land and have been subdivided into three groups: (a) normal or

splash-form tektites, (b) aerodynamically shaped tektites, and (c) Muong Nong-type tektites (or layered tektites). Tektites can be associated with smaller (≤ 1 mm) microtektekties (Montanari and Koeberl 2000).

Currently, on the basis of differences in location, age, and to some extent, the characteristics of tektites and microtektites, four strewn fields are known: (1) Australasian (0.78 Ma, source crater no yet identified); (2) Central European (15 Ma) from the Ries Crater, Germany; (3) Ivory Coast (1.07 Ma) from the Bosumtwi Crater, Ghana (Koeberl et al. 1997a); and (4) North American (35 Ma) from the Chesapeake Bay impact structure, USA (Fig. 2.6).

Tektites are formed as the product of melting and quenching of terrestrial rocks during hypervelocity impact on the Earth (see Montanari and Koeberl 2000), for a recent review). Their chemical and isotopic compositions are identical with those of the target rocks where the impact occurred:

- Typically high in silica composition (> 65 wt%), but their chemical and isotopic compositions are not volcanic, but closer to those of shales and similar sedimentary rocks. Containing low water content (≤ 0.02 wt%), and their flow-banded structure includes particles and bands of lechatelierite (monomineralic quartz melt).
- A few tektites contain partly melted inclusions of shocked and unshocked mineral grains (quartz, apatite, zircon) as well as coesite (Glass and Barlow 1979).

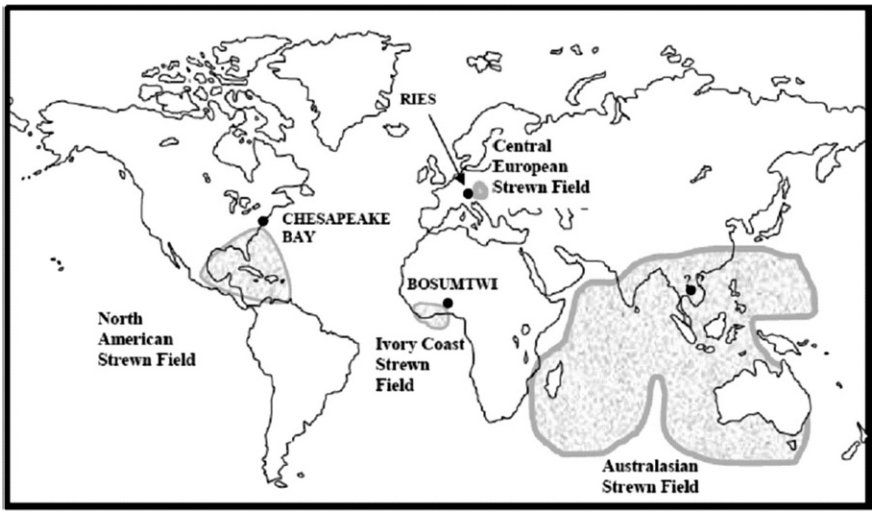

Fig. 2.6 Location (*solid circles*) known source craters (Chesapeake Bay, Ries, and Bosumtwi craters) and extension of the four tektite strewn fields. (modified after Montanari and Koeberl 2000; their Fig. 2.4.1.1

2.5 Diagnostic Shock Features in Impact Craters

The best diagnostic indicators for shock metamorphism are features that can be studied easily by using the polarizing microscope. They include planar microdeformation features; optical mosaicism; changes in refractive index, birefringence and optical axis angle; isotropization; and phase changes (Stöffler 1972, 1974; Stöffler and Langenhorst 1994; Grieve et al. 1996; Koeberl 1997).

2.5.1 Shatter Cones

Shatter cones (Fig. 2.7) are regarded as the only distinctive and unique shock deformation feature that develops on a macroscopic scale as hand specimen (Dietz 1968; French 1998). They are distinctive conical fractures produced in target rocks by shock waves of relatively low intensity, usually below the crater floor or in the central uplifts of large structures. They form in all kinds of target rocks subjected to the appropriate pressures, but they are most strikingly developed in fine-grained rocks, especially carbonates. Shatter cones can be distinguished from similar deformation features by the distinctive radiating striations (”horsetailing”) along the cone surface, and by the fact that the cones originally point in the direction of the source of the shock wave, i.e., inward and upward. They develop in a large volume of target rock and have been widely used to identify terrestrial impact structure. Shatter cones are good diagnostic structural criteria that are easy to recognize and are found in many terrestrial impact structures.

Fig. 2.7 Well-developed finely sculptured shatter cone, in fine-grained Ordovician limestone from the Charlevoix impact crater, Canada (photo by author)

The formation mechanism for shatter cones is poorly understood. The conical shapes might be related to the interactions of shock waves with point inhomogeneites in rocks, or interactions between the main compressive shock and rebound waves (Gash 1971). However, these models do not explain the dominant features of shatter cones such as characteristic striations, the ”horse-tail” cone hierarchy, and the variety of complete cones. More recently, Shagy et al. (2002) have shown that the shatter cones are branched tensile fractures. Shatter-cone striations are the preserved tracks of fracture front waves. Their analysis of the striations shows that shatter cones develop only at extreme propagation velocities, between $0.9V_R$ and the maximal permitted velocity of V_R. The angles of the striations (α), which are shown to increase systematically with the distance from the impact, reflect both the stresses and the energy flux driving the fracture at a given site, and may be used as a general tool to evaluate extreme local stresses in the field (Shagy et al. 2002).

2.5.2 Mosaicism

The term mosaicism describes the internal fragmentation of a single crystal into a mosaic of slightly disoriented crystal domains. Mosaicism is a microscopic expression of shock metamorphism observed in a number of rock-forming minerals (see, e.g., Horz and Quaide 1973) and appears as an irregular, mottled optical extinction pattern. This is distinctly different from the undulatory extinction that occurs in tectonically deformed quartz and, generally, accompanied in many minerals by indications of plastic deformation structures or deformation bands (Stöffler 1972). Mosaicism can be semi-quantitatively investigated by X-ray diffraction.

2.5.3 Kink Bands

Kink bands appear in sheet silicates, other sheet-like structures in shocked quartz and feldspar (Bunch 1968). They are not oriented parallel to rational crystallographic planes and display variable disorientation with respect to the host lattice compared to the deformation twins. Kink banding is considered as supporting evidence for the impact origin of a structure, but it cannot be used as a single diagnostic criterion, as it occurs also in metamorphic rocks.

2.5.4 Planar Microstructures

Two types of planar microstructures are apparent in shocked minerals: planar fractures (PFs) and planar deformation features (PDFs). Their essential characteristics are summarized in Table 2.1. The PDFs occur as either non-decorated or decorated

Table 2.1 Characteristics of planar fractures and planar deformation feature in quartz

Nomenclature	1. Planar fractures (PF) 2. Planar deformation features (PDF) 2.1. Nondecorated PDFs 2.2. Decorated PDFs
Crystallographic orientation	1. PFs: usually parallel to (0001) and $\{10\bar{1}1\}$ 2. PDFs: usually parallel to $\{10\bar{1}3\}$,$\{10\bar{1}2\}$, $\{10\bar{1}1\}$, (0001), $\{11\bar{2}2\}$, $\{11\bar{2}1\}$, $\{10\bar{1}0\}$,$\{11\bar{2}0\}$, $\{21\bar{3}1\}$, $\{51\bar{6}1\}$, etc.
Optical microscope properties	Multiple sets of PFs or PDFs Thickness of PDFs: $< 2-3\mu m$ Spacing: >15 μm (PFs), 2-10 μm (PDFs)
TEM properties (PDFs)	Two types of primary lamellae are observed: 1. Amorphous lamellae with a thickness of about 30 nm (pressures of <25 GPa) and about 200 nm (at pressures of >25 GPa) 2. Brazil twin lamellae parallel to (0001)

Data from Stöffler and Langenhorst (1994).

PDFs (Stöffler and Langenhorst 1994). Planar deformation features in rock-forming minerals (e.g., quartz, feldspar, or olivine) are generally accepted to provide diagnostic evidence for shock deformation (see, e.g., French and Short 1968; Stöffler and Langenhorst 1994; Grieve et al. 1996; French 1998, and references therein).

2.5.4.1 Planar Fractures (PFs)

Planar fractures are parallel sets of multiple planar cracks or cleavages in quartz grains; they develop at the lowest pressures characteristic of shock waves ($\sim 5-8$ GPa) (French 1998). As French (1998) noted, they are parallel to rational crystallographic planes with low Miller indices, such as (0001) and $\{101\}$. The fractures are typically $5-10\mu m$ wide and spaced $15-20\mu m$ or more apart in individual quartz grains. Similar cleavage occurs also rarely in quartz from non-impact settings, and therefore planar fractures cannot be used independently as a single criterion for meteorite impact. However, the development of intense, widespread, and closely spaced planar fractures are frequently accompanied in impact structures by other features clearly formed at higher shock pressures (French 1998, and references therein). Planar deformation features, together with the somewhat less specific planar fractures (PFs), are usually well developed in quartz (Stöffler and Langenhorst 1994).

2.5.4.2 Planar Deformation Features (PDFs)

PDFs in various minerals (especially in quartz) have long been known as evidence of impact-induced deformation. In contrast to planar fractures, PDFs are not open cracks. They occur as multiple sets of more closely spaced (typically $2-10\mu m$), narrow (typically $< 2-3\mu m$), parallel planar regions than planar fractures. PDFs occur in planes corresponding to specific rational crystallographic orientations. The basal (0001) or c, $\{10\bar{1}3\}$ or ω, and $\{10\bar{1}2\}$ or π, orientations are the most common planes in quartz. In addition, PDFs often occur in more than one crystallographic orientation per grain. At pressures about ≥ 35 GPa, the distances between the planes decrease, and the PDFs become more closely spaced and more homogeneously distributed over the grain. Depending on the peak pressure, PDFs are observed in $2-10$ (maximum 18) orientations per grain (Robertson et al. 1968; Stöffler 1972; Stöffler and Langenhorst 1994; Grieve et al. 1996; Koeberl 1997). To properly characterize PDFs, it is necessary to measure their crystallographic orientations optically by using either a universal stage (Emmons 1943) or a spindle stage (Medenbach 1985), or by transmission electron microscopy (see, e.g., Goltrant et al. 1991; Leroux et al. 1994).

The formation mechanisms of these features in naturally shocked quartz might be explained by the pressure dependence of the shear modulus (decreasing linearly with increasing pressure and, for some planes even discontinuously, for a critical pressure of the order of 10 GPa) of quartz for various planes and directions. The Si-O-Si bonds are more easily broken, allowing the corresponding atoms to move towards energetically more favourable positions. This progressive reorganization leads to the formation of a new structure (dense amorphous silica lamellae). The transformation occurs very rapidly, as it is driven by the front of the shock wave. This explanation predicts that the density of PDFs should markedly increase with shock intensity (Goltrant et al. 1992).

2.5.5 Diaplectic Glass

Diaplectic glass is formed at shock pressures in excess of about 35 GPa without melting by solid-state transformation and has been described as a phase intermediate between crystalline and normal glassy phases (Stöffler and Hornemann 1972). It is found at numerous impact craters and shows the original crystal defects, planar features, and absence of flow structures and vesicles. Maskelynite is a diaplectic plagioclase glass formed in a similar way and at similar pressure range as diaplectic quartz glass. Diaplectic glass has a refractive index that is slightly lower than that of synthetic quartz glass. Other minerals (mafics) tend to oxidize or decompose.

2.5.6 Lechatelierite

At pressures that exceed about 50 GPa, lechatelierite forms by fusion of quartz. In contrast to diaplectic glass, lechatelierite is formed by a liquid state transformation associated with the melting of quartz at higher temperatures ($> 1700°C$) than occur in volcanic processes. This is a good indicator of a meteorite impact origin. Other minerals also melt at sufficiently high temperatures, e.g., feldspar (Stöffler and Langenhorst 1994).

2.5.7 High-Pressure Polymorphs

The high-pressure SiO_2polymorphs, coesite (pressure range: $30-60$ GPa) and stishovite (pressure range: $12-45$ GPa), occur as very fine-grained aggregates that are formed by partial transformation of the host quartz during shock metamorphism (Grieve et al. 1996). Under conditions of static equilibrium, where reaction rates are slower and kinetic factors less important, coesite forms from quartz at lower pressures (> 2 GPa) than does stishovite ($10-15$ GPa) (French 1998). The identification of coesite and stishovite at several impact sites in the early 1960s provided one of the earliest criteria for establishing the impact origin of several structures, most notably the Ries crater, Germany (Chao et al. 1960; Shoemaker and Chao 1961), and the Bosumtwi crater (Littler et al. 1961). Impact-derived coesite occurs as very fine-grained, colorless to brownish, polycrystalline aggregates, up to $100-200\mu m$ in size, usually embedded in diaplectic quartz glass, or rarely, in nearly isotropic quartz with abundant planar deformation features and a mean refractive index below 1.48 (Stöffler and Langenhorst 1994). Coesite occurs also in metamorphic rocks of ultra-high pressure origin or in kimberlites.

Other high-pressure mineral phases include jadeite formed from plagioclase, majorite from pyroxene, and ringwoodite from olivine (Stöffler 1972). Impact derived diamonds (the high-pressure cubic modification of carbon) have also been found at various craters. These diamonds form from carbon in the target rocks, mainly in graphite-bearing (e.g., graphitic gneiss) or coal-bearing rocks (Koeberl et al. 1997b).

2.6 Cathodoluminescence Properties of the Shocked Minerals

2.6.1 Quartz

The CL luminescence emission in the unshocked quartz might be associated with defect structures. The silicon dioxide structure is modified by different types of defect structures (impurities, vacancies, etc), which occur in the short range order. Hence, similar types of defects are found in crystalline and amorphous polymorphs of silicon dioxide (Kalceff et al. 2000-and references therein). Generally, the lu-

minescence of quartz shows different CL colors depending on its origin. Previous work on CL properties of shocked quartz is limited. Owen and Anders (1988), in a pioneering study, showed that quartz from intrusive igneous and high-grade metamorphic rock shows darker purple-blue CL, whereas quartz from low-grade metamorphic rocks exhibit reddish-brown CL, and that shocked quartz from the Cretaceous-Tertiary (K/T) boundary exhibits CL colors similar to those of low-grade metamorphic quartz. Owen and Anders (1988) used these observations to demonstrate that shocked quartz from the K-T boundary was not derived from volcanic sources. At that time (1988), this was an important contribution to the study of the then controversial origin of the K-T boundary. Ramseyer et al. (1992) reported CL luminescence changes for quartz and feldspar from the granitic rocks of the Siljan impact structure, Sweden, and related their findings to complex alteration of the minerals during a post-impact hydrothermal overprint. Seyedolali et al. 1997) reported CL studies of shocked quartz grains from the Mjølnir impact structure (Barents Sea) in comparison with quartz from a variety of other sources. These authors studied patterns of variable-intensity CL, including zoning, healed fractures, complex fractures, complex shears and planar microdeformations from different source rocks, using a combined scanning electron microscopy (SEM)-CL fabric-analysis technique. Recently, Boggs et al. (2001) studied planar deformation features (PDFs) in shocked quartz from the Ries crater, Germany, using a SEM-CL imaging facility. He found that (in contrast to planar microstructures associated with tectonic fracturing) these features are filled by amorphous silica and appear as dark lines in the CL images, which indicate absence of recombination centers to the emission of photons. More recently, Gucsik et al. (2004a) described that cathodoluminescence spectra of unshocked and experimentally shock-deformed quartzite samples show broad bands in the near-ultraviolet range and the visible light range, at all shock pressures. These broad bands might be associated with defect centers on, e.g., SiO_4 groups. There are distinct differences between the CL spectra of the unshocked and the shocked samples, and shifts in the center positions of the broad bands are evident with increasing shock pressure. This might indicate that recombination centers or traps for the photon emission are more closely-spaced in the band gap between VB and CB as a function of the increasing shock pressure, which is probably caused by partial amorphization.

2.6.2 Feldspars

Sippel and Spencer (1970) observed that the shock metamorphism caused peak shifts from green peak toward the red peak, peak broadening and decrease of luminescence intensity than in the undamaged counterpart in the CL spectra of shock-metamorphosed lunar feldspars. They noted that the distortions or disorder in the crystal field results in crystal field perturbations and these local variations occur broadened distribution of excited state energies. More recently, CL spectral measurements were performed on natural and experimentally shocked

oligoclases (An19.7 single crystal shocked between 10.5 and 45 GPa) and plagioclases from the equilibrated ordinary chondrites (Dar al Gani, Tenham) (Kaus and Bischoff (2000,). They observed disappearance of the crystal field sensitive Mn^{2+} and Fe^{3+}-related peaks resulting from breakdown of the crystal structure (i.e., occurrence of diaplectic glass) at around 35 GPa.

2.6.3 Zircon

Thorough understanding of the shock metamorphic signatures of zircon will provide a basis for the application of this mineral as a powerful tool for the study or recognition of old, deeply eroded, and metamorphically overprinted impact structures and formations.

According to Gucsik et al. (2004b and references therein) the unshocked samples show crosscutting, irregular fractures in the images. The 38 GPa sample exhibits a dense pattern of narrow-spaced lamellar features, in CL mode, that could represent the twinning effect noted in a 40 GPa sample by earlier workers and which was ascribed to partial conversion from the zircon phase to the more voluminous scheelite-structure phase. The CL images of experimentally, at 40, 60, and 80 GPa, shocked samples show subplanar and nearly parallel microdeformations. All experimentally shocked zircon, as well as all investigated naturally shocked samples from the Ries crater, shows an inverse relationship between the brightness of the backscattered electron (BSE) signal and the corresponding cathodoluminescence intensity of the zonation patterns. The CL spectra of unshocked and experimentally shock-deformed specimens and naturally shock-metamorphosed zircon samples are characterised by narrow emission lines and broad bands in the region of visible light and in the near-ultraviolet range. The emission lines result from rare earth element activators and the broad bands might be associated with lattice defects.

2.6.4 Impact-Derived Glasses

According to Gucsik et al. (2003 and references therein) CL images of the Aouelloul impact glass, Muong Nong-type tektite, and Libyan Desert Glass samples show more variety than the BSE images. In all three cases are brightness and contrast variations inversely correlated between the BSE and the CL images, and features that appear in the BSE image can usually also be discerned in the CL image. In fact, the CL images show more pronounced contrast and brightness variations than the BSE images. The CL images seem to preserve target rock textures much better than any other electron image, even though the samples appear to be totally glassy. The Aouelloul sample shows quite clearly a granular structur, which might be related to the texture of the original sandstone. Most spectacular are the CL images of the Libyan Desert Glass, which show a distorted original texture, probably indi-

cating high-temperature glass flow, which is not apparent at all in the BSE images. The inverse relationship between BSE and CL brightness might be caused by high concentrations of Al, Li and Na, which can lead to quenching of the CL signal.

Broad bands in the CL spectrum indicate that excited and ground states of the electronic radiative transitions are strongly coupled with the vibrating lattice. Stronger coupling indicates that more phonons are emitted in the electronic transition. (1) Broad intrinsic emission generally results from self trapped exciton (STE) which are highly localised excitons trapped by their own self-induced lattice distortion. The emission energy of the STE is usually much lower than the band gap of the material due to the energy lost by phonon emission during the electronic transition. (2) Excitation of electrons or holes trapped (dangling bonds in covalent crystals) at point defects such as vacancies, interstitial and point defect clusters usually produce broad CL peaks at all temperatures.

According to Stevens Kalceff et al. (2000, and references therein) the normal defect free configuration of (low pressure) silicon dioxide polymorphs can be represented as ($\equiv Si - O - Si \equiv$) indicating that each silicon atom is surrounded by four tetrahedrally configured oxygen atoms and the adjacent silicon atoms are bridge bonded through a single oxygen atom. The silicon dioxide structure may be modified by the presence of defects (e.g., impurities, vacancies, etc.). The detected luminescence bands of the crystalline and amorphous modifications of SiO_2 are attributed to three optical active luminescence centers: (1) two-fold coordinated silicon (=Si:), non-bridging oxygen hole centre (NBOHC) and the self trapped exciton (STE). They found a red band at 650 nm due to a band-band recombination centre, a blue at 460 nm triplet-singlet and an ultraviolet at 290 nm singlet-singlet defect luminescence band.

- Thus, the two broad bands observed at 332 (3.73 eV) and around 440 (2.79 eV) nm in the cathodoluminescence spectra of Aouelloul impact glass and Muong Nong-type tektite might be related to the presence of such defect centers. The broad band at 332 nm (3.73 eV) might be attributed to the dominant defects, which occur in the short range order involving the slightly distorted SiO_4 tetrahedra. These defects are common to both the crystalline and amorphous SiO_2 structures. The band at 444 nm (2.79 eV) is probably associated with the radiative relaxation of the STE in quartz, which is strongly polarized along the c-axis (Kalceff et al. 2000). The broad band at 390 nm (3.17 eV) in the cathodoluminescence spectrum of the Libyan Desert Glass might be related to defect centers in the SiO_2 structure (e.g., $-O-O-;O_2$) (Stevens Kalceff et al. 2000). The CL images of the tektite show only a few areas with brightness variations, whereas the Aouelloul glass and the Libyan Desert Glass CL images show significant variations in contrast and brightness.

References

Blum JD, Chamberlain CP, Hingston MP, Koeberl C, Marin LE, Schuraytz BC, Sharpton VL (1993) Isotopic comparison of K-T boundary impact glass with melt rock from the Chicxulub and Manson impact structures. Nature 364:325-327

Boggs S, Krinsley DH, Goles GG, Seyedolali A, Dypvik H (2001) Identification of shocked quartz by scanning cathodoluminescence imaging, Meteorit Planet Sci 36: 783-793

Bunch TE (1968) Some characteristics of selected minerals from craters. In: French BM, Short NM (eds) Shock metamorphism of natural materials. Mono Book Corporation, Baltimore, 413-432 pp.

Chao ECT, Shoemaker EM, Madsen BM (1960) First natural occurrence of coesite. Science 132: 220-222

Dence MR (1972) The nature and significance of terrestrial impact structures. 24th International Geological Congress, Montreal, Canada. Proceedings Section 15: 77-89

Deutsch A (1998) Examples for terrestrial impact structures. In: Marfunin, S.A. (ed), Mineral matter in space, mantle, ocean floor, biosphere, environmental management, and jewelry. Adv Min vol. 3, Springer-Verlag, Berlin, Heidelberg, pp 119-129

Dietz RS (1968) Shatter cones in cryptoexplosion structures. In: French MB, Short NM (Eds.) Shock metamorphism of natural materials. Mono Book Corporation, Baltimore 267-285 pp.

Emmons RC (1943) The Universal Stage (With Five Axes of Rotation). Geol Soc Am Memoir 8:205 pp.

French BM (1998) Traces of Catastrophe: A Handbook of Shock-Metamorphic Effects in Terrestrial Meteorite Impact Structures. LPI Contribution No. 954, Lunar and Planetary Institute, Houston, 120 pp.

French BM, Short NM, (Eds) (1968) Shock metamorphism of natural materials. Mono Book Corporation, Baltimore, 644 pp.

Gault DE, Quaide WL, Oberbeck VR (1968) Impact cratering mechanics and structures. In: French BM, Short NM (Eds.), Shock metamorphism of natural materials. Mono Book Corporation, Baltimore, pp. 87-99.

Gash PFJ (1971) Dynamic mechanism for the formation of shatter cones. Nature 230:32-35

Glass BP, Barlow RA (1979) Mineral inclusions in Muong Nong-type indochinites: Implications concerning parent material and process of formation. Meteoritics 14:55-67

Goltrant O, Cordier P, Doukhan JC (1991) Planar deformation features in shocked quartz: a transmission electron microscopy investigation. Earth Planet Sci Lett 106:103-115

Goltrant O, Leroux H, Doukhan J-C, Cordier P. (1992) Formation mechanism of planar deformation features in naturally shocked quartz. Phys Earth Planet Inter 74:219-240

Gucsik A, Koeberl Ch, Brandstätter F, Libowitzky E, Ming, Z. (2004a) Infrared, Raman, and cathodoluminescence studies of impact glasses. Meteoritics and Planetary Science 39: 1273-1285

Gucsik A, Koeberl C, Brandstätter F, Libowitzky E Reimold WU (2004b) Cathodoluminescence, electron microscopy, and Raman spectroscopy of experimentally shock metamorphosed zircon crystals and naturally shocked zircon from the Ries impact crater. In: Dypvik H, Burchell M, Claeys Ph, (eds.) Cratering in Marine Environments and on Ice, Springer-Verlag, Heidelberg, pp 281-322.

Gucsik A, Koeberl Ch, Brandstätter F, Libowitzky, E, Reimold, WU (2003) Scanning electron microscopy, cathodoluminescence, and Raman spectroscopy of experimentally shock-metamorphosed quartzite. Meteorit Planet Sci 38:1187-1197

Grieve RAF (1987) Terrestrial impact structures. Annu Rev Earth Planet Sci 15:245-270

Grieve RAF (1991) Terrestrial impact: The record in the rocks. Meteoritics 26: 175-194

Grieve RAF, Langenhorst F, Stöffler D. (1996) Shock metamorphism of quartz in nature and experiment: II. Significance in geoscience. Meteorit Planet Sci 31:6-35

Hörz F (1982) Ejecta of the Ries crater, Germany. In: Silver LT, Schultz PH (eds.), Geological implications of impacts of large asteroids and comets on the Earth. Geol Soc Am Spec Paper 190: 39-55

Hörz F, Quaide WL (1973) Debye-Scherrer investigations of experimentally shocked silicates. Moon 6: 45-82

Kaus A, Bischoff A, (2000) Cathodoluminescence (CL) properties of shocked plagioclase, Meteorit Planet Sci 35:A 86

Kieffer SW, Simonds CH (1980) The role of volatiles and lithology in the impact cratering process. Rev Geophys Space Phys 18:143-181

Koeberl C (1992) Water content of glasses from the K/T boundary, Haiti: indicative of impact origin. Geochim Cosmochim Acta 56:4329-4332

Koeberl C (1997) Impact cratering: the mineralogical and geochemical evidence. In: Johnson KS, Campbell JA (eds) Ames structure in northwest Oklahoma and similar features: origin and petroleum production (1995 symposium). Okl Geol Surv Circ 100: 30-54

Koeberl C, Bottomley R, Glass BP, Storzer D (1997a) Geochemistry and age of Ivory Coast tektites and microtektites. Geochim Cosmochim Acta 61: 1745-1772

Koeberl C, Masaitis VL, Shafranovsky GI, Gilmour I, Langenhorst F, Schrauder M (1997b) Diamonds from the Popigai impact structure, Russia. Geology 25:967-970

Leroux H, Reimold WU, Doukhan J-C (1994) A T.E.M. investigation of shock metamorphism in quartz from the Vredefort dome, South Africa. Tectonophysics 230:223-239

Littler J Fahey JJ Dietz RS Chao ECT (1961) Coesite from the Lake Bosumtwi crater, Ashanti, Ghana. Geol Soc Am Spec Paper 68:218

Martinez I, Agrinier P (1998) Meteorite impact craters on Earth: major shock induced effects in rocks and minerals. Earth Planet Sci 327:75-86

Martinez I, Deutsch A, Schärer U, Ildefonse P, Guyot F, Agrinier P. (1995) Shock recovery experiments on dolomite and thermodynamical calculations of impact induced decarbonation. J Geophys Res 100:15,465-15,476

Medenbach O (1985) A new microrefractometer spindle stage and its application. Fortsch Mineral 63: 111-133

Meisel T, Krähenbühl U, Nazarov MA (1995) Combined osmium and strontium isotopic study of the Cretaceous-Tertiary boundary at Sumbar, Turkmenistan: A test for an impact vs. volcanic hypothesis. Geology 23:313-316

Melosh HJ (1989) Impact Cratering: A geologic process. Oxford University Press, New York, 245 pp.

Melosh HJ (1992) Impact crater geology. In: Nierenberg WA (Ed.), Encyclopedia of earth system science 2. Academic Press, San Diego, pp 591-605.

Montanari A, Koeberl C (2000) Impact stratigraphy: The italian record. Lecture Notes in Earth Sciences 93, Springer, Heidelberg, 364 pp.

Owen MR, Anders HM (1988) Evidence from cathodoluminescence from non-volcanic origin of shocked quartz at the Cretaceous/Tertiary boundary, Nature 334:145-147

Ramseyer K, AlDahan AA, Collini B, Lindström O (1992) Petrological modifications in granitic rocks from the Siljan impact structure: evidence from cathodoluminescence. Tectonophysics 216:195-204

Reimold WU (1995) Pseudotachylite in impact structures - generation by friction melting and shock brecciation?: A review and discussion. Earth Sci Rev 39: 247-265

Robertson PB, Dence MR, Vos MA (1968) Deformation in rock-forming minerals from Canadian craters. In: French BM, Short NM, (Eds.) Shock metamorphism of natural materials. Mono Book Corporation, Baltimore, pp. 433-452.

Seyedolali A, Krinsley DH, Boggs S, O'Hara PF, Dypvik H, Goles G (1997) Provenance interpretation of quartz by scanning electron microscope-cathodoluminescence fabric analysis, Geology 25:787-790

Shagy A, Reches Z, Fineberg J, (2002) Dynamic fracture by large extraterrestrial impacts as the origin of shatter cones. Nature 418: 310-313

Sharpton VL, Grieve RAF (1990) Meteorite impact, cryptoexplosion, and shock metamorphism; A perspective on the evidence at the K/T boundary. Geol Soc Am Spec Paper 247: 301-318
Shoemaker EM, Chao ECT (1961) New evidence for the impact origin of the Ries Basin, Bavaria, Germany. J Geophys Res 66: 3371-3378
Sippel RF, Spencer AB (1970) Luminescence petrography and properties of lunar crystalline rocks and breccias, Proc. Apollo 11 Lunar Sci.Conf. 3:2413-2426
Kalceff MAS, Phillips MR, Moon AR, Kalceff W (2000) Cathodoluminescence microcharacterisation of silicon dioxide polymorphs: In: Pagel M, Barbin V, Blanc Ph, Ohnenstetter D (eds) Cathodoluminescence in Geosciences. Springer, Heidelberg, p. 193-224
Stöffler D (1972) Deformation and transformation of rock-forming minerals by natural and experimental shock processes: I. Behaviour of minerals under shock compression. Fortsch Mineral 49: 50-113
Stöffler D (1974) Deformation and transformation of rock-forming minerals by natural and experimental processes: II. Physical properties of shocked minerals. Fortsch Mineral 51: 256-289
Stöffler D, Grieve RAF (1994) Classification and nomenclature of impact metamorphic rocks. 25th Lunar and Planetary Science Conference 1347-1348
Stöffler D, Langenhorst F (1994) Shock metamorphism of quartz in nature and experiment: I. Basic observation and theory. Meteoritics 29:155-181
Stöffler D, Hornemann U (1972) Quartz and feldspar glasses produced by natural and experimental shock. Meteoritics 7:371-394

Chapter 3
Petrological Modifications in Continental Target Rocks from Terrestrial Impact Structures: Evidence from Cathodoluminescence

Thomas Götte

3.1 Introduction

The impact of meteorites or asteroids on the Earth Surface is a drastic event and leads to an extreme and rapid change of the prevailing physical conditions. The high amount of energy that is added to the target rocks at once and very much localised with impacts. During crater formation, ejection and shock metamorphism of the target material and the meteorite itself it is transformed to mechanical energy of the shock wave, mechanical energy of the blown out material, thermal energy for heating of the target rocks, energy that is "stored" in deformed minerals and lattice defects, and energy that is required for brittle and plastic deformation of the target rocks. Following the models of Grieve (1988) and Dressler and Reimold (2001) the formation of impact craters is supposed to proceed in three overlapping periods after the impact:

1. Contact and compress ional shockwave: brecciation, melting and vaporisation of the target rocks and the impacting body.
2. Excavation of the transient crater: shocked and commonly molten material is ejected over distances of hundreds of kilometres. Melt is forced downwards into the target rocks forming melt dikes and veins. The shockwave weakens into elastic waves. Decompression results in brecciation and melting. Fallout suevite and Bunte Breccia are formed.
3. Crater modification: gravitational collapse of the crater uplift and the crater walls inward. Movement of melt into the basement fractures and formation of allogenic breccias. The final form of the impact structure is developed. Subsequent cooling and infiltration results in hydrothermal convection inducing mineralisation, alteration of the target rocks, impact melt and metasomatism.

The effects observed in rocks that experienced shock metamorphism have been classified by the strength of deformation (Table 3.1 near here.; Stöffler 1972; Engelhardt 2003). Brittle failure of rocks and minerals starts at shock pressures

Thomas Götte (✉)
Institute for Geological Sciences, University of Bern , Baltzerstrasse 1+3 , CH-3012 Bern, Switzerland
e-mail: thomas.goette@geo.unibe.ch

A. Gucsik (ed.), *Cathodoluminescence and its Application in the Planetary Sciences*,

Table 3.1 Stages of shock metamorphism (Engehardt 2003)

Stage	P[Gpa]	T[°C]	Q_z	Alkalifeldspar	Plagioclase	Biotite	Amphibole Pyroxene	Granitoids
0	< 10	0 – 100	Mosaic formation undulous distinction, deformation bands			Kink bands		Shatter cones, brecciation
I	10 – 35	100 – 300	PDF	PDF	PDF	Kink bands	Mechanical twinning	
II	35 – 45	300 – 900	Diaplectic glass	Diaplectic glass	Diaplectic glass	Kink bands	Mechanical twinning, PDF?	
III	45 – 60	900 – 1300	Diaplectic glass	Melt glass	Diaplectic glass	PDF, thermal degradation	Mechanical twinning, PDF?	
IV	60 – 80	1300 – 3000	Impact melt	Impact melt	Impact melt	Impact melt	Impact melt	Impact melt

<10 GPa, and temperatures are below 100°C. With increasing pressures and temperatures the characteristic microfabrics such as planar deformation features (PDF) and diaplectic glasses are developed. Planar deformation features are developed at lower stress in quartz and feldspars than in chain silicates and phyllosilicates which seem to be more stress resistant. The framework silicates also tend to form diaplectic glasses at pressures above 35 GPa. Impact melts are formed at temperatures above 30°C and as a result of decreasing stresses immediately after the peak of the shock-wave and due to exhumation of deeper parts of the crust in the course of crater formation (Dressler and Reimold 2001). The conditions that are introduced by the impact of a large body need tens of thousands to millions of years to reequilibrate again with their surroundings (Turtle et al. 2003).

Cathodoluminescence microscopy has been found to be an excellent tool to visualise growth and alteration fabrics in minerals and rocks, which cannot be observed in plane polarised light microscopy. Originally introduced to sedimentary petrology in the 1960 s (Sippel 1965, 1968), it provides also a great potential in metamorphic (e.g., Schertl et al. 2004; Leichmann et al. 2003) and magmatic petrology (e.g., Müller et al. 2000, 2005). It has been used to investigate mineral reactions, alteration, growth zoning in metamorphic and magmatic minerals. The spectroscopic analysis of the cathodoluminescence emission, which has become of increasing importance in the last decades gives further information about the nature of the defects which act as luminescence centres. Since the CL-properties of minerals are influenced by the trace element composition as well as by lattice defects, it is particularly powerful in combination with chemical analysis.

The continental crust is predominantly composed of plutonic and metamorphic granitoid rocks consisting mainly of plagioclases, alkali feldspars, quartz and phyllosilicates as well as some accessorial minerals of less importance. Of those, quartz and feldspars commonly exhibit moderate to bright luminescence. Accessorial minerals such as apatite, zircon may show strong luminescence emission. In contrast, many phyllosilicates (especially micas) are usually non-luminescent. Only the kaolinite-group minerals and pyrophyllite have been found to exhibit luminescence emission (Götze et al. 2002). Most of the mafic minerals commonly contain iron (up to several weight % FeO and Fe_2O_3), which is the most important quencher element and might inhibit the luminescence emission completely. So, many mafic minerals are non-luminescent in common continental rocks. However, in some exotic environments these minerals can show luminescence properties that deviate from their common appearance. Nevertheless, this overview will focus on the major components quartz and feldspars as well as some hydrothermal minerals and not on the alteration of mafic minerals.

Modification of the defect structure of the minerals that is induced by shock-metamorphism might be detectable by cathodoluminescence. Heating can only be recognised if it is sufficiently high to induce mineral reactions or melting. A second type of processes is at least as important as the processes directly related to the meteoritic impact. After heating and fracturing new, highly permeable pathways are opened for fluid flow. Hydrothermal convection cells are set up, which are responsible for subsequent mineralisation and metasomatism (Osinski et al. 2001).

3.2 Alteration of Target Rocks and Rock Forming Minerals

The modifications that are introduced to continental target rocks can be classified into effects of the impact itself due to changing pressure and temperature and "post-impact" effects due to infiltration of meteoric water and the development of hydrothermal convection cell, which induce hydrothermal mineralisation and alteration of the shock-metamorphosed rocks in the impact crater. The results of investigation of samples from the Siljan ring structure (Central Sweden, 61°2′N, 14°52′E, Boden and Eriksson 1988), the Charlevoix impact structure (E Canada 47°32′N, 70°18′W, Rodot 1971; Roy 1979) and from the Wabar impact site (S Saudi Arabia, 21°30′N, 50°28′E, Shoemaker and Wynn 1997).

3.2.1 Modifications Related Directly to the Impact

3.2.1.1 Luminescence of Minerals Affected by Shock Metamorphism and Heating

The features that are induced in quartz and feldspars by the high stress of the shock-wave starts with formation of dislocations and mosaic formation and proceeds over the formation of planar deformation features (PDF) with partial amorphisation of the gliding planes (Stöffler and Langenhorst 1994) up to a complete amorphisation in diaplectic glasses (Stöffler 1972; Engelhardt 2003).

Shocked quartz crystals of the Siljan- and Järna-granite from the central part of the Siljan impact structure have been found to show blue luminescence (Ramseyer et al. 1992). This CL deviates significantly from quartz of the northern part of the crater where more intensive alteration took place and the quartz predominantly shows a patchy reddish and blue CL-pattern. However, unaltered primary quartz of the granitic rocks also shows blue luminescence.

Remnant quartz containing PDF has also been found in metasomatically altered samples from the Charlevoix structure. The quartz in samples from the peak ring shows PDFs parallel to (001) and {103}, which indicate pressures at approximately 9 GPa. In the area of the central uplift, PDFs parallel to {103} and {102} point to pressures of about 13 GPa (according to Robertson and Grieve 1977). These quartz grains show similar bright blue luminescence behaviour as primary quartz in adjacent unshocked rocks of the same formation (Fig. 3.1a, b; Trepmann et al. 2005).

Boggs et al. (2001) investigated shocked quartz with PDF from the Miocene Ries Crater (S Germany) by means of SEM-CL with a high resolution. The 1–2 μm thick shock lamellae exhibit no CL in contrast to the more brightly luminescing host quartz. The authors assumed that the formation of glassy SiO_2 would favour non-radiative release of energy rather than by luminescence emission and appear as dark lines in cathodoluminescence images. Boggs et al. (2001) argued that numerous traps in the glass favour non-radiative electron transitions and quench the luminescence. However, there seems to be a fundamental difference between SiO_2-glass

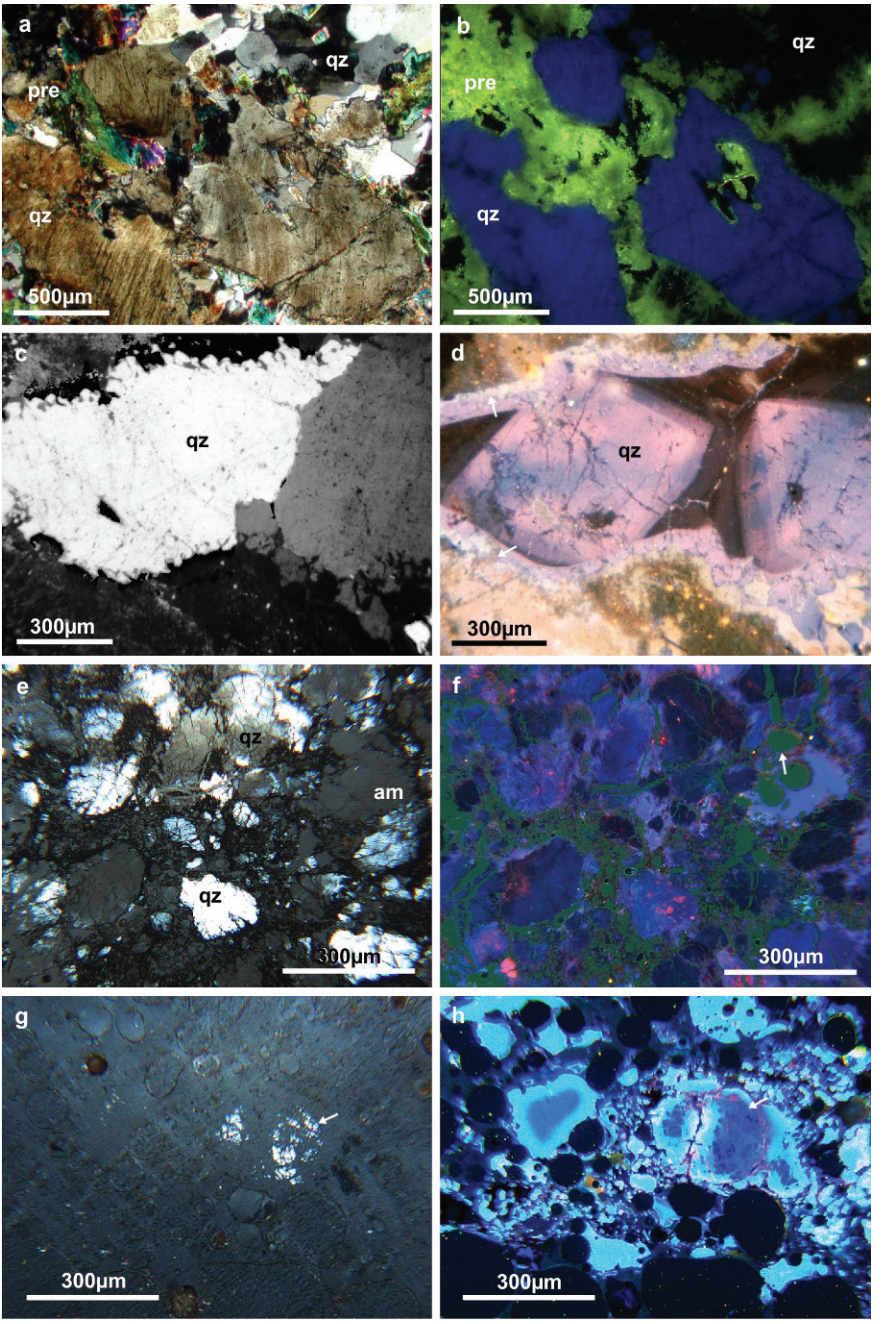

Fig. 3.1 (Caption on next page)

which has been formed from a melt and diaplectic SiO_2-glass because the first one can show quite intensive blue luminescence. One possible reason for this fact might be a high number of unpaired electrons in non-bonding orbitals which result from the breaking of bonds during the vitrification in diaplectic glass.

3.2.1.2 Luminescence Properties of Suevite and Impact Melt Glasses

High grade shock metamorphism results in the formation of impact melt. Parts of this melt can be ejected over several tens or hundreds of kilometres as they have been observed in moldavites, which originate from the Ries Crater Impact in southern Germany and can be found in Slovakia (Engelhardt et al. 2005). Impact-derived glasses are discussed in more detail by Gucsik et al. (2003) (and Chap. 2 in this volume).

Suevite commonly show remnant material of the target rocks of which the primary texture is at least partly preserved and glassy material originating from the impact event. Suevite samples with a porous, partly glassy texture have been found in the Wabar impact area. The target material consists of sandy desert sediments. The suevitic samples show primary quartz grains in a glassy matrix which contains numerous bubbles. The quartz grains display blue to bright blue CL-colours, and the matrix has only a very weak greenish luminescence (Fig. 3.1c, d).

Samples of the Wabar impact site that are stronger affected by temperature are completely vitreous, but inhomogenities with nearly pure SiO_2-domains (lechatelierite) in an Al-alkali-enriched matrix. The internal texture reported by can be observed in the CL, because the lechatelierite-domains show bright blue luminescence colours at the rim and a slightly darker core while the matrix display dark greenish blue luminescence (Fig. 3.1d, e). The SiO_2-enrichments are interpreted to be former quartz grains which are embedded in an impact melt of different composition. Probably the molten material was too viscous to homogenise completely and the chemical inhomogenities have been conserved. Gucsik et al. (2004) found identical textures in impact melt glasses from Mauritania and observed the inhomogenities in BSE-images as well as by CL. They compared this luminescence with the properties

◄

Fig. 3.1 (continued) CL-images of minerals and rocks altered by meteorite impacts: (**a**, **b**) shocked and secondary quartz (qz) and secondary prehnite (pre) from the Charlevoix structure (E Canada, Trepmann et al. 2005), (**a**) crossed polars, shocked quartz show many fluid inclusions and PDFs, (**b**) CL, *blue* luminescing shocked quartz in a matrix of green luminescing prehnite and dark secondary quartz. (**c**, **d**) Quartz (qz) with a complex zonation and characteristic reddish luminescence embedded in brownish luminescing feldspars from the Siljan crater (Central Sweden, Ramseyer et al. 1992), (**c**) crossed polars, (**d**) CL, arrows mark fine intergrowth of quartz and alkali feldspar. e, f: Suevitic sandstone from the Wabar impact site (S Saudi Arabia), (**e**) crossed polars, remnant quartz grains (qz) and amorphous particles (am) in a glassy matrix, (**f**) CL, *dark greenish* resin fills the large bubbles (*arrow*). (**g, h**) Impact melt glass from the Wabar impact site (S Saudi Arabia), (**g**) crossed polars, the arrow marks remnants of a quartz particle, (**h**) CL, *bright blue*, zoned domains of SiO_2-rich lechatelierite in a glassy, dark, Al- and alkali-enriched matrix

of impact melt glasses of the Libyan Desert and from Asia. The intermediate glass from the Libyan Desert seems to be homogeneous in BSE-images but display chemical inhomogenities, which can be visualised by CL. Similar fabrics have been observed in moldavites from the Ries Crater impact (Southern Germany, Engelhardt et al. (2005). The tektites which were formed during this Miocene event can be found in a large area in Central Europe. They show schlieren with a high SiO_2-content and others enriched in Al_2O_3, CaO, FeO and MgO in BSE-images. The eastern Asian glass, which has been assumed to have experienced the highest temperatures shows a homogeneous dark luminescence (Gucsik et al. 2004).

3.2.2 "Post-Impact" Alterations

The extensive production of heat energy, which starts to influence the properties of minerals and rocks immediately after the impact event has the potential to induce further alteration in the target rocks and acts much longer than the shock wave and so might overprint shock-pressure induced metamorphism. The most obvious effect of elevated temperature is the production of impact melts, but the minerals of the target rocks might also be affected themselves. The blue luminescing, homogeneous primary quartz of the Dalan and Järna-granites of the Siljan impact structure has been found to show reddish luminescence and reddish zonations or reddish and blue patches depending on the degree of alteration (Fig. 3.1e, f; Ramseyer et al. 1992). Similar effects have been observed in the Dellen, the Araguainha and the Lappajärvi craters and have been interpreted to be an effect of heating by the impact melt immediately after the impact (Ramseyer et al. 1992; Ramseyer and Mullis 2000).

Hydrothermal activity induced by the heating by overlying impact melt and hot fallback as well as elevation of deeper crystalline rocks and waste shock-induced heat is probably one of the most effective mechanisms of alterating the target rocks. Intensive fracturing of the basement by the shockwave opens the pathways of deep convection cells of meteoric water. In granites of the Siljan impact structure, Ramseyer et al. (1992) found intensively altered feldspars and quartz, which contained sealed fractures and were replaced by secondary minerals. Unaltered plagioclases show yellowish (up to 40% albite) to pinkish (albite-rich) luminescence while primary alkali feldspar (95% orthoclas) have a bright blue to violet CL-colour. In altered samples reaction rims and replacements indicate the decomposition of the feldspars to a secondary paragenesis with albite, sericite, chlorite, calcite, quartz, hematite and epidote in the case of plagioclase and albite, kali feldspar, sericite, hematite and calcite in case of alkali feldspars. The secondary feldspar shows dark brownish (albite) to brown (kali feldspar) CL-colours. Secondary kali feldspar is accompanied by yellow luminescing epidote, orange luminescing calcite as well as zoisite and fluorite showing dark to bright blue CL, respectively. Brownish luminescing albite occurs additionally in fracture fillings. The temperature of the hydrothermal alteration has been suggested to range from $100 - 300°C$ (Komor and Valley, 1990).

Trepmann et al. (2005) observed a new-formed mineralisation of prehnite, quartz and calcite replacing the original Ca-rich plagioclase and quartz of the charnokitic target rocks of the Charlevoix impact structure. The metasomatic alteration is suggested to be related to the impact due to its spatial distribution, the restriction of Ca-rich zones and the high temperature of the mineralisation. Remnant shocked quartz with several sets of PDFs shows bright blue luminescence. In contrast, hydrothermal quartz displays only a weak luminescence and prehnite shows a greenish yellow CL-colour that is activated by incorporation of Mn^{2+}. The temperature of the mineralisation was between 250 and 380°C. Similar CL-properties like in the secondary quartz have been observed in quartz from low-grade metamorphic rocks and some hydrothermal quartz that have been formed at similar conditions (Götte and Richter 2006). Weak initial CL-colour is characteristic of quartz that has been formed relatively slowly from an aqueous solution at moderate to low temperatures. Commonly, the colour shifts toward brownish or reddish during increasing irradiation time.

3.2.3 Characteristics of the Luminescence Spectra of Shock-Metamorphosed and Secondary Minerals

The CL-spectra of shocked quartz from the Charlevoix crater show broad emission bands at 440, 505 and 630-650 nm (Fig. 3.2a). The primary quartz of the unaltered charnocitic gneiss display a similar spectrum but slightly lower intensities of the 440 nm and the emission band at 650 nm is missing (Fig. 3.2b; Trepmann et al. 2005). This is in accord with observations of Ramseyer et al. (1992), who found blue luminescing quartz in the central part of the Siljan ring structure and similar CL-properties of quartz in unaltered granite of this area. The emission bands in the ultra-violet and blue range of the spectrum are commonly assigned to intrinsic defects such as Si-vacancies (Botis et al. 2005) or self-trapped excitons.

Reddish to pinkish luminescing quartz has been found in the northern part of the Siljan crater as well as in the Araguainha crater (Central Brasil, Ramseyer et al. 1992; Ramseyer and Mullis 2000). The unusual colour is caused by an increased emission at 630 to 650 nm additionally to the blue luminescence (Fig. 3.3b). This emission band is commonly assigned to non-bridging oxygen hole centres (NBOHC, Stevens Kalceff and Phillips 1995).

It might be produced by thermal breaking of OH-groups which are incorporated in the quartz. Similar effects have been observed in silica nanoparticles after thermal treatment above 1000°C (Glinka et al. 1999, 2000) as well as in naturally heated quartz in the contact area of magmatic dykes which also show emission bands at 630–650 nm (Ramseyer 2000).

The CL-spectra of blue to bright blue luminescing quartz particles in the suevite samples of the Wabar impact site are dominated by a broad emission band at 390 nm (Fig. 3.3a) and subordinate bands at 415, 450, 500 and 645 nm. The intensity varies according to the visual impression, but the maxima of the emission bands

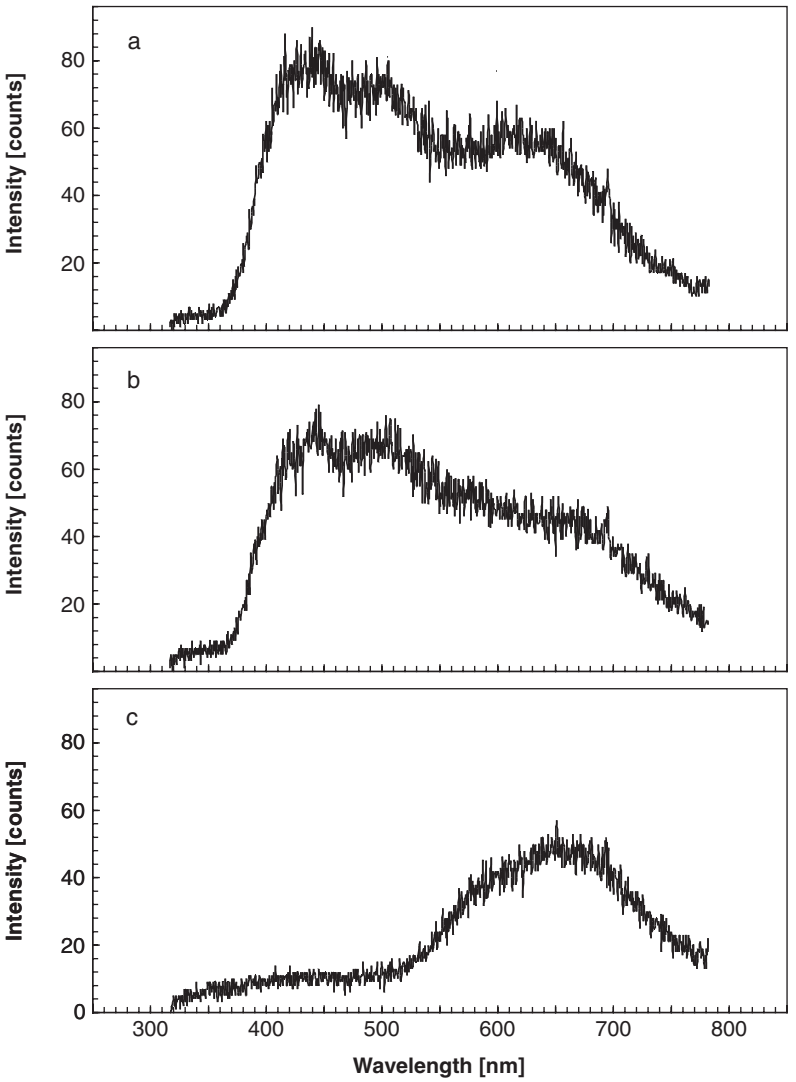

Fig. 3.2 CL-spectra of shocked quartz (**a**), unaltered primary quartz (**b**) and secondary quartz (**c**) from the Charlevoix structure (E Canada, Trepmann et al., 2005)

are constant. The intensity of the 380 nm band slightly decreases and the emission at 650 nm increases during electron irradiation. The similarity of the CL-spectra of remnant shocked quartz and quartz particles in suevite points to a similar defect structure that cause the emission in the blue range of the spectrum. Factors that influence the luminescence are the initial composition of quartz, the temperature and pressure conditions during shock-metamorphism and the velocity of cooling.

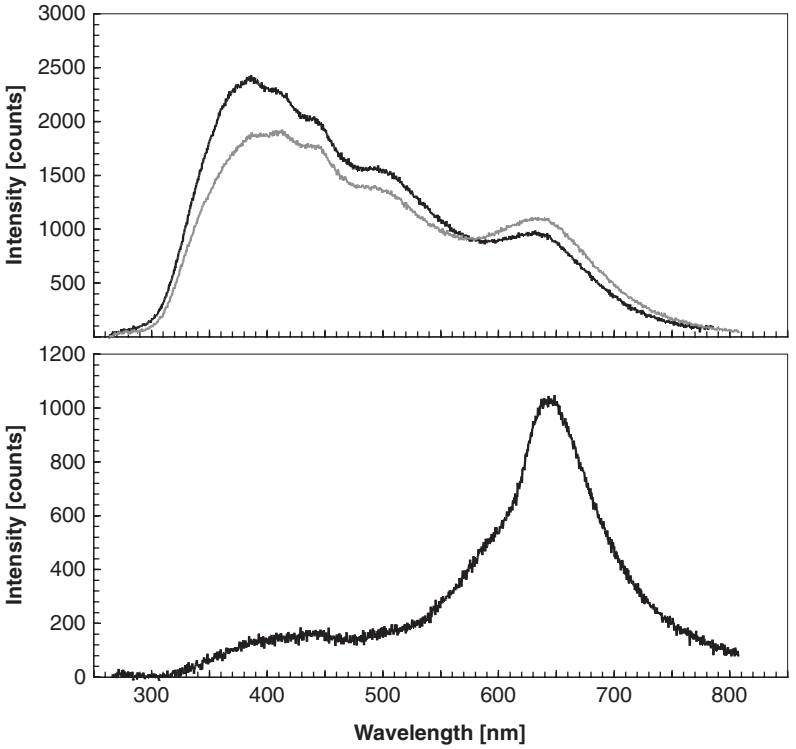

Fig. 3.3 Inital (*black*, 0–10 s) and final (*grey*, 190–200s of irradiation) CL-spectra of quartz from impact structures: (**a**) blue luminescing quartz from a suevite sample of the Wabar impact site (S Saudi Arabia), (**b**) pinkish luminescing quartz from the Siljan impact structure (Central Sweden)

The lechatelieritic domains in the impact melt glasses of the Wabar impact area show bright blue luminescing rims and slightly darker central parts. The CL-colour is caused by predominant emission bands at 375 and 450 nm (Fig. 3.4a). Subordinately, emission bands at 570 and 650 nm have been observed which are also common in quartz. The intensity of the 375 nm band has been found to decrease with increasing radiation dose. This phenomenon has frequently been observed in quartz as well and has been interpreted as an effect of destruction of Al-centres which are compensated by monovalent alkali cations (Li^+,Na^+, Perny et al. 1992; Götze 2000). The spectra of slightly darker cores of the domains display a more intensive emission at 450 nm which even increased with ongoing irradiation (Fig. 3.4b). The CL of the "matrix"-domains is very dark and the luminescence spectra show weak emission bands at 380 and 550 nm (Fig. 3.4c).

Secondary quartz and feldspars (adular as well as albite) has been found to be either non-luminescent or show a weak brownish CL (AlDahan et al. 1988; Ramseyer et al. 1992; Trepmann et al. 2005). The CL-spectrum of secondary, brownish luminescing quartz that has been formed during the hydrothermal alteration of charnocitic host rocks show emission bands at 580 and 650 nm and

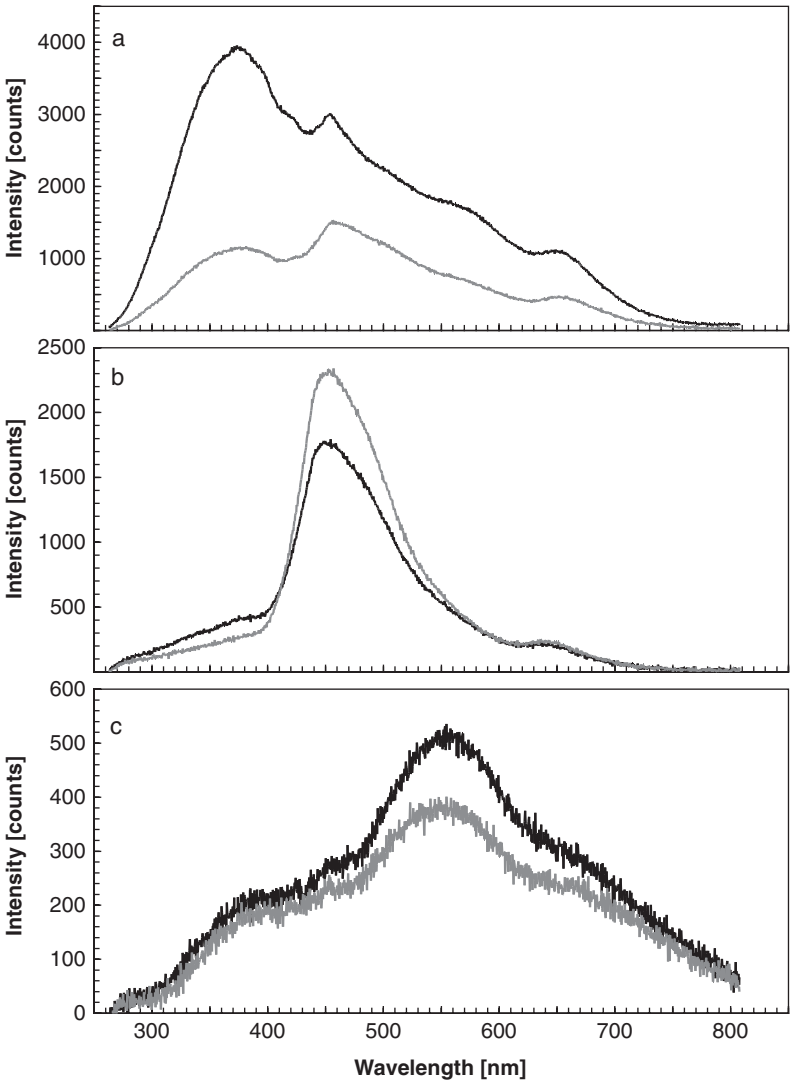

Fig. 3.4 Inital (*black*, 0–10 s) and final (*grey*, 190–200s of irradiation) CL-spectra of impact melt glasses: (**a**) rim and – I**b**) central part of a lechatelierite domain in impact melt glass from the Wabar site (S Saudi Arabia); (**c**) matrix of impact melt glass from the Wabar site (S Saudi Arabia)

exhibit no significant emission in the UV and blue range of the spectrum (Fig. 3.2c, Trepmann et al. 2005). Especially the band at 650 nm which increases with ongoing irradiation is characteristic of quartz which formed from aqueous solution at low temperatures. It has been supposed to result from breaking of silanol and peroxy-defects in the quartz (Stevens Kalceff and Phillips 1995). Brownish CL-colours are rarely observed in magmatic feldspar but are more common in crystals that formed

from aqueous solutions at low temperatures in sediments or in hydrothermal mineralisation (Götze 2000; Richter et al. 2002, 2003). This result is in accord with the interpretation that the secondary minerals related to impact were formed from hydrothermal fluids percolating through the fractured basement.

3.3 Distribution of Impact Related Alterations: A Discussion

Meteorite impacts on the Earth are suggested to occur relatively regular in time except in the early history of the earth. Since only approximately 30% of the earth surface is covered by continents, most impacts probably hit the oceans. Unfortunately, most of these structures are either destroyed by subduction of the oceanic crust ($\sim$ 200Ma) or are extremely difficult to investigate because they are covered by ocean water and young sediments. Terrestrial impact structures in contrast have a much greater potential to be preserved and are much easier accessible. Furthermore, they are eroded to different levels. This fact gives the chance to summarize the phenomena that are observed on terrestrial impact structures in a generalised template which should match to many different locations. A sketch of the distribution of impact induced phenomena is shown in Fig. 3.5.

The impact crater itself is commonly filled with impact melt, suevite and/or allogenic breccias (cf. compilation of Dressler and Reimold 2001). It might be overlain by lake deposits and younger sediments in many cases. This inner ring of complex craters is surrounded by a zone where mega-blocks and breccias ejected after the impact were deposited and which might be twice as large as the crater itself. Megablocks of the target rocks and "Bunte Breccias" may be only minor affected by the impact and show no textural alterations which can be visualised by means of CL.

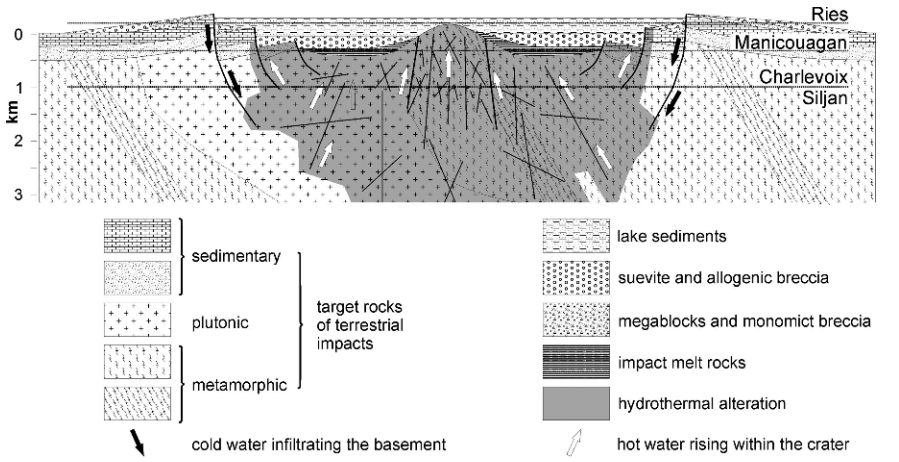

Fig. 3.5 Schematic sketch of an impact structure and distribution of rock types and alterations observable with CL

The uppermost part of the target rocks seems partly to be ejected without noteworthy shock metamorphism (e.g. in the Ries Crater, Engelhardt 1997). Tektites which are ejected high in the atmosphere might be distributed several hundreds of kilometres as in the case of the Moldavites from the Ries Impact (Engelhardt 1995, 1997) and other impact sites (Gucsik et al. 2004). On the surface the occurrence of tektites and suevite particles and impact melt glasses that show remarkable characteristic CL-features is the most obvious indicator of an impact. The origin of the blue luminescence of quartz in suevitic rocks and of lechatelierite in impact melt glass has not been fully understand up to now. It might be either correlated to Al^{3+}-defects (Perny et al. 1992) or to intrinsic Si-defects (Botis et al. 2005).

The basement beneath the crater is eroded in many paleozoic and mesozoic impact structures (e.g., Charlevoix structure, Siljan structure). Even at greater depth, however, shock-metamorphic minerals with planar deformation features are commonly found in target rocks of eroded impact craters. The basement below the impact site is intensively fractured, and increased fluid flow and elevated temperatures gave rise to intensive hydrothermal alteration down to depths of several kilometres. Especially the deeply eroded structures of the Charlevoix structure and the Siljan structure clearly show that petrological modification and hydrothermal alteration of the target rocks which can be visualised by cathodoluminescence reach depths of more than 1000 m.

AlDahan et al. (1988) and Ramseyer et al. (1992) found hydrothermal alteration at low temperatures in the granitic target rocks of the Siljan crater which is assumed to be eroded to approximately 1500 m (Grieve 1988). Especially plagioclases are susceptible for albitisation and dissolution. The alteration of feldspars has been found down to 4000 m below the present surface. The amount of unaltered feldspars increased from less than 50% in samples of surface outcrops and the uppermost 1000 m to more than 70% in samples at a depth of 4200 m in the Gravenberg I-well according to CL-investigations (AlDahan et al. 1988; Ramseyer et al. 1992). The altered feldspars are accompanied by patchy, reddish luminescing quartz in the uppermost 2000 m. Additionaly, the amount of biotite, which is transformed to chlorite, phengite, hematite and Ti-oxide, increases in the depth as well as the amount of Fe-Ti-oxides and magnetite which are transformed to hematite and Ti-oxides in the uppermost 2000 m. The meteoric water is supposed to circulate as deep as 7000 m and up to 50 km beyond the original rim due to deep fracturing and impact shock heating (AlDahan et al. 1988). The Ca-metasomatism in the Charlevoix-structure, which is eroded at least 1 km (Roy 1979), also indicates circulation of reactive fluids in greater depths below the impact crater. Hydrothermally altered charnockitic host rocks are found in the central uplift as well as in the discontinuous crater rim. The relatively high temperature of the mineralising fluid and the restriction of the deep metasomatism to Ca-rich zones indicate that the mineralisation is closely related to the impact event.

The mechanisms of feldspar alteration can be imagined as reaction of a thermodynamically unstable mineral and formation of a stable paragenesis. The reaction is promoted by elevated temperatures and increased fluid flow. The causes for the uncommon brownish luminescence of secondary feldspar remains unclear but

is probably correlated to lattice defects rather than to trace element incorporation (Richter et al. 2002). The weak brown luminescence of secondary quartz indicates that low-grade metamorphic conditions prevailed during the formation since similar CL-properties are commonly observed in low-grade metamorphic quartz (Götte and Richter 2006). The altered reddish luminescence of primary quartz is more complicated. It has been interpreted to be an effect of high temperatures after the impact (Ramseyer et al. 1992), especially because it can also be produced by heat treatment of natural quartz in the laboratory and is observed in fulgurite (Ramseyer, pers. comm.) and in volcanic rocks. However, shocked quartz never shows reddish CL although it has experienced similar temperatures.

3.4 Summary

Numerous processes are going forward in continental rocks after a meteorite impact, which cause characteristic changes of the primary plutonic, metamorphic and sedimentary rocks. These processes can be visualised by cathodoluminescence investigation if they result either in changes of the structure of luminescence active defects in minerals or result in mineral reactions that can be observed by cathodoluminescence but not necessarily by conventional petrographic analyses. The following processes can be commonly observed in shock-influenced rocks:

1. Quartz particles in suevitic rocks show blue luminescence of variable brightness that is similar to that of shocked quartz.
2. Lechatelieritic domains in chemically inhomogeneous impact melt glasses show a bright blue luminescence. Chemically homogeneous impact melt glasses show only weak or no luminescence.
3. Shocked quartz (and feldspar) contains planar deformation features and shows a characteristic blue luminescence. Diaplectic glasses probably show no luminescence.
4. Heated quartz tend to develop reddish patches or zones which are not observed in primary quartz of the target rocks but might correspond to reddish or pinkish quartz-phenocrysts in volcanic rocks or in sandstones in contact with magmatites.
5. Hydrothermal solutions circulating through the fractured basement beneath the impact crater and elevated temperatures due to overlying impact melts and hot fallback, uplift of basement rocks and waste shock-induced heat cause alteration of reactive minerals such as feldspars that can be visualised by cathodoluminescence in some cases. Secondary feldspars and quartz show weak brownish luminescence emission, which is very different form the CL-properties of the primary magmatic minerals.

Acknowledgements Thanks are due to K. Ramseyer (Bern) who kindly promoted this study and provided samples and CL-images of the Wabar impact site as well as CL-images of the Siljan impact structure and to C. Trepmann (Bochum) who provided CL-spectra and –images of altered target rocks from the Charlevoix impact structure.

References

AlDahan AA, Ramseyer K, Morad S, Collini B (1988) Low temperature alterations in granitic rocks from the Siljan Ring Structure, Central Sweden. In: Bodén, A. and Eriksson, K. G. (eds) Deep Drilling in Crystalline Bedrock, vol. I. Springer, Berlin, pp 209–216

Boden A, Eriksson KG (1988) Deep drilling in crystalline bedrock, Vol. I. Springer, Berlin, Heidelberg, New York

Boggs Jr. S, Krinsley DH, Goles GG, Seyedolali A, Dypvik H (2001) Identification of shocked quartz by scanning cathodoluminescence imaging. Meteorit Planet Sci 36:783–791

Botis S, Nokhirn SM, Pan Y, Xu Y, Bonli Th (2005) Natural radiation-induced damage in quartz. I. Correlations between cathodoluminescence and paramagnetic defects. Can Mineral 43:1565–1580

Dressler BO, Reimold WU (2001): Terrestrial impact melt rocks and glasses. Earth-Sci Rev 56:205–284

Engelhardt W v (1995) Suevite breccia from the Ries crater, Germany: Origin, cooling history and devitrification of impact glasses. Meteoritics 30:279–293

Engelhardt W v (1997) Suevite breccia of the Ries impact crater, Germany: Petrography, chemistry and shock metamorphism of crystalline rock clasts. Meteoritics and Planetary Science 32:545–554

Engelhardt W v (2003) Struktur und frühe Morphologie des Rieskraters. Geologica Bavarica 108:159–200

Engelhardt W v, Berthold Ch, Wenzel Th, Dehner Th (2005) Chemistry, small-scale inhomogeneity, and formation of moldavites as condensates from sands vaporized by the Ries impact. Geochim Cosmochim Acta 69:5611–5626

Glinka YD, Lin S-H, Chen Y-T (1999) The photoluminescence from hydrogen-related species in composites of SiO2 nanoparticles. Appl Phys Lett 75(6):778–780

Glinka YD, Lin S-H, Hwang LP, Chen YT (2000) Photoluminescence from mesoporous silica: Similarity of properties to porous silicon. Appl Phys Lett 77(24):3968–3970

Götte Th, Richter DK (2006) Cathodoluminescence characterization of quartz particles in mature arenite. Sedimentology 53:1347–1359

Götze J (2000) Cathodoluminescence microscopy and spectroscopy in applied mineralogy. Freiberger Forschungshefte C 485:128

Götze J, Plötze M, Götte Th, Neuser RD, Richter DK (2002) Cathodoluminescence (CL) of clay minerals. Mineral Petrol 176:195–212

Grieve RAF (1988) The formation of large impact structures and constraints on the nature of Siljan. In: Bodén, A, Eriksson, KG (eds) Deep Drilling in Crystalline Bedrock, vol. I. Springer, Berlin, pp 328–348

Gucsik A, Koeberl Ch, Brandstätter F, Libowitzky, E, Reimold, WU (2003) Scanning electron microscopy, cathodoluminescence, and Raman spectroscopy of experimentally shock-metamorphosed quartzite. Meteorit Planet Sci 38:1187–1197

Gucsik A, Koeberl C, Brandstätter F, Libowitzky E, Ming, Z. (2004) Infrared, Raman, and cathodoluminescence studies of impact glasses. Meteorit Planet Sci 39:1273–1285

Komor SC, Valley JW (1990) Deep drilling at the Siljan Ring impact structure: oxygen isotope geochemistry of granite. Contrib Mineral Petrol 105:516–532

Leichmann J, Broska I, Zacholeva K (2003) Low-grade metamorphic alteration of feldspar minerals: a CL-study. Terra Nova 15:104–108

Müller A, Seltmann R, Behr H-J (2000) Application of cathodoluminescence to magmatic quartz in a tin granite – case study from the Schellerhau Granite Complex, Eastern Erzgebirge, Germany. Mineralium Deposita 35:169–189

Müller A, Breiter K, Seltmann R, Pecskay Z (2005): Quartz and feldspar zoning in the eastern Erzgebirge volcano-plutonic complex (Germany, Czech Republic): evidence of multiple magma mixing. Lithos 80:201–227

Osinski GR, Spray JG, Lee P (2001) Impact-induced hydrothermal activity within the Haughton impact structure, arctic Canada: Generation of a transient, warm, wet oasis. Meteorit Planet Sci 3:731–745

Perny B, Eberhardt E, Ramseyer K, Mullis J, Pankrath R (1992) Microdistribution of Al, Li and Na in a-quartz: possible causes and correlation with short lived cathodoluminescence. Am Mineral 77: 534–544

Ramseyer K, Mullis J (2000) Geologic application of cathodoluminescence of silicates. In: Pagel M, Barbin V, Blanc P, Ohnenstetter D (eds) Cathodoluminescence in geosciences. Springer, Berlin, pp 177–191

Ramseyer K, AlDahan AA, Collini B, Landström O (1992) Petrological modifications in granitic rocks from the Siljan impact structure: evidence from cathodoluminescence. Tectonophysics 216:195–204

Richter DK, Götte Th, Habermann D (2002) Cathodoluminescence of authigenic albite. Sediment Geol 150:367–374

Richter DK, Götte Th, Götze J, Neuser RD (2003) Progress and application of cathodoluminescence (CL) in sedimentary petrology. Mineral Petrol 79:127–166.

Robertson PB, Grieve, RAF (1977) Shock attenuation at terrestrial impact structures. In: Roddy DJ, Pepein RO, Merill RB (eds) Impact and explosion cratering. Pergamon Press, New York, pp 687–702

Rodot J (1971) Impactite of the charlevoix structure, Quebec, Canada. J Geophys Res 76:5414–5423

Roy DW (1979) Origin and evolution of the charlevoix cryptoexplosion strucutre. Ph.D. thesis, Princeton University, Princeton, New Jersey

Schertl H-P, Neuser, RD, Sobolev NV, Shatsky VS (2004) UHP-metmorphic rocks from Dora Maira/Western Alps and Kokchetav/Kazakhstan: New Insight using cathodoluminescence petrography. Eur J Mineral 16:49–57

Shoemaker EM, Wynn JC (1997) Geology of the Wabar meteorite craters, Saudi Arabia. Proceedings of the XXVIII lunar and planetary science conference, Houston, Texas vol 3: pp 1313–1314

Stevens Kalceff MAS, Phillips MR (1995) Cathodoluminescence microcharacterization of the defect structure of quartz. Phys Rev B 52(5):3122–3134

Sippel RF (1965) Simple device for luminescence petrography. Rev Scient Intr 36:556–558

Sippel RF (1968) Sandstone petrology, evidence from luminescence petrography. J Sediment Petrol 38:530–554

Stöffler D, Langenhorst F (1994) Shock metamorphism of quartz in nature and experiment I. Basic observation and theory. Meteoritics 29:155–181

Stöffler D (1972) Deformation and transformation of rock-forming minerals by natural and experimental shock processes II. Behaviour of minerals under shock compression. Fortschritte der Mineralogie 49:50–113

Trepmann CA, Götte Th, Spray JG (2005) Impact-related Ca-metasomatism in crystalline tragetrocks from the Charlevoix structure, Quebec, Canada. Can Mineral 43:553–567

Turtle EP, Pierazzo E, O'Brien, DP (2003) Numerical modeling of impact heating and cooling of the Vredefort impact structure. Meteorit Planet Sci 38:293–303

Chapter 4
Impact Diamonds: Formation, Mineralogical Features and Cathodoluminescence Properties

Giovanni Pratesi

4.1 Introduction

Impact diamonds represent the product of uncommon, although important, natural phenomena. The planetary bodies that have retained portions of the cratered surfaces witness a long history of collisions: such collisions have been effective for accretion of planetesimals and planets themselves and, therefore, represent a dominant process throughout the early solar system (French 1998; Gehrels 1994; Chapman and Morrison 1989; Koeberl 2006).

When a collision between two bodies occurs, the kinetic energy of the impactor rapidly converts into high pressures and temperatures that may, in turn, yield mineralogical transformations. Depending on several factors (i.e. mass of the impactor, velocity of impact, density of the impacting object, angle of impact, density and porosity of the target material) the formation of new phases may interest the target, the impactor or both of them (Melosh 1989, Melosh 2007). The dynamic pressures connected with the impact shock waves act in a different way in comparison with those occurring in the depth of the Earth; in particular, although the absolute values may be similar, the durations of the shock pressures are several orders of magnitude shorter (Migault 1998) and the strain rates are orders of magnitude greater than those achieved in normal crustal deformation.

As previously stated, impact processes – and the related formation of impact diamonds – are not exclusively confined to the Earth but are widespread in solar system, affecting planets and asteroids as well. Many groups of meteorites contain diamonds: typically CV and CO carbonaceous chondrites may contain hundreds ppm of diamonds whereas CM and CI show amounts even higher than 1000 ppm (Daulton et al. 1996; Hoppe and Zinner 2000). But also iron meteorites, ureilites, enstatite chondrites, unequilibrated H, L, LL ordinary chondrites may be diamonds carrier (Huss and Lewis 1995) as well as some interplanetary dust particles (IDPs). Nevertheless, while micro-diamonds in iron meteorites and ureilites are supposed to be connected with static or dynamic pressure effects (i.e. mainly

Giovanni Pratesi (✉)
Dipartimento di Scienze della Terra, Università di Firenze, Via G. La Pira 4, 50121 Firenze, Italy; Museo di Scienze Planetarie, Provincia di Prato, Via Galcianese 20/H, 59100 Prato, Italy
e-mail: giovanni@unifi.it

A. Gucsik (ed.), *Cathodoluminescence and its Application in the Planetary Sciences*,

related with dynamic shock wave occurring during impact processes) (Lipschutz and Anders 1961; Hanneman et al. 1967; Masaitis et al. 1990), the origin of nanodiamonds in chondrites is still actively debated (Daulton et al. 1996; Dai et al. 2002a, b; Bradley 2003). In particular nanodiamonds seem to be absent or very depleted in fragile, carbon-rich interplanetary dust particles, and therefore most nanodiamonds may have formed within the inner Solar System and be not presolar at all (Dai et al. 2000b).

Since this chapter deals with impact diamonds whose origin has to be undoubted, only diamonds coming from impact craters and showing characteristic features of impact processes (see Sect. 4.2.2) have been investigated by means of cathodoluminescence (CL). However, the discussion on the cathodoluminescence properties of impact diamonds will be extended to all optical centres that could be potentially yielded by natural or artificial high-pressure shock-induced metamorphism.

4.2 Occurrences and Features of Impact Diamonds

4.2.1 Occurrences

The first discovery of diamonds in planetary materials dates back to 1888, when diamonds were found in the Novo Urei, Russia, ureilite (Yerofeev and Lachinov 1888). Soon after (Foote 1891) impact diamonds were discovered in Canyon Diablo iron meteorites, although, at that time, their impact origin was not recognized; in fact, it was only in the 1950s that a shock origin for the diamonds of the Canyon Diablo meteorite was put forward (Nininger 1956). Finally, in the 1970s, the first occurrence of impact diamonds in the rocks of a terrestrial meteoritic crater, at the Popigai astrobleme in Russia, was announced (Masaitis et al. 1972; Vishnevskya and Palchik 1975).

4.2.1.1 Popigai Crater

As stated above, the first crater where abundant impact diamonds have been found is the Popigai crater in Russia (Masaitis et al. 1990). Here diamonds of up to 2 mm in size can be collected in areas that result to be function of the initial distribution of coal- or graphite-bearing rocks as well as the temperature and pressure fields (Koeberl et al. 1995): where the temperatures were too high (e.g. in the central part of the crater), no impact diamonds are recovered because the carbon was burned; conversely, in the adjacent areas, the temperatures were low enough and the pressure high enough to form many impact diamonds. At Popigai the most of diamonds have been found in impact melt rocks (tagamites) and suevites but some diamonds also occur in situ, in the target rocks (Koeberl et al. 1995). Some authors (Valter and Dobraynskii 2002) demonstrated that the cooling down mode may influence the impact diamond distribution: tests of the Popigai crater tagamites invariably reveal the highest diamond content in quenched near-contact areas.

According to Langenhorst and Masaitis (1996), at Popigai two main types of diamonds have been described: paramorphs diamonds (idiomorphic diamond platelets) form inclusions in strongly shocked (>30 GPa) gneiss clasts of suevites; xenomorphic, polycrystalline aggregates, occur in impact melt rocks (tagamites) and impact melt clasts of suevites.

4.2.1.2 Ukrainian Impact Structures (Obolon, Ilyinets, Zapadnaya, Terny)

The highest concentration of diamonds was detected in Zapadnaya (Belilovka) crater, although impact diamonds may also be found in the rocks of Obolon, Ilyinets, Terny and some other impact structures of the Ukrainian shield (Gurov 1995).

At Zapadnaya, only impactites with glass fragments (suevites) and glass matrix (tagamites) appear to be diamantiferous; the diamond contents in these rocks varies from $\sim$ 1.2 carats per ton in suevites, to $\sim$ 4.7 carats per ton in tagamites and up to 9.1 carats per ton in rich tagamite veins (Valter et al. 2000). They look like tabular grains, from tens of micrometers up to 0.5 mm in diameter, whose color ranges from colorless, white, yellowish to gray, dark gray and black. Deformation structures are revealed by undulatory extinction and up to four systems of planar features per grain (Gurov et al. 1996). Studies performed using X-ray powder pattern disclosed a cryptoaggregatic structure of the apparently monocrystalline grains of diamond. The cubic phase is prevalent in all investigated diamonds; however, all the grains contain variable percents (from 10 to 78%) of the hexagonal phase lonsdaleite (Gurov et al. 1996; Valter et al. 2000; Oleinik et al. 2003).

4.2.1.3 Yanis-Järvi Crater

Three main species of the carbon matter occur at Yanis-Järvi: graphites, duly carbon matter and shiny carbon matter (Vishnevsky and Palchik 2002).

Duly carbon matter, containing a great number of superfine particles with cubic diamond structure, is made up of strongly shock-disordered graphite preserving the structural sheet feature.

Shiny carbon matter is mainly formed of amorphous phase with a multiple development of fine cubic diamond crystallites; this carbon matter probably represents the result of shock metamorphism of schungite or anthraxolite of the target and, therefore, it appears to be similar to some togorites (high-pressure species of shocked coal) found in Kara impact structure (Ezersky 1982, 1986; Vishnevsky et al. 1997).

A remarkable feature of Yanis-Järvi impactites is the extreme rarity, if any, of complete impact diamond paramorphs derived from parental graphite, in spite of its broad presence in target and impact melt rocks (Vishnevsky and Palchik 2002).

4.2.1.4 Ries Crater

The diamond, in the Ries crater, was first discovered in 1978 (Rost et al. 1978). At Ries the impact diamonds (in concentration ranging from 0.06 to 0.7 ppm) can be only found in suevite whole rock samples, glass bombs and highly shocked

fragments of the suevite (Schmitt et al. 1999) whereas lithic breccias and impact melt breccias do not contain any diamond. In particular, the glass bombs of the fallout suevite, formed by melting at shock pressures above 60 GPa, are the main carrier of diamonds; crater suevite also contain diamonds but in lower concentration (Schmitt et al. 1999).

Impact diamonds from Ries occur as polycrystalline aggregates, reach sizes up to 300 μm and show colour varying from colourless, yellowish and greenish to grayish-black (Abbott et al. 1996). All the diamonds found in glass bombs from Otting, Aumühle, Seelbronn and Zipplingen appear in pseudo-hexagonal plates and show parallel intergrowth of platelets, sometimes showing Veselowski twinning, as a common morphological feature (Schmitt et al. 1999). Moreover they contain impurities of graphite, often oriented in lamellae, and some of them show a transition from graphite to diamond (Siebenschock et al. 1998). Very often the diamond plates are kinked or bent (Fig. 4.1). Under the TEM the diamonds reveal their polycrystallinity being made up of microcrystals of 15–140 nm size (Siebenschock et al. 1999). Finally, very rare xenomorphic diamond grains were observed (Schmitt et al. 1999).

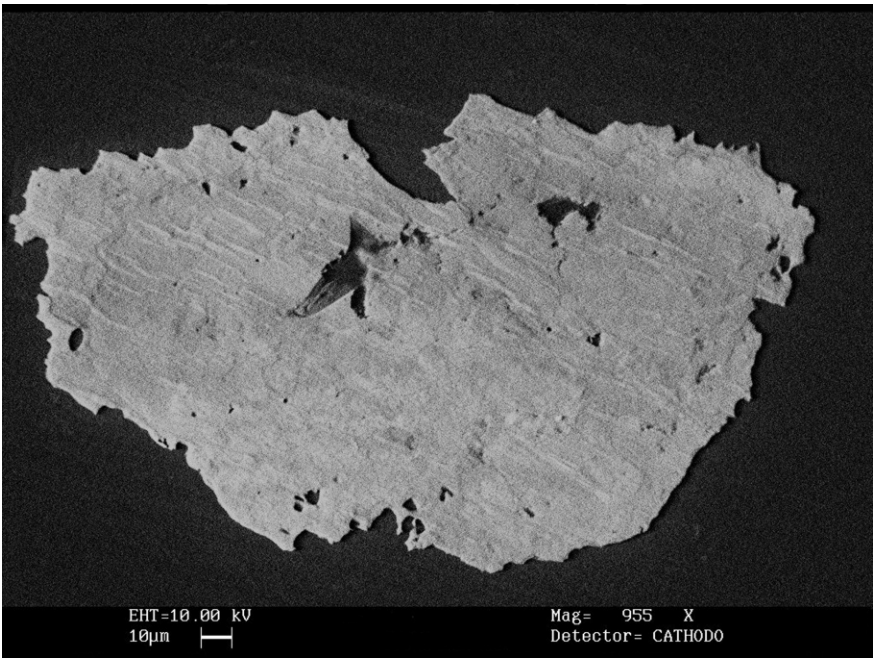

Fig. 4.1 Panchromatic CL image of a diamond grain from Ries crater: the kink bands, visible in this impact diamond, are inherited from the shock metamorphosed graphite precursor

4.2.1.5 Lappajärvi Crater

According to Hough et al. (1999), the cubic diamond grains from Lappajärvi appear yellow to white and often milky due to surface textures. The platey, rounded and

angular grains, as well as the occasional so-called volume-xenomorphic, range from below 0.1 to 0.4 mm in size. The surface textures of Lappajärvi diamonds show corrosion whereas basal surface are characterized by twinning striation appearing as scalariform or striae Masaitis et al. 1998; Hough et al. 1999); such a feature could indicate corrosion from late stage oxidation and reaction with other gases (Fig. 4.2). It is worth mentioning that the flank surface of tabular grains show the typical layering of graphite precursor.

4.2.1.6 Sudbury Crater

Samples from the 1.85 Ga Sudbury impact structure, and in particular from the C-bearing Black Onaping formation interpreted as reworked suevite breccias, were studied by several authors (Masaitis et al 1997, 1999; Langenhorst et al. 1998). These diamonds, occurring in a variety of colors, are mainly cubic: nevertheless, up to 30% of lonsdaleite may be found. Diamonds from Sudbury – differently from the compact Popigai, Ries and Lappajärvi diamonds – are generally friable due to inclusions and polycrystallinity. Although TEM study reveals similar microstructural characteristics in the diamonds from all four craters (Langenhorst et al. 1998), the mean grain size of individual crystallites of Sudbury diamonds is smaller, ranging from 50 to 100 nm.

4.2.1.7 Cretaceous-Tertiary Boundary

Impact nanodiamonds were reported in the K/T boundary layers from Berwind Canyon, Brownie Butte and Knudsens Farm (Carlisle and Braman 1991; Gilmour et al. 1992) these cubic diamonds appear as clusters of cubic 10 nm-sized grains. Moreover polycrystalline aggregates up to 30 μm in size (Fig. 4.3) have been found at Arroyo el Mimbral in northeast Mexico (Hough et al. 1997). None of the K/T diamonds yield any lonsdaleite; however, the Mimbral diamonds contain numerous stacking faults and microtwins (Hough et al. 1998).

4.2.1.8 Other Occurrences

Impact diamond discoveries have been made at other sites: Kara (Ezersky 1982) and Puchezh-Katunski (Firsov 1965) impact structures of Russia and inside the “catastrophic layer” of the 1908 Tunguska impact event (Kvasnitsa et al. 1979).

According to Shelkov et al. (1998), five diamond samples (5–7 mm in size) from Ebeliakh river placers seem to be formed in an impact event.

Two single crystals Czech diamonds, because of their extraordinary dirty orange color (under UV light with λ = 366 nm) very similar to that of Popigai and ureilites diamonds (Masaitis et al. 1990), were believed to have an impact origin (Skala and Bouska 1992).

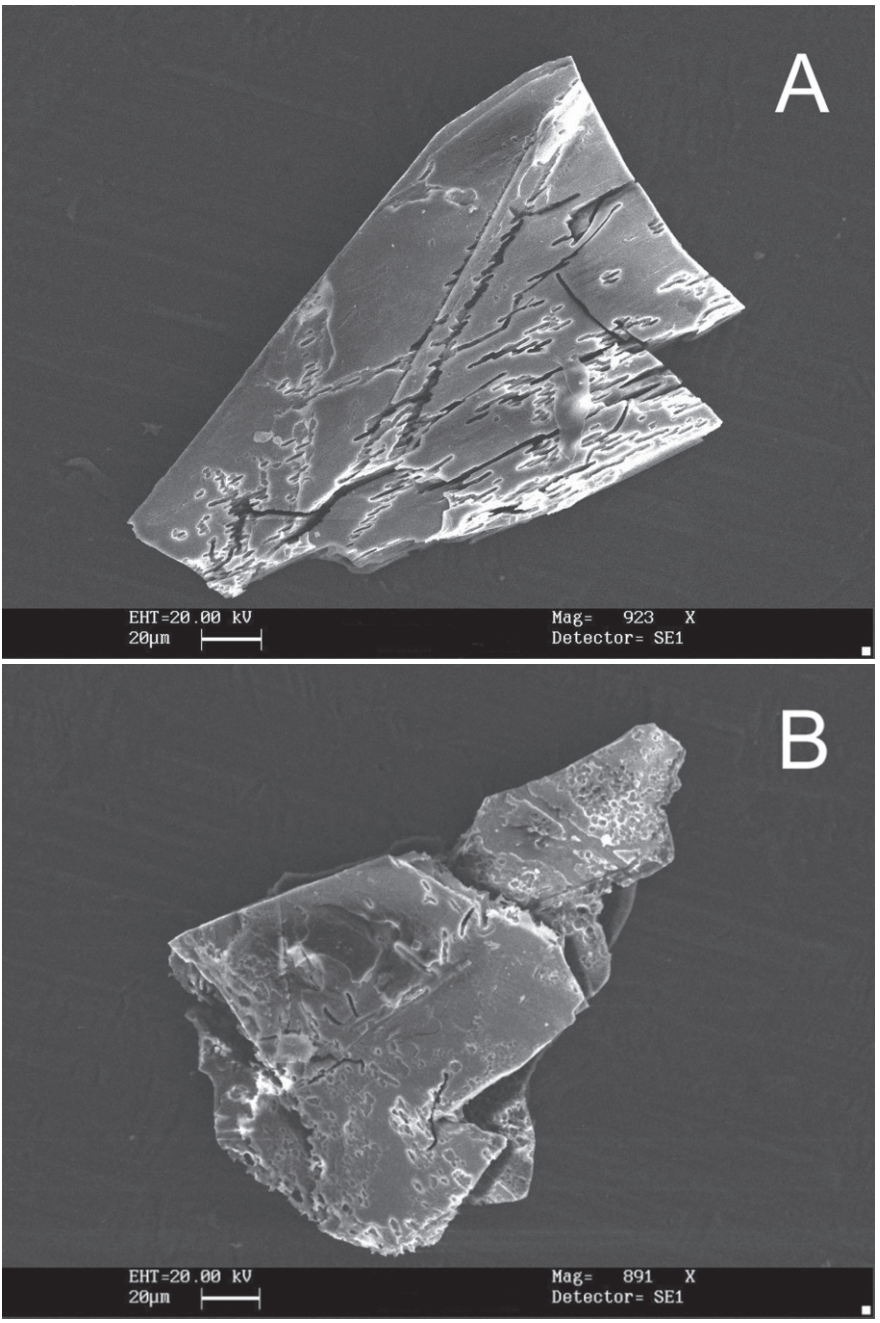

Fig. 4.2 SEM images showing surface textures in impact diamond grains from Lappajärvi: the corrosion patterns, characterized by fine pitted relief, indicate corrosion while the grains are still hot after the impact

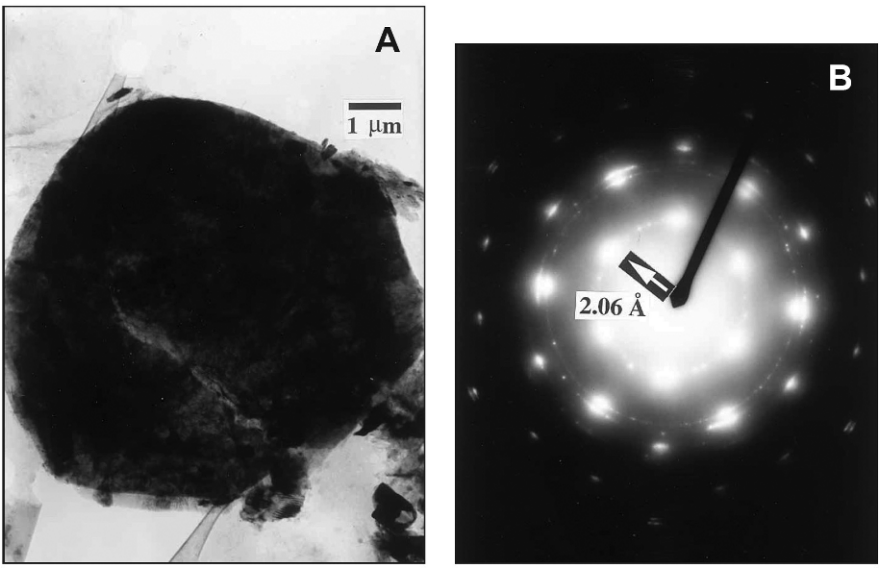

Fig. 4.3 (**A**) TEM image of a pseudohexagonal polycrystalline diamond from Arroyo el Mimbral, Mexico. (**B**) Selected area electron diffraction (SAED) pattern of the same sample, showing reflection corresponding to cubic diamond. (Figure from Hough et al. 1997; reprinted with permission of The Geological Society of America)

Finally nano- and micrometer-sized, flake-shaped diamonds have been identified inside the cell-like structure of carbonaceous spherules from soils throughout Europe (Yang et al. 2008).

4.2.1.9 The Carbonado's Puzzle

Carbonado is a polycrystalline diamond found in Central African Republic and Brazil: it occurs, in alluvial placers, as black and irregularly shaped porous nodules (De et al. 1998). Cathodoluminescence investigations performed on carbonado have revealed a bimodal grain size distribution that correlates with emissions (De et al. 2001). According to Kagi et al. (1994, 2007), carbonado may be classified into Group A, which exhibit a strong photoluminescence band at 504 nm interpreted as the result of 3H defects (Kagi et al. 1994; Magee and Taylor 1999), and Group B, with the major band at 575 nm attribute to an N-V center (Milledge et al. 1998); carbonado specimens with intermediate spectra also were observed. Moreover cubic euhedral diamonds in carbonado, zoned with respect to their CL emissions and exhibiting three main peaks at 520, 580 and 665 nm, where also found (Milledge et al. 1998; Magee and Taylor 1999).

Anyway, considering that the largest known carbonado is around 10 cm diameter, it is highly unlikely that carbonado could be impact diamond since the maximum

diameter of a diamond, that could be formed and quenched in a natural impact (before the pressure decay), was estimated to be around 1 cm (DeCarli et al. 2002). This just corresponds to the surprisingly large size reported for single grains of impact diamond from Popigai Masaitis 1996.

4.2.2 Features of Impact Diamonds

Impact diamonds occur as platey, rounded and angular grains, sometimes xenomorphic, ranging in size from a few nanometer up to about 2 mm (rarely up to 5 mm according to Vishnevsky et al. 1997). These diamonds show a variety of colors – from colourless, yellowish and greenish to grayish-black – depending on the presence of structural defects or graphite and carbonaceous residues. Impact diamonds are also usually characterized by polycrystallinity, revealed under the TEM as crystallites of nanometric size; both X-ray analyses and selected area electron diffraction indicate a preferred orientation of the crystallites within the polycrystalline grains (Hough et al. 1999).

According to Langenhorst et al. (1999) and Langenhorst et al. (2003), impact diamonds show very complicated defect structures and their lattice defects take place at two different scales.

At the micrometer scale, impact diamonds are characterized by up to 1 μm wide twin bands and kinkband inherited from the precursor graphite that was deformed by shock compression prior to transformation (Valter et al. 1992; Langenhorst et al. 1999). Such a transformation may be revealed also at a greater scale: indeed, very often the entire diamond plates are kinked or bent (Oleinik et al. 2003).

At the nanometer scale, a large number of lineation, stacking faults and microtwins bounded by partial dislocations may be observed (Fig. 4.4) (Hough et al. 1999). It is noteworthy that both the preservation of graphite twins and the planar faulting of the diamond lattice derive from the lack of time for the formation of a well ordered diamond due to a rapid solid-state transformation (Langenhorst et al. 2003).

4.3 Formation of Impact Diamonds

4.3.1 Laboratory Impact Experiments

In the same years the diamonds in the Canyon Diablo iron meteorite were suggested to have formed by shock compression during impact with the Earth (Lipschutz and Anders 1961), the synthesis of diamond by shock compression of graphite to a peak pressure of $\sim$ 30 GPa for a duration of $\sim$ 1 μs was attained (DeCarli and Jamieson 1961).

Subsequently, many other experiments have been performed by several authors but their results are not always in perfect agreement. The main reason of such disagreement is related to the lack of control of the several parameters involved in the

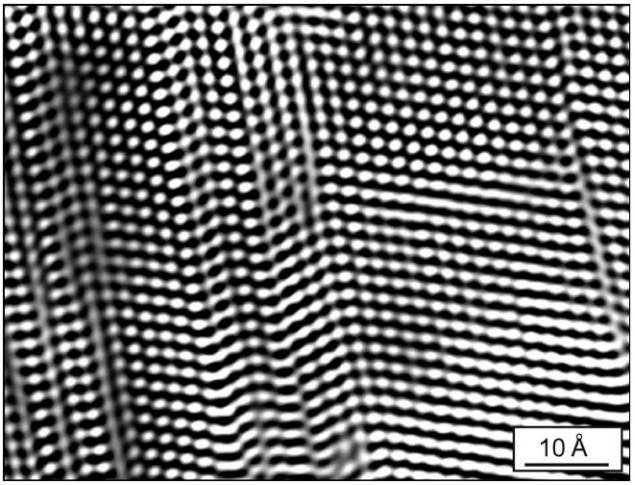

Fig. 4.4 HRTEM image of an impact diamond from the Popigai crater. Bright dots, representing channels in the diamond structure, stacking faults and microtwins are described in this view along the [110] axis. (Figure from Langenhorst 2003; reprinted with permission of Mitteilungen der Österreichischen Mineralogischen Gesellschaft)

transformation. In particular one must consider, in addition to the peak shock pressure, the pre-shock state of the rock, the loading path, the shock duration, the geometry of the shock event and the post-shock cooling history (DeCarli et al. 2002).

However, according to DeCarli et al. (2006), there are many evidences that graphite-diamond transformations under shock compression are governed by the same kinetics as phase transitions under static compression.

4.3.1.1 Experimental Parameters

The preshock state comprises the crystallinity of the starting material. So, when the source carbon is a well-ordered dense graphite, mixture of diamond and lonsdaleite may be yielded above $\sim$15 GPa in the temperature range 1300–2000 K; conversely, when the source is a not well-ordered graphitic carbon, pure cubic diamond may be made above $\sim$15 GPa but requires temperature above 3000 K (Bundy and Kasper 1967; DeCarli 1995). In case of disordered carbon precursor, two types of diamond may develop: the first one comprises black polycrystalline particles, ranging in size from micrometers to tens of micrometers and showing an X-ray pattern line broadening implying crystallite size $<$50 nm; the second type is nanodiamond, showing particle diameters in the range of 2–7 nm (quite similar to those formed during detonation of oxygen-deficient high explosives) (DeCarli 1995). Other interesting experiments, concerning the impact diamond formation from porous disordered carbons, established that diamond forms in hot spots, where temperature increase (T $>$ 3000 K) owing to the shock interactions around pores, and must be

quenched before the beginning of the graphitization that follows the pressure release (DeCarli 1998).

Regarding the loading path importance, it should be remembered that matched impedance experiments (i.e. when impedances of target and container are quite similar) with a porous commercial graphite at $\sim$ 20 GPa gives up more than 25% diamond whereas in high impedance conditions (same target but in high impedance container) less than 0.1% diamond is produced (DeCarli et al. 2002). However, since the increasing of internal energy during shock compression is correlated with the thermodynamic loading path (conditioned by the nature of material), upper pressure limits of formation and survival of impact diamonds depend on post shock temperatures which have to be low enough ($<$2000 K) to retard graphitization. Therefore, the peak temperature range of 1300–2000 K corresponds to peak pressure in the range 27–40 GPa for graphite in a gneiss, and to peak pressure in the range 60–120 GPa for graphite in a Fe-Ni meteorite (DeCarli 1998).

The shock duration of laboratory impact experiments is typically around microsecond or lesser, depending on the method employed (Langenhorst et al. 2003); no one has been able, up to date, to get duration of 10 μs or greater, as the shock-duration scales approximately with the cube root of the dimension of the experiment (Melosh 1989; Migault 1998; Langenhorst et al. 2003). It is noteworthy that, in natural impact processes, the duration of peak pressure may range from milliseconds up to $\sim$ some seconds for the bigger astroblemes.

The geometry of the shock event (i.e. the exact position of the target with respect to the shock) is relevant since it may influence the detail of the pressure and temperature history at any point. In particular it has been found (Yamada 2003) that shock compression along the basal plane of graphite favors the formation of defects compared to shock-compression perpendicular to the basal plane: as a consequence, diamond are more easily produced when shock compression is applied along the basal plane because the defects are driving force for the diamond formation.

Finally, the post-shock cooling history is simply fundamental in order to preserve the diamond or to favor the graphitization of it. Therefore, both in laboratory and natural processes, temperature of the diamond should be $<$2000 K on release of pressure to avoid a rapid graphitization: data from the kinetics of graphitization of a single crystal diamond indicate that, in absence of oxygen, a 100 mg diamond is completely graphitized within one week at 1960 K, whereas the graphitization process requires $\sim$ 1000 years to be completed at 1640 K (Evans and James 1964).

4.3.1.2 Experimental Techniques

As concerns the technique employed for the shock synthesis of diamond, it should be noted that other effective methods exist other than the classic high-explosive shock device; among them, electric-discharge gun, laser irradiation experiments and explosive ampoule-less apparatus should be emphasized.

Some authors (He et al. 2002) demonstrated that diamond loses its structure stability and transforms to lonsdaleite in massive, when subjected to shock wave

compression by the high velocity impact of an Al foil plate (∼10 μm thick and 2 mm in diameter) driven with a strong pulsed laser beam. This transformation was achieved in nanoseconds within the thermodynamic stability field of cubic diamond (shock pressure and temperature were only tens of GPa and hundreds of K). The formation of the hexagonal phase is interpreted as a direct transition (solid–solid) of cubic phase by a kinetic mechanism due to the shear stress and enhanced temperature induced by the rapid shock wave compression.

A study on stress-strain relation in diamond to over 1000 GPa, performed through a tailored-radiation drive at the Omega laser, put in evidence an elastic-plastic transition of diamond at 60–70 GPa, in good agreement with the elastic limit from shock experiments (Eggert et al. 2007).

Explosive detonation processes yielded nanodiamonds characterized by a crystallite size of 4–10 nm (Xu and Tan 2003). An interesting observation is that the detonation can be used not only for producing ultrafine-dispersed (nanoscale) diamonds (UDDs) but also for their sintering, during the same explosion (Danilenko 2004).

4.3.1.3 Mechanism of Formation

Several considerations seem to suggest that, at temperature in the range 1300–2000 K (e.g. when diamonds form starting from a well-ordered dense graphite according to Bundy and Kasper 1967), the mechanism for the transformation should be nearly diffusionless as the temperature is only about one-fourth of the absolute melting point of the carbon (DeCarli et al. 2002). A clearly martensitic transformation to a diamond-like state, for highly ordered pyrolytic graphite shocked normal to the basal plane of the graphite crystal, has been invoked by (Erskine and Nellis 1992).

On the other hand, when the source is a less well-ordered graphitic carbon and the temperature are above 3000 K, the speculation that the mechanism is nucleation and growth may be justified. This hypothesis was confirmed by (Chen and Yun 2000) who studied the mechanism of formation of nano-sized diamonds in detonation of carbon-rich explosives: they argued that liquid carbon micro drops may form and convert into tiny diamond crystallites during the expansion and cooling of the detonation products. A melting of ultrafine-dispersed diamonds was suggested to explain the shock-wave compaction of nanodiamonds to form a transparent isolated diamond single crystal 0.6 mm in size with an impurity content of less than 0.05% (Danilenko 2004).

4.3.1.4 Natural Impact Events

A characteristic feature of the shock diamonds is their crystallinity. All the impact diamonds, produced in natural processes or yielded in laboratory, are polycrystalline: the crystallite size is usually $<$100 nm with a mean size of tens of nanometers; only the nanodiamonds, obtained by shocking disordered carbon or

through detonation of carbon-rich explosives, may be as little as 2–7 nm in diameter. Conversely many mantle-derived diamonds are monocrystalline and, even though polycrystalline, have crystallite sizes that are a minimum of several orders of magnitude larger than impact diamond (DeCarli et al. 2002).

Impact diamonds with different shape and size have been found in many impact craters, mainly where the target rocks contain graphite or coal which was transformed by shock pressure (Masaitis et al. 1998). As an example, in the first in situ discovery of shock-induced graphite-diamond phase transition (El Goresy et al. 2001), it was demonstrated that the shock-induced transformations were promoted only in unkinked and undeformed graphite booklets at the graphite-garnet, graphite-sillimanite, or graphite-rutile interfaces, where the difference in shock impedance is very high (Fig. 4.5).

Typically the diamonds that formed after graphite – called paramorphs impact diamonds (PIDs) (Vishnevsky et al. 1997), idiomorphic or apographitic (Langenhorst and Masaitis 1996) – commonly occur as pseudohexagonal plates, inheriting the shape of the precursor parental graphite grains and sometimes also preserving growth twins of the precursor mineral graphite (Masaitis et al. 1990); however, in case of relatively thick segregations of the graphite, volume-xenomorphic grains of PIDs may be also originated (Vishnevsky et al. 1997). Furthermore, impact diamonds may also occur as skeletal laths, as minor nanodiamonds and as much more anhedral forms lacking any platey or hexagonal structure (sometimes referred as togorites (Vishnevsky et al. 1997) or apocoal impact diamonds Masaitis 1995) probably due to a poorly crystalline carbon source (Hough et al. 1999).

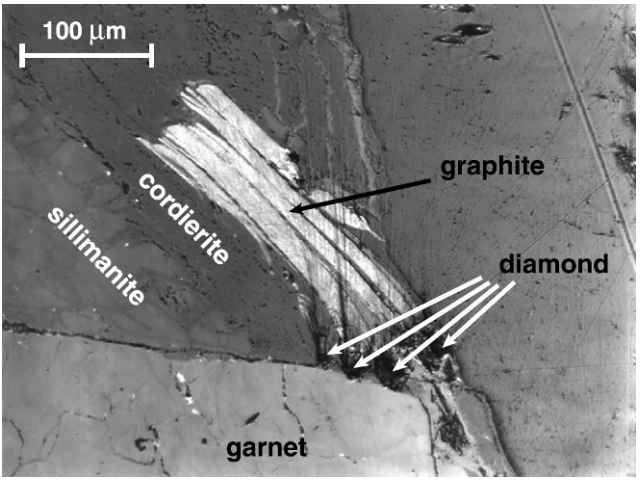

Fig. 4.5 Garnet-cordierite-sillimanite gneisses in suevites of the Ries meteorite impact crater. The diamonds occur in graphite grains, either at their prismatic faces or basal planes, exactly at the contacts with the denser phases (garnet in this case) where the difference in shock impedance is very high. (Figure from El Goresy et al. 2001; reprinted with permission of Mineralogical Society of America)

These two upper mentioned groups of impact diamonds are probably related to different formation processes or to similar processes involving different precursor materials. The paramorphs or apographitic impact diamonds form through martensitic solid-state transformations (Langenhorst and Masaitis 1996; Siebenschock et al. 1998; Masaitis et al. 1999; Vishnevsky and Palchik 2002; Oleinik et al. 2003) mainly starting from a crystalline precursor carbon (i.e. graphite) that exert an important control on the resulting characteristics of diamonds (Langenhorst et al. 1998). Conversely, the togorites or apocoal impact diamonds, having as precursor an amorphous or a poorly crystalline carbon source, form through shock transformation achieved by diffusion mechanism (nucleation and growth) (Ezersky 1982, 1986; Vishnevsky and Palchik 2002).

Amartensitic mechanism seems to drive also the graphite-lonsdaleite-diamond transformation, as showed by selected area diffraction pattern of studied block areas of diamond from Belilovka (Zapadnaja) astrobleme (Ukraine). This conclusion is also confirmed by the typical orientation of structures and the kink-band – like surface features (Oleinik et al. 2003).

More controversial are the occurrences of diamond originated from condensation of impact vapour or carbon vapour deposition processes (CVD). Such possible occurrences have been pointed out in impact melts from the Ries crater, where the skeletal intergrowth of diamond with SiC seems to be a strong argument for the formation of impact diamonds by chemical vapour deposition (Hough et al. 1995). Other occurrences have been reported at Popigai crater, where SiC may be find along with some fine grained skeletal diamond aggregates (Langenhorst and Masaitis 1996; Shelkov et al. 1998), at the K/T boundary, where nano-sized diamonds occur in clay of Alberta (Carlisle and Braman 1991) and in the iridium-rich K-T boundary layer at Arroyo el Mimbral (Gilmour et al. 1992; Hough et al. 1997). Nevertheless, according to Siebenschock et al. (1998), at least some occurrence of CVD diamonds are doubtful: in fact, no large SiC grains have been found in the glass bombs from suevite of Ries and moreover, the diamond from the dike suevite of Lehberg quarry, Unterwilfingen, has to be surely formed from graphite of the highly shocked basement rocks since the dike was never part of the central ejecta plume where impact diamonds may have formed from vaporized material by chemical vapor deposition (Siebenschock et al. 1999). Even DeCarli et al. (2002) stated that it is not necessary to assume an exotic mechanism, such as chemical vapor deposition (CVD) growth of diamond and silicon carbide in a low-pressure plasma, since the high temperature $>1800^{\circ}C$ and the duration of the peak pressure in the Ries event may account for the reaction of carbon with silica.

A question arises about the role played by an intermediate vitreous phase which recrystallizes as cubic-diamond (Bundy et al. 1973; Nassau 1993) through a martensitic-type mechanism (Erskine and Nellis 1991). Hard transparent carbon platelets, intercalated between fine-grained diamond and deformed graphite and supposed to be either dense amorphous carbon or an unknown dense crystalline carbon phase, have been also found in the shocked garnet-cordierite-sillimanite gneisses in suevites of the Ries meteorite impact crater, Germany (El Goresy et al. 2001).

4.4 Cathodoluminescence (CL) Properties of Impact Diamonds

4.4.1 Nitrogen, Boron and the Physical Classification of Diamonds

Considering that the nitrogen content in about 98% of natural diamonds has a concentration detectable in optical absorption, the classification relies on the amount of nitrogen and the way it is arranged inside the structure. The conventional physical classification of diamonds comprises four main categories: type Ia, type Ib, type IIa, and type IIb. As a matter of fact, there is a smooth change in arrangement between the four types so that intermediate varieties also exist.

Type I diamonds, containing nitrogen as the major impurity, can be divided into type Ia diamonds and type Ib diamonds. Type Ia contains nitrogen impurities – whose mean concentration is about 500 ppm but may be as high as 3000 ppm (Nazare and Neves 2001 – in an agglomerated state: such agglomerates are called "A Centers" when occur as pairs of nitrogen atoms (type IaA), "B centers" when occur as four nitrogen atoms surrounding a common vacancy (type IaB); it is noteworthy that mixtures of them (type IaA/B) may also occur. Type Ib – mostly represented in synthetic diamonds but very rare (about 0.1%) among natural diamonds – contain nitrogen as isolated single nitrogen atoms called "C Centers". Sometimes type I diamonds may also contain clusters of three nitrogen atoms called "N3 Centers".

Type II comprises diamonds – rare in nature (only about 1–2% of natural diamond) (Zaitsev 2001) – devoid of optical and paramagnetic absorption connected to nitrogen-related defects. In type IIa there is no trace of IR absorption due to boron or hydrogen; conversely, in type IIb optical absorption due to boron may be detected.

4.4.2 CL Features of Natural Diamonds

On the whole, many optical bands have been detected in diamonds. An excellent review of the optical properties of diamond, including all the CL centers, has been provided by (Zaitsev 2001).

In this paragraph only the bands and centers related to untreated natural diamonds will be reported; more attention will be paid for those bands that could be specifically connected with defects arising from impact processes.

- 992 nm (1.25 eV): this broad band (0.3 eV FWHM) has been observed in type IaA diamonds containing platelets (Zaitsev 2001).
- 981 nm (1.26 eV): detected in some natural diamonds (Davies 1977).
- 885 nm (1.40 eV): sometimes observed in type Ib diamonds (Zaitsev 2001).
- 793 nm (1.56 eV): especially strong in type IaB diamonds. Usually it correlates with the content of S2 and S3 centers.
- 737 nm (1.68 eV): although this center, known as the Si-V defect, may be occasionally found in natural type Ia, IIa (Breeding and Wang 2008) and Ib diamonds (Bachmann and Wiechert 1992), it is typical of CVD diamonds (see

Sect.4.3). The 737 nm photoluminescence feature (actually a doublet at 736.5 and 736.9 nm at 77 K) occurred in association with several additional and previously unreported peaks at 524.4, 550.4, 554.3, 557.9, 558.2, 573.5, 593.3, 594.8, and 714.7 nm, as well as two series of peaks in the ranges 535–539 and 644–652 nm (Breeding and Wang 2008).

- 690 nm (1.8 eV): the B-band, probably due to dislocations (Collins 1992a, b; Zaitsev 2001), has been observed in type II diamonds as well as in natural brown diamonds. The FWMH of 0.35 eV is justified by a fine structure (only visible at 50 K).
- 670 nm (1.85 eV): a band (FWHM $\sim$ 0.3) detected in some IIa type diamonds (Walker 1979).
- 550–580 nm (2.14–2.25 eV): this broad band (0.4–0.54 eV) may be originated by the platelets (Field 1992; Davies 1994), often gather together in areas marked by a change of intensity of the A-band (Lang 1979).
- 579 nm (2.14 eV): observed in type I diamonds which exhibit N3 and H3 luminescence (Bienemann-Kuespert et al. 1967; Zaitsev 2001).
- 578 nm (2.14 eV): this center was recognized in those natural brown diamonds which emit a yellow luminescence under excitation at 365 nm (Zaitsev 2001); whether the diamond is polycrystalline, a splitting at 578.7 and 581.1 may occur (Bokii et al. 1986).
- 575 nm (2.16 eV): a center naturally occurring in nitrogen-containing diamonds. The structure of this centre is reported to involve nitrogen atoms and one or more vacancies (N-V), and is commonly associated with plastic deformation (Brookes et al. 1999).
- 525 nm (2.36 eV): a broad band, associated with the H3 center (Graham and Buseck 1994), may be detected in natural brown diamonds.
- 516 nm (2.40 eV): this center may be observed in natural brown diamonds showing yellow photoluminescence under a 365 ultraviolet source (Field 1992).
- 503 nm (2.46 eV): the H3 center, along with the N3 center, is the most typical naturally occurring feature of diamonds containing nitrogen (Lipatov et al. 2007). It is noteworthy that the H3 center may decorate single dislocations and may be yielded by strong mechanical deformations (Lang 1977; Kanda and Jia 2000).
- 500 nm (2.48 eV): a center (B-line) detected in natural brown diamonds showing yellow luminescence under a 365 nm ultraviolet lamp (Mohammed et al. 1982; Field 1992; Zaitsev 2001).
- 496 nm (2.50 eV): this center, knowledge also as the H4 center, may naturally occur in type IaB diamonds. According to Kurdumov et al. (1994) it seems to correlate with concentration of the B-aggregates of nitrogen; in fact, the prevailing model describe the H4 as a B-aggregate of nitrogen (3N-V-N) bound to a vacancy V, yielding the complex 3N-V-V-N (van Wyk and Woods 1995).
- 492 nm (2.52 eV): a line detected in type IIb diamonds (Davies 1977).
- 491 nm (2.52 eV): a center that may occur in areas of brown diamonds lacking of fault (Zaitsev 2001)
- 491 nm (2.52 eV): according to Nahum and Halperin (1962), this center may be observed in type IaB diamonds, in type I diamonds devoid of N3 center

luminescence (Bienemann-Kuespert et al. 1967) and in carbonado as well (Bokii et al. 1986). Often connected with defects decorating slip traces, it may be generated by plastic deformation.
– 468 and 459 nm (2.65 and 2.70 eV): these centers, identified respectively as C-line and D-line, usually occur in brown diamonds which exhibit yellow luminescence under a 365 nm source (Zaitsev 2001).
– 455 nm (2.73 eV): a narrow line detected in type IIb diamonds (Davies 1977).
– 451 nm (2.75 eV): this center was recognized in brown diamonds which emit a yellow luminescence under excitation at a wavelength of 365 nm (Field 1992).
– 440 nm (2.82 eV): this interesting center has been observed both in brown diamonds and in high-silicon natural diamonds (Pereira et al. 1992).
– 438 nm (2.83 eV): a weak line sometimes detected in type IIb diamonds (Davies 1977).
– 435 nm (2.88 eV): the A-band, FWHM of 0.22 to 0.45 eV, may range from 445 eV to 415 eV. Such band – readily observed in all natural, CVD and HPHT diamonds – is particularly strong in all low-nitrogen diamonds (Lang 1977; Sumida and Lang 1981) and is one of the most characteristic features of type IIa diamonds with a mosaic texture (Hanley et al. 1977).
– 424 nm (2.92 eV): a center, detected in type IIa diamonds, easily destroyed by electron irradiation (Yokota et al. 1992).
– 415 nm (2.98 eV): the N3 center, related to B-aggregates of nitrogen (three nearest substitutional nitrogen atoms bonded to a common vacancy), mostly occurs in type Ia natural diamonds which represent about 95% of all natural diamonds (Lang 1977; Yelisseyev 1977). The N3 center may be localized at regions of plastic deformations, within stacking fault in brown diamonds (Graham and Buseck 1994) and in correspondence of platelets (Field 1992). According to Lipatov et al. (2007), when pulsed cathodoluminescence is applied to natural IIa-type diamond, the N3-system reveals a decay time of 30–50 ns whereas the A-band has a decay time of 8.5–8.8 ms.
– 393 nm (3.15 eV): this center, naturally occurring in brown diamonds which exhibit yellow luminescence, may be also created in nitrogen-containing diamonds by electron irradiation (Bienemann-Kuespert et al. 1967).
– 391 nm (3.17 eV): this center was observed both in brown diamonds exhibiting yellow luminescence (Field 1992) and in type IIb diamonds (Zaitsev 2001). A fine structure, with at least seven components, appears at temperature below 60 K.
– 387 nm (3.20 eV), 385 nm (3.22 eV) and 384 nm (3.23 eV): three different centers occurring in brown diamonds with yellow photoluminescence when excited with a 365 nm light (Mohammed et al. 1982; Jorge et al. 1983; Field 1992).
– 259 nm (4.78 eV): the 2BD(F) center may be observed in type IIb diamonds. It consists of four components probably related to the presence of interstitial boron atoms (Kanda et al. 2005).
– 256 nm (4.85 eV) and 255 nm (4.86): two centers, occurring in type IaB diamo nds, possibly due to a single defect (Zaitsev 2001).

– 249 nm (4.98 eV), 248 nm (4.99), 246–247 nm (5.03–5.04 eV), 244 nm (5.09 eV): these centers – designated respectively as N center, M center, L center and K center – naturally occur in type IaB diamonds (Davies 1977; Denisenko and Zaitsev 1992).
– 241 nm (5.14 eV): this center, related to an impurity defect (Ronning and Hofsaess 1999), has been observed in some natural diamonds.
– 239 nm (5.18 eV): a naturally occurring center, defined as E_0 center, detected in type IIa and IIb diamonds (Davies 1977; Zaitsev 2001).
– 235 nm (5.27 eV): low-energy threshold of the B_1 line, which is particularly strong in perfect natural IIa diamonds (Bienemann-Kuespert et al. 1967; Thonke et al. 2000).

4.4.3 CL Features of CVD Diamonds

The debated occurrence of natural CVD diamonds is really important in order to understand the impact processes. Here the main cathodoluminescence lines of CVD will be reported for a comparison with those detected in impact diamonds.

– 737 nm (1.68 eV): the Si center is typical of CVD diamond films grown on silicon substrates (Wang et al. 1996) or Si doped HPHT-grown synthetic diamonds, where probably arises from the plasma interaction with the Si substrate (Bergman et al. 1993). It is worth mentioning that the Si center intensity seems correlated, in CVD diamond, with the graphite amount (Dollinger et al. 1995). Although found also in some natural diamonds (see Sect. 4.2), this center could be present in CVD impact diamond intergrowth with SiC.
– 575 nm (2.16 eV): this center, other than in some natural type IIa diamonds, may also be found in CVD diamond.
– 534 nm (2.32 eV) and 531 nm (2.34 eV): this center represents a dominating feature in CVD diamonds. It may be considered typical of CVD as it has never seen in other natural diamonds (Martineau et al. 2004).
– 500 nm (2.48 eV): a center found in some CVD diamond films (Zaitsev 2001).
– 467 nm (2.65 eV): this center may be observed in CVD, mainly in high-quality single crystals, but not in other natural diamonds (Martineau et al. 2004).
– 415 nm (2.98 eV): the N3CVD center has been detected in some CVD diamond films (Collins 1992a, b) and in HPHT treated CVD synthetic diamond (Martineau et al. 2004). The relationship with the N3 center (a common optical feature of Ia natural diamonds) is still questioned (Zaitsev 2001; Martineau et al. 2004).
– 389 nm (3.20 eV): this center may be observed in some synthetic CVD diamonds where is removed by HPHT treatment (Martineau et al. 2004).
– 225 nm (5.5 eV): observed in CVD diamond grown from gas mixtures containing oxygen (Zaitsev 2001).

4.4.4 CL Spectra of Impact Diamonds

Despite the effectiveness of cathodoluminescence for studying diamonds (Panczer et al. 2000; Zaitsev 2001), at our knowledge, only two studies regarding the characterization of diamonds from terrestrial impactites are available (Valter et al. 1992; Pratesi et al. 2003). In particular, cathodoluminescence spectra of both rectangular flattened plates and shapeless volume-xenomorphic impact diamonds from three terrestrial craters (Lappajärvi, Ries and Popigai) have been collected by (Pratesi et al. 2003) using a SEM Leica Cambridge StereoScan 420 (5 keV, 200 pA for high luminescent grain and 1000 pA for low luminescent grain) equipped with a MONO-CL2 Oxford system and an HAMAMATSU R376 photomultiplier (spectral range 200–800 nm).

Panchromatic images clearly show that the luminescence intensity of diamond depends on the amount of carbonaceous material present: the greater the amount, the less intense the luminescence (Fig. 4.6) (Lo Giudice et al. 2001).

As concerns the spectroscopic measurements, it is worth mentioning that spectra collected at liquid nitrogen temperature (LNT) appear slightly different in comparison to those collected at room temperature (RT), mainly in the 480–560 nm (2.20–2.55 eV) range where new features appeared.

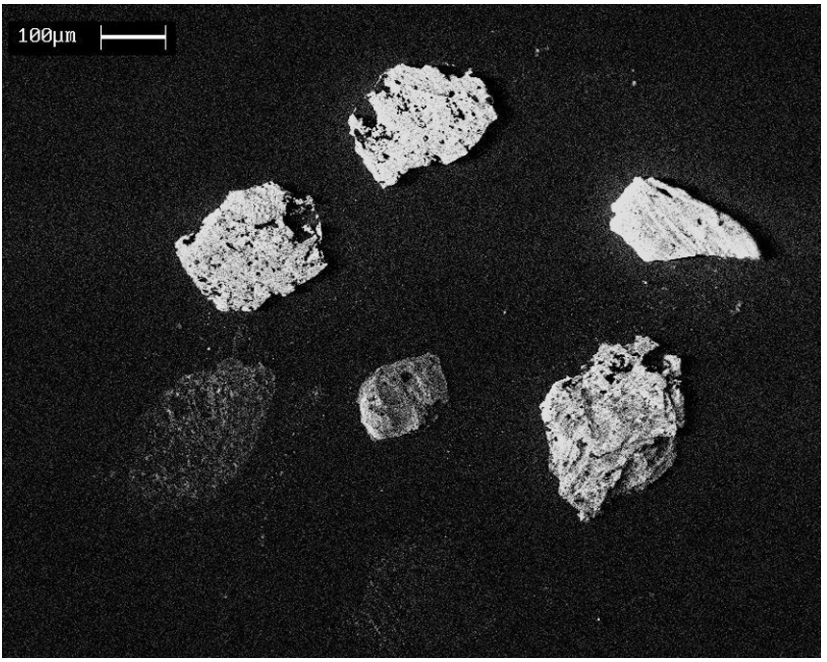

Fig. 4.6 Panchromatic CL image of diamond grains from Popigai impact crater, Russia. (After Pratesi et al. 2003 [117])

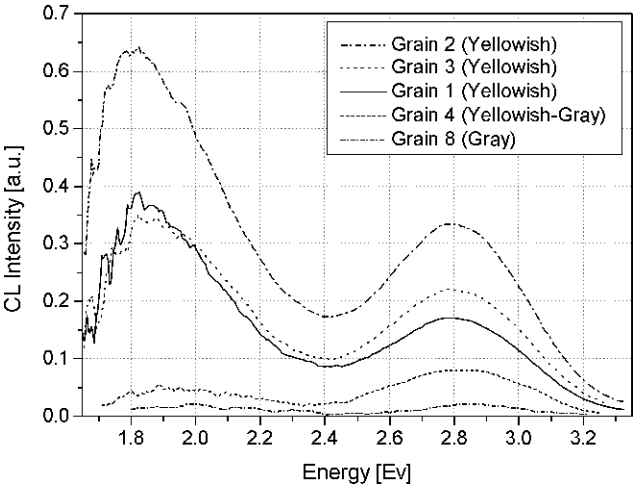

Fig. 4.7 CL spectra (probe current 200 pA) of five impact diamond grains from Popigai crater, Russia. (Figure from Pratesi et al. 2003; reprinted with permission of Mineralogical Society of America)

The A-band, with a FWHM of about 0.4 eV, appears at 2.81–2.91 eV (443–427 nm) in both RT and LNT spectra and is always present in the samples investigated (Fig. 4.7). Lower-energies were observed in high-luminescence grains from all impact sites whereas higher-energies were measured in the less luminescent black and brownish grains. Despite the origin and significance of this band are not yet completely understood, it could be reasonably related to vibronic levels corresponding to dislocation defects.

According to Pratesi et al. (2003), impact diamonds then show a strong contribution from the B-band at 1.8 eV (688 nm) that is characterized by FWHM of 0.4–0.5 eV and an asymmetric tail at high energies.

The intensity of this band is higher in yellowish grains, where its area is greater than that of the A band. CL maps from the A-band and B-band allowed ascertaining that the centers responsible for these bands are highly correlated with one another. Since the B-band was revealed in all the impact diamonds investigated, it could be distinctive of the genetic environment considering that it usually relates to dislocations (Davies 1977; Bokii et al. 1986; Collins 1992a, b), surely abundant in impact diamonds formed by wave pressure.

As stated above, new peaks appear at LNT (Fig. 4.8). In particular, a shoulder at 2.23 eV, slightly visible in some samples at RT, grows to become a pronounced peak with a FWHM of about 0.1 eV. Moreover, in all of the impact diamonds analysed, an important new peak can be seen at 2.32 eV (FWHM $\sim$ 0.05 eV); this peak is more intense in the Lappajärvi and Popigai samples, whereas it appears less pronounced in the Ries samples. Both the 2.23 eV and the 2.32 eV peaks represent the most important feature in the gray and brownish-gray grains. A further shoulder at 2.39 eV is visible in some of the less luminescence grains from Lappajärvi and Ries as well

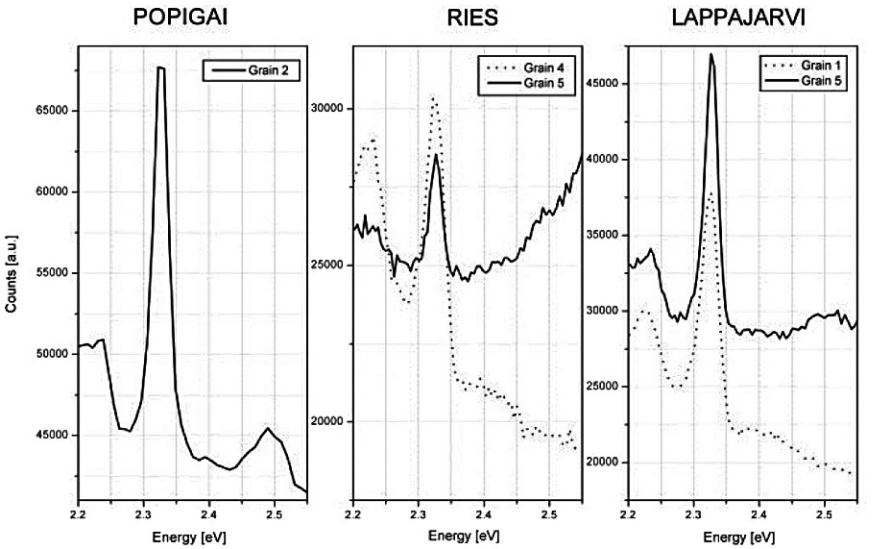

Fig. 4.8 CL spectra (collected at liquid nitrogen temperature) of impact diamonds from Popigai, Ries and Lappajärvi impact craters. Figure shows the spectral range from 2.20 to 2.55 eV where new features, with respect to the spectra collected at room temperature, can be seen. (Figure from Pratesi et al. 2003; reprinted with permission of Mineralogical Society of America)

as in a grain from Popigai. Many explanations may be invoked for these three lines (2.23, 2.32 and 2.39 eV), occurring only in the less luminescent grains which show a gray or brownish-gray colour under white light: the presence of H3 centers was claimed by (Valter et al. 1992); conversely, a correlation with the amount of amorphous diamond-like carbon material, possessing a mixed hybridization (sp^3+ sp^2), was suggested by (Bergman et al. 1993).

Only the more luminescent samples show a slight band at 2.49 eV, easily visible in two grains (from Popigai and from Lappajärvi), but merely outlined in another grain from Ries (Fig. 4.8). This band may be related to a center, called the B-line, that has been observed in natural brown diamonds at 2.48 eV (Field 1992; Brookes et al. 1999) although the assignment to the H4 center cannot be excluded.

4.5 Conclusions

Although the cathodoluminescence represents only a complementary technique for studying and characterizing diamonds, its application may result very interesting when particular diamonds have to be investigated.

Whenever a diamond is studied by cathodoluminescence, information about impurities and defects may be easily obtained. Sometimes cathodoluminescence spectra slightly differ each other even for diamond coming from a same deposit;

nevertheless the spectra always reveal particulars that may be useful in order to identify similarities and common features.

As concerns impact diamonds, centers possibly connected with the condition of formation have been detected and described.

References

Abbott JI, Hough RM, Gilmour I, Pillinger CT (1996) Impact diamonds in glass from otting quarry, ries crater, Germany. Met Planet Sci 31:Abs A5

Bachmann PK, Wiechert DU (1992) Optical characterization of diamond. Diam Rel Mat 1:422–433

Bergman L, Stoner BR, Turner KF, Glass JT, Nemanich RJ (1993) Microphotoluminescence and Raman scattering study of defect formation in diamond films. J Appl Phys 73:3951–3957

Bienemann-Kuespert E, Brennecke E, Flachbart I, Pietsch-Wilke G, Stiess P, Wagner J (1967) In: Kirschstein G, Koschel D, Kugler HK (eds) Gmelins Handbuch der Anorganischen Chemie. Verlag Chemie GmbH, p 237 (in German)

Bokii GB, Bezrukov GN, Kluev JA, Naletov AM, Nepsha VI (1986) Natural and synthetic diamonds. Nauka, Moscow (in Russian)

Bundy FP, Kasper JS (1967) Hexagonal diamond – A new form of carbon. J Chem Phys 46:3437–3446

Bundy FP, Strong HM, Wentorf RH (1973) Methods and mechanisms of synthetic diamond growth. Chem Phys Carbon 10:250–251

Bradley JP (2003) The Astromineralogy of interplanetary dust particle. In: Henning Th. (ed) Astromineralogy. Springer-Verlag, Berlin Heidelberg, pp 217–235

Breeding CM, Wang W (2008) Occurrence of the Si–V defect center in natural colorless gem diamonds. (To be published in Diam Relat Mater)

Brookes EJ, Greenwood P, Xing G (1999) The plastic deformation and strain-induced fracture of natural and synthetic diamond. Diam Relat Mater 8:1536–1539

Carlisle DB, Braman DR (1991) Nanometre-size diamonds in the Cretaceous/Tertiary boundary clay of Alberta. Nature 352:708–709

Bradley JP (2003) Collins AT (1992a) The characterisation of point defects in diamond by luminescence spectroscopy. Diam Relat Mater 1:457–469

Bradley JP (2003) Collins AT (1992b) In: Purdes AJ (ed) Proc. 2nd Int. Symp. on Diamond Materials. Electrochem Soc Inc p. 408

Chapman CR, Morrison D (1989) Cosmic Catastrophes, Plenum Press, New York

Chen Q, Yun S (2000) Nano-sized diamond obtained from explosive detonation and its application. Mat Res Bull 35:1915–1919

Dai ZR, Bradley JP, Joswiak DJ, Brownlee DE, Genge MJ (2002a) Nanodiamonds in interplanetary dust particles (IDPs), micrometeorites and meteorites. Lun Planet Sci Conf XXXIII: abs. 1321

Dai ZR, Bradley JP, Joswiak DJ, Brownlee DE, Hill HGM, Genge MJ (2002b) Possible in situ formation of meteoritic nanodiamonds in the early Solar System. Nature 418:157–159

Bradley JP (2003) Danilenko VV (2004) Shock-save sintering of nanodiamonds. Phys Solid State 46:711–715

Daulton TL, Eisenhour DD, Bernatowicz TJ, Lewis RS, Buseck PR (1996) Genesis of presolar diamonds: comparative high-resolution transmission electron microscopy study of meteoritic and terrestrial nanodiamonds. Geochim Cosmochim Acta 60:4853–4872

Davies G (1977) The optical properties of diamond. In: Thrower PA, Walker Jr PL (eds) Chemistry and physics of carbon. vol 13, Marcel Dekker, New York, pp. 1–143

Davies G (1994) Properties and growth of diamond. INSPEC, London, UK

DeCarli PS (1998) More on the possibility of impact origin of carbonado. In: Schmidt SC, Dandekar DP, Forbes JW (eds) Shock compression of condensed matter – 1997. Am Inst Phys, Conference Proceedings 429:681–684

DeCarli PS (1995) Shock wave synthesis of diamond and other phases. Mater Res Soc Symp Proc 383:21–31

DeCarli PS, Jamieson JC (1961) Formation of Diamond by explosive shock. Science 133:1821–1822

DeCarli PS, El Goresy A, Xie Z, Sharp TG (2006) On the concordance of static high pressure phase transformation data on minerals with shock wave data. AGU Fall Meeting 2006, abstract #MR53D-08

DeCarli PS, Bowden E, Jones AP, Price GD (2002) Laboratory impact experiments versus natural impact events. In: Koeberl C, MacLeod KG (eds) Catastrophic events and mass extinctions: impacts and beyond. Geol Soc Am Special Paper 356, Boulder, Colorado, 595–605

De S, Heaney PJ, Vicenzi EP, Wang J (2001) Chemical heterogeneity in carbonado, an enigmatic polycrystalline diamond. Earth Planet Sci Lett 185:315–330

De S, Heaney PJ, Hargraves RB, Vicenzi EP, Taylor PT (1998) Microstructural observations of polycrystalline diamond: a contribution to the carbonado conundrum. Earth Planet Sci Lett 164:421–433

Denisenko AV, Zaitsev AM (1992) Cathodoluminescence studies of some natural yakutian diamonds. Belarussian State University, Minsk

Dollinger G, Bergmaier A, Frey CM, Roesler M, Verhoeven H (1995) Impurities of light elements in CVD diamond. Diam Relat Mater 4:591–595

Eggert J, Bradley D, Celliers P, Collins G, Hicks D, Braun D, Prisbrey S, Smith R, Boehly T (2007) Ramp compression of diamond to over 1000 GPa. American Physical Society, 15th APS Topical Conference on Shock Compression of Condensed Matter, June 24–29,2007, abstract #Q3.003

El Goresy A, Gillet P, Chen M, Künstler F, Graup G, Stähle V (2001) In situ discovery of shock-induced graphite-diamond phase transition in gneisses from the Ries Crater, Germany. Am Min 86:611–621

Erskine DJ, Nellis WJ (1992) Shock-induced martensitic transformation of highly oriented graphite to diamond. J Appl Phys 71:4882–4886

Erskine DJ, Nellis WJ (1991) Shock-induced Martensitic phase transformation of oriented graphite to diamond. Nature 349:317–319

Evans T, James PE (1964) Graphitization of diamond at zero pressure and at a high pressure. Proc R Soc Lond Set A 277:260–269

Ezersky VA (1986) The high-pressure polymorphs originated by shock transformation of coal. Zapiski Vsesoyuznogo Mineralogicheskogo Obstchestva 115:26–33 (in Russian)

Ezersky VA (1986) Ezersky VA (1982) The shock-metamorphosed carbon matter in impactites. Meteoritika 41:134–140 (in Russian)

Field JE (1992) The properties of natural and synthetic diamond. Academic Press, London

Firsov LV (1965) On the meteoritic origin of the Puchezh-Katunsky crater. Geotectonika 2:106–118 (in Russian)

Foote AE (1891) A new locality for meteoric iron with a preliminary notice of the discovery of diamonds in the iron. Am J Sci 42:413–417

French BM (1998) Traces of Catastrophe. Lunar and Planetary Institute, Houston, Tx

Gehrels T (1994) Hazards due to comets and asteroids. Univ. Arizon Press, Tucson, Az

Gilmour I, Russell SS, Arden JW, Lee MR, Franchi IA, Pillinger CT (1992) Terrestrial carbon and nitrogen isotopic ratios from cretaceous-tertiary boundary nanodiamonds. Science 258:1624–1626

Gurov EP, Gurova EP, Rakitskaya RB (1996) Impact diamonds of the Zapadnaja crater: phase composition and some properties. Met Planet Sci 31:A56

Gurov EP, Gurova EP, Rakitskaya RB (1995) Impact diamonds in the craters of the Ukrainian shield. Meteoritics 31:515–516

Graham RJ, Buseck PR (1994) Cathodoluminescence of brown diamonds as observed by transmission electron microscopy. Philos Mag B 70:1177–1185
Hanley PL, Kiflawi I, Lang AR (1977) On topographically identifiable sources of cathodoluminescence in natural diamond. Philos Trans R Soc London A 284:329–368
Hanneman RE, Strong HM, Bundy FP (1967) Hexagonal diamonds in meteorites: Implications. Science 155:995–997
He H, Sekine T, Kobayashi T (2002) Direct transformation of cubic diamond to hexagonal diamond. App Phys Lett 81:610–612.
Hough RM, Vishnevsky S, Abbott JI, Pal'Chik N, Raitala J, Gilmour I (1999) New data on the nature of impact diamonds from the Lappajärvi impact structure, Finland. Lun Planet Sc Conf XXX: abs. 1571
Hough RM, Gilmour I, Pillinger CT (1998) Impact nanodiamonds in Cretaceous-Tertiary boundary fireball and ejecta layers: comparison with shock-produced diamonds and a search for lonsdaleite. Met Planet Sci 33:abs. A70
Hough RM, Gilmour I, Pillinger CT, Langenhorst F, Montanari A (1997) Diamonds from the iridium-rich K-T boundary layer at Arroyo el Mimbral, Tamaulipas, Mexico. Geology 25:1019–1022
Hough RM, Gilmour I, Pillinger CT, Arden JW, Gilkes KWR, Yuan J, Millegde HJ (1995) Diamond and Silicon Carbide in Impact Melt Rock from the Ries Impact Crater. Nature 378:41–44
Huss G, Lewis RS (1995) Presolar diamond, SiC, and graphite in primitive chondrites: abundances as a function of meteorite class and petrologic type. Geochim Cosmochim Acta 59:115–160
Hoppe P, Zinner E (2000) Presolar dust grains from meteorites and their stellar sources. J Geophys Res 510:10371–10385
Jorge MIB, Pereira ME, Thomaz MF, Davies G, Collins AT (1983) Decay times of luminescence from brown diamonds. Portugal Phys 14:195–210
Kagi H, Sato S, Akagi T, Kanda H (2007) Generation history of carbonado inferred from photoluminescence spectra, cathodoluminescence imaging, and carbon-isotopic composition. Am Min 92:217–224
Kagi H, Takahashi K, Hidaka H, Masuda A (1994) Chemical properties of Central African carbonado and its genetic implication. Geochim Cosmochim Acta 58:2629–2638
Kanda H, Jia X (2000) Change of luminescence character of Ib diamonds with HPHT treatment. Diam Relat Mater 10:1665–1669
Kanda H, Ahmadjan A, Kitawaki H (2005) Change in cathodoluminescence spectra and images of type II high-pressure synthetic diamond produced with high pressure and temperature treatment. Diam Relat Mater 14:1928–1931
Koeberl C (2006) Impact processes on the early earth. Elements 2:211–216
Koeberl C, Masaitis VL, Langenhorst F, Stoffler D, Schrauder M, Lengauer C, Gilmour I, Hough RM (1995) Diamonds from the Popigai impact structure, Russia. Lun Planet Sc Conf XXVI: 777–778
Kurdumov AV, Malogolovets VG, Novikov NV, Piljankevich AH, Shulman LA (1994) Polymorphous modification of carbon and boron nitride. Metallurgija, Moscow (in Russian)
Kvasnitsa VN, Sobotovich EV, Kovalukh NN, Litvak AL, Rybalko SI, Sharkin OP, Egorova LN (1979) High-pressure carbon polymorphs in mosses from the Tunguska impact site. Doklady Ukrainskoi Akademii Nauk B 12:1000–1004 (in Russian)
Lang AR (1979) Internal structure. In: Field JE (ed) The properties of diamond. Academic Press, London, pp 425–469
Lang AR (1977) Defects in natural diamonds: recent observations by new methods. J Crystal Growth 42:625–631
Langenhorst F (2003) Nanostructures in ultrahigh-pressure metamorphic coesite and diamond: a genetic fingerprint. Mitt Österr Miner Ges 148:401–412
Langenhorst F, Masaitis VL (1996) Microstructural characteristics of impact diamonds from the Popigai crater, Russia. Met Planet Sci 31:A77
Langenhorst F, Boustie M, Deutsch A, Hornemann U, Matignon Ch, Migault A, Romain JP (2003) Experimental techniques for the simulation of shock metamorphism: A case study on calcite.

In: Davison L, Horie Y, Sekine T (eds) High-pressure shock compression of solids V. Springer-Verlag, New York, pp 1–27.
Langenhorst F, Shafranovsky G, Masaitis VL, Koivisto M (1999) Discovery of impact diamonds in a Fennoscandian crater and evidence for their genesis by solid-state transformation. Geology 27:747–750
Langenhorst F, Shafranovsky G, Masaitis VL (1998) A comparative study of impact diamonds from the Popigai, Ries, Sudbury and Lappajärvi craters. Met Planet Sci 33:abs. A90
Lipatov EI, Lisitsyn VM, Oleshko VI, Tarasenko VF (2007) Spectral and kinetic characteristics of the pulsed cathodoluminescence of a natural IIa-type diamond. Russ Phys J 50:52–57
Lipschutz ME, Anders E. (1961) The record in the meteorites–IV: Origin of diamonds in iron meteorites. Geochim Cosmochim Acta 24:83–88
Lo Giudice A, Pratesi G, Vishnevsky SA (2001) New SEM-CL data on the Popigai, Ries and Lappajärvi impact diamonds. Met Planet Sci 36:abs A115.
Magee CW, Taylor WR (1999) Constraints from luminescence on the history and origin of carbonado. In: Gurney JJ, Pascoe MD (eds) Seventh International Kimberlite Conference, vol 2, Cape Town, pp. 529–532
Martineau PM, Lawson SC, Taylor AJ, Quinn SJ, Evans DJF, Crowder MJ (2004) Identification of synthetic diamond grown using chemical vapor deposition (CVD). Gems & Gemology 40:2–25
Masaitis VL (1996) Impact diamonds from astroblemes. In: Mineralogical Society of America 1996 Spring Meeting, May 20–24, Baltimore, Maryland. Abstract supplement to Eos Transactions. Washington: AGU Press, S142–S143
Masaitis VL (1995) The origin and distribution of diamond-bearing impactites. Meteoritics 30:541
Masaitis VL, Shafranovsky GI, Grieve RAF, Langenhorst F, Peredery WV, Therriault AM, Balmasov EL, Fedorova IG (1999) Impact diamonds in the suevitic breccias of the black member of the onaping formation, Sudbury structure, Ontario, Canada. In: Dressler BO, Sharpton VL (eds) Large meteorite impacts and planetary evolution II: Boulder, Colorado, Geol Soc Am, Special Paper 33:317–321
Masaitis VL, Shafranovsky GI, Fedorova IG, Koivisto M, Korhonen JV (1998) New data on the nature of impact diamonds from the Lappajärvi impact structure, Finland. Lun Planet Sci Conf XXIX: abs. 1171
Masaitis VL, Shafranovsky GI, Grieve RAF, Langenhorst F, Peredery WV, Balmasov EL, Fedorova IG, Therriault AM (1997) Discovery of impact diamonds at the Sudbury structure. In: International Conference on Large Meteorite Impacts and Planetary Evolution. LPI contribution no. 922. Houston. Lunar and Planetary Institute Press: p 33
Masaitis VL, Shafranovskii GI, Ezerskii VA, Reshetniak NB (1990) Impact diamonds in ureilites and impactites. Meteoritika 49:180–196 (in Russian)
Masaitis VL, Futergendler SI, Gnevyshev MA (1972) The diamonds in the impactites of the Popigai meteoritic crater. Zapiski Vsesouznogo Mineralogicheskogo Obstchestva 101:108–113
Melosh HJ (2007) The contact and compression stage of impact cratering. Bridging the gap II: effect of target properties on the impact cratering process, Proceedings of the conference held September 22–26, 2007 in Saint-Hubert, Canada. LPI Contribution No. 1360, p 71–72
Melosh HJ (1989) Impact Cratering – A Geological Process. Oxford University Press, New York.
Migault A (1998) Concepts of shock waves. In: Benest D, Froeschlé C (eds) Impact on Earth. Springer, Berlin, pp 79–112
Milledge HJ, Woods PA, Beard AD, Shelkov D, Willis B (1998) Cathodoluminescence of polished carbonado. In: Seventh International Kimberlite Conference Extended Abstracts, Capetown, South Africa, pp. 589–590
Mohammed K, Davies G, Collins AT (1982) Uniaxial stress splitting of photoluminescence transitions at optical centres in cubic crystals: theory and application to diamond. J Phys C 15:2779–2788
Nahum J, Halperin A (1962) Excitation spectra and temperature dependence of luminescence and photoconductivity of diamond. J Phys Chem Solids 23:345–358
Nassau K (1993) Synthesis of bulk diamond: History and present status. In: Davis RF (ed) Diamond Films and Coatings, Noyes Publ, Westwood, pp 58–59

Nazare MH, Neves AJ (2001) Properties, growth and applications of diamond. INSPEC, The Institution of Electrical Engineering, London, UK.
Nassau K (1993) Nininger HH (1956) Arizona's meteorite crater: Its past, present and future, World Press Inc., Denver, Colorado, 232 p.
Oleinik GS, Valter AA, Erjomenko GK (2003) The structure of high lonsdaleite diamond grains from the impactites of the Belilovka (Zapadnaja) astrobleme (Ukraine). Lun Planet Sci Conf XXXIV: abs. 1561.
Panczer G, Gaft M, Marfunin A (2000) Systems of interacting luminescence centers in natural diamonds: Laser-induced time-resolved and cathodoluminescence spectroscopy. In: Pagel M, Barbin V, Blanc P, Ohnenstetter D (eds) Cathodoluminescence in Geosciences, Springer-Verlag, Berlin, 514 p.
Pereira E, Pereira L, Raue L (1992) Time resolved photoluminescence and cathodoluminescence of CVD diamond films. Diam Relat Mater 1:901–905.
Pratesi G, Lo Giudice A, Vishnevsky S, Manfredotti C, Cipriani C (2003) Cathodoluminescence investigations on the Popigai, Ries, and Lappajärvi impact diamonds. Am Min 88:1778–1787
Ronning C, Hofsaess H (1999) Ion implantation and annealing of diamond studied by emission channeling and cathodoluminescence. Diam Relat Mater 8:1623–1630
Rost R, Dolgov YA, Vishnevsky SA (1978) Gas inclusions and high-pressure polymorphs of carbon in the impact glasses of the Ries crater. Doklady Dok AN SSSR 241:695–698
Schmitt RT, Siebenschock M, Stöffler D (1999) Distribution of impact diamonds in the Ries crater, Germany. Met Planet Sci 34:abs. 5125.
Siebenschock M, Schmitt RT, Stöffler D (1998) Impact diamonds in glass bombs from suevite of the Ries crater, Germany: new observations. Met Planet Sci 33:abs A145.
Siebenschock M, Langenhorst F, Schmitt RT, Stöffler D (1999) Impact diamonds in the dike suevite of Unterwilfingen, Ries crater, Germany. Lun Planet Sci Conf XXX: abs. 1172.
Shelkov DA, Verchovsky AB, Milledge HJ, Kaminsky FV, Pillinger CT (1998) Carbon, nitrogen, argon and helium study of impact diamond from Ebeliakh alluvial deposits and Popigai crater. Met Planet Sci 33:985–992
Skala R, Bouska VJ (1992) Characteristics of Impact Diamonds. Meteoritics 27:290.
Sumida N, Lang AR (1981) Cathodoluminescence evidence of dislocation interactions in diamond. Philos Mag A43:1277–1287
Thonke K, Schliesing R, Teofilov N, Zacharias H, Sauer R, Zaitsev AM, Kanda H, Anthony TR (2000) Electron–hole drops in synthetic diamond. Diam Relat Mater 9:428–431
Xu K, Tan H (2003) Shock wave chemistry and Ultrafine diamond from explosives in China. In: Davison L, Horie Y, Sekine T (eds) High-pressure shock compression of solids V. Springer-Verlag, New York, pp 139–162
Yamada K (2003) Shock-Induced Phase transitions in oriented pyrolytic graphite. In: Davison L, Horie Y, Sekine T (eds) High-pressure shock compression of solids V. Springer-Verlag, New York, pp 117–138
Yang ZQ, Verbeeck J, Schryvers D, Tarcea N, Popp J, Rösler W (2008) TEM and Raman characterisation of diamond micro- and nanostructures in carbon spherules from upper soils. Diam Relat Mater 17:937–943
Yelisseyev AP (1977) Thermostimulated luminescence and delayed luminescence of natural diamonds. Ph D thesis, Sverdlovsk, Ural Pedag Institut (in Russian)
Yerofeev MV, Lachinov PA (1888) About the Novo Urei meteorite. Zhurnal Russkogo Physiko-Khimicheskogo Obstchestva XX: 185–213 (in Russian).
Yokota Y, Kotsuka H, Sogi T, Ma JS, Hiraki A, Kawarada H, Matsuda K, Hatada M (1992) Formation of optical centers in CVD diamond by electron and neutron irradiation. Diam Relat Mater 1:470–477
Valter AA, Dobraynskii Yu P (2002) The cooling history of layered glassy impactites (Tagamites): Influence upon preservation of impact diamonds. Lun Planet Sc Conf XXXIII: abs. 1116.
Valter AA, Gurskij DS, Erjomenko GK (2000) Distribution of impact diamond in the Belilovka (Zapadnaja) astrobleme on the Ukrainian Shield. Lun Planet Sc Conf XXXI: abs. 1215.

Valter AA, Er'omenko GK, Kvasnitsa VN, Polkanov YA (1992) The shock-metamorphic minerals of carbon. Naukova Dumka Press, Kiev, 172 p. (in Russian).
van Wyk JA, Woods GS (1995) Electron spin resonance of excited states of the H3 and H4 centres in irradiated type Ia diamonds. J Phys Condens Matter 7:5901–5912
Vishnevsky SA, Palchik NA (2002) Carbon matter in impactites of the Yanis-Järvi astrobleme, Russia: high pressure shock transformations. Lun Planet Sc Conf XXXIII: abs. 1676.
Vishnevsky SA, Palchik NA (1975) Graphite in the rocks of the Popigai structure: its destruction and transformation into other phases of the carbon system. Sov Geol Geoph 16:55–61
Vishnevsky SA, Afanas'ev VP, Argunov KP, Pal'chik NA (1997) Impact diamonds: their features, origin and significance. Transactions of the UIGGM SO RAN, issue no. 385. Novosibirsk: Siberian Branch of Russian Academy of Sciences Press, 1997, 110 p. (in Russian & English).
Walker J (1979) Optical absorption and luminescence in diamond. Rep Prog Phys 42:1605–1659
Wang WN, Fox NA, May PW, Knapper MP, Meaden G, Partridge PG, Ashfold MNR, Steeds JW, Hayward IP, Pitt GD (1996) Laser raman studies of polycrystalline and amorphic diamond films. Phys Stat Sol (a) 154:255–268
Zaitsev AM (2001) Optical properties of diamond: a data handbook. Springer-Verlag, Berlin, Heidelberg

Chapter 5
Cathodoluminescence Microscopy and Spectroscopy of Lunar Rocks and Minerals

Jens Götze

5.1 Introduction

The Moon, our nearest celestial body, orbits the Earth at a distance of 385,000 km and has a diameter of ca. 3,480 km, which is one-quarter of the Earth's diameter. The basic knowledge about the composition and the structure of the Moon was obtained especially during the space missions of the USSR (Luna since 1959) and the USA (Ranger and Surveyor since 1964). The highlights for geological research have been the first Moon landing in 1969 (Apollo 11 with Neil Armstrong and Edwin Aldrin) with the first sampling of geological material, and the following lunar missions by Apollo 12–17 between 1969 and 1972 (ca. 2200 samples, 380 kg) and Luna 16, 20 and 24 between 1971 and 1976, respectively (Taylor 1982).

The detailed investigation of the lunar material and additional samples from lunar meteorites (Warren 1994) resulted in a lot of information about the geology and origin of the Moon. On the other hand, the limited sample material and the small size of most samples caused a tremendous development of advanced analytical methods. Cathodoluminescence (CL), which was developed for geological applications by Sippel (1965) and Smith and Stenstrom (1965) plays an important role among the modern methods applied to lunar material (e.g., Sippel and Spencer 1970a, b; Sippel 1971; Geake et al. 1970, 1971 1972; Götze et al. 1999a,b; Akridge et al. 2004; Gucsik et al. 2006a).

CL microscopy (petrography) is a useful addition to conventional mineralogical and petrographic techniques. Several studies have shown that CL can provide detailed information about texture, composition or defects otherwise unobtainable. For instance, details of original structures, or effects of radiation damage or impact events may be revealed in lunar materials, which cannot be observed by other methods. These investigations can effectively be accompanied by other analytical techniques with high spatial resolution such as microprobe, PIXE, laser ablation ICP-MS or SHRIMP for micro-chemical analysis or detailed isotope studies. In addition, spectroscopic luminescence studies can provide information about defect

Jens Götze (✉)
TU Bergakademie Freiberg, Institute of Mineralogy, Brennhausgasse 14,
D-09596 Freiberg, Germany
e-mail: goetze@mineral.tu-freiberg.de

A. Gucsik (ed.), *Cathodoluminescence and its Application in the Planetary Sciences*,

density or the incorporation and distribution of certain trace elements (e.g., Eu^{2+}, REE^{3+}, Mn^{2+}, Fe^{3+}, Cr^{3+}). Because of the fact that certain geological processes create specific defects in mineral phases, the knowledge of the relationship between crystal-chemical properties and specific luminescence characteristics can be used to reconstruct the processes of mineral formation and alteration.

Despite these advantages of CL techniques in the investigation of chemistry and structure of lunar rocks and minerals, up to now only a few studies have been published. The present study is an attempt to summarize the data from literature concerning the luminescence characteristics of lunar material and to present results of some recent studies on lunar minerals.

5.2 Mineralogy and Petrology of Lunar Rocks

5.2.1 Evolution and Geology of the Moon

The origin of the Moon is still in discussion and in general based on two different theories. The first one assumes that the Moon was formed by accretion of cosmic dust parallel to the Earth and the other planets of the solar system (ca. 4.6 Ga), whereas the other theory supposes that the lunar material has been erased from the Earth's surface due to a giant impact event (Cameron 1996). The further geological evolution of the Moon is characterized by continuous magmatism (4.6 to ~2.0 Ga) in several stages and strong bombardment by cosmic material (Shearer and Papike 1999 and references therein).

The results of geophysical measurements and the investigated geological material indicate that the internal structure of the Moon is similar to that of the Earth and consists of a core, a differentiated mantle and a thin crust (~60 km; Taylor 1982). The formation of the anorthositic crust and a differentiated lunar interior took already place in an early stage (ca. 4.4-4.5 Ga) of lunar differentiation and associated magmatism (Shearer and Papike 1999). Magma formation and intrusion of Mg- and alkali rocks as well as extrusion of KREEP and high-alumina mare basalts were caused by the following strong brecciation and partial anatexis of the early crust due to catastrophic bombardment of the Moon surface by meteorites. In the result of these impact events, large basins (e.g., Mare Nectaris, Mare Imbrium), debris flows and ejecta blankets were formed. The last stage of the magmatic evolution of the Moon (3.8–3.0 Ga) was characterized by the eruption of mare basalts (high-Ti-group) due to partial melting of hybrid cumulate sources in the lunar mantle (Shearer and Papike 1999).

The appearance of the recent lunar surface can be related to the formation and alteration of the thick (up to 10 km) regolith cover during the last 3.0 Ga (Fig. 5.1). The Moon lacks an atmosphere and water, therefore, no weathering or sedimentation processes occur. The exogenic processes are restricted to the ongoing bombardment by cosmic material resulting in the formation of large crater regions and the accumulation of debris due to the destruction (and partially melting) of rocks.

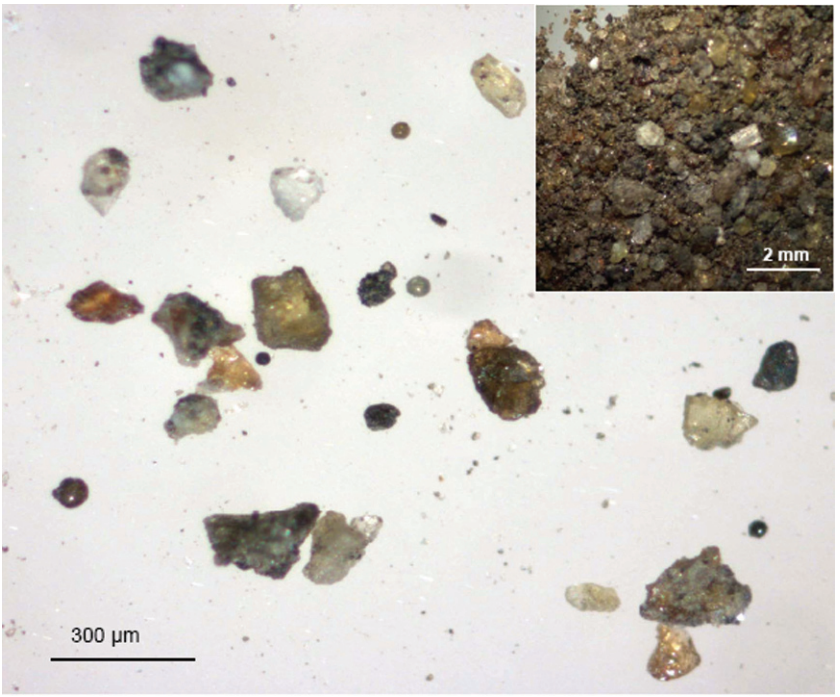

Fig. 5.1 Regolith sampled by Luna 24 (inset) and separated coarse-grained fraction containing small crystals and fragments of pyroxene, plagioclase, Fe-Ti oxides and glassy spheres

5.2.2 Lunar Rocks and Minerals

5.2.2.1 Lunar Rock Types

In general, three main lunar rock types can be distinguished: (1) anorthosites and anorthositic gabbros (*ANT suite*: Anorthositic-Noritic-Troctolithic), (2) basalts rich in K, REE, P, Zr, Ba and U (*KREEP basalts*), and (3) basalts rich in Fe and Ti (*FETI suite*) (Smith 1974). This classification is often closely connected with the differentiation between highland and mare regions on the moon. Numerous impact events in the *highland regions* lead to the formation of characteristic impact craters, breccias and regolith, whereas the *mare regions* are characterized by up to 400 m thick layers of basaltic lava flows (porphyric texture with glass components).

The lunar *highland region* is dominated by a variety of gabbros ranging from anorthositic to noritic and troctolitic in bulk composition. The *ANT suite* mostly occurs as metabreccias, and is believed to come from the crust. The anorthosites mainly comprised of calcic plagioclase, orthopyroxene and olivine and seem to result from early differentiation with gravity separation of crystals and liquid (Warren 1990). Mg-rich gabbros (Mg/(Mg+Fe) ratio of 0.7–0.9) with less plagioclase but more olivine are composed of plagioclase and pyroxene (norite),

plagioclase and olivine (troctolite) or subordinately only olivine (dunite). In contrast, alkaline anorthosites, gabbronorites and minor granites and rhyolites belong to the group of alkali-dominated rocks (alkali suite) (Smith and Steel 1976).

Rocks of the *KREEP suite* also occur in the highland regions, in particular as glasses and meta-breccias but also as crystalline rocks with basaltic texture (Shearer and Papike1999). The origin of these rocks is still in discussion and can probably be related to liquids resulting from primary differentiation at the crust-mantle interface and/or a liquid from partial melting of ANT rocks. The mineral composition is dominated by plagioclase, low-Ca pyroxene and minerals with high contents of the characteristic elements such as apatite and zircon (Smith 1974).

Tholeitic basalts with a composition similar to the oceanic crust of the Earth are the characteristic rocks of the *mare region*. It is assumed that these rocks result from the re-melting of cumulates rich in pyroxenes and opaque minerals, modified by near-surface differentiation in lava suites. The final residuum may contain minor granitic components with rare minerals (Smith 1974). Because of the general high Fe and Ti content (>9 % TiO_2), these rocks are often named *FETI suite*. Additionally, a low-Ti-group (1.5–9% TiO_2) and a very-low-Ti-group (VLT with <1.5% TiO_2) exist. The mineral composition of the mare basalts is dominated by zoned pyroxenes (mainly augitic), calcic plagioclase and ilmenite.

5.2.2.2 Lunar minerals

The mineral composition of lunar rocks is closely connected with their chemical composition and is much simpler than that of terrestrial rocks (see Fig. 5.1, Table 5.1). Plagioclase is the most abundant mineral of the highland rocks (enriched in Ca and Al), whereas pyroxene, plagioclase and ilmenite dominate the mare basalts (pyroxene together with plagioclase 75-90%). Olivine and the high-temperature silica modifications tridymite and cristobalite mostly occur in contents between 1 and 10% (Smith 1974).

In general, *plagioclases* in lunar rocks are CaO-rich (anorthite, bytownite) and the most calcic plagioclases (An_{95}) were reported from ANT rocks. The chemical compositions of plagioclases from KREEP rocks (An_{75}-An_{90}) and FETI basalts (An_{85}-An_{95}) show a tendency of increasing iron content (up to 1 wt% in FETI basalts) with higher albite component (Smith 1974). In contrast to the abundant plagioclase, alkali feldspars are rare and were only reported as K,Ba-feldspar (Basanidine) from granitic or rhyolitic residua. Additionally, feldspar with uncommon composition of $An_{50}Or_{40}Ab_{10}$ was found, which may have crystallized under non-equilibrium conditions.

Minerals of the *pyroxene group* belong to the most frequent minerals on the moon. The chemical composition is very complex and includes all major elements (Si, Al, Mg, Ca, Fe, Mn, Ti, Cr) but only minor Na and K (Smith 1974). Clinopyroxenes (augite, Ti-augite, hedenbergite, pigeonite) are common in all rock types, whereas the highland rocks also contain orthopyroxenes (enstatite-hypersthene). In contrast to minerals of the pyroxene group, *amphiboles* are very rare. Minor

Table 5.1 Mineral groups and minerals in lunar rocks

Mineral/Mineral group	Chemical composition/Remarks	
Feldspar group	***(Ca,Na)[(Al,Si)$_4$O$_8$]***	
	mostly An$_{\geq 90}$ (Anorthite, Bytownite)	
	rare K,Ba-feldspar	
	rare An$_{50}$Or$_{40}$Ab$_{10}$ composition	
Pyroxene group	***(Mg,Ca,Fe,Al,Ti,Cr)[(Si,Al)$_2$O$_6$]***	
	very low in Na, K	
	Augite, Ti-augite, Hedenbergite, Pigeonite;	
	in highland rocks Enstatite-Hypersthene	
Ilmenite	***FeTiO$_3$***	
	frequent in mare basalts (FETI)	
Olivine	***(Mg,Fe)$_2$[SiO$_4$]***	
	Mg rich, mostly Fa$_{30}$	
Silica group	***SiO$_2$***	
	Cristobalite, Tridymite	
	rare Quartz	
Armalcolite	*(Fe,Mg)Ti$_2$O$_5$*	
	in metamorphosed Mg-rich rocks	
Accessories		
Apatite	Ca$_5$[(F,Cl)[PO$_4$)$_3$]	KREEP rocks
Whitlockite	β-Ca$_3$(PO$_4$)$_2$	KREEP rocks
Zircon	Zr[SiO$_4$]	KREEP rocks and
Baddeleyite	ZrO$_2$	residua of FETI basalts
Spinel	MgAl$_2$O$_4$	Mg-rich rocks
Cromite	FeCr$_2$O$_4$	FETI basalts
Ulvöspinel	Fe$_2$TiO$_4$	FETI basalts
Troilite	FeS	FETI basalts
Iron	Fe	FETI basalts
Copper	Cu	FETI basalts
Amphibole group	in FETI basalts rare Alumino-Tschermakite and Magnesio-Arfvedsonite-Richterite	
Pyroxferroite	(Ca,Fe)(Fe,Mn)$_6$[Si$_7$O$_{21}$]	only on the moon
Tranquillityite	Fe$_8$Ti$_3$[Zr,Y)$_2$[O$_{12}$/(SiO$_4$)$_3$]	only on the moon

alumino-tschermakite and magnesio-arfvedsonite-richterite was detected in FETI basalts (Gay et al. 1970).

Olivine is an early-crystallizing phase which is present as major and minor constituent (up to 10%) in ANT and FETI rocks; it is rare or absent in KREEP rocks (Smith 1974). The composition is in general Mg-rich (ANT suite: Fo$_{65-85}$, FETI suite: Fo$_{30-70}$) with highest forsterite components of mg = 0.93-0.83 in ultrabasic rocks and fragments (Steel and Smith 1972).

Ilmenite is the most frequent mineral among the *Fe-Ti minerals*. It is a main constituent of mare basalts with up to 24 wt%. *Armalcolite* (Fe,Mg)Ti$_2$O$_5$ was detected as minor component in FETI basalts (low Cr, Zr) and metamorphosed Mg-rich rocks (high Cr, Zr). Ulvöspinel (Fe$_2$TiO$_4$), rutile (TiO$_2$) and perovskite (CaTiO$_3$) only occur as accessory minerals. The lack of Fe^{3+}-bearing minerals and the existence of troilite and metallic iron (and Cu) indicate a low oxygen fugacity during crystallization of lumar rocks and minerals (Smith and Steel 1976).

Silica modifications especially occur in form of *tridymite* and *cristobalite* as late crystallization products in rocks of mare basalts. *Quartz* is rare in lunar rocks. The presence of the high-temperature modifications indicates temperatures of crystallization of the basalts above 1100°C (Smith 1974). James (1972) detected silica and pyroxene as inclusions in ANT plagioclases and proposed another mechanism of mineral formation by the break down of the component $Ca(Fe,Mg)Si_3O_8$ into pyroxene ($Ca(Fe,Mg)Si_2O_6$) and silica (SiO_2) with falling temperature.

A couple of *accessory phases* were found in lunar rocks (Table 5.1), which are not all common in terrestrial rocks. For instance, the two silicates *pyroxferroite* $(Ca,Fe)(Fe,Mn)_6[Si_7O_{21}]$ and *tranquillityite* $Fe_8Ti_3(Zr,Y)_2[O_{12}/(SiO_4)_3]$ have been detected only on the Moon up to now (Smith 1974). The Zr-minerals zircon ($ZrSiO_4$) and baddeleyite (ZrO_2), and the phosphates apatite ($Ca_5[(F,Cl)/(PO_4)_3]$ - OH free) and whitlockite ($Ca_3(PO_4)_2$) are common especially in KREEP rocks. Monazite was detected as accessory phase in a phosphate-rich clast in Apollo 17 impact-melt breccia (Jollife 1993). The general absence of water-bearing phases and the rare occurrence of OH-bearing minerals are a result of the almost complete lack of water and H_2O-bearing fluids. Roedder and Weiblein (1970) found even no fluid inclusions in 168 examined lumar samples.

The regolith of the lunar surface is not only composed of mineral and rock fragments but also of high amounts of *glassy particles*. These glasses may derive from either volcanic activities or from the melting of target material during impact events. Lunar pyroclastic glass often has a green colour and a picritic composition (11-19 wt% MgO), which is more primitive than most lunar basalts (Delano 1986; Shearer and Papike 1993). The chemical composition of impact glasses (colourless, yellow, orange) in general reflects the composition of the parent rocks and minerals, respectively (Delano et al. 1981; Zeigler et al. 2006). *Maskelynite* is a special type of naturally occurring glass having the composition of plagioclase, created by the vitrification of feldspar by shock melting.

5.3 CL Properties of Lunar Minerals

5.3.1 General Overview

In general, many minerals of all mineral classes can show usable luminescence properties. The luminescence of these mineral phases is often highly variable depending on the specific conditions during formation. Certain ions can be encountered in natural minerals in different combinations resulting in characteristic sets of ions for various types of rocks or different regions. On the other hand, certain geological processes may create specific defects in mineral phases, which reflect these specific conditions of formation. The knowledge of the typical luminescence characteristics of minerals can be used to reconstruct the processes of crystallization, alteration and damage. Thus, CL can provide information otherwise unobtainable (e.g., Figs. 5.2 and 5.6).

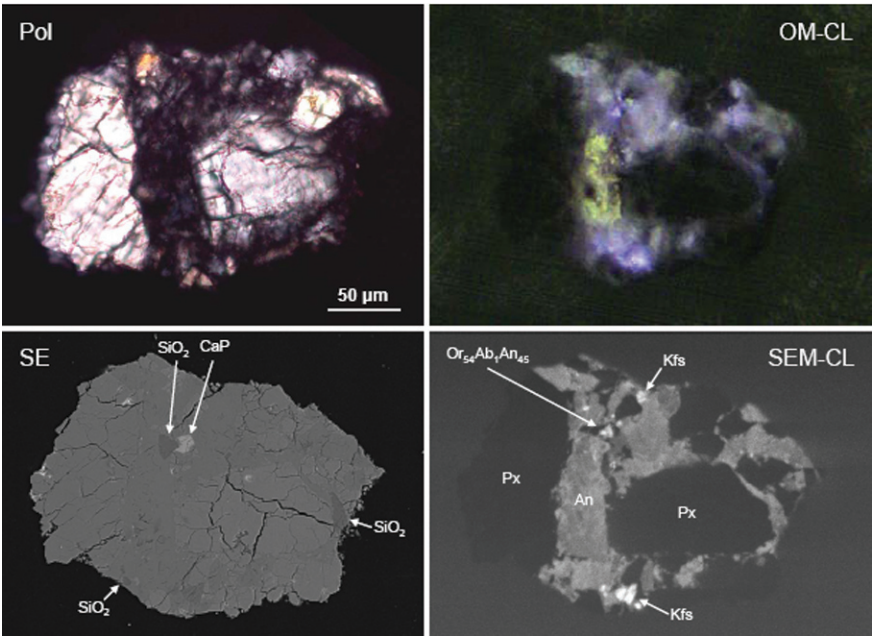

Fig. 5.2 Fine-grained breccia from Luna 16 regolith with complex mineralogical composition; the micrographs are obtained with polarizing microscopy (Pol), CL microscopy (OM-CL), SEM-SE imaging (SE) and SEM CL (SEM-CL). CL reveals *greenish* and *bluish* plagioclase, small spots of *bright blue* luminescent K-feldspar (spectra in Fig. 5.3), *dark blue-violet* whitlockite (CaP - compare CL spectrum in Fig. 5.11) and dark blue luminescent quartz (SiO_2); pyroxene is non-luminescent

As already outlined in the previous chapter, the number of common lunar minerals is limited. In view of the potential luminescence behaviour, the general high iron content of most lunar material additionally prevents luminescence activation. Therefore, only a few, more or less iron-free minerals have to be considered within the group of luminescent minerals. Sippel and Spencer (1970) and Sippel (1971) mentioned that calcic plagioclase, the silica modifications tridymite and cristobalite, and traces of alkali feldspar are the dominant luminescent minerals in lunar crystalline rocks and breccias. Other potential luminescent silicates could be the iron-free end members of olivine (forsterite) and orthopyroxene (enstatite), which have been found in meteoritic material (e.g., Steel et al. 1985; Steel 1986; Benstock et al. 1997; DeHart and Lofgren 1993). Some additional accessory minerals have to be considered in respect to their luminescence behaviour, among them the Zr-minerals zircon and baddeleyite, and the phosphates apatite and whitlockite. The luminescence behaviour of spinel is still unclear because of the common presence of an iron component, which quenches the luminescence. Other luminescent minerals, which were observed in meteorites (Steel 1989), have not been detected in lunar samples up to now.

The mineralogical and physical background of the specific luminescence properties of these minerals and possible applications are discussed in the following chapters. The explanations are based on data from literature and own results from the investigation of material, which have been sampled by the Russian lunar missions Luna 16, 20 and 24. This material represents lunar soil (regolith) of different regions. The landing site of Luna 16 was Mare Fecunditatis (similar in its geological setting to Apollo 11), Luna 20 is located in the highland region between Mare Fecunditatis and Mare Crisium (3°32'N and 56°33'E), whereas the landing site of Luna 24 was located in the south-eastern part of Mare Crisium, which fills most of the Crisium multiringed basin (Vinogradov 1972).

Luminescence studies were carried out by a combination of CL microscopy and spectroscopy using an optical microscope (OM-CL) and a scanning electron microscope (SEM-CL), respectively. Microchemical analyses by SEM-EDX, microprobe and PIXE provided additional data concerning the chemical composition of the investigated rocks and minerals. Details about the luminescence basics and the analytical procedures are given in Chap. 1 of this volume and in Götze (2008).

5.3.2 Feldspar Minerals

Feldspar minerals are basic mineral constituents in both terrestrial and extraterrestrial rocks and show valuable CL properties (Götze et al. 2000). Plagioclase is the dominant luminescent mineral in lunar rocks and breccias, whereas alkali feldspar is only a minor component especially in more acidic lithic fragments. The CL of feldspars shows a wide range of colour and intensity depending on chemical composition and structural state. The luminescence colours and spectra can vary between rocks of different lunar regions but also within single grains or crystals.

5.3.2.1 K-feldspar

Luminescent alkali feldspar is rare on the moon and was only sporadically found in fine-grained breccias of Apollo and Luna samples. Sippel and Spencer (1970) and Sippel (1971) first reported 10-40 μm blebs of alkali feldspar intergrown with silica. These alkali feldspar grains with a compositional range of $Or_{72-85}Ab_{15-28}An_{0-1}$ in general exhibited a bright blue CL, similar to that of terrestrial feldspars. The same type of alkali feldspar was also found in Luna 16 samples (Fig. 5.2) together with pyroxene, plagioclase, silica and calcium phosphate. The alkali feldspar contains up to 0.6 wt% Ba and shows a broad emission band in the blue comparable to terrestrial alkali feldspar. The broad band consists of two overlapping emissions at ca. 450 and 500 nm, respectively (Fig. 5.3).

The luminescence emission around 450 nm is caused by the substitution of Al^{3+} for Si^{4+} in feldspar (Marfunin 1979). The Al-O^--Al centre forms with two Al atoms, one of which is 'structural Al' and the other 'impurity Al'. This oxygen hole centre adjacent to two Al ions is the most common centre in all terrestrial feldspars,

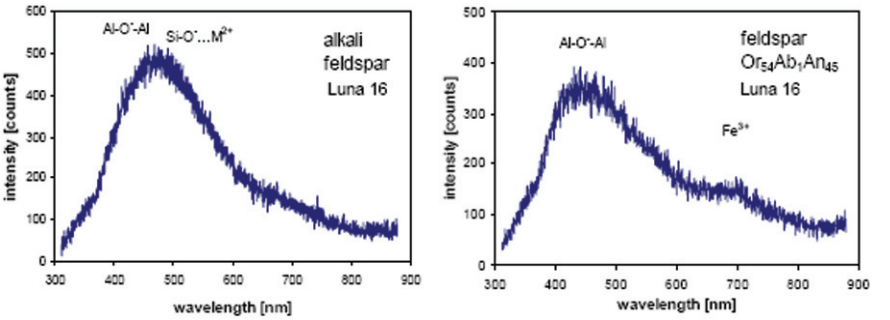

Fig. 5.3 CL emission spectra of K-feldspar and feldspar with uncommon composition of Or_{54} Ab_1 An_{45} from Luna 16 (see Fig. 5.2); both feldspars show a dominant blue emission band due to Al-O^--Al defects

except in those with very high An content (Speit and Lehmann 1982). The Al-O^--Al centres are preferentially formed in feldspar with large M cations (K, Ba) such as orthoclase, sanidine or hyalophane. Therefore, the intensity of the blue emission is generally higher in alkali feldspars compared to plagioclases. Variations in the peak position are caused by different types of Al-O^--Al centres, associated with two non-equivalent sites for the impurity Al (Kirsh et al. 1987). The additional emission band at ca. 500 nm was related to a hole centre on an oxygen adjacent to a divalent impurity ion (Si-O^-...M^{2+}). Marfunin and Bershov (1970) and Matyash et al. (1982) suggested that this centre must be stabilized by a divalent metal ion M^{2+} in T site adjacent to oxygen (e.g., Mg^{2+}, Zn^{2+}, Be^{2+}).

Another type of luminescent alkali feldspar was found in fine-grained lithic fragments of luna 20 material, where the yellow-olive luminescent feldspar is intergrown with SiO_2 (Fig. 5.4).

The CL spectrum shows two emission bands at ~450 and 700 nm. In contrast to the Luna 16 samples, the 500 nm emission is absent and the alkali feldspar contains no detectable Ba but 0.62 wt% iron. The pronounced red emission is the evidence that at least some of the iron is Fe^{3+} incorporated in the Al^{3+} lattice position (Fig. 5.4).

A luminescent feldspar grain with the composition $Or_{54}Ab_1An_{45}$ was detected in a lunar breccia of Luna 16 (Fig. 5.2). This uncommon feldspar composition, which probably crystallized on the moon under non-equilibrium conditions, shows a bright blue CL like K-feldspar. The luminescence emission spectrum (Fig. 5.3) is also similar to that of alkali feldspar with a dominant blue emission band (Al-O^--Al defect) and an additional weak band at 700 nm, which can be ascribed to the activation by Fe^{3+}.

5.3.2.2 Plagioclase

The visible luminescence of plagioclase shows a wide range of intensity and colour ranging from pale blue to green (Figs. 5.5 and 5.6). Many of the crystals appear more or less homogeneous under CL, others show zoning or irregular areas with

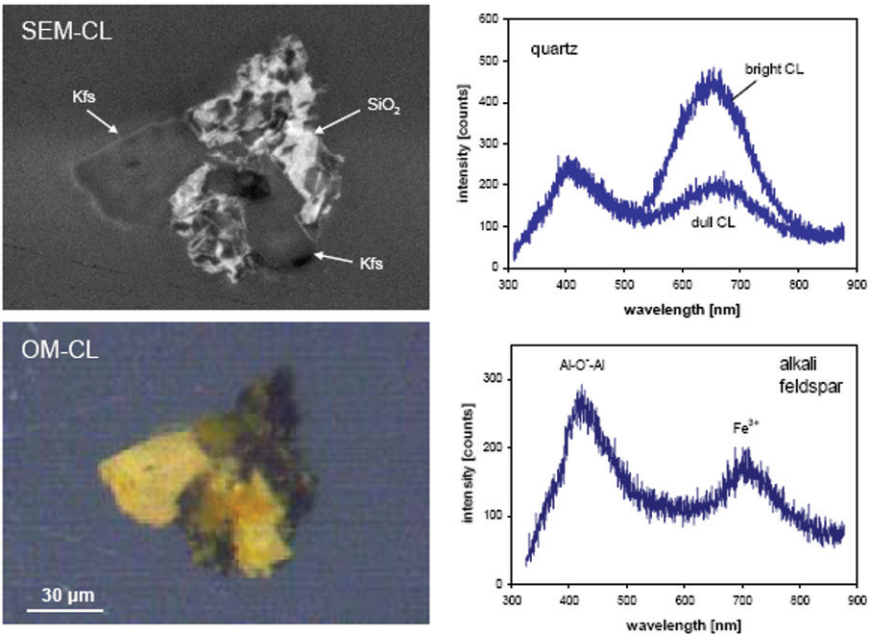

Fig. 5.4 K-feldpar/silica intergrowth in a fragment from Luna 20 soil; the heterogeneous internal CL structure of silica is not visible in the SE image and is caused by the varying intensity of the 650 nm emission; the CL emission spectrum of the yellow-olive luminescent K-feldspar shows a two bands at 450 nm and in the red at 700 nm due to Fe^{3+}

slightly different CL colours, which are not discernable with other microscopic techniques. Lath-shaped crystals often exhibit a brightly greenish luminescent central part, whereas the rims are dull luminescent (Fig. 5.5). This zoning is often correlated with a chemical trend from An-rich crystal cores to more albitic rims, which can be related to preferential partitioning of activator ions (e.g. Mn^{2+}) in the crystallizing plagioclase, so that they become impoverished in the melt during proceeding crystallization (Sippel 1971). Figure 6d shows a plagioclase grain from Luna 24, where the zone with the brightest CL is Ca rich (An_{95}) grading to An_{71} in the zone with the dullest CL. However, other plagioclase grains with significant variations in the chemical composition show no differences in the CL behaviour. Another phenomenon was reported by Sippel and Spencer (1970), who detected a partially polarized CL of plagioclase, which is often visible due to variations of the intensity in differently oriented crystals (e.g., twinning).

CL spectra of lunar plagioclases show significant similarities but also differences to terrestrial samples. Spectral analysis of the CL emission revealed that the lunar plagioclases show in general three main CL emission bands in the blue around 450 nm, in the green at ~560 nm and in the red/IR at ~690 nm (Fig. 5.6). These are also the most common emission bands found in terrestrial plagioclases (e.g., Geake et al. 1972; Marshall 1988; Götze et al. 2000). The intensities of these emission bands vary between plagioclases of the different samples as well as within single feldspar

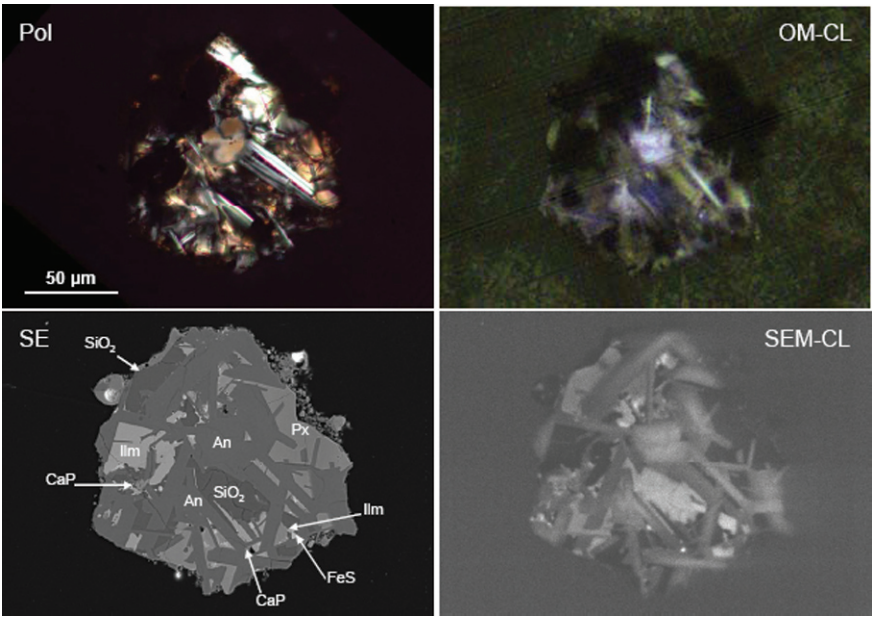

Fig. 5.5 Lithic fragment of Luna 16 regolith with complex mineral composition; the plagioclase shows different luminescence colours and also variations of the CL intensity within the single anorthite laths

grains, causing the different CL colours and CL zoning (Fig. 5.6). CL emission related to rare earth elements as reported by Götze et al. (1999a) in terrestrial feldspars was not detected.

The green peak at ~560 nm is the most dominant emission in most of the investigated lunar plagioclases (Fig. 5.6). According to Geake et al. (1971, 1972) this emission band centred at ca. 560 nm is due to Mn^{2+} in M sites (most probably Ca^{2+} sites). They reported this luminescence emission in almost all plagioclases from Apollo samples and meteorites and concluded that Mn^{2+} is the dominant activator in lunar and other extraterrestrial material because of its wide availability and the common substitution for Ca and Mg. Quantitative measurements on synthetic and natural plagioclases (Telfer and Walker 1978; Mora and Ramseyer 1992; Götze et al. 2000) have shown a clear correlation between the intensity of the green emission band and the Mn content. Based on this fact, observed CL zoning in single lunar plagioclase grains can be explained by variations in the Mn concentration (Götze et al. 1999a). First calculations by quantitative spectrometric analysis yield Mn concentrations between 7 and 47 ppm in plagioclases from Luna 20 and 24 (see Fig. 5.6d).

In contrast to the 560 nm CL emission, the intensity of the blue emission at ~450 nm in most lunar plagioclases is relatively weak (Fig. 5.6). Only some of the shock-damaged anorthites show a dominant emission in the blue. Walker (1985) related the blue emission, which occurs in both alkali feldspars and plagioclases, to

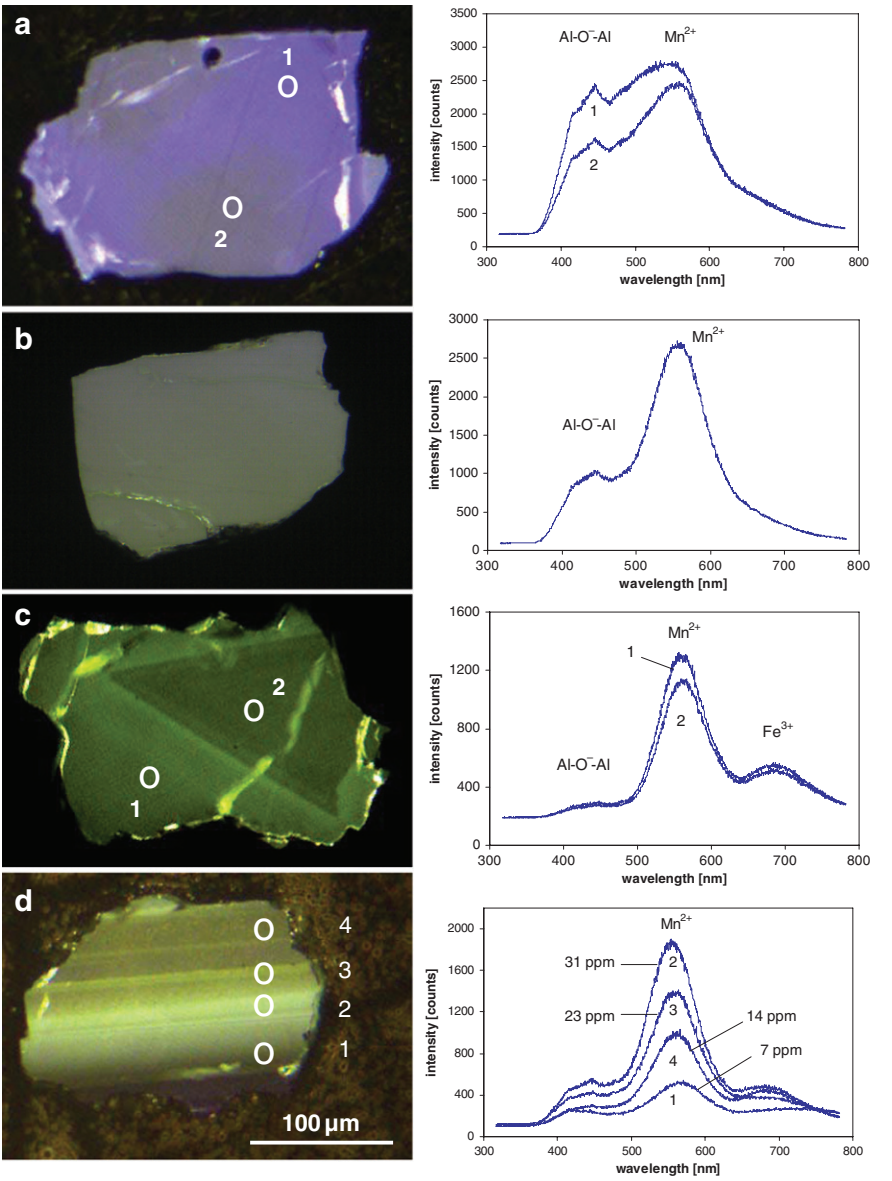

Fig. 5.6 Single feldspar grains from the coarse fraction of Luna 20 and Luna 24 regolith and related CL spaectra; (**a**) plagioclase grain from Luna 20 showing different shades of bluish CL; the variations in CL colour are mainly cause by differences in the intensity of the blue emission band (Al-O^- -Al defect); (**b**) homogeneous plagioclase grain from Luna 20 with dominant Mn^{2+} emission; (**c**) sector zoned plagioclase from Luna 24 regolith with a two emission bands at 570 nm due to Mn^{2+} and at ~690 nm due to Fe^{3+}; (**d**) Luna 24 plagioclase with distinct oscillatory zoning under CL; the intensity of the visible CL in the different zones (1-4) correlates well with the intensity of the Mn^{2+} related emission band; Mn contents between 7 and 31 ppm were analyzed using PIXE (Götze et al. 1999a)

structural defects (electron-hole recombinations at various hole centres) similar to those in other silicates. The CL emission band around 450 nm may be caused by the substitution of Al^{3+} for Si^{4+} in the feldspar structure. Although the intensity of the blue emission is generally higher in alkali feldspars compared to plagioclases, the formation of short-range disordered domains can be related to Al-O-Al clustering associated with structural defects in their local environment (Petrov et al. 1993). Thus, the strong blue CL emission in some of the lunar plagioclases indicates high abundances of lattice defects in these samples.

In some plagioclase crystals of the lunar material an emission band in the red/IR at ~690 nm was clearly detected (Fig. 5.6). This is of special interest, since Geake et al. (1972), Telfer and Walker (1975, 1978) and White et al. (1986) showed that the red emission band around 700 nm is due to Fe^{3+} which occupies Al^{3+} tetrahedral sites in the feldspar lattice ($^4T_1$ 6 $^6A_1$ electronic transition). Several previous studies have been focused on the question of the oxidation state of transition elements in lunar samples and it was assumed that iron occurs predominantly as Fe^{2+} (e.g., Forester 1973, Burns et al. 1973). Indeed, Sippel and Spencer (1970) found no evidence of a red-infrared peak in any of more than one hundred investigated lunar plagioclase grains, and the red emission band was not detected with any certainty in all investigated plagioclases of Luna 20 (Götze et al. 1999a). The weak or absent red emission band in lunar plagioclases has been ascribed to low f_{O2} during plagioclase crystallization (Geake et al. 1972). Nevertheless, the occurrence of the CL emission band at 690 nm indicates that Fe^{3+}-activated CL is common in lunar plagioclases. Although this emission is generally less intense in lunar compared to most terrestrial feldspars, the results indicate that at least some of the iron in lunar plagioclases is ferric iron. Differences could be detected in the concentration of Fe^{3+} between samples or grains as well as within single grains. Using spectral CL, Fe^{3+} is detectable in concentrations probably below 100 ppm and with a lateral resolution of ~30 µm, which is not possible with other analytical methods.

The sensitivity of the red peak position to anorthite content in terrestrial feldspars has been previously reported (e.g., Sippel and Spencer 1970; Geake et al. 1972; Telfer and Walker 1975; Mora and Ramseyer 1992; Götze et al. 2000). Both the structural state of the plagioclase and the tetrahedral site occupancy of Fe^{3+} can affect the position of the red peak (Telfer and Walker 1978; Petrov et al. 1989). The investigations on lunar anorthite samples have shown that the band position of the red/IR emission correlates well with the results of Ca-rich terrestrial plagioclases (Krbetschek et al. 2002; compare Fig. 1.9 in Chap. 1).

Another Phenomenon detected by CL in lunar feldspars is the change of CL properties by shock damage. Anomalous orange luminescence of plagioclase fragments with small birefringence and maskelynite with dull reddish CL were first reported by Sippel and Spencer (1970) in lunar breccias. Under the influence of the meteoritic bombardment on the lunar surface, shock damage produced distorsion and disorder of the feldspar lattice resulting in changes of the CL properties. The shock damage is detectable by features of brecciation, internal fragmentation and mosaic extinction patterns up to the isotropization of plagioclase and the formation

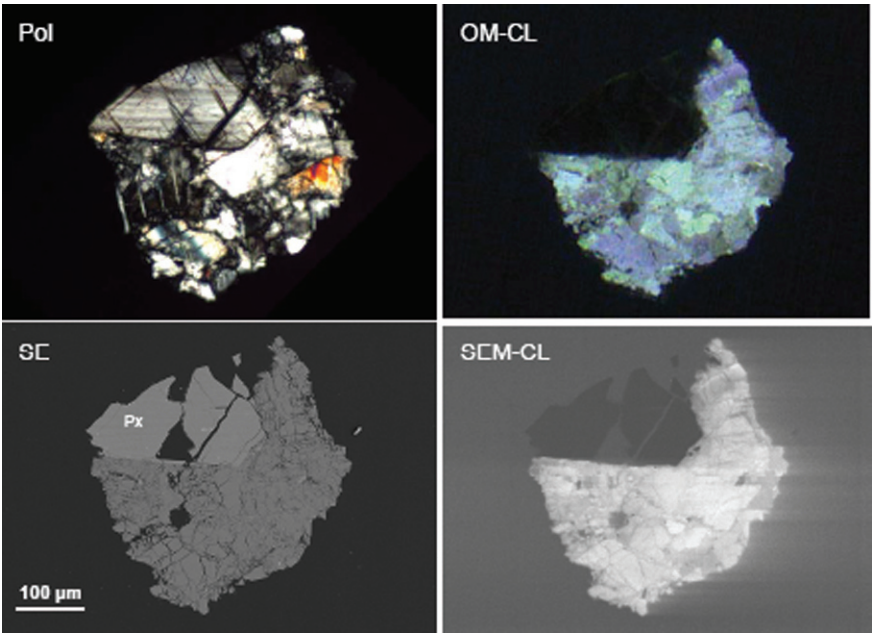

Fig. 5.7 Grain fragment from the coarse fraction of Luna 20 regolith with intergrown pyroxene (px) and plagioclase; the feldspar shows features of brecciation and internal fragmentation due to shock damage; the different grain fragments show various luminescence properties

of maskelynite (Fig 5.7 and 5.8). The degree of shock damage can in general be related to the magnitude of spectral CL shifts.

The investigation of natural and experimentally shocked plagioclase between 10.5 and 45 GPa revealed a systematic change of the related CL spectra (e.g., Kaus and Bischoff 2000; Gucsik et al. 2005). Due to distorsion and disorder in the crystal lattice, the creation of new defects as well as the amorphization of crystals, the resulting CL spectra exhibit effects such as peak shift and broadening, as well as decreasing or disappearing emission bands. Changes in the crystal field parameters cause variations of excited state energies or the appearance of non-radiative electron transitions. Compared to the unshocked samples, the Mn^{2+} activated CL emission band shifted from initially 578-618 nm at 20 GPa (Gucsik et al. 2005). The formation of diaplectic glass above 26 GPa resulted in the disappearance of the crystal field sensitive Mn^{2+} and Fe^{3+} related peaks (Kaus and Bischoff 2000). Moreover, the spectra of the isotropic plagioclase showed an additional emission maximum at 425 nm, which overlaps the band at 465 nm. In the visible CL, these spectral changes can be observed by a colour change from green via orange to blue with increasing shock damage. This is in accordance with observations on lunar plagioclases, where the blue enhanced spectra were found in grains whose state of disorder approaches that of fused plagioclase (Fig. 5.8).

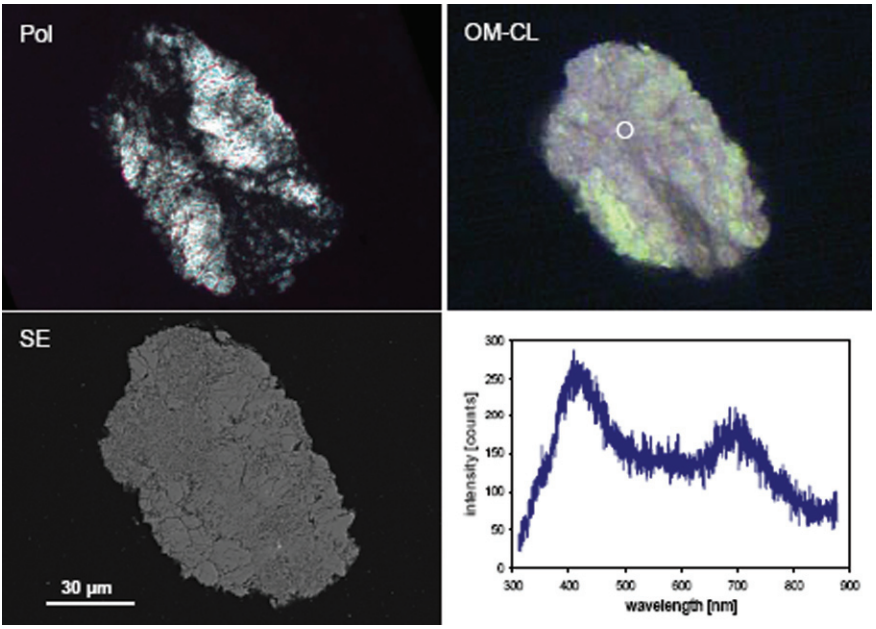

Fig. 5.8 Plagioclase grain from Luna 20 regolith showing strong features of shock damage such as brecciation, internal fragmentation up to partial isotropization (maskelynite?); the alteration of the plagioclase resulted in a strong change of CL properties due to lattice damage; the isotropic area shows a strong emission band in the blue at ca. 430 nm

5.3.3 Silica Modifications (Tridymite, Cristobalite, Quartz)

Silica forms 14 modifications of crystalline and amorphous SiO_2 (Strunz and Tennyson 1982). Three of them - tridymite, cristobalite and the trigonal alpha-quartz - were detected in lunar rocks (Smith 1974). The silica assemblage changes between different rock types. Tridymite and cristobalite are dominant in coarse-grained rocks, whereas quartz is absent (Sippel 1971). In the finer grained rocks, the silica assemblage is cristobalite-quartz and lacks tridymite.

Because of the structural differences, the silica modifications exhibit different luminescence properties and thus, are distinguishable by CL in lunar and meteoritic material (Sippel and Spencer 1970; Aoudjehane and Jambon 2007). *Tridymite* is often intergrown with plagioclase in coarse-grained rocks and shows a bright blue luminescence (Fig. 5.9). Sippel and Spencer (1970) reported brightly luminescent tridymite laths up to 2 mm in length in Apollo 12 rocks. The CL emission spectrum of tridymite is dominated by a broad band centred at ca. 500 nm (Fig. 5.9). *Cristobalite* exhibits a dark blue CL with a much less luminescence intensity compared to that of tridymite. Nevertheless, the CL emission spectrum is very similar, showing a broad band at ca. 500 nm (Sippel 1971). Both silica polymorphs show modifications of the CL properties under the electron beam. The luminescence intensity of

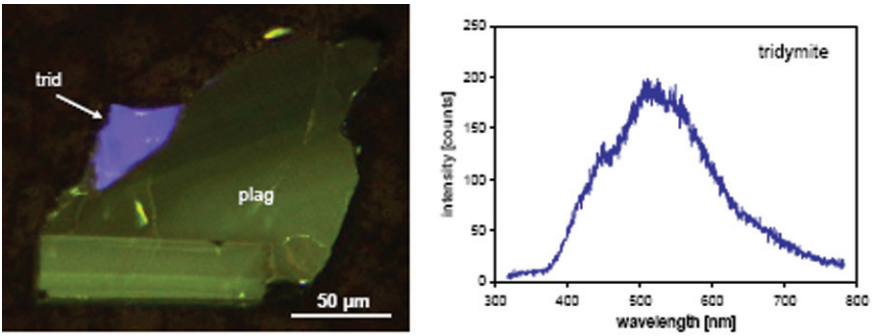

Fig. 5.9 Plagioclase grain from Luna 24 soil intergrown with a small grain fragment of tridymite that shows bright blue CL; the related CL spectrum shows a broad emission band around 500 nm

tridymite increases with increasing beam current. However, after prolonged electron irradiation the bright luminescence can be irreversibly extinguished with a remaining dull blue component (Sippel 1971). The CL of cristobalite is stable under moderate irradiation but develops a reddish luminescence during intense electron bombardment (Sippel and Spencer 1970)

Quartz is absent in coarse-grained lunar rocks, but was reported from fine-grained rocks of Apollo 11 and 12 (e.g. Sippel 1971), as well as Luna 16 and 20 (this study). In general, dull blue and/or pink luminescent quartz was detected together with alkali feldspar or plagioclase (Figs. 5.4 and 5.5). The CL emission spectrum consists of two broad bands with maxima at 420 and 650 nm (Fig. 5.4). This is similar to emission spectra of crystalline quartz from terrestrial rocks (e.g. Götze et al. 2001).

Several emission bands in natural and synthetic quartz and amorphous silica have been detected, which were related to various intrinsic and extrinsic defects (e.g., Stevens Kalceff and Phillips 1995; Götze et al. 2001). The blue emission band (~420 nm) is due to the recombination of the so-called self-trapped exciton (Stevens Kalceff and Phillips 1995), an electron hole pair on an oxygen vacancy and a peroxy linkage. Recent results showed that the intensity of this emission is especially high in oxygen-deficient SiO_2 samples (Skuja 1998). The orange to red emission band at about 620-650 nm is attributed to the recombination of electrons in the non-bridging oxygen band-gap state with holes in the valence-band edge (Siegel and Marrone 1981). A number of different precursors of this non-bridging oxygen hole centre (NBOHC) have been proposed such as hydrogen or sodium impurities, peroxy linkages (oxygen-rich samples), or strained silicon-oxygen bonds, which may influence the band position (Stevens Kalceff and Phillips 1995). In lunar samples, strained and damaged silicon-oxygen bonds may be responsible for the red emission similar to terrestrial quartz samples from metamorphic rocks. Effects of radiation damage could not be found in lunar samples.

Small, anhedral quartz crystals often show irregular internal structures under CL, which are not discernable with conventional microscopy (Fig. 5.4). The comparison

of the CL spectra of grain-areas with different luminescence intensity revealed that the blue band is relatively constant, whereas the bright areas show a much more intense emission band in the red (Fig. 5.4).

Sippel (1971) reported another effect of the quartz CL when observing the luminescence under a nicol prism. The quartz CL shows strong polarization effects with variations of the CL colour from red to blue through a rotating polarizer. He found that the blue oscillators are aligned with the c-axis, whereas the red emission is unpolarized. This effect may be interpreted by anisotropic luminescing centres that have oriented the oscillation in a strong internal crystal field.

5.3.4 Zircon and Baddeleyite

Zircon and *baddeleyite* are accessory Zr-minerals which occur especially in lunar KREEP rocks. They are often rapidly recognizable under CL, even if only one small grain is present in the viewed area. Both minerals were used for fission track and isotope dating of lunar rocks (e.g. Hutcheon and Price 1972; Hutcheon et al. 1974; Braddy et al. 1975; Wopenka et al. 1996; Taylor et al. 2007; Pidgeons et al. 2007). Single zircon grains often show growth zoning or very complex internal structures under CL reflecting different primary and secondary geological events and therefore, inherit a wealth of genetic information.

Pidgeons et al. (2007), for instance, investigated the age and origin of a zircon from lunar breccia 73235 (Apollo 17). CL studies revealed a complex internal structure of the sector zoned primary zircon crystal, which additionally shows a dark secondary rim. The dull luminescence of the secondary zircon matrix has been related to the presence of amorphous components due to a shock event. SIMS U-Pb analyses provided a primary zircon age of 4.315+0.015 Ga and a younger age of 4.187+0.011 Ga for the secondary rim.

The origin of the luminescence emission in zircon is still in discussion (Nasdala et al. 2003 and references therein). In general, zircon shows bright blue or yellow luminescence. Radiation damage, metamictization and amorphization/vitrification (e.g. by shock damage) result in a decrease of the luminescence intensity. The luminescence emission spectra of zircon exhibit both broad luminescence bands caused by lattice defects and/or narrow emission lines due to the incorporation of trace elements such as rare earth elements (REE).

The understanding of the broad emission bands in zircon is still relatively poor. An emission band centred at ca. 365 nm (visible as blue CL of many zircon grains) is probably caused by a delocalized electron on the $[SiO_4]$ groups similar to defects in many other silicates (e.g. Kempe et al. 2000). The broad emission band in the yellow region around 560 nm is of radiogenic origin in zircons that were exposed to radioactive irradiation (e.g., Remond et al. 1992; Kempe et al. 2000; Gaft et al. 2005), although there is no direct correlation between the intensity of the yellow emission with the U and Th concentrations in zircon.

Incorporation of trivalent REE by substitution of Zr^{4+} is common in zircon. Dy^{3+} is the dominant luminescence activator element, whereas other REE such as Sm^{3+},

Tb^{3+}, Er^{3+}, Gd^{3+}, Nd^{3+} are of minor importance (Marfunin 1979). Investigations of natural and doped synthetic zircon crystals showed that the REE^{3+} (except of Ce^{3+}) produce sharp emission lines, which are specific for each REE ion (e.g. Cesbron et al. 1995; Blanc et al. 2000). Wopenka et al. (1996) reported the REE activated laser-induced fluorescence in a zoned lunar zircon from an Apollo 14 soil, which they related to Eu^{3+}, Er^{3+}, Tb^{3+} and Dy^{3+}. The intensities of the luminescence peaks correlated with the concentrations of the REEs.

Another application of CL is the detection of shock-induced alterations in zircon. Different types of shock deformation including planar micro-deformation, granular textures and amorphous areas have been detected in experimentally shock-metamorphosed zircon using CL in combination with SEM and micro-Raman (Gucsik et al. 2002, 2006b). These deformations can result either in the decomposition of zircon to baddeleyite and silica (Kleinmann 1969) or the transformation of the zircon structure into a shock-pressure modification with scheelite structure (Kusaba et al. 1985). The structural changes do not only cause the formation of lattice defects but also variations in the energy levels of the activator elements. Therefore, CL in combination with other micro-techniques is a sensible tool to detect the structural changes in lunar zircon due to impact events.

5.3.5 Calcium Phosphates

Among the minerals of the phosphate group, OH-free *apatite* (general formula $Ca_5[(F,Cl)/(PO_4)_3]$) and *whitlockite* ($Ca_3[PO_4]_2$) occur as accessory constituents of lunar KREEP rocks (Smith 1974). Both are being used as dating material for fission track geochronology (e.g. Braddy et al. 1975). Moreover, investigations of Martian apatite and whitlockite have shown that CL is a powerful tool to obtain detailed information concerning structural and compositional variations within single crystals or aggregates (e.g., Stirling 2000; Stirling et al. 2001).

Apatite is the most common calcium phosphate mineral in terrestrial rocks and plays an important role as indicator mineral in geological processes. Certain ions can be encountered in natural apatite (e.g., Eu^{2+}, REE^{3+}, Mn^{2+}, Fe^{3+}) in different combinations yielding characteristic sets of ions for various types of rocks or different regions. Luminescence studies on synthetic and naturally occurring apatite have revealed characteristic emission bands (Mn^{2+}, Eu^{2+}, Ce^{3+}) or sets of emission peaks (REE^{3+}) that can be related to specific activator ions (e.g., Marfunin 1979; Mitchell et al. 1997; Blanc et al. 2000; Kempe and Götze 2002). Additionally, lattice defects (electron defects on oxygen of the phosphate group) can also activate a luminescence emission around 400 nm (Habermann et al. 1997). Sippel (1971) described apatite with yellow-orange luminescence in Apollo 12 samples, which is similar to many terrestrial specimens. Although no CL spectra were published, the observed luminescence colour indicates the role of Mn^{2+} as activator ion in lunar apatite (emission band at 565 nm). This would emphasize the role of Mn^{2+} as dominant activator ion in extraterrestrial material. Minerals with the approximate composition $Ca_3(PO_4)_3$ (*whitlockite*) are frequent as accessory minerals in

extraterrestrial (meteorites, lunar rocks) and terrestrial rocks. The crystal structure and composition of these minerals can vary significantly leading to marked differences in dependence on the origin. Compared to pure synthetic ß-$Ca_3(PO_4)_3$, terrestrial whitlockite is hydrous with a composition close to $Ca_{18}X_2H_2(PO_4)_{14}$ (X = Mg, Fe, Mn, etc.), whereas extraterrestrial calcium phosphates are anhydrous and are often called *merrillite* (Dowty 1977). In contrast to terrestrial occurrences, lunar whitlockite is enriched in REE relative to associated apatite (Griffin et al. 1972). Therefore, Dowty (1977) suggested the general formula $Ca_{16}(Y,REE)_2(Mg,Fe)_2(PO_4)_{14}$).

Whitlockite in lunar rocks was detected as small spots with bluish-violet CL. The CL spectra are dominated by strong emission peaks of several rare earth elements. The CL spectrum of whitlockite from Luna 16 (Fig. 5.10) is similar to that in the Mars meteorite ALH84001 reported by Stirling et al. (2001). The emission peaks of the REE are relatively broad and do not show the typical fine structure. This is probably due to the extreme high concentrations of the REE, which were analyzed in the range between 1.34 and 2.41 wt% for the light REE Ce, Sm and Nd. Additionally, high concentrations of Th (0.97 wt.-%) were detected.

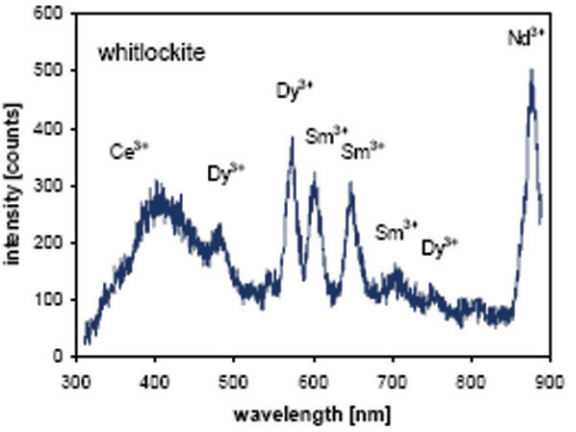

Fig. 5.10 CL emission spectrum of whitlockite from Luna 16 (compare Fig. 5.2); the CL emission is dominated by strong peaks of the REE ions

5.3.6 Other Minerals and Glass

Many of the lunar samples from Apollo and Luna missions contain glass of different types. The material includes glass bound fragments and lithic clasts showing different degree of vitrification, as well as spheres and shards of diverse composition. Because of the general high iron content, most of the glass fragments are non-luminescent. However, bright blue, dark blue and reddish luminescent glasses were detected, which mostly show silica or feldspar composition (Sippel 1971). It can be assumed that these glass particles originate from the vitrification of mineral components due to impact events.

Steel (1989) published a list of minerals from different types of meteorites showing visible CL. Although certain of these minerals haven't been detected in lunar

samples up to now, it can not be excluded that these minerals exist on the moon. Therefore, low iron-bearing or iron free end members of the pyroxene or garnet group, of olivine (forsterite) or spinel could be potential minerals with usable luminescence properties.

5.4 Conclusions

The present compilation clearly shows that luminescence studies on lunar minerals and rocks can provide a wealth of detailed information. Several of the main minerals occurring on the moon show visible CL, which can be used for a rapid recognition and differentiation of the various (especially small) constituents. Moreover, luminescence studies provide important information concerning micro-textures, internal structures, growth zoning or intergrowth not observable with other analytical methods. Spectral CL measurements additionally can be used to obtain data about variations in composition and defect structure of the crystals. The most effective way is to combine CL microscopy and spectroscopy with other advanced analytical methods with high spatial resolution.

The CL studies on specific minerals and mineral groups brought a lot of information about the geological history of the moon and the physico-chemical conditions of mineral formation. For instance, CL studies provided no indications concerning hydrothermal or aqueous mineralization or alteration. Therefore, the process of rock formation on the moon is interpreted as crystallization by simple freezing of melts with basaltic composition. Other studies have been focused on the question of the oxidation state of transition elements in lunar samples. It was assumed that iron, the most abundant transition element in lunar rocks and soil (regolith), occurs predominantly as Fe^{2+}. The spectral CL measurements on lunar plagioclases and alkali feldspars clearly confirmed that at least some of the iron is present as Fe^{3+}. Additionally, effects such as peak shift, depressed CL intensities and/or the formation of new luminescence defects can be interpreted as a result of shock damage on the lunar surface due to the meteoric bombardment.

The comparison of luminescence properties of lunar, terrestrial and synthetic minerals contributed to a deeper understanding of processes of rock formation and factors influencing the chemical composition and real structure of specific minerals. In some cases, the luminescent minerals on the moon show similar CL behaviour compared to terrestrial ones, but specific features or differences of the luminescence of certain minerals (e.g. feldspars, silica minerals, whitlockite) can significantly contribute to the development of extraterrestrial mineralogy.

Acknowledgements The mineralogical collection of the TU Bergakademie Freiberg kindly provided samples from the Luna 16, 20 and 24 space missions and D. Dettmar (Bochum) is thanked for the careful sample preparation. Ulf Kempe (Freiberg) is gratefully acknowledged for the help with SEM analyses.

References

Akridge DG, Akridge JMC, Batchelor JD, Benoit PH, Brewer J, DeHart JM, Keck BD, Lu J, Meier A, Penrose M, Schneider DM, Sears DWG, Symes SJK, Zhang Y (2004) Photomosaics of cathodoluminescence of 60 sections of meteorites and lunar samples. J Geophys Res 109:07S03

Aoudjehane C and Jambon A (2007) Determination of silica polymorphs in eucrites by cathodoluminescence. Lunar Planet Sci Conf XXXVIII, Abstracts, p 1714

Benstock EJ, Buseck P, Steele IM (1997) Cathodoluminescence of meteoritic and synthetic forsterite at 296 and 77 K using TEM. Amer Mineral 82:310–315

Blanc P, Baumer A, Cesbron F, Ohnenstetter D, Panczer G, Remond G (2000) Systematic cathodoluminescence spectral analysis of synthetic doped minerals: anhydrite, apatite, calcite, fluorite, scheelite and zircon. In: Pagel, M, Barbin, V, Blanc, P, Ohnenstetter, D (eds) Cathodoluminescence in geosciences Springer Verlag, Berlin, Heidelberg, New York, pp 127–160

Braddy D, Hutcheon ID, Price PB (1975) Crystal chemistry of Pu and U and concordant fission track ages of lunar zircons and whitlockites. Proc Lunar Sci Conf 6:3587–3600

Burns RG, Vaughan DJ, Abu-Eid RM, Witner M (1973) Spectral evidence for Cr^{3+}, Ti^{3+}, and Fe^{2+} rather than Cr^{2+} and Fe^{3+} in lunar ferromagnesian silicates. Proc Fourth Lunar Sci Conf, Geochim Cosmochim Acta, Suppl 4:983–994

Cameron AGW (1996) The origin of the Moon and the single impact hypothesis. Icarus 126:126–137

Cesbron F, Blanc P, Ohnenstetter D, Remond G (1995) Cathodoluminescence of rare earth doped zircons I Their possible use as reference materials. Scanning Microsc (Supplement) 9:35–56

DeHart JM and Lofgren GE (1993) Cathodoluminescence properties of components in enstatite chondrites. Lunar Planet Sci Conf XXIV, Abstract, 387–388

Delano JW (1986) Pristine lunar glasses: criteria, data, and implications. Proc Lunar Planet Sci Conf 16:D201–213

Delano JW, Lindsley DH, Rudowski R (1981) Glasses of impact origin from Apollo 11, 12, 15, and 16: evidence for fractional vaporization and mare/highland mixing. Proc Lunar Planet Sci Conf 12B:339–370

Dowty E (1977) Phosphate in Angra DOS REIS: structure and composition of the $Ca_3(PO_4)_3$ minerals. Earth Planet Sci Letters 35:347–351

Forester DW (1973) Mössbauer search for ferric oxide phases in lunar materials and simulated lunar materials. Proc Fourth Lunar Sci Conf, Geochim Cosmochim Acta, Suppl 4:2697–2707

Gaft M, Reisfeld R, Panczer G (2005) Luminescence spectroscopy of minerals and materials. Springer-Verlag, Berlin Heidelberg, 356 p

Gay P, Bancroft GM, Bown MG (1970) Diffraction and Mössbauer studies of minerals from lunar soils and rocks. Proc Apollo 11 Lunar Sci Conf1:351–362

Geake JE, Dollfus A, Garlick GFJ, Lamb W, Walker G, Steigmann GA, Titulaer C (1970) Luminescence, electron paramagnetic resonance and optical properties of lunar material from Apollo 11. Proceedings Apollo 11 Lunar Sci Conf 3:2127–2147

Geake JE, Walker G, Mills AA, Garlick GFJ (1971) Luminescence of Apollo lunar samples. Proc Second Lunar Sci Conf 3:2265–2275

Geake JE, Walker G, Telfer DJ, Mills AA, Garlick GFJ (1972) Luminescence of lunar, terrestrial, and synthesited plagioclase, caused by Mn^{2+} and Fe^{3+}. Proc Fourth Lunar Sci Conf 3:3181–3189

Götze J, Kempe U (2008) A comparison of optical microscope (OM) and scanning electron microscope (SEM) based cathodoluminescence (CL) imaging and spectroscopy applied to geosciences. Miner Mag (submitted)

Götze J, Habermann D, Kempe U, Neuser RD, Richter DK (1999a) Cathodoluminescence microscopy and spectroscopy of plagioclases from lunar soil (Luna20, Luna 24). Amer Mineral 84:1027–1032

Götze J, Habermann D, Neuser RD, Richter DK (1999b) High-resolution spectrometric analysis of REE-activated cathodoluminescence (CL) in feldspar minerals. Chem Geol 153:81–91

Götze J, Krbetschek MR, Habermann D, Wolf D (2000) High-resolution cathodoluminescence of feldspar minerals. In: Pagel M, Barbin V, Blanc Ph, Ohnenstetter D (eds): Cathodoluminescence in geosciences Springer Verlag, Berlin Heidelberg New York Tokyo, pp. 245–270

Götze J, Plötze M, Habermann D (2001) Cathodoluminescence (CL) of quartz: origin, spectral characteristics and practical applications. Mineral Petrol 71:225–250

Griffin WL, Åmli R, Heier KS (1972) Whitlockite and apatite from lunar rock 14310 and from Ödegården, Norway. Earth Planet Sci Letters 15:53–58

Gucsik A, Koeberl C, Brandstätter F, Reimold WU, Libowitzky E (2002) Cathodoluminescence, electron microscopy, and Raman spectroscopy of experimentally shock-metamorphosed zircon. Earth Planet Sci Lett 202:495–509

Gucsik A, Nishido H, Ninagawa K, Toyoda S, Bidló A, Brezsnyánsky K, Tsuchiyama A (2005) Cathodoluminescence spectral studies of the experimentally shock-deformed plagioclase: A possible explanation of CL peak shifts. Lunar Planet Sci Conf XXXVI, Abstract 1239

Gucsik A, Nishido H, Ninagawa K, Okumura T, Wilcox JZ, Urguiles E, Götze J, Bérczi Sz, Kereszturi A, Hargitai H, Polgári M, Nagy Sz (2006a) Cathodoluminescence and its application in the planetary sciences: A review. Annual Lunar Planet Sci Conf XXXVII, Abstract 1543

Gucsik A, Bérczi Sz, Kereszturi A, Hargitai H, Nagy Sz (2006b) Shock metamorphism of zircon in nature and experiment: a review. Lunar Planet Sci Conf XXXVII, Abstract 1544

Habermann D, Götze J, Neuser R, Richter DK (1997) The phenomenon of intrinsic cathodoluminescence: Case studies of quartz, calcite and apatite. Zentralblatt für Geologie und Paläontologie Teil 1, Heft 10–12:1275–1284

Hutcheon ID and Price PB (1972) Plutonium-244 fission tracks: Evidence in a lunar rock 395 billion years old. Science 176/4037:909–911

Hutcheon ID, MacDougall D, Stevenson J (1974) Apollo 17 particle track studies: Surface residence times and fission track ages for orange glass and large boulders. Proc 5th lunar Conf In: Geochim Cosmochim Acta suppl 5, 3:2597–2608

James O (1972) Lunar anorthosite 15415: texture, mineralogy, and metamorphic history. Science 175:432–436

Jollife BL (1993) A monazite-bearing clast in Apollo 17 melt breccia 24th. Lunar Planet Sci Conf Part 2, G-Mp:725–726

Kaus A, Bischoff A (2000) Cathodoluminescence properties of shocked plagioclase. Meteoritics and Planet Sci 35:A86

Kempe U and Götze J (2002) Cathodoluminescence (CL) behaviour and crystal chemistry of apatite from rare-metal deposits. Mineral Mag 66:135–156

Kempe U, Gruner T, Nasdala L, Wolf D (2000) Relevance of cathodoluminescence fort he interpretation of U-Pb zircon ages, with an example of an application to a study of zircons from the Saxonian Granulite Complex, Germany. In: Pagel, M, Barbin, V, Blanc, P, Ohnenstetter, D (eds) (2000) Cathodoluminescence in geosciences Springer Verlag, Berlin Heidelberg New York, pp. 425–456

Kirsh Y, Shoval S, Townsend PD (1987) Kinetics and emission spectra of thermoluminescence in the feldspars albite and microcline. Phys Stat Sol (a) 101:253–262

Kleinmann B (1969) The breakdown of zircon observed in the Libyan desert glass as evidence of its impact origin. Earth Planet Sci Lett 5:497–501

Krbetschek MR, Götze J, Irmer G, Rieser U, Trautmann T (2002) The red luminescence emission of feldspar and its wavelength dependence on K, Na, Ca - composition. Mineralogy and Petrology 76:167–177

Kusaba Y, Syono Y, Kikuchi M, Fukuoka K (1985) Shock behaviour of zircon: phase transition to scheelite structure and decomposition. Earth Planet Sci Lett 72:433–439

Marfunin AS (1979) Spectroscopy, luminescence and radiation centres in minerals. Springer-Verlag, Berlin, 352 p

Marfunin AS, Bershov LV (1970) Electron-hole centers in feldspars and their possible crystal-chemical and petrological significance (in Russ). Dokl AkadNauk 193:412–414

Marshall DJ (1988) Cathodoluminescence of geological materials. Unwin-Hyman, Boston, 146 p

Matyash IV, Bagmut NN, Litovchenko AS, Proshko VYa (1982) Electron paramagnetic resonance study of new paramagnetic centers in microcline-pethites from pegmatites. Phys Chem Miner 8:149–152

Mitchell RH, Xiong J, Mariano AN, Fleet ME (1997) Rare-earth-element-activated cathodoluminescence in apatite. Canadian Mineral 35:979–998

Mora CI, Ramseyer K (1992) Cathodoluminescence of coexisting plagioclases, Boehls Butte anorthosite: CL activators and fluid flow paths. Amer Miner 77:1258–1265

Nasdala L, Zhang M, Kempe U, Panzer G, Gaft M, Andrut M, Plötze M (2003) Spectroscopic methods applied to zircon. Rev Mineral Geochem 53/1:427–467

Petrov I, Yude F, Bershov LV, Hafner SS, Kroll H (1989) Order-disorder of Fe^{3+} ions over the tetrahedral positions in albite. Amer Mineral 74:604–609

Petrov I, Mineeva RM, Bershov LV, Agel A (1993) EPR of $[Pb\text{-}Pb]^{3+}$ mixed valence pairs in amazonite type microcline. Amer Mineral 78:500–510

Pidgeon RT, Nemchin AA, Van Broswijk W, Geisler T, Meyer C, Compston W, Williams IS (2007) Complex history of a zircon aggregate from lunar breccia 73235. Geochim Cosmochim Acta 71:1370–1381

Remond G, Cesbron F, Chapoulie R, Ohnenstetter D, Roques-Carmes C, Schvoerer M (1992) Cathodoluminescence applied to the microcharacterization of mineral materials: A present status in experimentation and interpretation. Scann Micr 6:23–68

Roedder E, Weiblein PW (1970) Lunar petrology of silicate melt inclusions, Apollo 11 rocks Proc Apollo 11. Lunar Sci Conf 1:801–837

Shearer CK, Papike JJ (1993) Basaltic magmatism on the Moon: a perspective from volcanic picritic glass beds. Geochim Cosmochim Acta 57:4785–4812

Shearer CK, Papike JJ (1999) Magma evolution of the Moon. Amer Mineral 84:1469–1494

Siegel GH, Marrone MJ (1981) Photoluminescence in as-drawn and irradiated silica optical fibers: An assessment of the role of nonbridging oxygen defect centres. J Non-Cryst Solids 45:235–247

Sippel RF (1965) Simple device for luminescence petrography. Rev Scient Instr 36:556–558

Sippel RF (1971) Luminescence petrography of the Apollo 12 rocks and comperative features in terrestrial rocks and meteorites. Proc Second Lunar Sci Conf 1:247–263

Sippel RF, Spencer AB (1970a) Luminescence petrography and properties of lunar crystalline rocks and breccias. Proc Apollo 11 Lunar Sci Conf 3:2413–2426

Sippel RF, Spencer AB (1970b) Cathodoluminescence properties of lunar rocks. Science 167/3918:677–679

Skuja L (1998) Optically active oxygen-deficiency-related centers in amorphous silicon dioxide. J Non-Crystall Solids 239:16–48

Smith JV (1974) Lunar Mineralogy: A heavenly detective story Presidential Address, Part I. Amer Mineral 59:231–243

Smith JV, Stenstrom RC (1965): Electron-excited luminescence as a petrological tool. J Geol 73:627–635

Smith JV, Steel IM (1976) Lunar Mineralogy: A heavenly detective story, Part II. Amer Mineral 61:1059–1116

Speit B, Lehmann G (1976) Hole centers in the feldspar sanidine. Phys stat solidi A36:471–481

Steel IM (1986) Cathodoluminescence and minor elements in forsterites from extraterrestrial samples. Amer Mineral 71:966–970

Steel IM (1989) Cathodoluminescence mineralogy of meteorites. Lunar Planet Sci Conf XX, Abstracts, 1052–1053

Steel IM and Smith JV (1972) Ultrabasic lunar samples. Nat Phys Sci 240:5–6

Steel IM, Smith JV, Skirius C (1985) Cathodoluminescence zoning and minor elements in forsterites from the Murchison (C2) and Allende (C3V) carbonaceous chondrites. Nature 313:294–297

Stevens Kalceff MA and Phillips MR (1995) Cathodoluminescence microcharacterization of the defect structure of quartz. Phys Rev B 52:3122–3134

Stirling JAR (2000) Preliminary results of cathodoluminescence spectral analysis of ß-Ca-phosphates (”whitlockite”) in the Mars meteorite ALH84001. Lunar Planet Sci XXXI, Abstract 2021

Stirling JAR, Venance K, Protheroe WJ Jr (2001) Cathodoluminescence analysis of Nakhla 1401 chloroapatites. Lunar Planet Sci XXXII, Abstract 1638

Strunz H, Tennyson C (1982) Mineralogische Tabellen. Akad Verlagsgesellschaft Geest & Portig, Leipzig, 621 p

Taylor DJ, McKeegan KD, Harrison TM, McCulloch M (2007) ^{176}Lu-^{176}Hf in lunar zircons: Identification of an early enriched reservoir on the Moon. Lunar Planet Sci Conf XXXVIII, Abstracts, 2130–2131

Taylor SR (1982) Planetary Science: A Lunar perspective. Lunar and Planetary Institute, Houston, Texas

Telfer DJ, Walker G (1975) Optical detection of Fe^{3+} in lunar plagioclase. Nature 258:694–695

Telfer DJ, Walker G (1978) Ligand field bands of Mn^{2+} and Fe^{3+} luminescence centres and their site occupancy in plagioclase feldspars. Mod Geol 6:199–210

Vinogradov AP (1972) Preliminary data on lunar ground returned by automatic station Luna-20 (in Russian). Geokhimia 7:763–774

Walker G (1985) Mineralogical applications of luminescence techniques In: Berry FJ and Vaughan DJ (eds): Chemical bonding and spectroscopy in mineral chemistry. University of Birmingham, pp. 103–140

Warren PH (1990) Lunar anorthosites and the magma-ocean plagioclase-floating hypothesis. Amer Mineral 75:46–58

Warren PH (1994) Lunar and martian meteorite delivery services. Icarus 111:338–363

White WB, Masako M, Linnehan DG, Furukawa T, Chandrasekhar BK (1986) Absorption and luminescence of Fe^{3+} in single-crystal orthoclase. Amer Mineral 71:1415–1419

Wopenka B, Jollife BL, Zinner E, Kremser DT (1996) Trace element zoning and incipient metamictization in a lunar zircon: Application of three microprobe techniques. Amer Mineral 81:902–912

Zeigler RA, Korotev RL, Jollif BL, Haskin LA, Flos C (2006) The geochemistry and provenance of Apollo 16 mafic glasses. Geochim Cosmochim Acta 70:6050–6067

Chapter 6
Cathodoluminescence Instrumentation for Analysis of Martian Sediments

Roger Thomas, Vincent Barbin, Claire Ramboz, Laurent Thirkell, Paul Gille, Richard Leveille and Karl Ramseyer

6.1 Introduction

The morphologic study of the surface of Mars reveals that liquid water existed during the first few hundred millions of years of the planet's history (e.g. Smith et al. 1999). The flow of water produced extensive erosion in some place, but also large sedimentary basins. With a long enough duration of the presence of liquid water and the oxidation of basalts, the emergence of biological activity may have eventually occurred, as on Earth. The detection of biomarkers at the surface of Mars is one of the main challenges of current and planned planetary exploration missions (e.g. Westall et al. 2000).

Looking for a fossil or present biological activity may be approached by the search for cells, but also by the study of the results of their activity and their interface with the sedimentary environment. Such bio-sedimentations are known among the oldest terrestrial fossils and testify to the earliest terrestrial bioactivity. A discovery of such bio-sedimentations on the Martian surface would be of prime interest for addressing some of the key goals in exobiology.

Cathodoluminescence (CL) is a method relevant to the search for life, as it is in line with these analytical goals of detecting bio-sedimentations (Barbin et al. 1999), and it fits well with robotic facilities usable in modern space missions (Blanc et al. 1999, Thomas et al. 2002. 2005). An established technique, cathodoluminescence is a newcomer to Martian exploration, whereit is expected to contribute to the mineralogical characterisation of sedimentary rocks, to the search for biomarkers revealing past biological activity, and to identify past geochemical conditions (Melezhik et al. 1999; Denson et al. 2007). CL is one of the best methods when the growth dynamics, microstructure, and origin of minerals need to be determined, such as with Martian sediments.

CL has become an important standard technique for studying geological materials, offering a wide spectrum of applications (Marshall 1988; Barker and Kopp 1991; Barbin and Schvoerer 1997; Pagel et al. 2000). However, it is in the field of sedimentology and petrography that CL has proved to be especially valuable. The

Vincent Barbin (✉)
GEGENAA, EA 3795, Université de Reims Champagne-Ardenne, France
e-mail: vincent.barbin@univ-reims.fr

A. Gucsik (ed.), *Cathodoluminescence and its Application in the Planetary Sciences*,

capabilities of CL are very interesting for Martian exploration since no present results provide evidence for the presence of carbonates or biomarkers, while these questions remain of prime importance for elucidating the history of Mars.

Nevertheless it is imperious to design a new concept of CL instrumentation to avoid the critical difficulty imposed by the Martian atmosphere. The introduction of a surface sample into a vacuum chamber with a pressure compatible with the use of a standard electron gun is mechanically too difficult and would result in an instrument much too heavy for a practical planetary mission. The application of CL as an exploration tool for the Martian environment requires some specific adaptations. On the one hand, electrons can only be produced under vacuum. On the other hand, because the range of 20–25 keV electrons in air is only $\approx 450\mu m$ (Gledhill 1973), which is much smaller than the working distance of a binocular or objectives, CL on Earth is performed with both the electron gun and the sample being placed under vacuum. On Mars by contrast, the range of 20–25 keV electrons is expected to be around a few cm, due to the atmospheric CO_2 pressure of $\approx$ 6mbar (Gledhill 1973). In such conditions, the concept of an "electron lamp" can be developed, where the sample is kept at atmospheric pressure and the electron source is located in a separate volume closed by an electron-transparent window maintained in good vacuum condition by a chemical getter. In such a configuration, the sample would be irradiated by electrons while it would stay in the rather high Martian atmospheric pressure. Such a concept is currently under development by the authors.

The topic of this chapter is to show preliminary results concerning the design of a CL instrument in compliance with the requirements of an in-situ Martian experiment and with the scientific goals of exobiology.

6.2 Scientific Goals

So far, our knowledge of the mineralogy of the rocks and soils of Mars relies firstly upon direct measurements by spacecrafts that have orbited (Mariner 9, the Viking Orbiters, Phobos 2, Mars Global Surveyor, Mars Odyssey, Mars Express, Mars Reconnaissance Orbiter) and landed on Mars (Viking Landers 1 and 2, Mars Pathfinder and Mars Exploration Rovers), and secondly from the detailed mineralogical and geochemical studies of SNC meteorites (e.g. McSween 1994), and complemented by geochemical modelling (Chevrier and Mathé 2007). The most abundant minerals on Mars are silicates. Primary igneous silicates in Martian basalts or andesitic basalts are olivine, pyroxene and plagioclase. Only iron-poor olivine is expected to display cathodoluminescence (e.g., Steele et al. 1985), but pyroxenes (both clinopyroxene and orthopyroxene) and plagioclases emit commonly CL due to Ca-REE substitutions (e.g., Marshall 1988; Ramseyer and Mullis 2000).

It is worth mentioning at this point that CL is indeed observed in SNC meteorite ALH 84001 from the glass, maskelynite and clinopyroxene. Also note that, besides providing information on the soil mineralogy, CL can reveal important features of the crystal fine structure, such as zoning reflecting changes in growth conditions, or

shock effects (e.g. Owen and Anders 1988; Gucsik et al. 2006). Finally, advanced magmatic differentiation processes can account for the presence of CL emitting silica-rich quartzo-feldspathic minerals on the Mars surface (Bandfield et al. 2004).

Phyllosilicates, present in SNC meteorites and expected to form by hydrous alteration of basalts, have been mapped in Noachian terranes of Mars by the OMEGA infrared spectrometer on Mars Express (Poulet et al. 2005). Recorded IR spectra point out to smectites with a wide range of Fe-Mg-Al compositions. Of these, the Fe-poor end members (Mg- and Al-rich) could be good candidates for CL emission.

The Mars Pathfinder mission uncovered clues, in the form of pebbles and conglomerates, for probable sedimentary processes occurring in the past and attesting to warmer and wetter early climatic conditions (Smith et al. 1997). More recently, the Mars Exploration Rovers have identified sedimentary minerals (e.g., sulfates, iron oxides, silica) most likely deposited by liquid water. These findings are in accordance with ample, planetary-scale, geomorphological evidence also suggesting the past presence of liquid water. It is generally recognized that conditions for the origin and evolution of life existed on Mars at the same time it appeared on Earth (e.g., Westall et al. 2000). The record on Mars of such biochemical activity, if any, are to be found in the deposits of old (> 3Ga) aqueous sedimentary basins or groundwater springs and hydrothermal systems associated with volcanoes or impact craters. However, detection of past hydrothermal activity requires detection of as yet unobserved hydrothermal minerals. CL microscopy as a tool for identifying hydrothermal alteration (such as albitization or myrmekitization; Ramseyer et al. 1992; Garcia et al. 1996) could be of substantial help in this regard. More generally, it is precisely in the study of Martian sedimentary deposits that CL microscopy will prove to be especially effective, revealing for instance zonations in diagenetic carbonates in relation with changes in pH/Eh (among other factors), precipitation rate, salinity and temperature. Last but not least, CL microscopy has a considerable potential in highlighting fossil biogenic structures, either carbonated, siliceous or phosphatic, formed by living organisms, even at the microscopic or sub-microscopic level (Barbin 2000).

6.3 Potential of CL for In-Situ Study of Martian Surface Samples

We shall now review what is currently achieved with CL microscopy and spectroscopy and see how and with what confidence it can be applied to such issues as Mars mineralogy, geology and exobiology.

i) CL is widely used to determine paragenetic sequences, to unravel the chemical conditions during growth and dissolution of cements (e.g. calcite, quartz), to visualize relict structures overprinted by recrystallization and quantify single phases of cements. CL zonations in magmatic minerals, like feldspars, zircons or apatite may provide important insights in the genetic history of the magmatic body (e.g. Ginibre et al. 2004). CL depends upon the feldspar composition (itself related to the rock composition). For example, the Mn^{2+} activated CL in calcitic plagioclase (An_{87} to An_{97}) is yellow, while intermediate plagioclases exhibit a

greenish luminescence. We also know that the red emission is sensitive to the anorthite content as the emission peak shifts from 687 to 744 nm for changes in composition from An_{94} to An_{38} (e.g., Barbin 1997).

ii) CL is a property of the ordered solid. The crystalline state optimises the probability of observable radiative transitions while the vitreous state decreases this probability. In fact, CL emission of glass is correlated to the degree of devitrification, or cristallinity. Both glass and microlthes may present luminescence bands but only micro-crystallites yield CL lines characterstic of elements under strong crystal field (Panzer et al. 2003). Along the same lines, it should be noted that CL is a powerful tool for distinguishing between brittle and ductile deformed minerals and rocks as well as for determining the relationship between different generations of fractures. Microfractures can be detected using CL while unobservable by other methods (e.g., in volcanic quartz; Boggs and Krinsley 2006), thus enabling microtectonic studies and determination of detritical quartz provenance. CL is a key method for the study of shocked minerals and impact structures.

iii) CL spectroscopy can detect elements at the trace concentration level. A detection level of 2 ppm for REE's in anhydrite, for instance, permits the differentiation between different possible origins for this mineral (Baumer et al. 1997) CL spectroscopy also helps in determining trace element distributions in poly-activated minerals and the Eh conditions of the mineralizing fluid.

iv) CL may be an effective tool to enlighten hydrothermal processes in a basaltic environment. Basalt-derived fluids are particularly enriched in REE (Michard 1989), which can occasionally precipitate in micro-assemblages of strongly luminescent minerals: apatite, monazite, xenotime, zircon (e.g. Schärer et al. 1999). CL enhances these accessory minerals (Poitrasson et al. 2002) which are easily unnoticed by microscopic observation with a resolution of around 10 μm.

v) *CL can help to distinguish biogenic minerals from non-biogenically formed ones.* This is highlighted below.

Most frequently, CL is used to decipher biological rhythms or uncommon events in carbonate shell material (Barbin 2000; Barbin et al. 2008). It has been shown, for instance, that the micritic calcium carbonate microstructure of well-preserved stromatoporoids shows up perfectly under CL microscopy and that CL can help in the identification of poorly preserved stromatoporoids by means of the contrast existing between infilled sediment and skeleton (Kershaw 1994). In a more general way, biogenic carbonates show smooth CL emission patterns as opposed to the sharp geometrical ones exhibited by their abiogenic counterparts. Smooth patterns reflect biologically controlled growth, whereas sharp ones indicate crystallographically controlled growth. This difference is an easy and efficient mean to answer the question of the origin of a carbonate. We expect similar results for non-carbonated biomineralizations (biogenic siliceous deposits on Mars have been envisioned).

6.4 Experiment Objectives

In order to design a CL apparatus for exploring the environment of Mars, one has to face the problem that electrons must be produced under vacuum, whatever the chosen production technique is, which is incompatible with the atmospheric pressure of 6–8 mbar CO_2. On Mars, the introduction of the sample to be studied into a vacuum chamber connected to a pump cannot be envisaged, because such a system would be mechanically too complex and would not fit with the weight and energy constraints of space instrumentation. An alternative concept is an 'electron lamp', where the sample and the electron source are separated by a membrane which is both electron-transparent and impervious to atmospheric CO_2.

This experimental work is aimed at validating the 'electron lamp' concept. It is limited to describing the consequences of adding a membrane in-between the electron source and the sample, and of varying the pressure gradient on both parts of the membrane, on the quality of the electron beam (size, intensity, energy), on the quality of CL images and of CL spectra, including the possible detection of a spectral signal originating from the atmosphere. A key point is choosing which of two membranes (polycarbonates or Si_3N_4) displays the maximum resistance to a pressure difference of a few bars, and induces a minimum diffusion effect on the electrons with minimum decrease of the beam intensity and energy.

6.4.1 Experimental Setup

The experimental apparatus is composed of 4 parts: (1) a cold cathode source; (2) a mechanical part, mainly the sample carrier; (3) the membrane mount that separates the parts 1 and 2; (4) the optical device composed of a microscope, a camera, and a UV-VIS spectrometer.

6.4.1.1 Electron Source

A cold cathode source electron gun (discharge following the Paschen law) provided by OPEA (France) has been chosen for its simplicity and its ability to produce a stable electron beam (intensity-current fluctuations $<1\%$). The characteristic current-tension relationship of our electron beam, at an Ar pressure of 40×10^{-3}mbar, is shown in Fig. 6.1. Note however that the flux of electrons activating CL emission on the sample represents less than 10% of the discharge current.

6.4.1.2 Mechanical Mount

The mount consists of an aluminium chamber connected to a turbomolecular pump. Three angles of incidence are possible: $30°, 45°, 60°$.

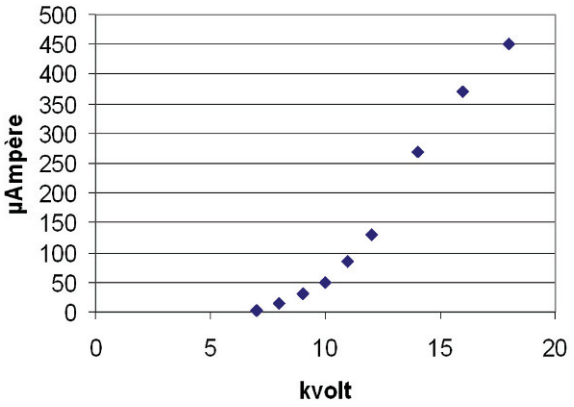

Fig. 6.1 Tension-current relationship of an OPEA cathodyne cold cathode instrument at an Ar pressure of 40×10^{-3}mbar

– it includes the membrane carrier, which acts as an interface between the electron gun and the sample carrier
– it allows microscopic observation of CL
– its large volume allows observation of both standard petrographic thin-sections and pluricentimetric raw rock samples
– it allows pressurization of the sample chamber, so as to observe CL at a CO_2 static pressure of several tens of bar.

6.4.1.3 The Membranes and its Mount

This is the critical part under study. The membrane carrier fixes the membrane along the beam path, It must be impervious in a pressure gradient of a few tens of mbar. It must exert minimal mechanical constraints on the membrane and must allow its easy replacement. The nature of the membrane, namely its density and constitutive atoms (the lighter, the best) controls the interaction with electrons. Two types of membranes have been tested:

– *Commercial polycarbonate membranes* in use for electron microscopy. They are very easy to mount and un-mount. The one we tested consists of a 100 nm-thick film deposited on a 300 µm-mesh Ni grid, to reinforce its resistance to pressure. It is pressed against a rubber o-ring gasket that allows a differential pressure gradient of 1 bar to be sustained.
– $30-100\,nm-thick\,Si_3N_4\,windows$. They are made of 250 µm-thick, 5 mm-wide, silicon nitride square films that have been thinned to the desired thickness on a 1.5 mm-wide square area at their center. The membrane is pressed on a rubber o-ring via a steel spring in order to ensure airtightness.

The membrane-to-sample distance is currently of 50 mm, comparable to that of most commercial cold CL devices.

6.4.1.4 The Optical Device

It consists of an Olympus SZ 60 stereozoom with a 6 x zoom lens. It is equipped with a JVC KY-F75U tri-CCD digital camera. The 3 sensors, 12 mm in size, have a resolution of 1360 $\times$ 1024 pixels ($1,4\ 10^6$ pixels, pixel size 7μm) The characteristic features of images acquired with the stereozoom and the camera are given in Table 6.1. A Zeiss MM1 spectrometer using a fiber optic coupling is either mechanically mounted on the sample chamber or attached on the stereozoom ocular. It operates in the 0.3-1 mm range with a 3.3 nm spectral resolution.

Table 6.1 Characteristic features of images acquired with our optical setup a JVC KYF75U tri-CCD digital camera and with an Olympus SZ60 stereozoom

Magnification	X 1	X 6
Size of the imaged field ($mm^2 \times mm$)	10×7	1.6×1
Pixel size in the object plane (μm)	7	1.2

6.5 Results

6.5.1 Membrane Behaviour

6.5.1.1 Commercial Polycarbonate Membranes

As soon as the membrane was irradiated, its color changed and the membrane became brittle. In particular, it broke in response to any constraint relaxation due to pressure drop (Plate 6.1a). This kind of membrane therefore, of unique use, is inappropriate to our experimental objectives.

6.5.1.2 Si_3N_4 Membranes (Plate 6.1b)

Mechanical constraints are clearly the limiting-factor for the longevity of Si_3N_4 membranes, whether they arise from mounting or un-mounting the window, or result from pressure blows. Provided attention is paid to these two critical steps of the experiments (particularly one must ensure smooth pressure variations), longevity of Si_3N_4 membranes is satisfactory at the scale of laboratory experiments. It is however clearly insufficient for long duration space experiments. The steel spring ensuring airtightness has to be replaced, as it generates excessive constraints on the silicon nitride film. In the following, experiments involving Si_3N_4 membranes only will be considered.

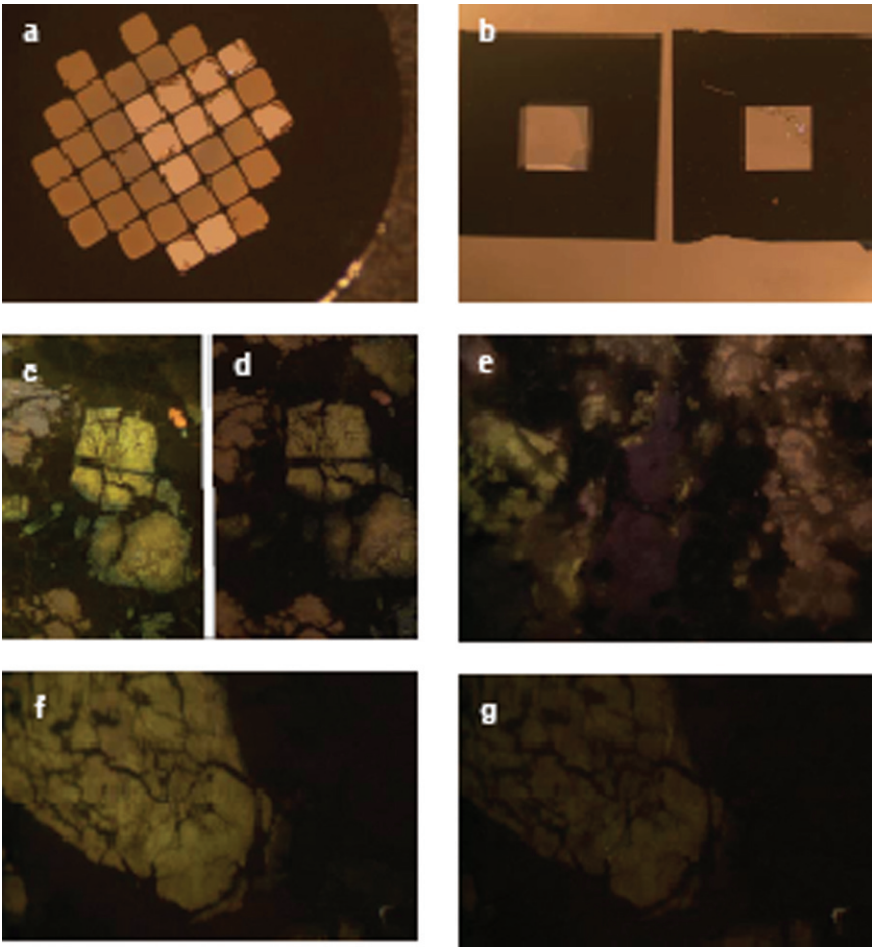

Plate 6.1 (**a**) Microphotograph of the Polycarbonate membrane window on a Ni grid after rupture. The size of an individual membrane is 400×400 µm. (**b**) Microphotograph of the Si_3N_4 membrane window after rupture. The window is 1.5 × 1.5 mm in size. (**c**) CL image of a basaltic breccia (Puy de la Vache, Chaîne des Puys, France). Beam conditions: 17 kV, 80 µA, Ar pressure $< 40 \times 10^{-3}$ mbar. Size of the imaged field: 2.5×2 mm. Exposure duration: 4s. (raw image without any treatment). (**d**) CL image of a basaltic breccia with a 50 nm-thick Si_3N_4 window placed at the electron gun exit (Puy de la Vache, Chaîne des Puys, France). Beam conditions: Ar pressure of 40×10^{-3} mbar, 17 kV, 80 µA.0CO_2 pressure in the chamber. Size of the imaged field: 2.5×2 mm. Exposure duration: 4s. (**e**) CL image of the raw (unsawn, unpolished) surface of a piece of basaltic nodule from the Puy de la Vache volcano, at a controlled, martian-like, CO_2 pressurize of 10 mbar (membrane thickness: 100 nm). Beam conditions: 17 kV, 120 µA. Size of the imaged field: $10 \times$ 8mm. Exposure duration time: 4s. (**f**) Effect of a CO_2 pressure on the CL image of a brecciated plagioclase (Puy de la Vache volcano, Chaîne des Puys, France). For both microphotographs, a 50 nm-thick Si_3N_4 window is placed at the electron gun exit and the beam path length is 50 mm. Beam path in an Ar pressure of 40 10^{-3} mbar, 0 mbar CO_2 pressure, beam conditions: 20 kV, 110 µA. Size of the imaged field: 2.5×2 mm. (**g**) Effect of a CO_2 pressure on the CL image of a brecciated plagioclase (Puy de la Vache volcano, Chaîne des Puys, France). For both microphotographs, a 50 nm-thick Si_3N_4 window is placed at the electron gun exit and the beam path length is 50 mm. Beam path in 20 mbar CO_2 pressure, beam conditions: 22 kV, 220 µA . Size of the imaged field: 2.5×2 mm. Exposure duration time: 4s

6.5.2 Electron Beam Properties

6.5.2.1 Beam Energy Loss

The energy loss due to the intercalation of the membrane on the beam path was calculated using the ESTAR program provided by the National Institute of Standards and Technology. The results, calculated for two membrane thicknesses of 50 and 100 nm, are shown in Table 6.2. The energy lost by an electron beam along a 50 mm-long path in pressurized CO_2 at 10 and 20 mbar has also been considered. The results are shown in Table 6.3.

Table 6.2 Energy lost by an electron beam passing through a 50 or 100 nm-thick Si_3N_4 membrane

CO_2 pressure (mbar)	10			20		
Beam energy (keV)	10	15	20	10	15	20
Energy loss (eV)	1920	1410	1130	3810	2790	2230
	(19)	(9.4)	(5.7)	(38)	(19)	(11)

Table 6.3 Energy lost by an electron beam along a 50 mm- path in pressurized CO_2. Numbers between are energy losses in%

Membrane thickness(nm)	50			100		
Beam energy (keV)	10	15	20	10	15	20
Energy loss (eV)	284	210	169	569	419	338
	(2.8)	(1.4)	(0.9)	(5.7)	(2.8)	(1.7)

The predictions show that, for a given beam energy, the energy loss is roughly increased by a factor 2 when the Si_3N_4 membrane thickness or the CO_2 pressure is doubled. Besides, for a given media, the beam energy loss decreases as the beam energy increases. Clearly, the energy loss through the 50 or 100 nm-thick Si_3N_4 membranes appears negligible for beam energies higher than 15 keV. Therefore, when the sample is kept under vacuum, the addition of a membrane on the electron gun does not significantly modify the conditions of CL emission. By contrast, the energy loss along a 50 mm-long path in CO_2 pressurized at 10 and 20 mbar appears critical as it ranges from 10 to 38%, depending on beam energy. Clearly, the optimization of our experimental set-up for the purpose of CL imagery on Mars will necessarily require a minimization of the membrane-to-sample distance.

6.5.2.2 Angular Diffusion of the Electron Beam

A preliminary experiment has been performed in order to evaluate the impact of a membrane or of atmospheric CO_2 on angular diffusion of the electron beam. The electron gun being inclined at 60° relative to the normal of the surface sample and

the membrane-to-sample distance being fixed at 50 mm, the spot has been visualized on strongly CL emitting powdered ZnS. Its diameter has been estimated at 3–4 mm in the sample chamber at 0 mbar CO_2 pressure. The beam size increased to >20 mm when a 20 mbar CO_2 pressure was maintained in the chamber, with all other conditions being equal. This preliminary experiment points to the fact that angular diffusion will have to be controlled in the future, either actively using an electro-magnetic device or passively within the framework of a new set up with optimized geometry constraints. A larger atmospheric pressure in the chamber or a larger incidence angle of the beam would still enhance angular diffusion.

6.5.3 CL Imagery and Spectroscopy

In order to test the effects of putting a membrane at the electron gun exit and/or a CO_2 pressure in the sample chamber on CL images, a thin section of basaltic volcanic breccia originating from the Puy de la Vache volcano (Chaîne des Puys, France) has been chosen. The thin section displays 500µm-sized pyroxenes and brecciated feldspath phenocrysts in a glassy matrix, minor olivine plus accessory minerals.

6.5.3.1 Reference CL Image and Spectrum

Plate 6.1c shows a conventional CL image of the volcanic breccia (no membrane, chamber under vacuum). In order to increase the beam energy at a constant current value, the discharge has been obtained with an Ar pressure less than the commonly used value of $\approx 40\ 10^3$ mbar (see Fig. 6.1). The discharge current obtained in these conditions is 80 µA. Optimisation of the coupling electron source- sample will be a key point to consider in the context of a space applications where the power supply has to be reduced to a minimum. Plate 6.1c illustrates the capability of CL to enhance the petrologic features of a basaltic breccia. Two types of phenocrysts, 200–500 µm-thick, are easily discriminated by their specific color: fresh feldspath luminesces in blue to beige whereas altered feldspath luminesces in yellow. Both phenocrysts are fractured and passively penetrated by the dark glassy matrix along cracks with sharp edges. Fresh feldspaths are corroded by the glass at their periphery whereas altered feldspath rims luminesce in green. A 110×60µm-wide apatite crystal shows a bright orange CL color. The contour of a 270 µm-long lath of relicts of Fe-Mg amphiboles partly replaced by Fe-Ti oxides is underlined by a green CL color. Finally, CL allows 50–100 µm-wide glass beads to be individualized in the matrix, limited by 10 µm-large brown CL rims.

A CL spectrum corresponding to the field imaged is shown in Fig. 6.2. It displays three main bands. The band centered at 550 nm originates from the Mn^{2+} activator, the band centered at 420 nm probably originates from Eu^{2+} in feldspath, the shoulder around 650-700 nm corresponds to Fe^{3+}.

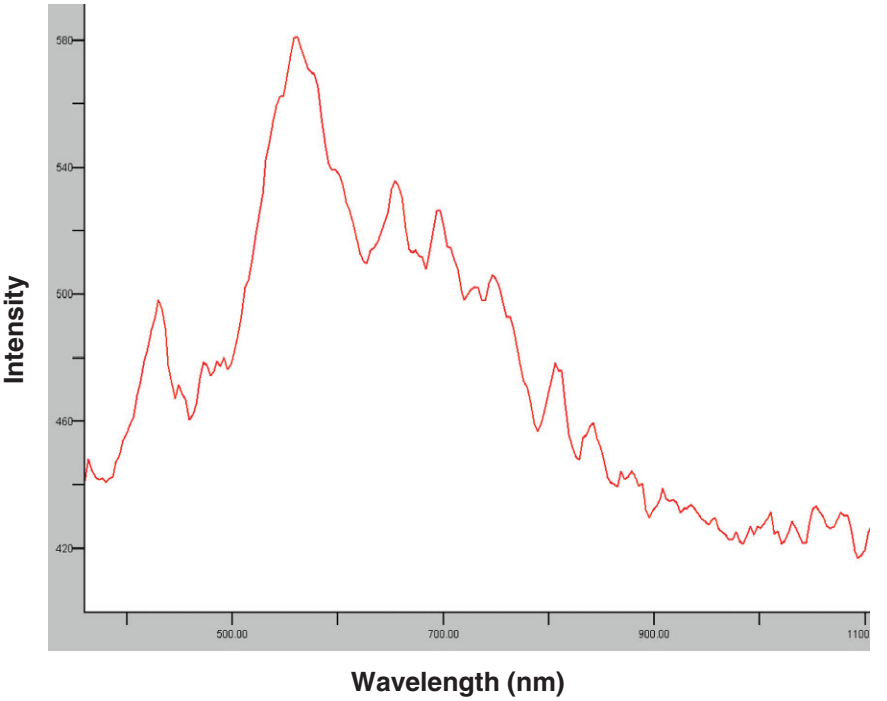

Fig. 6.2 CL spectral response corresponding to an area of $\approx 2.5 \times 2$ mm. The conditions are 17 keV, 80 µA, Ar pressure of $< 40 \times 10^{-3}$ mbar and 0 mbar CO_2 pressure as used for Image c on Plate 6.1

6.5.3.2 CL and Spectral Degradation Due to the Membrane

The decrease in luminance induced by a 50 nm-thick membrane appears obvious on Plate 6.1d. However, the two types of phenocrysts (altered and unaltered feldspaths) and their brecciated texture are still visible and the green luminescent rim around altered feldspath is observed. The bright orange-luminescent accessory mineral can also be seen. Only the phyllosilicate lath does not appear any more in the matrix and the glass beads are no more visible either. Probably, longer exposure times or more sensitive CCD could have compensated for the loss of luminance due to addition of the membrane, but this could not be tested with our present acquisition program. The spectrum obtained with the membrane contains essentially the same spectral information as the spectrum acquired without a membrane, only the emission intensity is decreased by 30%.

6.5.3.3 Unpolished Surface Sample

Plate 6.1e shows the CL image of the raw, broken (unsawn, unpolished) surface of a piece of basaltic nodule from the Puy de la Vache volcano, at a controlled,

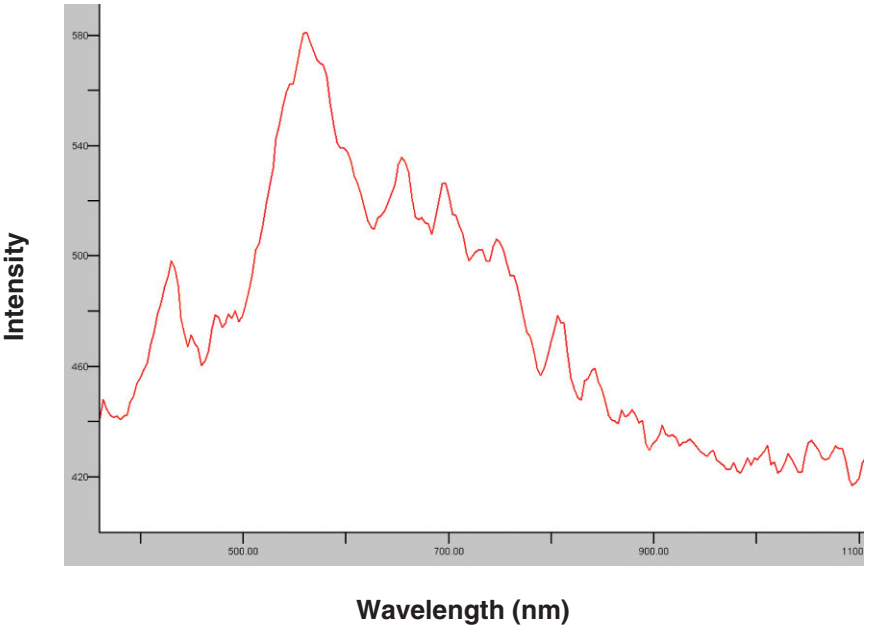

Fig. 6.3 CL spectral response corresponding to an area of $\approx 2.5 \times 2$ mm through a 50 nm-thick Si_3N_4 window. The conditions are 17 keV, 80 µA, Ar pressure of 40×10^{-3} mbar and 0 mbar CO_2 pressure as used for Image d on Plate 6.1

martian-like, CO_2 pressure of 10 mbar (membrane thickness: 100 nm). The rock sample can be only imaged at small magnification, because of the sample roughness. The field imaged in Plate 6.1e is therefore 4 times larger than the one in Plate 6.1d. This is the reason why the luminance appears to be a less critical parameter in the case of the rock sample CL image. The brecciated feldspath phenocrysts are still visible by their yellow and pink color, respectively. The dark brown CL-emitting mineral is clinopyroxene. The spatial resolution is however too low, for any further structural detail to be visible (Fig. 6.3).

6.5.3.4 CL and Spectral Degradation Due to the Membrane Plus a CO_2 Atmospheric Path

Plate 6.1f,g show two CL images of a brecciated feldspath in a basaltic nodule from Puy de la Vache volcano (Chaîne des Puys, France), both acquired with a 50 nm Si_3N_4 membrane, and with 0 and 20 mbar atmospheric CO_2 pressure, respectively. One observes that a drastic decrease in luminescence is induced by the path in pressurized CO_2. Note however that the brecciated texture of the feldspath is still visible. The energy lost by electrons along a 50 mm-long path in CO_2 pressurized at 20 mbar was shown previously to amount to ≈ 2.20 keV only (see Table 6.3). In the case of

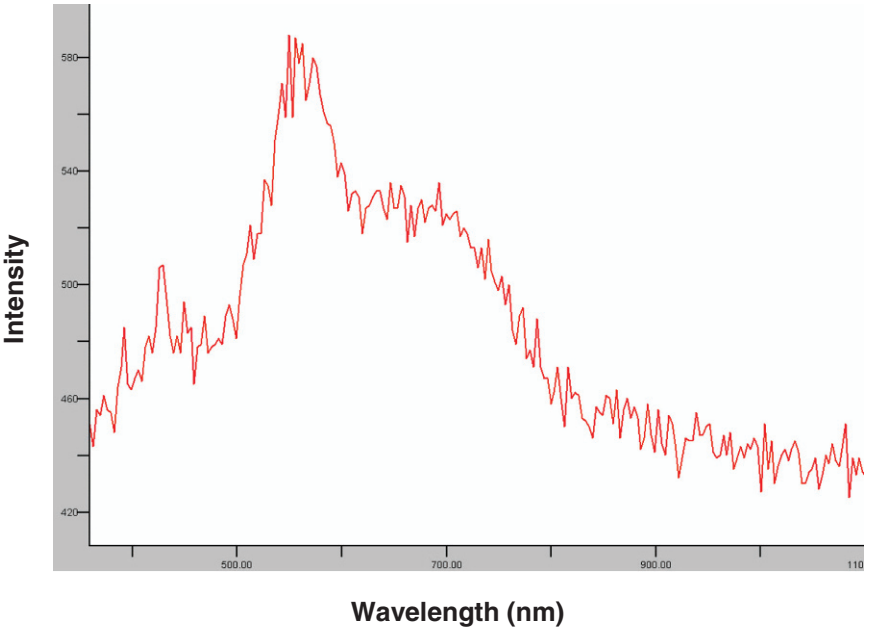

Fig. 6.4 CL spectral response corresponding to an area of $\approx 2.5 \times 2$ mm through a 50 nm-thick Si_3N_4 window at a distance of 50 mm. The conditions are 22 keV, 220 μA, and 20 mbar CO_2 pressure as used for Image f on Plate 6.1

the experiments shown in Plate 6.1f and g, the energy loss along the atmospheric CO_2 path was partly compensated by increasing the beam energy from 20 to 22 kV. This experiment reinforces the need for a minimization of the membrane-to-sample distance in a CL device designed for the Mars environment. The CL spectrum (Fig. 6.4) obtained from the field imaged on Image b, corresponding to a beam path in a 20 mbar CO_2 atmosphere, preserves the same spectral information as that obtained in a 0 mbar CO_2 atmosphere. The noise is increased as a result of the decrease in luminescence intensity. Note that the possible contribution of a CO_2 fluorescence is undetected.

6.5.3.5 Influence of Pressurized CO_2 on the Quality of CL Spectra

CL spectra of the polished surface of a synthetic YAG crystal (a REE-enriched Yttrium Aluminum garnet have been acquired at variable CO_2 pressures between 0 to 20 mbar (Fig. 6.5). Figure 6.5 shows that the spectral information remains essentially the same, whatever the CO_2 pressure. Only the noise increases with increasing CO_2 pressure, as well as does absorption (see lowered peak maxima).

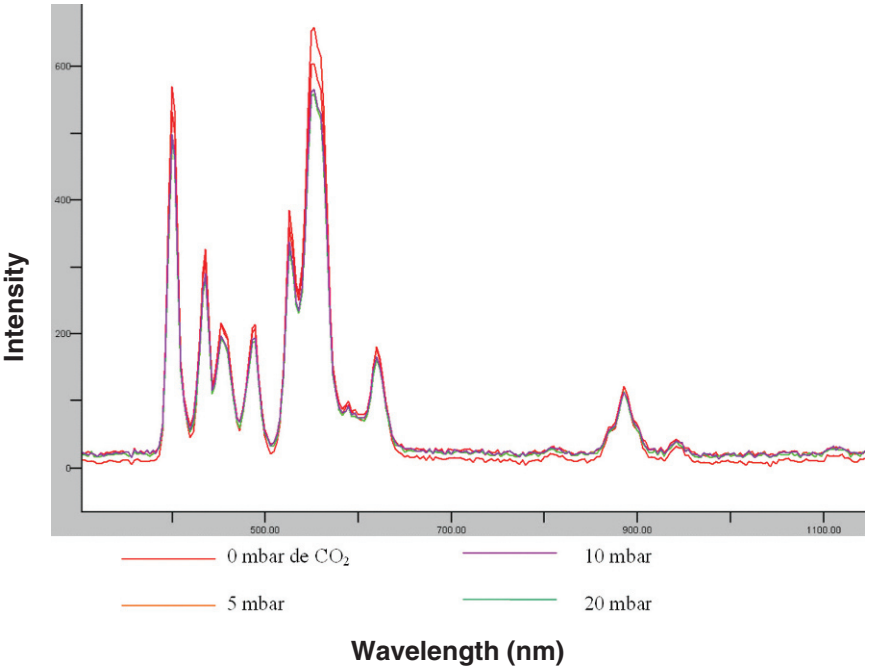

Fig. 6.5 CL spectra of the polished surface of a synthetic YAG crystal acquired at CO_2 pressures between 0 to 20 mbar

6.6 Conclusion: Perspective of Short Term Research

The concept of an electron lamp as an aid for the spatial exploration of Mars has been validated. However, the duration of life of the Si_3N_4 membrane has to be increased, particularly by minimizing the mechanical constraints applied on it. The diffusion and the geometrical interface between the membrane, the sample and the microscope were also identified as the most critical points to optimize in the context of spatial exploration. The following aspects should be studied:

- systematic experiments on the angular diffusion taking into account the membrane, the pressure of CO_2, the angle of incidence of the electron beam, and the geometry of the interface. The surface of a YAG crystal, whose CL emission is homogeneous and intense, will make it possible to easily visualise the surface irradiated by the electron beam.
- in parallel, theoretical considerations and numerical simulations will be carried out on an electrostatic (or electromagnetic) device with the objective of minimising the consequences of the electron diffusion in a CO_2 martian-like atmosphere.

Finally, a 10–20 keV electron beam does not induce any fluorescence in CO_2 pressurized at 10–20 mbar.

Acknowledgements This paper received financial support from CNES (R et T Lampe à électrons, analyse de sédiments martiens par cathodoluminescence' 2003). The authors are grateful to F. Westall, E. Vergès, L. Perdereau and X. Drothiere for their technical help and support.

References

Bandfield JL, Hamilton VE, Christensen PR, McSween Jr. HY, (2004) Identification of quartzofeldspathic materials on Mars. J. Geophys. Res. 109 (E10009)

Barbin V. (2000) Cathodoluminescence of carbonates shells: biochemical vs diagenetic process. In Pagel M, Barbin V, Blanc Ph, Ohnenstetter D, (eds), Cathodoluminescence in Geosciences, Springer Verlag, p. 303–329

Barbin V, Schvoerer M (1997) Cathodoluminescence et géosciences. ≪ Point sur: ≫ C. R. Acad. Sci. Paris., Sciences de la Terre et des Planètes, 325, p. 157–169

Barbin V, Ramseyer K, Elfman M (2008) Biologic record of added manganese in seawater: a new efficient tool to mark in vivo growth lines in oyster species Crassostrea gigas. Int J Earth Sci (Geol Rundsch) 97:193–199

Barbin V, Blanc Ph, Klossa B, Lorin Cl, Thomas R (1999) Cathodoluminescence: a new approach to the in situ study of martian surface mineralogy. Symposium International: Programme d'exploration de Mars & missions de retour d'échantillons (Paris), Résumé CNES. Edit.

Barker CE, Kopp OC (1991) Luminescence microscopy and spectroscopy: qualitative and quantitative applications, SEPM Short Course 25 (Tulsa, OK, 194 pp.).

Baumer A, Blanc Ph, Cesbron F, Ohnenstetter D (1997) Cathodoluminescence of synthetic (doped with rare-earth) and natural anhydrites. Chem Geol 138: 73–80

Blanc Ph, Thomas R, Klossa B, Lorin C, Barbin V (1999) Designing a cathodoluminescence equipment for mars exploration. Symposium International: Programme d'exploration de Mars & missions de retour d'échantillons (Paris)., Résumé CNES. Edit.

Boggs S, Krinsley D (2006) Application of Cathodoluminescence Imaging to the Study of Sedimentary Rocks. Cambridge University press, 165p.

Chevrier V, Mathé PE (2007) Mineralogy and evolution of the surface of Mars: A review. Planet Space Science 55:289–314

Denson J, Ivey DM, Sears DWG, Gucsik A, Vidéki R, Keck WM (2007) Cathodoluminescence and its application for biosignature analysis of Mn-containing biogenic minerals: a review. Lunar and Planetary Science Conference 38, 1009 (abstract)

Garcia D, Pascal ML, Roux J(1996) Hydrothermal replacement of feldspars in igneous enclaves of the Velay granite and the genesis of myrmekites. Eur J Min 8:703–717

Ginibre C, Wörner G, Kronz A (2004) Structure and dynamics of the Laacher See magma chamber (Eifel, Germany) from major and trace element zoning in sanidine: A cathodoluminescence and electron microprobe study. J Petrology 45: 2197–2223

Gledhill JA (1973) The range-energy relation for 0.1-600 keV electrons. J. Phys. A: Math. Nucl. Gen. 6:1420–1428

Gucsik A, Nishido H, Ninagawa K, Okumura T, Wilcox JZ, Urguiles E, Götze J, Bérczi S, Kereszturi Á, Hargitai H, Polgári M, Nagy S, (2006) Cathodoluminescence and its applications in the planetary sciences: a review. Lunar and Planetary Science 37.

Kershaw S (1994) Cathodoluminescence of Silurian stromatoporoids from Gotland, Sweden. Cour. Forsch. Inst. Senckenberg, 172: 307–318

McSween HY, Jr. (1994) What we have learned about Mars from SNC meteorites. Meteoritics 29:757–779

Marshall DJ (1988) Cathodoluminescence of geological materials. Unwin-Hyman, Boston, Mass.

Melezhik VA, Fallick AE, Medvedev PV, Makarikhin VV (1999) Extreme $13C_{carb}$ enrichment in ca. 2.0 Ga magnesite–stromatolite–dolomite–'red beds' association in a global context: a case for the world-wide signal enhanced by a local environment. Earth Sci Rev, 48:71–120

Michard A (1989) Rare earth systematics in hydrothermal fluids. Geochim. Cosmochim. Acta 53:745–750

Owen MR, Anders MH (1988) Evidence from cathodoluminescence for non-volcanic origin of shocked quartz at the Cretaceous/Tertiary boundary. Nature 334:145–147

Pagel M, Barbin V, Blanc Ph, Ohnenstetter D(2000) Cathodoluminescence in Geosciences: an overview and perspectives. In Pagel M, Barbin V, Blanc Ph, Ohnenstetter D (eds), Cathodoluminescence in Geosciences, Springer Verlag, Chap.1, p.1–21.

Panczer G,Ollierb N, Champagnon B, Gaft M, Boudeulle M, Moine B (2003) New development in time-resolved micro-photoluminescence spectroscopy of heterogeneous natural and synthetic inorganic materials. Optical Journal 23: 253–257

Poitrasson F, Hanchar JM, Schaltegger U (2002) The current state and future of accessory mineral research. Chem. Geol.191: 3–24

Poulet F, Bibring J-P, Mustard JF, Gendrin A, Mangold N, Langevin Y, Arvidson RE, Gondet B, Gomez C, the OMEGATeam (2005) Phyllosilicates on Mars and implications for the early Mars history. Nature 481:623–627

Ramseyer K, Boles JC, Lichtner PC (1992) Mechanism of plagioclase albitization. J Sediment Petr 62:349–356

Ramseyer K, Mullis J (2000) Geological application of cathodoluminescence of silicates in Pagel M, Barbin V, Blanc Ph, Ohnenstetter D (eds), Cathodoluminescence in Geosciences, Springer Verlag, Chap. 7, p.177–192.

Schärer U, de Parseval P, Polvé M, de Saint Blanquat M (1999) Formation of the Trimouns talc-chlorite deposit (Pyrenees) from persistent hydrothermal activity between 112 and 97 Ma. Terra Nova 11: 30–37

Smith PH, Bell JF III, Bridges, Britt DT, Gaddis L, Greeley R, Keller HU, Herkenhoff KE, Jaumann R, Johnson JR, Kirk RL, Lemmon J, Maki JN, Malin M C, Murchie SL, Oberst, Parker TJ, Reid RJ, Sablotny R, Soderblom LA, Stoker C, Sullivan R, Thomas N,Tomasko MG, Ward W, Wegryn E (1997) Results from the Mars Pathfinder Camera. Science 278: 1758–1764.

Smith DE, Zuber MT, Solomon SC, Phillips RJ, Head JW, Garvin JB, Banerdt WB, Muhleman DO, Pettengill GH, Neumann GA, Lemoine FG, Abshire JB, Aharonson O, Brown CD, Hauck SA, Ivanov AB, McGovern PJ, Zwally HJ, Duxbury TC (1999) The global topography of Mars and implications for surface evolution, Science, 284:1495–1503

Steele IM, Smith JV, Skirius C (1985). Cathodoluminescence zoning and minor elements in forsterites from the Murchison (C2) and Allende (C3V) carbonaceous chondrites. Nature 313:294–297

Thomas R, Gille P, Barbin V (2002) Detection of past biological activity in martian sediments under cathodoluminescence. Word-File for ESA-SP Exo/Astrobiology meeting in Graz. European Space Agency, (Special Publication) ESA SP, Issue 518, pp.563–564.

Thomas R, Barbin V, Gille P, Léveillé R, MacGibbon J, Miko L, Ramboz C, Westall F (2005) 5th Canadian Space Exploration Workshop, Longueuil, Quebec. "Cathodoluminescence instrumentation for planetary probes".

Westall F, Brack A, Hofmann B, Horneck G, Kurat G, Maxwell J, Ori GG, Pillinger C, Raulin F, Thomas N, Fitton B, Clancy P (2000) An ESA study for the search for life on Mars. Planet Space Sci 48: 181–202

Chapter 7
Astrobiological Aspect of Chemolithoautotrophic Bacterial Activity in the Role of Black Shale-Hosted Mn Mineralization and Cathodoluminescence Study of High Mn-Bearing Carbonates

Márta Polgári, Arnold Gucsik, Bernadett Bajnóczi, Jens Götze, Kazue Tazaki, Hiroaki Watanabe and Tamás Vigh

7.1 Introduction

The low temperature aquatic systems on the Earth as a planet are among the most important areas of microbial activity, where manganese as microbial indicator occurs. Manganese minerals are present on the Earth from the very thin, some μm thick desert varnish to the hundred million tons of ore deposits. The huge black shale-hosted Mn carbonate deposit at Úrkút (Hungary) is adequate case study for the interpretation of natural bacterial behaviour of manganese.

7.2 Black Shale-Hosted Manganese Carbonate Deposit (Úrkút)

The black shale-hosted Mn deposit of Jurassic age at Úrkút is among the 10 largest deposits in the world. The ore reservoir of Mn-carbonate is 80 million tons. Mn contents are about 20 wt.% whereas Fe contents are 10 wt.%. The Fe-rich chert formation linked to the ore deposit, exhibits approximately 5 million tons of SiO_2 and 1 million ton of Fe, respectively. The Mn deposit has been investigated by geological, mineralogical, and geochemical methods by Polgári et al. (2000). Manganese carbonate ore mineralizations occur in environments rich in organics (black shale, biogenic pyrite, etc.) and are characterized by laminitic texture. Evidences of the chemical composition and geochemical features, the joint occurrence of Fe and Mn, as well as the high Mn/Fe ratio, the local selective enrichment of P, Sr, Ba, Co, Mg, As, Si, and Ce are in harmony with the assumption of bacterial activity (Krumbein 1983; Ehrlich 1990; Polgári et al. 2004). Physical and geochemical studies of the deposit and the low stable carbon isotope composition of the Mn carbonate ore

Márta Polgári (✉)
Institute for Geochemical Research, Hungarian Academy of Sciences, H-1112, Budapest, Budaörsi str. 45, Hungary
e-mail: polgari@geochem.hu

A. Gucsik (ed.), *Cathodoluminescence and its Application in the Planetary Sciences*,

confirming the bacterially mediated Mn (IV, III) reduction via organic matter oxidation – i.e. existence of Mn-oxide proto ore – raised contradictions against black shale as anoxic sedimentary host of the deposit. A new interpretation of the ore formation due to microbial activity was suggested by Polgári et al. (2004). Physical properties like very fine grain size (~1 μm) of the ore, the huge enrichment of metals in the deposit during a geologically very short period (less than $5^{*}10^{5}$ year), and enrichments of peculiar bioessential elements (such as Mn, Fe, Si, Mg, S, P, As, Co, Sr) have supported the new theory of biomineralization together with morphological characteristics. The biomineralization was raised not only in the case of Mn minerals but also in the clay formation (Polgári et al. 2006a). According to the features of the deposit, two cycles of bacterial activity – a primary aerobe chemolitoautotrophic and an anaerobe bacterial cycle – are supposed to influence the mineralization. The anaerobe system overprinted the primary one, which is proved by the organic origin of carbon contained in the (CO_3^{2-}) radical of the carbonatic manganese ore, originating from bacterially influenced reduction of Mn(IV) or Mn(III) to Mn(II) accompanied by the oxidation of organic matter (Polgári et al. 1991; Larsen et al. 1998). The separation of the two cycles of bacterial activity is difficult, or not possible as some characteristics, like very fine grain size, enrichment of bioessential elements are characteristic of bacterial activity in general. In spite of these difficulties the following features can be attributed to the primary aerobe Mn(II) oxidation and sinking activity of the metals to sediments by chemolithoautotrophic bacterial activity:

– Formation of a huge mass of material at a high rate (x 10^5–10^6), during a short geological period,
– The high N/C ratio, as a possible evidence of cyanobacterial activity in the system (Sajgó personal communication , 2003),
– The high Mg content of the black shale-hosted Mn-carbonate deposits as an evidence of primary aerobe chemolithoautotrophic signature in formation of huge deposits can be assumed on the basis of recent analogies (Mandernack et al. 1995). Previous chemical investigations showed high Mg content of black shale-hosted Mn-carbonate deposit of Úrkút (2.5–8.11 wt.% MgO; Cseh et al. 1980) as well as for similar deposits, for Molango (12.62 wt.% MgO; Okita 1988), and Chinese deposits (e.g. 7.05 wt.% Fan et al. 1999).

According to geochemical element ratio characteristics, the source of mineralization was considered to be a local hydrothermal vent system, and the process of metal enrichment was supposed to be microbially mediated (Polgári et al. 2003a, 2006b, 2007a). Nano-scale mineralogical studies of celadonite also supported the local hydrotermal origin (Weiszburg et al. 2004). Mn-oxides (e.g. manganates) are formed by both chemical and bacterial oxidation from Mn(II) in variegated water systems but recent analogies support that bacterial activity is the most important in most of cases (Tebo et al. 2004; Bargar et al. 2005; Webb et al. 2005a, 2005b). Detailed studies made from powder samples cannot give information about the signs of formation processes; therefore we needed further micro- and nano-scale textural investigations of the ore samples.

7.3 General Geomicrobiological Aspects

Life arose on the young Earth as a result of natural chemical process. More than half a century of experimental research has underscored the dynamic interactions of atmosphere, oceans, and rocks that fostered this ancient transition from geochemistry to biochemistry (Hazen 2005). It is well known and understood that a wide variety of geological processes are largely biologically driven, including the formation of minerals of biogenic origin. Biogenic minerals can be produced by a number of distinct ways including intracellular, within the cellular envelope, within a biofilm, or in bulk extracellular modes. These syntheses can be directly related both to a biological process and as a secondary effect of that process, including simply nucleation involving the microbe itself (Ehrlich 1999; Fortin 2004). Many of the metabolic processes that result in mineral formation date back to the earliest history of life and hence it has been proposed that by directly modifying their extracellular environment microorganisms could potentially gain an advantage in energy acquisition (Fortin 2004). The formation of many of these minerals is directly related to the metabolic activities of the organisms, particularly oxidation and reduction reactions and can involve a wide variety of elements and their compounds including Fe, P, S, Ca, Mg and Mn. Biologically produced minerals have the potential to provide a wealth of knowledge about the history of life on Earth and a valuable tool for searching for its presence elsewhere. Clay minerals carry a kind of genetic information in their complex sequences of point defects, layer orientations, and metal cation substitutions. Examples of clay-biochemical interactions of Hanczyc et al. (2003) reported that montmorillonite catalyzes the polymerization of RNA from activated ribosome nucleotide and that montmorillonite accelerates the spontaneous conversion of fatty acid micelles into vesicles. Theng and Orchard (1995) discussed the physical and chemical interactions between microorganisms and soils in the ecosystems. Biomineralization of kaolinite, nontronite, and bentonite on living cells of microorganism in natural and cultivated systems has been reported (Tazaki 1997, 2000; Ueshima et al. 2000; Asada and Tazaki 2000). Bacterial cells can act as a nucleation site for minerals (Ferris et al. 1986; Sara and Sleytr 2000). Similarly, Tashiro and Tazaki (1999) showed that the layer of extracellular polymeric substances surrounding microbial cells acts as a template in the formation of iron hydroxides. Theng and Orchard (1995) also suggested that multivalent cations might have served as cation bridges in the interaction between clays and microbial extracellular polymeric substances. Manganese has a special role in microbial metabolic processes and in the field of biomineralization. From this reason this element has a special importance for astrobiological aspects.

Numerous microorganisms can cause metal enrichments from neighbouring water environments. Microbes play important role in the case of all natural elements of the Earth in their enrichments, mineralization, transportation and sedimentation. Microbes control or induce biomineralization.

Oxidation of Mn(II) to the higher oxidation states Mn(III, IV) by dissolved oxygen is one of the principal processes regulating the rate of Mn cycling in low temperature aqueous geochemistry (Ehrlich 1990).

The kinetic model of the oxidation pathway shows that the Mn(II) to Mn(III) step is rate-limiting, because the electron transfer from Mn(III) to Mn(IV) is nearly 30 times faster (Morgan 2005). This is caused by the non-equivalent energy of the two electrons removed form Mn(II), i.e. the Mn(II) oxidation step is less energetically favourable than the Mn(III) oxidation step at near-neutral pH. It is due to the fact that the Mn(II) + O_2 electron transfer follows an inner-sphere path according to thermodynamic considerations (e.g. Marcus outer-sphere electron transfer theory, Morgan 2005).

The available pathways in a particular water environment are: homogeneous solution oxidations, oxide surface catalysis or biologic oxidation (Morgan 2005).

7.3.1 Homogeneous Solution Oxidations

Mn(IV) is the thermodynamically favoured oxidation state in surface waters, yet abiotic Mn(II) oxidation is slow under most environmental conditions (Webb et al. 2005a). The stoichiometry of Mn(II) oxidation by dissolved O_2 at moderate alkaline pH is the following: 4 Mn(II)(aq) + O_2 = 4 MnOOH(s), where aq means dissolved phase and s means solid phase. Energetic information reveals that there is a substantial free energy barrier to a first one-electron oxidation step, e.g., Mn(II) + O_2 → Mn(III) + O_2^-, which is caused by the above-mentioned inner-sphere path electron transfer (Morgan 2005).

7.3.2 Oxide Surface Catalysis

Metal oxide surfaces are able to accelerate Mn(II) oxidation by O_2 (e.g. hematite, goethite, lepidocrocite and manganese-dioxide (Wilson 1980; Sung and Morgan 1981; Davies and Morgan 1989).

7.3.3 Bacterial Oxidation

Bacterial oxidation of Mn(II) to Mn(IV) is believed to drive the oxidative segment of the global biogeochemical Mn cycle (Krumbein 1983; Ehrlich 1990). It controls the concentration of dissolved Mn(II) in the oceanic water column, where it is a critical nutrient for planktonic primary productivity. Mn(II) oxidizing activity is expressed by numerous phylogenetically diverse bacteria and fungi (Tebo et al. 1997, 2004), suggesting that it plays a fundamental and ubiquitous role in the environment (Webb et al. 2005a). This important redox system is believed to be driven by an enzyme or enzyme complex involving a multicopper oxidase (Tebo et al. 1997). The Mn(II) oxidation by microbes is a result of two sequential one-step electron transfer processes, both requiring the putative multicopper oxidase, MnxG, in which Mn(III) is a transient intermediate stabilized through ligand-binding complexes (Webb et al. 2005a). This enzyme system may serve as a

source for environmental Mn(III), a strong oxidant and competitor for siderophore-bound Fe(III) in nutrient-limited environments. For example metabolically dormant spores catalyze an important biogeochemical process intimately linked to the C, N, Fe, and S cycles. Microbial processes catalyze the oxidation of Mn(II) to Mn(IV) by up to five orders of magnitude faster than surface catalyzed reactions, and most Mn-oxides found in soil, sediments, and aquatic environments are thus believed to be of biogenic origin (Nealson et al. 1988; Tebo 1991; Tebo et al. 2004).

The microbial oxidation model of Mn(II) consists of Mn(II) binding to the enzyme site, then undergoing two individual electron transfer steps to Mn(III) and finally to Mn(IV) (Fig. 7.1). The existence of Mn(III) intermediate is very short and can be visible only by strong ligand-binding mechanism (Webb et al. 2004).

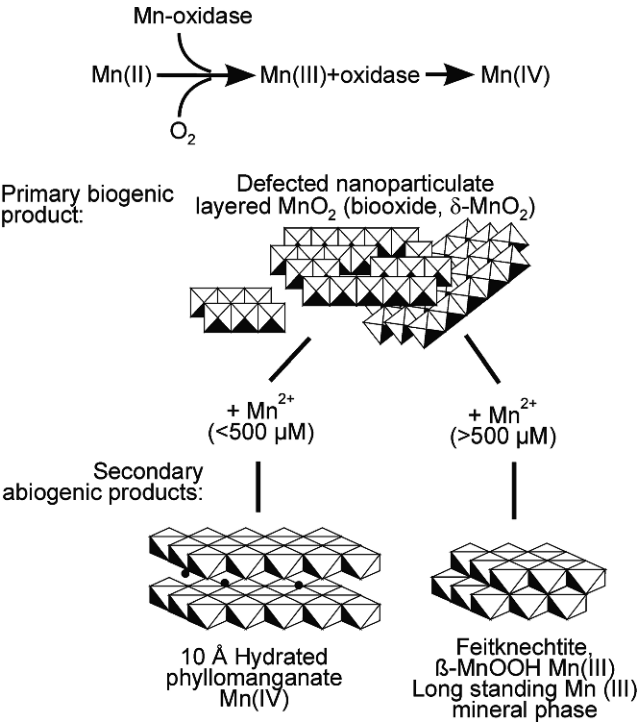

Fig. 7.1 Model reaction for the formation of Mn(III) intermediates in oxidation of Mn(II) by bacteria (after Webb et al. 2005a) and schematic model for biogenic Mn-oxides and secondary reaction products (after Webb et al. 2004; Tebo et al. 2004; Bargar et al. 2005)

7.3.4 The Forming Biooxide

The primary solid biogenic product of Mn(II) oxidation is an X-ray amorphous oxide similar to δ-MnO_2, which has a Mn oxidation state between 3.7–4.0. δ-MnO_2 biooxide is believed to be a disordered hexagonal phyllomanganate containing

Mn(IV) vacancy defects, having very small particle size (<100 nm lateral dimensions), and having only two or three MnO_2 layers (Mn is in octahedral coordination) stacked along the c axis (Villalobos et al. 2003). The small number of stacked layers causes the (00l) reflections to become broad and weak or to be completely absent. Successive MnO_2 layers are believed to be pseudo-randomly sheared in the a-b plane and rotated relative to one-another along the c axis (i.e. turbostractic disorder), which destroys the coherence required to generate well-defined (hkl) reflections (Chukrov et al. 1987; Lanson et al. 2000; Reynolds 1989; Villalobos et al. 2003). The resulting (hkl) reflections are weak, broad, and asymmetric. If the particles are sufficiently small and disordered, then their diffracted intensities may be too weak to detect above background (Reynolds 1989), resulting in an X-ray amorphous material.

Consideration of these points leads to a structural model for the initial biooxides by bacterial activity to oxidize Mn(III) to (IV) via an enzymatic pathway (Webb et al. 2004). The subsequent release of Mn(IV) should be followed immediately by hydrolysis and polymerization of biogenic Mn(IV), due to its low solubility in water (Baes and Mesmer 1976). Based on the present results, it is assumed that Mn(IV) polymerization leads to sheet polymers or nanoparticles with general structural formula $Mn_xO_2^{(4x-4)}$ ($x \leq 1$) that exhibit the basic hexagonal phyllomanganate topology, but contain numerous vacancy defects (i.e., $x < 1$) and other structural defects such as Mn(II) or Mn(III) bonded above vacancy sites in the hexagonal sheets as a result of reaction with aqueous Mn(II) (Fig. 7.1, Bargar et al. 2005). The sheet polymer model proposed for the initial biooxides assumes the hexagonal $Mn_xO_2^{(4x-4)}$ sheets to have nanoparticulate lateral dimensions (e.g. < 20 nm) and little or no staking normal to the layers, and therefore to be X-ray amorphous as measured.

Reaction of Mn(II) with the primary biogenic oxide results in the production of abiotic secondary products, feitknechtite or a 10Å Na-phyllomanganate (Bargar et al. 2005). The identity of the secondary product depends upon the Mn(II) concentration as described by thermodynamic relations (Mandernack et al. 1995). A decrease in the dissolved Mn(II) appears to act as a reductant toward the biogenic oxide and to control the stability of secondary reaction products.

Thermodynamic stability relationships in the Mn(II)/(III)/(IV) system were reviewed by Mandernack et al. (1995), and can be summarized as follows: the stability of Mn(III)-bearing phases such as MnOOH and Mn_3O_4 increases relative to that of Mn(IV)-bearing phases such as MnO_2 as pH and Mn(II) concentration increase. This behaviour can be appreciated from inspection of the reaction for MnOOH transformation to MnO_2 in aqueous solution:

$$2H^+ + 2MnOOH = MnO_2 + Mn(II) + 2H_2O$$

Mass action will cause this reaction to move towards the left-hand side of the equation when the activities of Mn(II) or OH^- increase. The point at which MnOOH and MnO_2 are in equilibrium is determined by free energies of the MnOOH polymorph and MnO_2 phases being compared. For feitknechtite (β-MnOOH) and Na-birnessite at 25°C and pH=7.8 Mn(II)(aq) concentration is about 500 μM (Mandernack et al. 1995). It means that Mn(II)(aq) concentration less than 500μM will cause

the formation of 10Å hydrated phyllomanganate, and higher Mn^{2+}concentration than 500μM will cause abiotic feitknechtite formation with reaction of the previously formed biooxide. In feitknechtite Mn(III) occurs. In ancient Mn ore beds long standing manganite is the common Mn(III) oxide phase, and it is widely supposed to reflect oxygen deficient formation conditions (Roy 1981). Taking into consideration of the recent results, the existence of manganite is document of high Mn(II) concentration contribution rather than indicator of suboxic environment. Giovanoli (1980) reported that the rate determining step in γ-MnOOH (manganite) formation is the transformation of the rapidly formed initial products, e.g. feitnechtite to manganite. On the basis of EXAFS spectra studies Webb et al. (2005b) suggest that the octahedral layers have relatively few Mn octahedral site vacancies in the lattice and the layer bends to accommodate Jahn-Teller distortions creating the change in symmetry, which can be assumed in the case of feitknechtite to manganite transformation.

According to detailed experimental studies it was shown that extracellular polymers of bacteria catalyze the adsorption of Mg on the surface of the cells (Mandernack et al. 1995). The substitution of Na for Mg in the instable Na-buserite, Na-birnessite to stabile todorokite is important, and can be responsible for the elevated Mg content in black shale-hosted Mn carbonate deposits. So the bacterial cells not only directly oxidize Mn(II) to Mn(IV) but also in the very early stages of oxidation bacterial activity influences the cation composition of the forming Mn-oxide mineral. Later chemical processes start to erase the biological signal (Mandernack et al. 1995). Mineralogical changes similar to these are likely to be commonplace in natural settings where bacterial Mn(II) oxidation is occurring and may liberate sorbed metal ions or alter the rates of important Mn-oxide surface-mediated processes such as the degradation of organic molecules. It is plausible that microbes may exploit such mineral transformation reactions to indirectly control specific chemical conditions in the vicinity of the cell (Mandernack et al. 1995).

In this study, natural occurrences of Mn-carbonate ores (brown Mn carbonate ore, main and second ore bed) of Jurassic age (Úrkút, Hungary) were investigated. The samples were observed at micrometer scale using electron microscopy to confirm the basic role of microbial activity in ore mineralization processes. Investigations were focused to observe cellular-materials because of a large quantity of microorganisms still remained in the banded structure. We also discuss the mechanism of banded Mn-Fe mineral formations and clays around microorganisms. Study of these small-scale biomineralization can also contribute to a better understanding of the proposed environments not only in Jurassic age but also in the case of other black shale-hosted Mn carbonate deposits, and astrobiological aspects.

7.4 Cathodoluminescence of Mn-rich Minerals, Mostly Carbonates

A large number of biogenic minerals have the potential to be analysed by cathodoluminescence (CL) Manganese is an especially interesting target. It is an ideal mineral to test the efficacy of CL in distinguishing biogenic vs abiogenic, as a variety of

manganese containing minerals of both forms are easily obtainable. Known biogenic Mn-containing minerals are produced by a wide variety of microorganisms ranging from Mn-oxides by various environmental isolates of Pseudomonas sp. to the hyperthermophilic archaea Pyrobaculum which has been reported to produce the Mn-carbonate (rhodochrosite, Kashefi and Lovley 2000). The utility of CL in acquiring good spectra from manganese is well documented. Some large-scale terrestrial deposits of manganese ores have been attributed to a biological origin and the production of the manganese containing minerals birnessite and todorokite by sub-surface microbes has been recently documented (Boston et al. 2001; McKay et al. 1996; Polgári et al. 2006a). CL could also be applied to a better understanding of the early history of life on Earth through the analysis of assumed biogenic manganese features, such as ancient metallogenium-like fossils, stromatolite like structures, or other diverse mineral deposits of a possible biological origin. It is intriguing mineralogical target from a planetary science perspective whereas Mn-oxides are known to be abundant on Mars. Desert varnish which consists of Fe- and Mn-oxides thought to be produced terrestrially through a combination of microbial action and weathering have also been viewed extensively on Mars. Minerals of unknown origin within meteoritic specimens could also provide an additional application (Ehrlich 1999; McKay et al. 1996; Denson et al. 2007).

The Mn oxidation and reduction processes are mediated by microbes so cathodoluminescence of Mn-bearing phases is assumed to give information about formation of the mineralizations, together with the signs of microbial activity as well. Cathodoluminescence of Mn-oxide minerals are not reported, but Mn-bearing carbonates are often cited as luminescent materials. Although it is well known that manganese is the most important CL activator in carbonates the CL method is rarely applied in the petrological investigation of Mn-carbonate ore beds or smaller enrichments due to the commonly accepted effect of concentration quenching or self-quenching. The decrease in CL intensity (self-quenching) occurs at high activator (Mn) concentrations, when the average space between activator ions becomes smaller and instead of emitted luminescence the excitation energy is transferred from the absorbing activator ion to neighbouring similar ions (Marshall 1988). Critical concentrations of 500–1000 ppm were documented for starting of self-quenching for Mn^{2+}-activated CL in the calcite structure (Mason 1987; Mason and Mariano 1990; El Ali et al. 1993; Haberman et al. 2000). A comprehensive knowledge about the luminescence behaviour of Mn-rich ($>$ 1 wt.% Mn) carbonates (manganocalcite, kutnohorite, rhodochrosite) still does not exist. The possible limit of concentration extinction is not known. A rhodochrosite ($MnCO_3$) with 46.0 wt.% Mn and 1.0 wt.% Fe was found to be virtually non-luminescent by Walker et al. (1989). At the same time, luminescent rhodochrosite, was reported by Gorobec et al. (1978) and Gaft et al. (1981,2005) which seems to indicate a non-total self-quenching for Mn(II) and support the suggestion of Machel et al. (1991) that luminescence up to the highest possible Mn concentrations might exist.

Cathodoluminescence (CL) microscopy is a routinely used technique in sedimentary petrology for the study of carbonate rocks and their diagenetic history (Marshall 1988; Machel 2000; Richter et al. 2003). Beside the texture revealed by CL

microscopy, nowadays the (quantitative) CL spectroscopy combined with trace element determinations (e.g. Particle-induced X-ray emission – PIXE) can give more information about the activator elements in carbonates regarding their coordination and ionic charge (Richter et al. 2003; Gaft et al. 2005). Much work has been done about CL characteristics of the most important and abundant carbonate minerals, like calcite, dolomite, and aragonite. Other less common carbonate species have received little attention both in CL microscopy and spectroscopy (e.g. rhodochrosite, Mn-rich carbonates, etc., Gaft et al. 2005).

It is generally accepted that Mn(II) ion (3d) and mostly trivalent rare earth elements (REEs) (4f) are the most important activators of extrinsic CL in carbonate minerals, while Fe(II) is a quencher of CL (e.g. Marshall 1988; Machel 2000). Concerning the different valence states of Mn, Machel et al. (1991) noted that it has not been investigated experimentally, but there is no reason to exclude the possibility that least some natural calcite contains sufficient amounts of Mn(IV) which could add an emission band that broadens the Mn(II) band, or it could broaden the Mn(II) band via distorting the octahedral coordination of Mn(II), also inducing different lattice defects, or a combination of the above.

The aim of this study is the investigation of CL behaviour of Mn-rich carbonates on the case study of the calcian kutnohorite from the Úrkút Mn carbonate deposit.

7.5 Geology

Úrkút is located in the central Bakony Mountains (Transdanubia), in the North Pannonian unit of the Alp-Carpathian-Pannonian (ALCAPA) region (Fig. 7.2a). Across the Transdanubian Range smaller-larger Mn mineralizations occur according to tectonic zones (Úrkút Mn Ore Formation, Fig 7.2b). The largest Mn-mineralizations occur in the Úrkút Basin which was formed by the NW-SE trending block faulting that characterized the Late Triassic and Jurassic of this region. The deposits are Early Jurassic (Late Lias) and occur within marine sedimentary rocks composed mainly of bioclastic limestone, radiolarian clay marlstone and dark-grey to black shale (Polgári 1993). The black shale-hosted Mn mineralization occurred in a clayey marlstone of Toarcian age in Falciferum ammonite zone (Géczy 1973). The marlstone rests conformably on Middle Lias carbonate rocks formed at the centre of the depositional basin. The marlstone is about 40 m thick at the centre and runs out towards the basin margins (Szabó et al. 1981). The manganese deposits form a NE-SW trending unit of approximately 12 km length and 4–6 km width. Recently, the ore deposit of economic importance covers an area of 8 km^2 (Fig. 7.3a).

Manganese mineralization is restricted to two intervals within the marlstone (Fig. 7.3b). The lower main bed is about 8–12 m thick and is underlain by 0.5–1 m thick clayey-marlstone; the upper mineral zone, Bed No. 2 or second bed, is 2–4 m in thickness and is separated from the main ore bed by 10–25 m thick clayey-marlstone (black shale). At the base, the ore sections begin with a thin, greenish, organic-rich, pyritiferous clayey-marlstone containing enrichments of trace

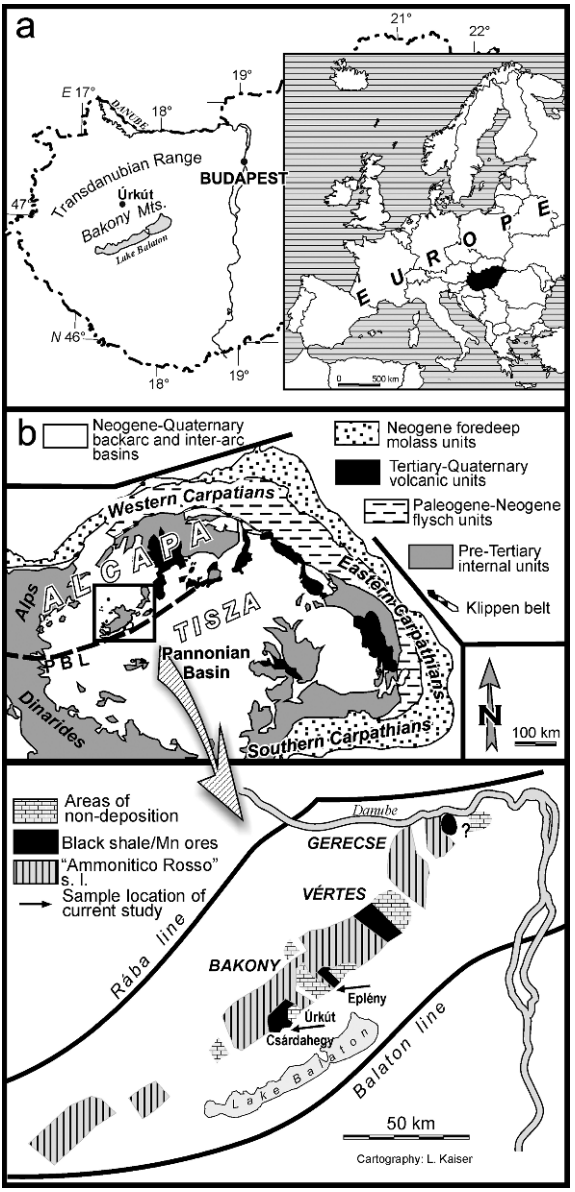

Fig. 7.2 Locality maps – location (**a**), tectonic unit and palaeogeographic map (**b**) – of Jurassic Mn deposits and indications in the Transdanubian Range, Hungary. Middle figure shows the tectonic unit of area, bottom figure shows the occurrence of Mn mineralizations in the Toarcian palaeogeographical map of the Transdanubian Range (modified after Vörös and Galácz, 1998). Mn deposits are structurally determined

elements, namely Co, Ni and As in sulphide form, and Sr-bearing barite (Polgári 1993; Polgári et al. 2003b). Concretions of thin layers with phosphate and chert are commonly found at the boundary of the marlstone and the underlying limestone. The rhodochrosite ore is composed of alternating grey, green, brown and black sections with finely laminated structure, and it is a mixture of very fine-grained clay minerals and carbonates (Cseh Németh and Grasselly 1966). Fine-grained (1–2 μm) rhodochrosite rock lacks coarse detrital clastics (Szabó-Drubina 1959).

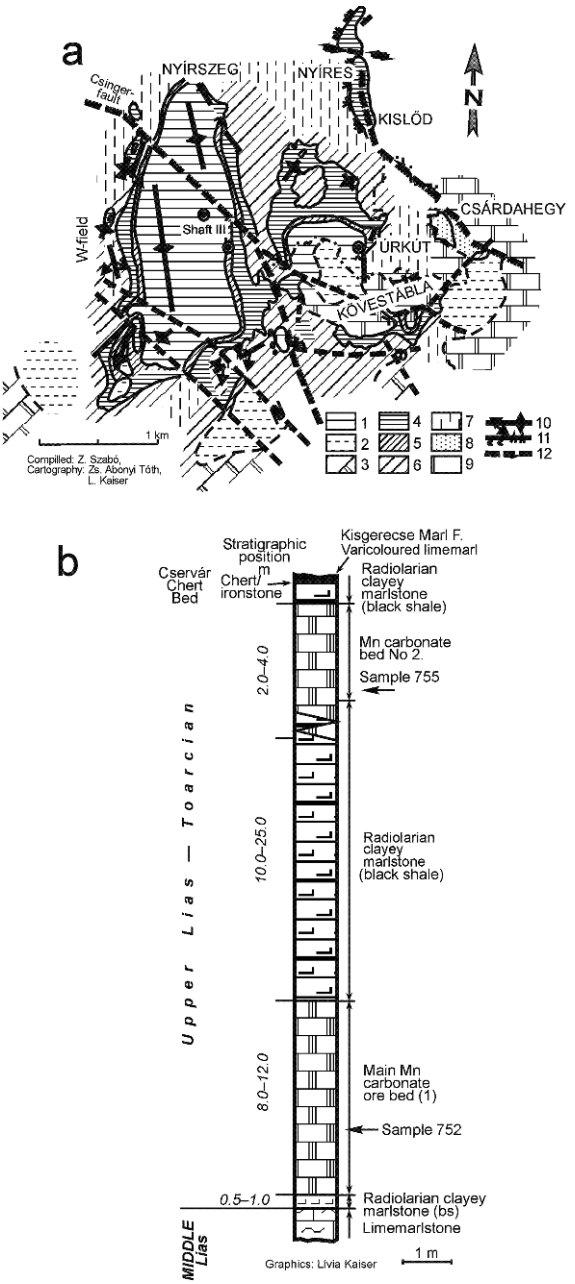

Fig. 7.3 Geological sketch map of the Úrkút Deposit (**a**) and the general profile of the Mn carbonate ore with sample locations (**b**). Key – 1: Mn carbonate complex. 2: Mn carbonate complex of reduced development. 3: Limestone. 4: Oxidized manganese formation. 5: Transitional zone between carbonate and oxide deposits. 6: Reworked manganese ore formation. 7: Denuded area. 8: Ferruginous manganese bed at Csárdahegy. 9: Bedrock outcrops. 10: Anticline, syncline. 11: Flexure. 12: Fault. Samples are from Shaft III

The formation is laminated with laminae $1.5^{*}10^{-5}$ m in thickness. The mineralized sections are in lack of fossils or traces of benthos fauna, and contain only fish remnants as well as rarely silicified, manganized or coalified plant fragments (Polgári et al. 2005).

The mineralogical composition of the Mn-carbonate ore beds are composed of various minerals of Ca-rhodochrosite, siderite, 10Å-phyllosilicate (celadonite), smectite (nontronite), goethite, quartz, phosphorite, pyrite, chlorite (trace), zeolite, feldspar (trace), while the black-shale consists of quartz, calcite, pyrite, smectite, 10Å-phyllosilicate (illite, celadonite), goethite, chlorite, zeolite (trace), and feldspar (trace) (Polgári 1993). The main and trace elemental contents are characterized by the enrichment of variable valences and other bioessential elements such as Mn, Fe, S, P, Si, As, Co, Sr, Ba, Mg, Cu, Zn and REE (Ce). The average of main and trace elements in the ore are summarized in Table 7.1.

Table 7.1 The average main and some trace element contents of the recently analysed ore types from Úrkút (numbers of analysed samples are in brackets)

Elements	Mn carbonate ore (main bed) Black type	Mn carbonate ore (main bed) Green type	Bed No. II. (second bed) Grey type	Black shale
Si↓[wt. %]	8.66 (15)	9.79 (14)	8.21 (10)	21.20 (14)
Al	1.93 (15)	1.24 (14)	1.55 (10)	4.14 (14)
Fe	8.88 (15)	7.94 (14)	13.75 (10)	5.96 (14)
Mn	22.90 (15)	19.38 (14)	12.75 (10)	3.12 (14)
Ca	2.70 (15)	1.71 (14)	7.91 (10)	5.25 (14)
Mg	2.73 (15)	1.25 (14)	1.76 (10)	1.34 (14)
K	1.05 (15)	1.77 (14)	0.73 (10)	1.26 (14)
Na	0.21 (15)	0.17 (14)	0.23 (10)	0.44 (14)
P	0.25 (15)	0.20 (14)	1.18 (10)	0.18 (14)
CO_2	17.48 (12)	15.80 (14)	22.24 (4)	6.87 (13)
Ba↓ [ppm]	473 (15)	170 (14)	263 (10)	335 (16)
Sr	131 (15)	93 (14)	608 (10)	265 (16)
Co	269 (15)	217 (14)	141 (10)	131 (16)
Cu	37 (9)	33 (10)	32 (9)	100 (15)
Ni	44 (15)	24 (8)	28 (10)	58 (16)
Zn	52 (15)	65 (14)	36 (10)	88 (16)
As	48 (13)	11 (11)	63 (10)	53 (14)
Hf	1.2 (11)	1.1 (13)	1.0 (4)	2.5 (13)
Th	3.3 (11)	2.8 (13)	3.5 (4)	8.8 (14)
U	0.83 (11)	0.86 (13)	1.22 (4)	1.94 (14)
La	46 (14)	47 (13)	46 (10)	39 (14)
Ce	153 (14)	143 (13)	119 (10)	145 (14)
V	45 (3)	–	60 (6)	101 (1)
C_{org}[wt. %]	0	–	0	2.94 (6)

(ICP, AAS, INAA and wet chemical methods were used, for more details see Polgári et al. 2000 and 2006a)

7.6 Materials and Methods

Rock samples were collected from black shale-hosted Mn deposits at Úrkút Mine. The sample locations are shown in Fig. 7.3b.

Mineralogical investigations of clays and ores were performed by X-ray powder diffraction (XRD). A Rigaku Rinto 1200 X-ray diffractometer (CuKα radiation) operating at 40 kV and 30 mA, and a scanning speed of 1–20 s./0.02°, was used.

Chemical investigations of the samples were carried out by X-ray fluorescence using a JEOL JSX-3201 type scanning electron microscope (SEM) equipped with an energy dispersive X-ray fluorescence detector (ED-XRF, Rh-Kα-ray, Kanazawa University, Kakuma, Japan).

The rock samples were cut in half and polished surface were used for optical microscopy and elemental content mapping. The analyses were carried out by an ED-XRF with equipment for X-ray probe scanning system (JEOL JSX-3600), using Rh Kα, which operated at an accelerating voltage of 30 kV under vacuum condition (Kanazawa University, Kakuma, Japan).

A JEOL JSM-5200LV type low-vacuum scanning electron microscope (LV-SEM) equipped with an energy dispersive X-ray (EDX) spectrometer (Philips EDAX PV9800EX) was used to observe the micromorphology of the samples (Kanazawa University, Kakuma, Japan).

Cathodoluminescence examinations were initially performed on polished rock chips using a Reliotron cold-cathode microscope operated at 5–7 kV accelerating voltage and 0.5–0.9 mA current (Institute for Geochemical Research, Hungarian Academy of Sciences, Budapest). Additionally, carbon-coated thin sections were studied using a hot-cathode CL microscope HC1-LM (cf. Neuser 1995) operated at 14 kV acceleration voltage and with a current density of ∼10 μA/mm^2(TU, Bergakademie, Freiberg). Luminescence images were captured on-line during CL operations by means of an adapted digital video-camera (KAPPA 961–1138 CF 20 DXC with cooling stage). CL spectra in the wavelength range 300–900 nm were recorded with an Acton Research SP-2356 digital triple-grating spectrograph with a Princeton Spec-10 400/B/XP CCD detector, which was attached to the CL microscope by a silica-glass fibre guide. CL spectra were measured under standardized conditions (wavelength calibration by a Hg lamp, spot width 30 μm). To prevent any falsification of the CL spectra due to electron bombardment, all spectra were taken on non-irradiated sample spots.

7.7 Results

7.7.1 Mn Carbonate Ore, Dark Brown Laminated Main Ore Bed

The Mn carbonate ore was collected from main ore bed (sample No: 752), which banded layer structure is dark brown in colour. In brown layers, smectite, rhodochrosite ($MnCO_3$), manganite (MnOOH), goethite, and calcite were identified by XRD analyses (Fig. 7.4). The peak at 1.53 nm has shifted to 1.71 nm as a result of ethylene-glycol treatment which confirms smectite . In white layer smectite, rhodochrosite, and calcite were determined.

The ED-XRF elemental maps of the sample showed that Mn, Fe and Ca elements were concentrated in dark brown layers whereas Si and Al elements were randomly distributed (Fig. 7.5). The traces of Ca and P elements were also located in light brown layers suggesting presence of microorganisms. The Mn contents closely correlate with the concentration of Fe, Ca, and P elements.

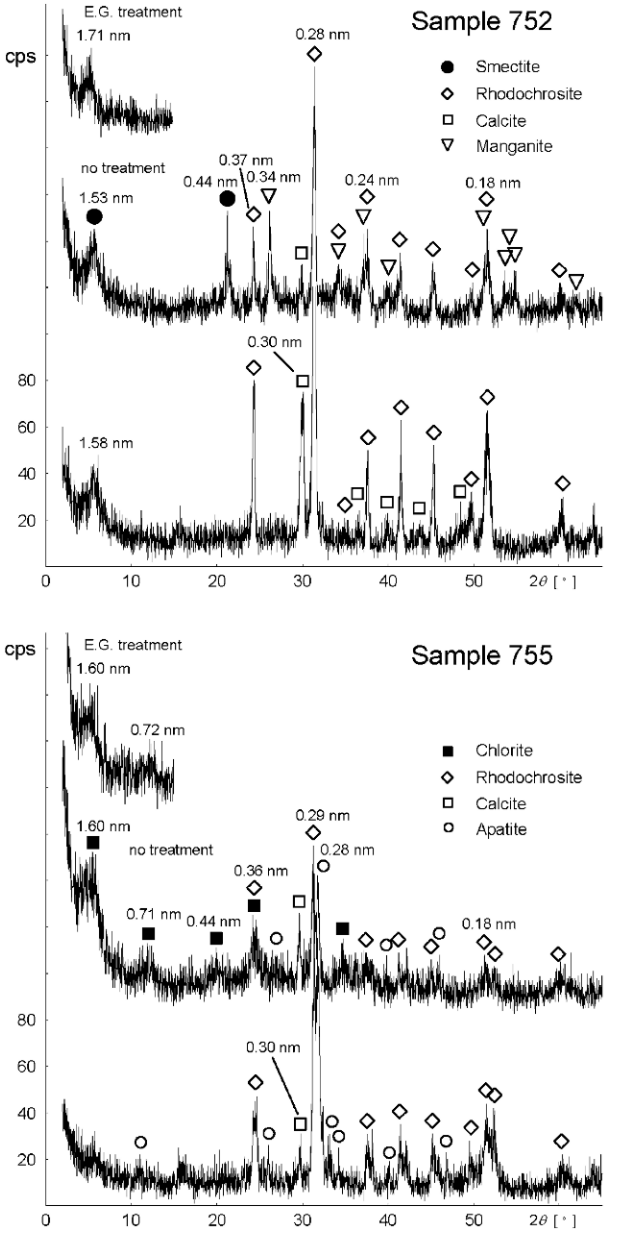

Fig. 7.4 X-ray powder diffraction profiles of bulk samples 752 and 755 showing clay minerals, Mn-minerals, calcite and apatite

The traces of Ca and P elements were also located in light brown layers suggesting presence of microorganisms. The Mn contents closely correlate with the concentration of Fe, Ca, and P elements.

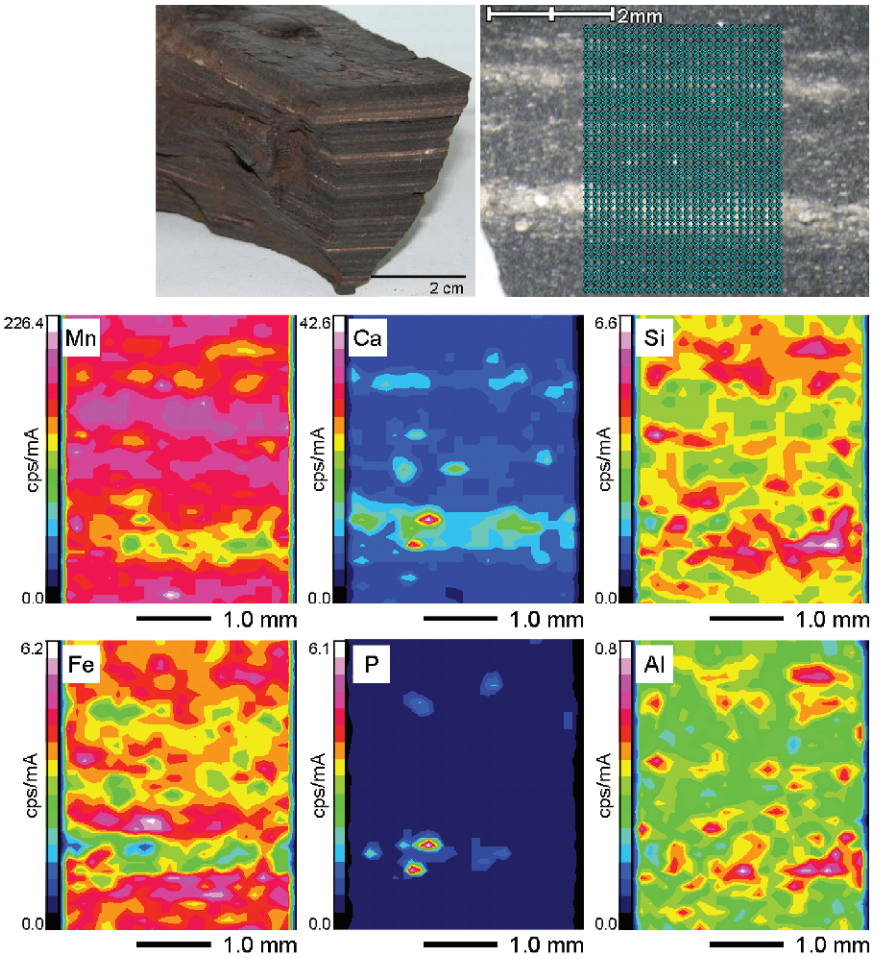

Fig. 7.5 ED-XRF elemental mapping of Mn-carbonate ores of sample 752 (main ore bed) showing Mn, Fe and Ca banded layer structures whereas Si and Al elements are randomly distributed

The optical microscopic observation of the sample showed abundant microorganisms presented in brownish and white brown layered structures (Fig. 7.6).

Microbes show coccoid (spherical), elliptical, and filamentous shapes in white lenses and layers.

The scanning electron microscopy study of the sample No. 752 revealed small microbes in the flaky materials which were difficult to found, because of covering materials (Fig. 7.7). The EDX analyses of covering materials on the microorganisms indicated that the flaky materials are the mostly Mn-rich components with Si, Ca and little amount of Fe contents (Fig. 7.7, a-1). The spherical, coccoid forms are much more Ca rich with lower Mn, Si and higher Fe contents (Fig. 7.7, a-2). The tubular

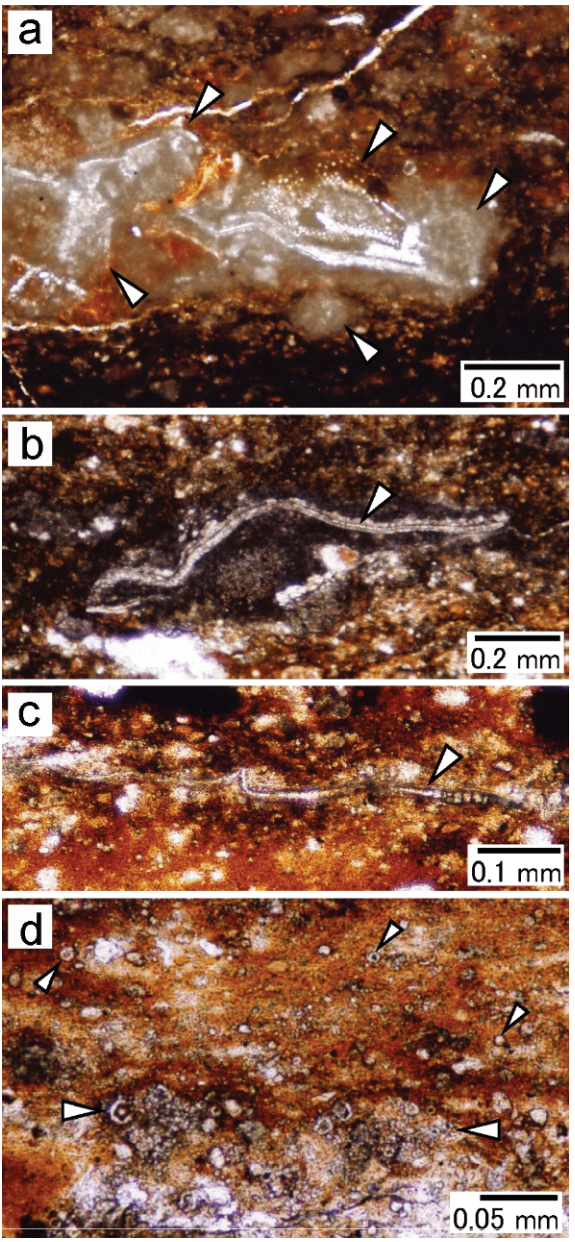

Fig. 7.6 Optical micrographs of Mn-carbonate ores of sample 752 (main ore bed) showing abundant microorganisms (*arrows*)

microorganisms are Si and Mn rich associated with Ca and smaller amounts of Mg, Al, K and P (Fig. 7.7, b-2, c-1). The angular materials mainly composed of Mn suggesting presence of rhodochrosite and manganite which were identified by XRD method (Fig. 7.7, c-2).

Transmission Electron Microscopy micrographs showed abundant nanometer-sized bacterial cells changed to graphene crystalline materials (0.33–0.35 nm,

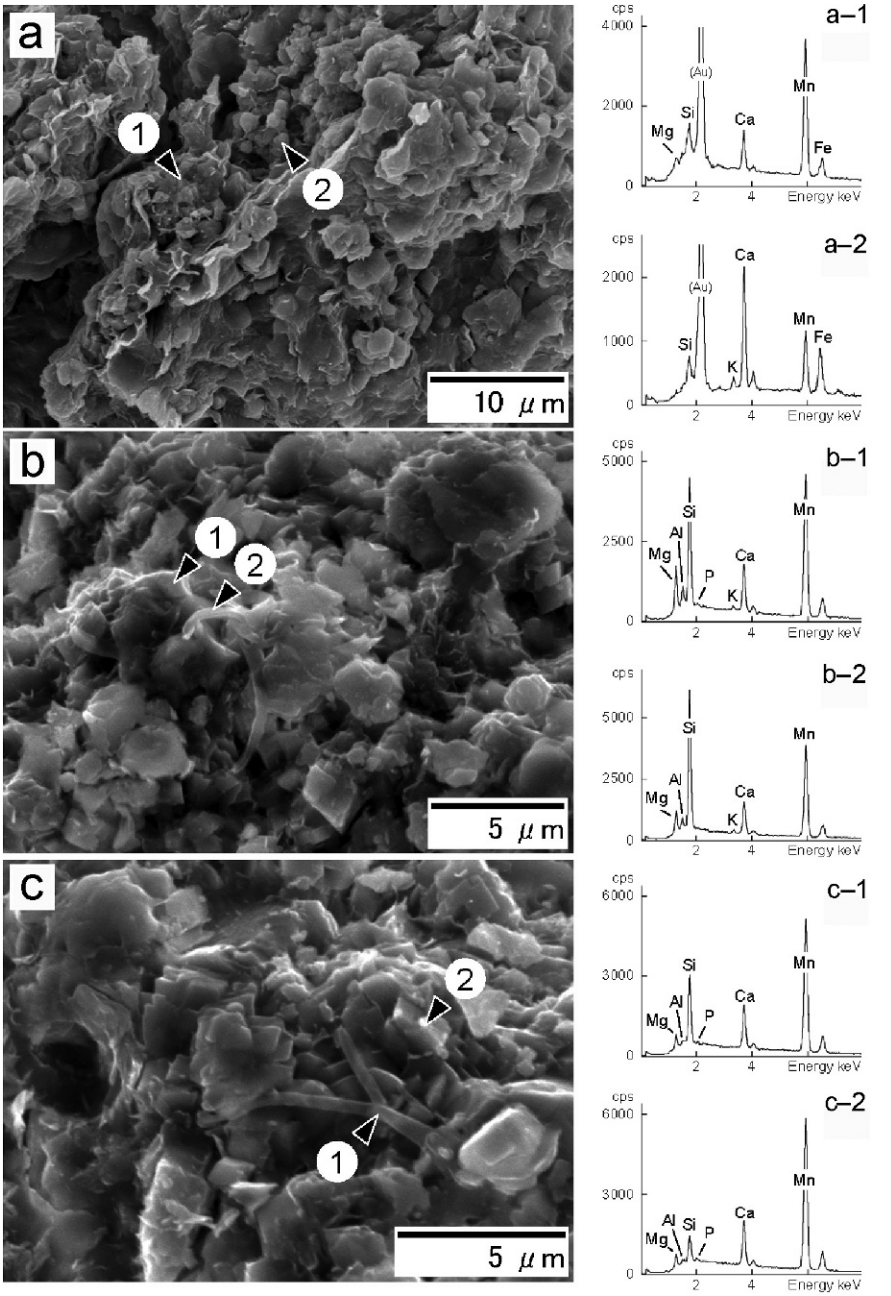

Fig. 7.7 Scanning electron micrographs of Mn-carbonate ores of sample 752 (main ore bed) showing small-sized microorganisms (arrows). The flaky materials are rich in Mn with Si, Ca and Fe (**a-1**). Coccoid forms are much more Ca-rich with lower Mn, Si and higher Fe (**a-2**). Tubular microorganisms are Si- and Mn-rich associated with Ca and lower amounts of Mg, Al, K and P (**b-2, c-1**). Angular phases are composed mainly of Mn suggesting rhodochrosite or manganite on the basis of XRD (**c-2**)

Fig. 7.8a, b, d, e), clay minerals around cells were also identified (∼1 nm, Fig. 7.8c). Most of XRD data were agreed with TEM micromorphology. But, flaky graphene could not be detected by XRD, because its amount was under detection limit.

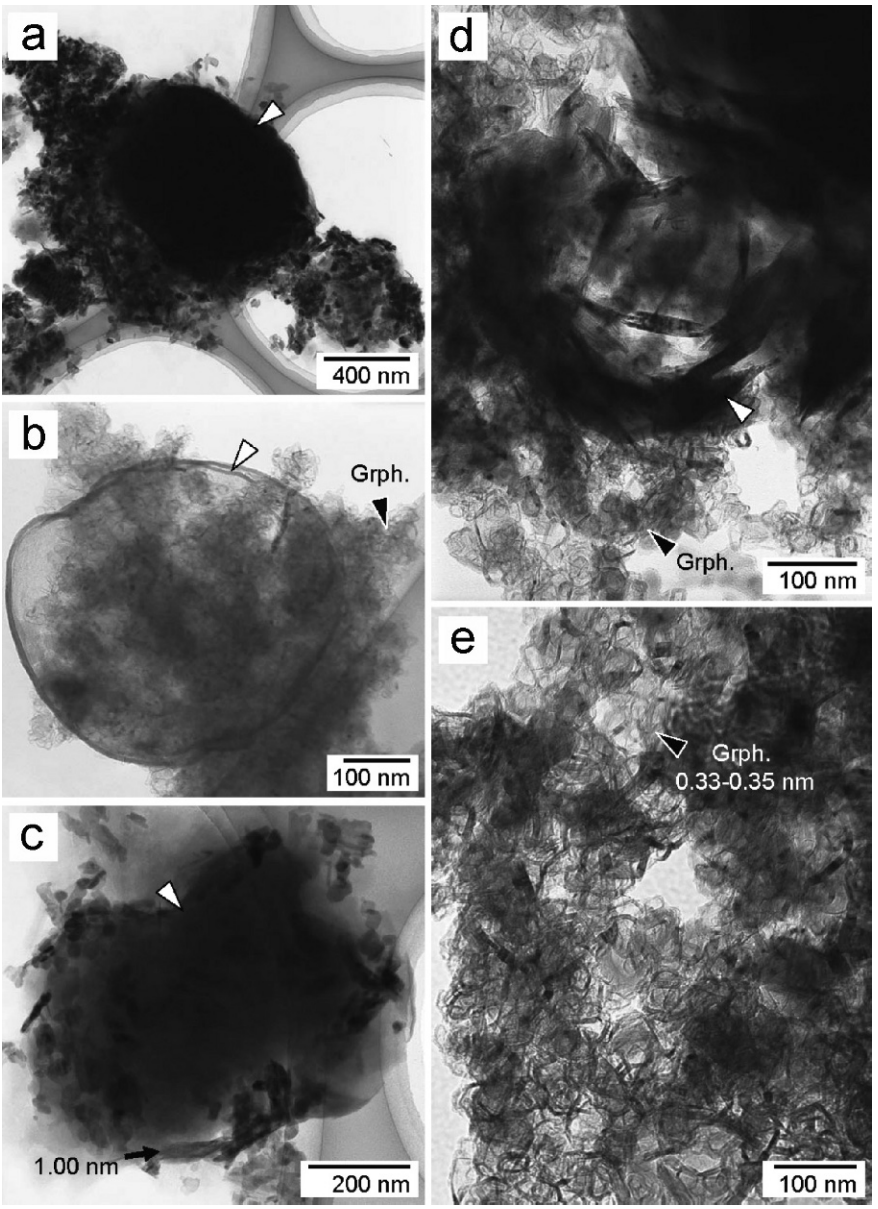

Fig. 7.8 Transmission electron micrographs of sample 752 (main ore bed) showing abundant nanometer-sized bacteria (white arrows on **a, b, c** and **d**). Most bacterial materials are replaced by graphene (0.33–0.35 nm, black arrows on **b, d, e**), or clay minerals (1.00 nm, black arrow on **c**)

7.7.2 Mn Carbonate Ore, Brownish Grey, Second Ore Bed

The sample No. 755 has layered structure of dark and light brownish gray in colour. According to XRD data both of the layers showed almost the same mineralogical composition, such as rhodochrosite, chlorite, apatite and calcite. The peak at 1.59 nm has partly shifted to 1.62 Å as a result of ethylene-glycol treatment suggesting presence of mixture of chlorite and smectite (Fig. 7.4).

The ED-XRF elemental content mapping showed high Fe content in almost all layered structures in sample No. 755 (Fig. 7.9). The Mn concentrates in darker

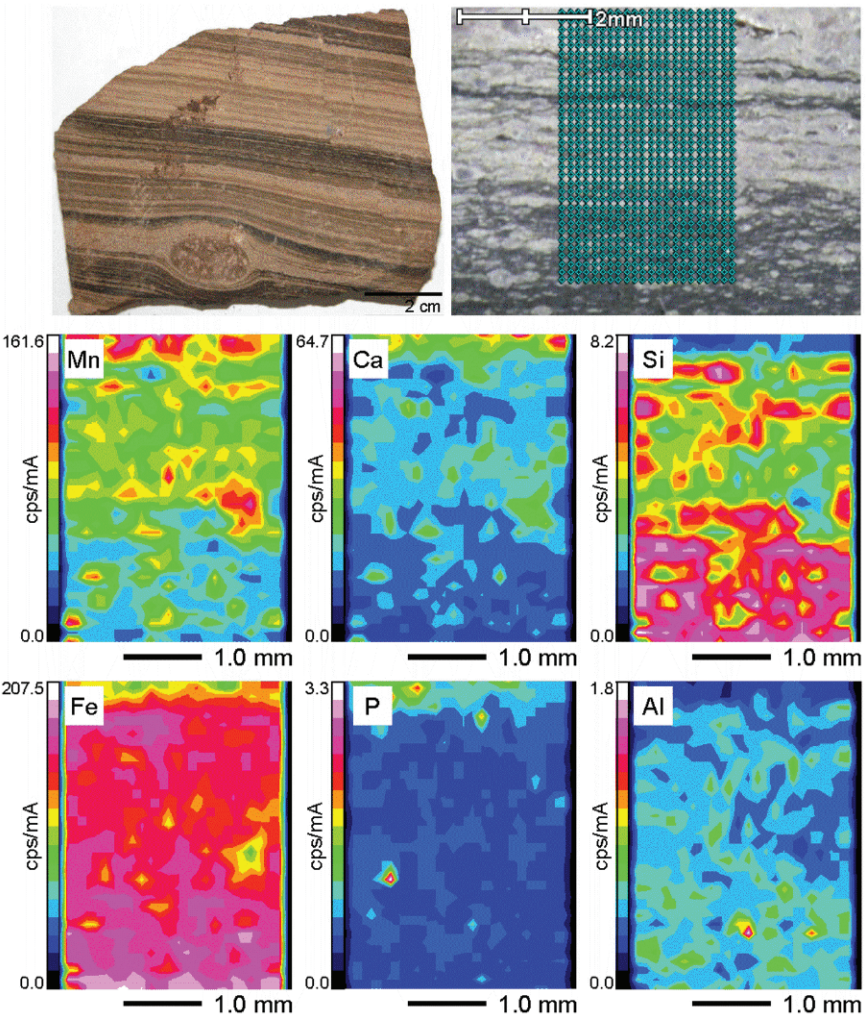

Fig. 7.9 ED-XRF elemental mapping of Mn-carbonate ores of sample 755 (second ore bed) showing high Fe content in all banded layer structures, whereas Mn and Si elements are located in darker gray layers

brownish gray layers as well as Ca, whereas high Si contents locate in lighter parts. The small amounts of Al and P were found in darker layers.

The optical microscopy study of the sample revealed spherical microorganisms lining-up in the banded structures (Fig. 7.10a). Framboidal pyrite crystals were also found (Fig. 7.10c, d). The filamentous materials were placed parallel to the banded layers (Fig. 7.10b, e).

The scanning electron microscopy study of sample 755 exhibited presence of various smaller microorganisms, such as filamentous, coccoid (spherical), tubular, and ribbon typed bacteria (Fig. 7.11). The fragments are rich in Ca and Mn elements with high background of organics (Fig. 7.11, a-1) whereas needle-like materials are P and Ca rich with low background due to inorganics (Fig. 7.11, a-2). Coccoid clumps of bacteria show also high background and mainly Si, Fe composition in

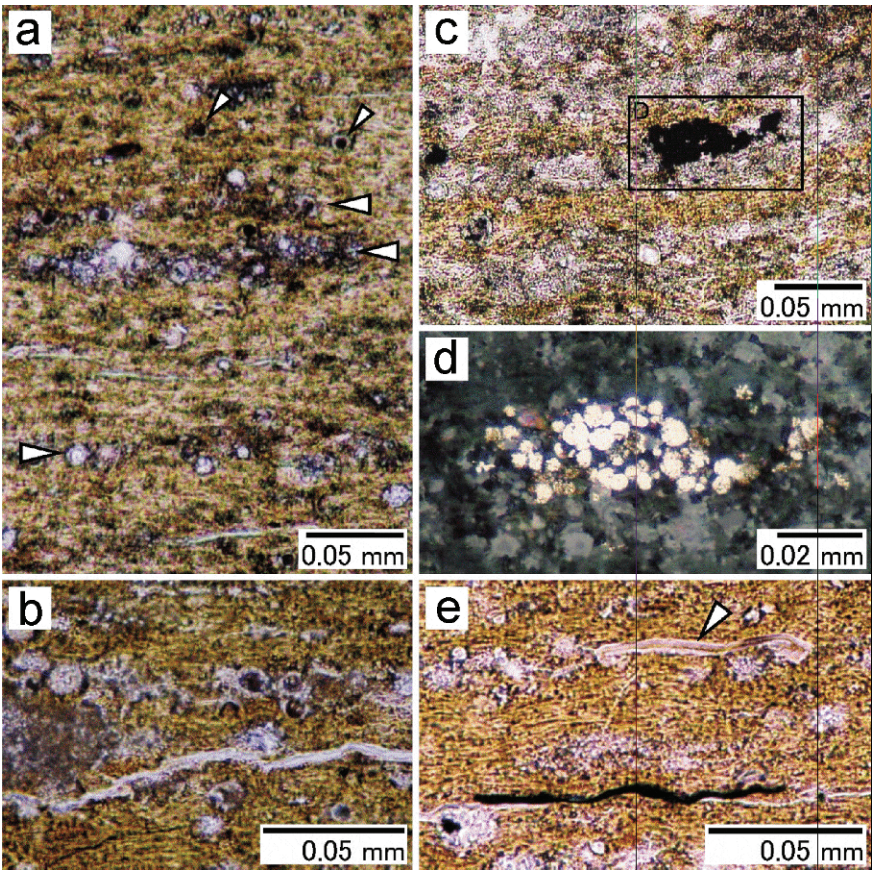

Fig. 7.10 Optical microsgraphs of Mn-carbonate ores of sample 755 (second ore bed) showing abundant microorganisms. Spherical microorganisms line up in banded structure (arrows on **a, b**). Framboidal pyrite located in certain layers can be detected using reflected light (**c, d**). Filamentous forms are parallel to banded layers (**b**, and arrow on **e**)

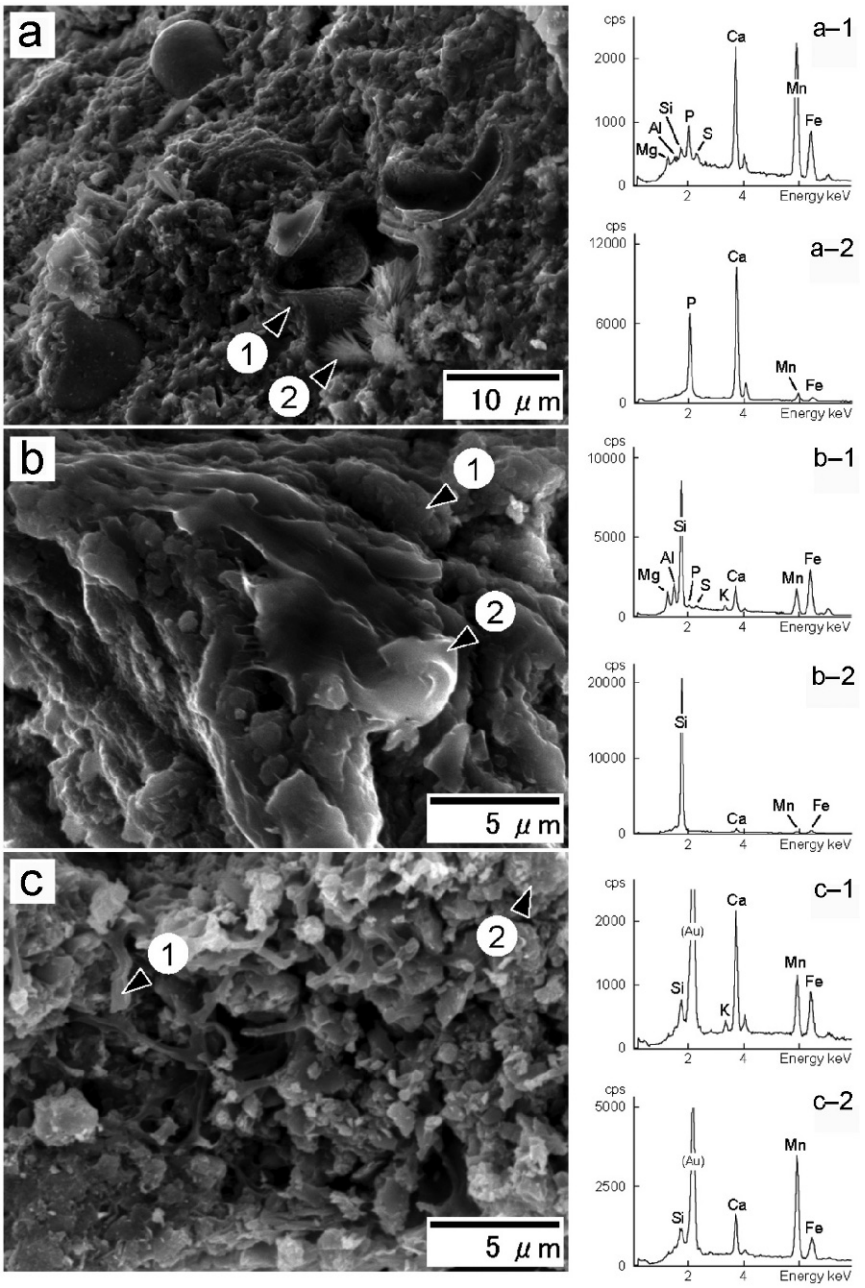

Fig. 7.11 Scanning electron micrographs of sample 755 (second ore bed) showing some bacterial cell walls, thin films (arrow, **b-2**). Coccoid clumps of bacteria (arrows **a-1, b-1**) and filamentous bacteria (arrow, **c-1**) are shown. EDS spectra of microorganisms indicated Mn-, Ca- and Fe-rich matrix composition. Inorganic Ca-phosphate (arrow, **a-2**) and Mn-rich Ca-, Fe-, Si-bearing matrix were also determined (arrow, **c-2**). High background on **a-1, b-1** and **c-1** supports organic contribution

addition to Mg, Al, P, S, Ca and Mn (Fig. 7.11, b-1). Thin filmy materials covering on the surface contained mainly Si with low background of organics (Fig. 7.11, b-2). Filamentous materials are composed of large amount of Ca with Mn-Fe elements and high background of organics (Fig. 7.11, c-1). For comparison, the matrix of the filamentous organics contained higher Mn content than that of the tubular ones (Fig. 7.11, c-2).

TEM analysis showed abundant nanometre-sized bacterial cells (Fig. 7.12a), clay minerals around cells were also identified (∼1.02–1.10 nm, Fig. 7.8bd).

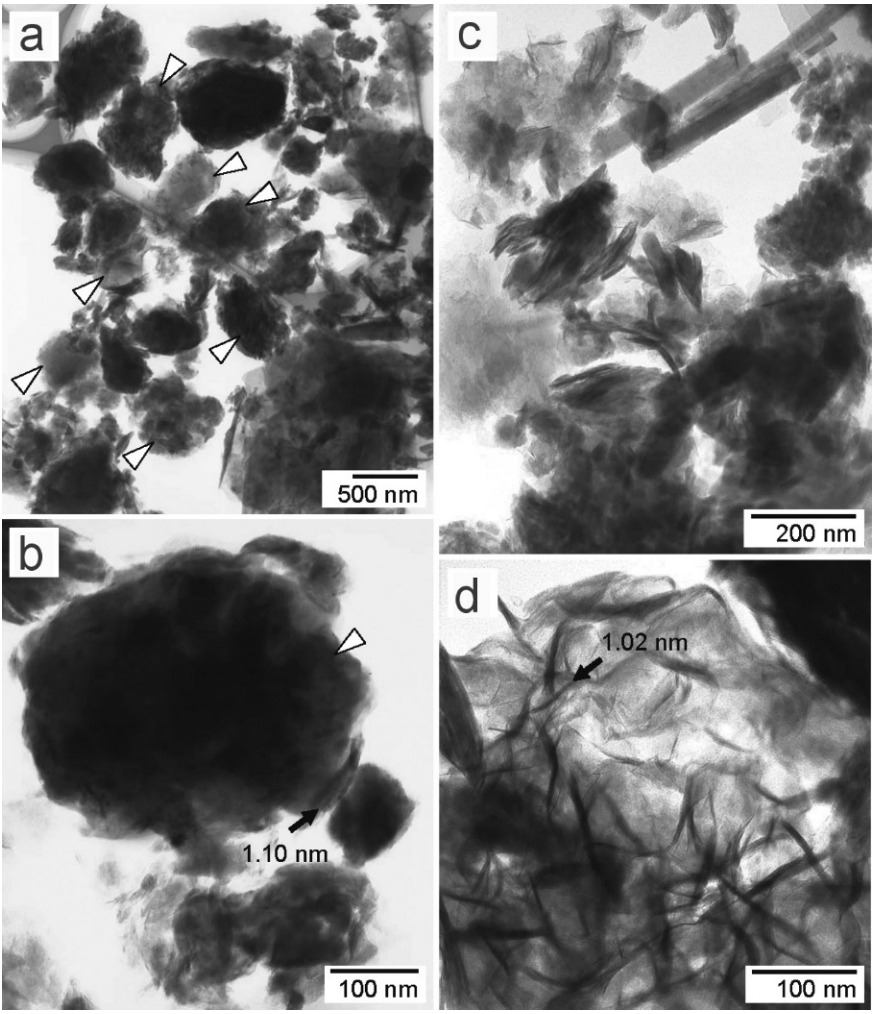

Fig. 7.12 Transmission electron micrographs of sample 755 (second ore bed) show abundance of nanometer-sized bacteria (white arrows on **a** and **b**). Abundant granular minerals of 1.02–1.10nm size (clay minerals) were observed with bacterial materials (black arrows, **b** and **d**)

In general the EDX spectra of microorganisms indicated that the most abundant elements (Si, Ca, Mn and Fe) were associated with high background suggesting the biomineralization around cells, whereas the low background indicated presence of inorganic minerals. SEM revealed only presence of 1–10 μm- sized microbes (Figs. 7.7 and 7.11). Bacteria were very small-sized and very hard to observe by SEM, because of Mn-Fe, Si and Ca minerals on the surface of the cells. Therefore TEM was needed for observation which revealed nanometer sized bacterial mineralization (Figs. 7.8 and 7.12).

7.7.3 Cathodoluminescence Study of Mn Ore

A brightly-moderately luminescent carbonate with elevated Mn content was found (8–10 wt.% Mn) in some Mn-carbonate (rhodochrosite) concretions with fish fossils collected from the main bed of the Úrkút Manganese Mine. X-ray powder diffraction revealed that this carbonate was kutnohorite. Kutnohorite is a dolomite-type double carbonate with the general formula $CaMn(CO_3)_2$ (hexagonal, R-3) (Frondel and Bauer 1955; Farkas et al. 1988). Polgári et al. (2007b) report the CL microscopic and spectroscopic properties of kutnohorite for the first time.

The investigated samples (mineral composition is rhodochrosite and kutnohorite) show moderate and bright orange-red luminescence in the form of layers, infiltration-like textures and veinlets (Fig. 7.13). In the matrix of the concretions areas with moderate and bright CL can be observed side by side together with non-luminescent areas. The crystals in the veinlets do not show zonation, only slight inhomogeneity, but their rims have brighter orange CL. The border of the veinlets shows an outer part with moderate red-brown CL and an inner part with bright orange-red CL. The composition difference in Mn content is around 1–2 wt.% (Polgári et al. 2007b).

The CL spectra of the studied luminescent phases both in the matrix and in the veinlets of the concretions uniformly show one emission peak without any visible shoulder at a mean wavelength of 630 nm (range: 629–636 nm, Polgári et al. 2007b).

According to the mineralogical (XRD, TEM) and textural (EMPA) studies the moderately and brightly luminescent carbonate phase with 630 emission peak is determined as calcian kutnohorite (average composition: $Ca_{1.53}\ Mn_{0.37}\ Mg_{0.09}\ Fe_{0.01}$) (Polgári et al. 2007b). The non-luminescent phase in the matrix is supposed to be rhodochrosite.

Mn^{2+} has an ionic radius between those of Ca^{2+} and Mg^{2+} (Reeder 1983), for this reason theoretically it can occupy both cationic positions (Ca and Mg) in the dolomite structure. Mn substitutes in the A site and has strong preference for the B site of the dolomite (e.g. Lumsen and Lloyd 1984), but this may be true only for low Mn concentrations and may not apply to kutnohorite with high Mn content (Peacor et al. 1987). Mn at high concentrations may have low ordering tendency, therefore strongly disordered kutnohorite can also form (Peacor et al. 1987). In the nature, disordered as well as ordered kutnohorite can exist. Peacor et al. (1987)

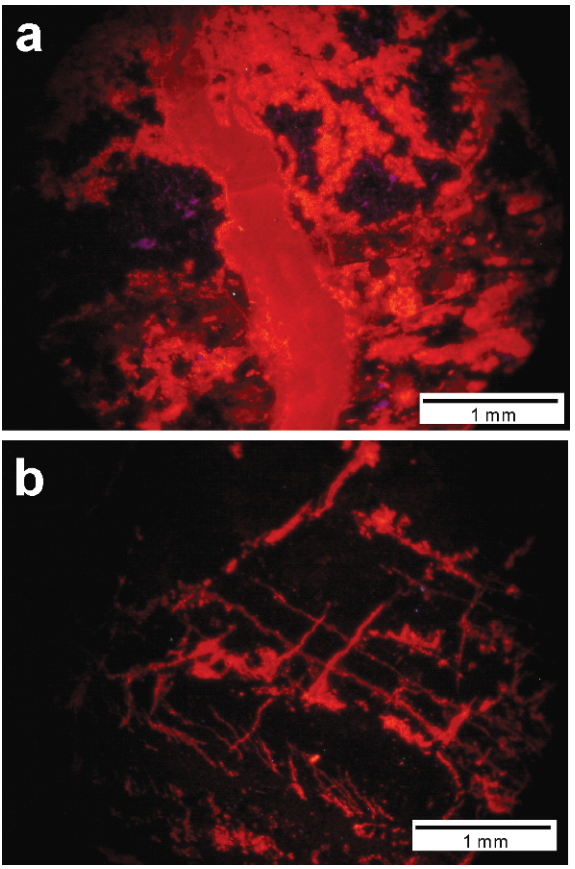

Fig. 7.13 Cold-cathode CL micrographs of theMn-carbonate concretions. (**a-b**) Luminescent carbonate veinlet with brighter rim in sample H4 (Shaft III, sample no. H4 in the Rock Archive of Institute for Geochemical Research, Budapest)

reported almost completely disordered and largely ordered kutnohorites with similar (near to stoichiometric) chemical composition. The high excess of Ca in the Úrkút kutnohorite suggests that some Ca occupies the B site, however, the site preference of Mn is not obvious (only B site or both in A and B sites).

According to the dolomite-type structure of kutnohorite, a composite luminescence band consisting of emission bands of Mn^{2+} in A and B positions, respectively, can be expected. The CL spectra of the Úrkút kutnohorite, however, revealed a single emission band at 630 nm, and differences were observed only in the intensity of spectra. While similar spectra with CL emission maxima at around 630 nm have been reported for e.g. calcitized dolomite (Richter et al. 2003), the Úrkút kutnohorite seems to be a monophase mineral and its CL spectra resemble to those of red luminescent dolomites with one CL peak.

For self-quenching of the CL the absolute concentration of the activator elements, therefore the distance between Mn ions seems to be a critical factor. Marfunin (1979) pointed out that the maximum CL intensity often occurs at about 0.1–1 wt.% concentration level of the activator ion and at higher concentrations

the self-quenching is dominant. Machel et al. (1991) suggested that bright Mn^{2+}-activated CL extends up to about 5 wt.% Mn. At higher Mn concentration dull luminescence exist due to self-quenching probably up to the rhodochrosite composition (48 wt.% Mn). This suggestion is strongly supported by the excess-Ca kutnohorite from Úrkút, which shows moderate-bright cathodoluminescence at 8.2–10.3 wt.% Mn concentration (Polgári et al. 2007b), which data are close to the luminescent manganocalcite (11.5 wt.% Mn, 0.5 wt.% Fe) described by Walker et al. (1989). Fe content up to 2400 ppm determined in the Úrkút kutnohorite could also partially influence its luminescent character with some Fe-quenching.

7.8 Conclusion

Carbonatic manganese ore mineralizations occur in environments rich in organics (black shale, biogenic pyrite, etc.) and are of laminitic texture. It has established that their chemical composition is characterized by the enrichment of bioessential elements (Mn, Fe, Mg, Sr, S, P, As, Co, Ni, Ce, U) and very small grain size ($\sim$1 μm). Evidences of the chemical composition and geochemical characteristics, the joint occurrence of Fe and Mn, as well as the high Mn/Fe ratio, the local selective enrichment of P, Sr, Mg, As, Si, and Ce, the micro texture, the results of recent laboratory experiments are in harmony with the assumption of bacterial activity.

Electron micrographs clearly supported the biological formation of banded Mn-Fe minerals and clay minerals in the Úrkút Mn-carbonate ore. The chemical analysis of the Mn-carbonate ore showed Mn, Fe, and Si, Al as the major elemental composition. X-ray diffraction, ED-XRF and SEM-EDX analyses suggested new type of Mn-, Fe-, and clay mineralization supporting that microbial activity might play a significant role in the formation of the Mn-Fe carbonate ore, a presumably common phenomenon during Jurassic. It is likely that the Mn-Fe banded minerals and clay minerals associated with microorganisms are the bioorganic product of microbial activity. The banded Mn-Fe mineral formation in the ore beds may be substantially enhanced by the presence of microorganisms.

According to the features of the deposit, two cycles of bacterial activity – a primary aerobe chemolitoautotrophic and an anaerobe bacterial cycle – are supposed to influence the mineralization. The anaerobe system overprinted the primary one, which is proved by the organic origin of the carbon contained in the (CO_3^{2-}) radical of the carbonatic manganese ore, originating from bacterially influenced reduction of Mn(IV) and/or Mn(III) accompanied by the oxidation of organic matter (Polgári et al. 1991). Numerous studies supported that the direct oxidation by aerobe chemolithoautotrophic bacteria is a general process in all natural environments and the most favourite. Mn-oxides and manganates are formed by both chemical and bacterial oxidation from Mn(II) in variegated water systems but recent analogies support that bacterial activity is the most important in most of cases (Emerson et al. 1982; Tebo et al. 1984, 1991; Nealson et al. 1988). In fresh waters similar bacterial activity was observed (Chapnick et al. 1982; Tipping et al. 1985) as well

as in hydrothermal vent systems and megaplumes (Cowen et al. 1986; Mandernack and Tebo 1993), in fresh water hydrothermal systems (Ferris et al. 1987a, 1987b) and in estuarine environments (Edenborn et al. 1985; Sunda and Huntsman 1987). The Mg and Ca contents of the very quickly forming Mn-oxide minerals are high. The Mg acts as structure stabilizing cation in interlayered position between MnO_6 octaeders. According to detailed experimental studies it was shown that extracellular polymers of bacteria catalyze the adsorption of Mg on the surface of the cells (Beveridge 1989; Geesey and Jang 1989). So the bacterial spores not only directly oxidize Mn(II) to Mn(IV) but in the very early stages of oxidation bacterial activity influence the cation composition of the forming Mn-oxide mineral. Later chemical processes start to erase the biological signal (Tebo et al. 1988).

The final conclusion from recent analogies and experimental studies is that aerobe chemolithoautotrophic bacterial activity is responsible for direct Mn(II) oxidation in natural marine and other water environments as a main process.

The present investigation strongly suggests that the Mn-Fe and Si minerals were associated with microorganisms as a biological organic product in the Úrkút ore. The identity of the bacteria responsible for Mn mineral formation is unknown, but is tentatively assigned to Mn and Fe bacteria on the basis of morphology. The genesis of rocks and minerals has played a pivotal role in Toarcian age, and they may even have acted as life genetic system.

Our cathodoluminescence investigations gave further contribution to the better knowledge of the CL characteristics of Mn-rich carbonates. Calcian kutnohorite from the Úrkút Mn carbonate ore turned out to be a natural example supporting the earlier assumptions that manganese does not show total self-quenching in carbonates at around 8–10 wt.% Mn concentrations (with up to 2400 ppm Fe). The cathodoluminescent behaviour of Mn-bearing carbonates even with high Mn concentrations, together with their complex mineralogical, morphological and geochemical study, permits exploration of Mn enrichments as signs of microbial activity at terrestrial and extraterrestrial sites, respectively. CL seems to be a potential tool for investigation of astrobiological structures built up by Mn minerals, e.g. Mn-oxides (biooxides) transformed to Mn carbonates via microbial processes.

Acknowledgements We gratefully acknowledge our collaborator, Ms. Rie Wakimoto for her technical assistance and useful contribution to this study. This study was supported by Grant-in-Aid for Science Research from the Ministry of Education, Science, and Culture, Japan (Grant-in-Aid for Scientific Research B). The study was supported by Hungarian Science Foundation (OTKA-NKTH No. K 68992).

References

Asada R, Tazaki K (2000) Observation of bio-kaolinite clusters. Clay Science, Japan 40:24–37

Baes CF, Mesmer RE (1976) The hydrolysis of cations. Wiley, New York

Bargar JR, Tebo BM, Bergmann U, Webb SM, Glatzel P, Chiu VQ, Villalobos M (2005) Biotic and abiotic products of Mn(II) oxidation by spores of the marine Bacillus sp. Strain SG-1. Am Mineral 90:143–154

Beveridge TL (1989) Metal ions and bacteria. In: Beveridge TL, Doyle RJ (eds) Metal ions and bacteria. Wiley, New York, pp 1–29
Boston PJ, Spilde MN, Northup DE, Melim LA, Soroka DS, Kleina LG, Lavoie KH, Hose LD, Mallory LM, Dahm CN, Crossey LJ, Schelble RT (2001) Cave biosignature suites: microbes, minerals, and Mars. Astrobiology 1:25–55
Chapnick S, Moore WS, Nealson KH (1982) Microbially mediated manganese oxidation in a freshwater lake. Limnol Oceanogr 17:1004–1014
Chukrov FV, Drits VA, Gorschkov AI, Sakharov BA, Dikov YP (1987) Structural models of vernadite. Int Geol Rev 29:1337–1347
Cowen JP, Massoth GJ, Baker ET (1986) Bacterial scavenging of Mn and Fe in a mid- to far-field hydrothermal particle plume. Nature 322:169–171
Cseh Németh J, Grasselly Gy (1966) Data on the geology and mineralogy of the manganese ore deposit of Úrkút II. Acta Miner Petr Univ Szegediensis 17: 2, 89–114
Cseh Németh J, Grasselly Gy, Szabó Z (1980) Sedimentary manganese deposits of Hungary. In: Varentsov IM, Grasselly Gy (eds) Geology and geochemistry of manganese II. Akadémiai Kiadó, Budapest pp 199–221
Davies SHR, Morgan JJ (1989) Manganese (II) oxidation kinetics on metal oxide surfaces. J Colloid Inter Sci 129: 63–77
Denson J, Ivey DM, Sears DWG, GucsikA, Vidéki R (2007) Cathodoluminescence and its application for biosignature analysis of Mn-containing biogenic minerals: a review. Lunar Planet Sci XXXVIII 1009.pdf
Edenborn HM, Paquin Y, Chateauneuf G (1985) Bacterial contribution to manganese oxidation in a deep coastal sediment. Estuar Coast Shelf Sci 21: 6 801–815
Ehrlich HL (1990) Geomicrobiology. 2nd edn. M. Dekker, New York
Ehrlich HL (1999) Microbes as geologic agents: Their role in mineral formation. Geomicro J 16:135–153
El Ali A, Barbin V, Calas G, Cervelle B, Ramseyer K, Bouroulec J (1993) Mn2+-activated luminescence in dolomite, calcite and magnesite: quantitative determination of manganese and site distribution by EPR and CL spectroscopy. Chem Geol 104:189–202
Emerson S, Kalhorn S, Jacobs L, Tebo BM, Nealson KH, Rosson RA. (1982) Environmental oxidation rate of manganese(II) – bacterial catalysis. Geochim Cosmochim Acta 46:6 1073–1079
Fan D, Yang P, Wang R (1999) Characteristics and origin of the Middle Proterozoic Dongshuichang chambersite deposit, Jixian, Tianjin, China. Ore Geol Rev 15:15–29
Farkas L, Bolzenius BH, Schäfer, W, Will G (1988) The crystal structure of kutnohorite CaMn(CO3)2. Neues Jb Miner Monat 12: 539–546
Ferris FG, Beveridge TG, Fyfe WS (1986) Iron-silica crystallite nucleation by bacteria in geothermal sediment. Nature 320:609–611
Ferris FG, Fyfe WS, Beveridge TJ (1987a) Bacteria as nucleation sites for authigenic minerals in a metal-contaminated lake sediment. Chem Geol 63: 225–232
Ferris FG, Fyfe WS, Beveridge TJ (1987b) Manganese oxide deposition in a hot spring microbial mat. Geomicrobiol J 5:33–42
Fortin D (2004) What biogenic minerals tell us. Science 303:1618–1619
Frondel C, Bauer L (1955) Kutnahorite: A manganese dolomite: CaMn(CO3)2. Am Mineral 40:748–760
Gaft M, Gorobets B, Naumova I, Mironova N, Grinvald G (1981) Correlation of luminescent properties with the crystallography of manganese minerals (in Russian). Mineralogiceskij Zurnal 3:80–90
Gaft M, Reisfeld R, Panczer G (2005) Modern luminescence spectroscopy of minerals and materials. Springer Verlag, Berlin
Géczy B (1973) The origin of the Jurassic faunal provinces and the Mediterranean plate tectonics. Ann Univ Sci R Eötvös (Budapest) Sect Geol 16: 99–114
Geesey GG, Jang L (1989) Intractions between metal ions and capsular polymers. In: Beveridge TL, Doyle RJ (eds) Metal ions and bacteria. Wiley, New York, pp 325–357

Giovanoli R (1980) On natural and synthetic Mn nodules. In: Varentsov IM, Grasselly Gy (eds) Geology and geochemistry of manganese I. Akadémiai Kiadó, Budapest pp 159–202
Gorobec B, Gaft M, Laverova L (1978) Photoluminescence of manganese minerals (in Russian). J Appl Spectrosc 28:750–752
Haberman D, Neuser RD, Richter DK (2000) Quantitative high resolution spectral analysis of Mn2+ in sedimentary calcite. In: Pagel M, Barbin V, Blanc P, Ohnenstetter D (eds) Cathodoluminesce in geosciences. Springer Verlag, Berlin, pp 331–358
Hanczyc MM, Fujikawa SM, Szostak JW (2003) Experimental models of primitive cellular compartments: Encapsulation, growth, and division. Science 24:302, 618–622
Hazen RM (2005) Genesis: Rocks, minerals, and the geochemical origin of life. Elements 1:135–137
Kashefi K, Lovley DR (2000) Reduction of Fe(III), Mn(IV), and toxic metals at 100°C by Pyrobaculum islandicum. Appl Environ Microbiol 66:1050–1056
Krumbein WE (1983) Microbial geochemistry. Blackwell Scientific Publications, Alden Press, Oxford
Lanson B, Drits VA, Silwester E, Manceau A (2000) Sructure of H-exchanged hexagonal birnessite and its mechanism of formation from Na-rich monoclinic buserite at low pH. Am Mineral 85:826–838
Larsen I, Little B, Nealson KH, Ray R, Stone A, Tian J (1998) Manganite reduction by Shewanella putrefaciens MR-4. Am Mineral 83:1564–1572
Lumsen DN, Lloyd RV (1984) Mn(II) partitioning between calcium and magnesium sites in studies of dolomite origin. Geochim Cosmochim Acta 48:1861–1865
Machel HG (2000) Application of cathodoluminescence to carbonate diagenesis. In: Pagel M, Barbin V, Blanc P, Ohnenstetter D (eds) Cathodoluminescence in Geosciences. Springer Verlag, Berlin, pp 271–301
Machel HG, Mason RA, Mariano AN, Mucci A (1991) Causes and emission of luminescence in calcite and dolomite. In: Barker CE, Kopp OC (eds) Luminescence microscopy and spectroscopy: Qualitative and quantitative applications. Society of sedimentary geologists, Short Course 25, pp 9–25
Mandernack KW, Post J, Tebo BM (1995) Manganese mineral formation by bacterial spores of the marine Bacillus, strain SG-1: Evidence for the direct oxidation of Mn(II) to Mn(IV). Geochim Cosmochim Acta 59:4393–4408
Mandernack KW, Tebo BM (1993) Manganese scavenging and oxidation at hydrothermal vents in vent plumes. Geochim Cosmochim Acta 57:3907–3923
Marfunin AS (1979) Spectroscopy, luminescence and radiation centres in minerals. Springer, Berlin
Marshall DJ (1988) Cathodoluminescence of geological materials. Unwin-Hyman, Boston
Mason RA (1987) Ion microprobe analysis of trace elements in calcite with an application to the cathodoluminescence zonation of limestone cements from the Lower Carboniferous of South Wales, U.K. Chem Geol 64: 209–224
Mason RA, Mariano AN (1990) Cathodoluminescence activation in manganese-bearing and rare earth-bearing synthetic calcites. Chem Geol 88:191–206
McKay DS, Gibson EK Jr, Thomas-Keprta KL, Vali H, Romanek CS, Clemett SJ, Chillier XDF, Maechling CR, Zare RN (1996) Search for past life on mars: Possible relic biogenic activity in martian meteorite ALH84001. Science 273:924–930
Morgan JJ (2005) Kinetics of reaction between O2 and Mn(II) species in aqueous solution. Geochim Cosmochim Acta 69:1 35–48
Nealson KH, Tebo BM, Rosson RA (1988) Occurrence and mechanisms of microbial oxidation of manganese. Adv Appl Microbiol 33:279–318
Neuser RD (1995) A new high-intensity cathodoluminescence microscope and its application to weakly luminescing minerals. Bochumer Geol Geotech Arb 44:116–118
Okita PM (1988) Geochemistry and mineralogy of the molango manganese orebody, Hidalgo State, Mexico. Ph.D. Thesis, Cincinatti University

Peacor D, Essene E, Gaines A (1987) Petrologic and crystal-chemical implications of cation order-disorder in kutnahorite [CaMn(CO3)2]. – Am Mineral 72:319–328
Polgári M (1993) Manganese geochemistry reflected by black shale formation and diagenetic processes – Model of formation of the carbonatic manganese ore of Úrkút. Spec series Hung Geol Inst Karpati Publish House, Ushgorod
Polgári M, Bajnóczi B, Kovács Kis V, Götze J, Dobosi G, Tóth M, Vigh T (2007b) Mineralogical and cathodoluminescence characteristics of Ca-rich kutnohorite from the Úrkút Mn-carbonate mineralization, Hungary. Mineral Mag 71:5 493–508
Polgári M, Dobosi G, Horváth P, Rálisch-Felgenhauer E, Vigh T. (2003b) As-bearing pyrite occurrence at Úrkút and in the Jurassic layers of the Iharosberény-I drillcore. Bull Hung Geol Soc 133:4 469–475
Polgári M, Hein JR, Tóth M, Vigh T, Bíró L (2007a) Did hydrothermal fluids contribute to the Huge Úrkút Carbonate ore Body? Geochim Cosmochim Acta Suppl Abst Vol A801
Polgári M, Okita PM, Hein JR (1991) Stable Isotope Evidence for the Origin of the Úrkút Manganese Ore Deposit, Hungary. J Sed Petr 61:3 384–393
Polgári M, Philippe M, Szabó-Drubina M, Tóth M (2005) Manganese-impregnated wood from a Toarcian manganese ore deposit, Eplény Mine, Bakony Mts, Transdanubia, Hungary. Neues Jb Geol Paläont Monat 3:175–192
Polgári M, Szabó Z, Szederkényi T (eds) (2000) Manganese Ores in Hungary – In commemoration of professor Gyula Grasselly - Mangánércek Magyarországon – Grasselly Gyula akadémikus emlékére. Regional Committee Hung Acad Sci Juhász Publish House, Szeged
Polgári M, Szabó-Drubina M, Abonyi Tóth Zs (2006b) Role of hydrothermal supply and bacterial metal enrichment effects in black shale hosted Mn-carbonate mineralization, Úrkút, Hungary, Europe. 12th IAGOD Congr Moscow, Russia, Abst CD ROM
Polgári M, Szabó-Drubina M, Szabó Z (2004) Theoretical model for the Mid-European Jurassic Mn-carbonate mineralization Úrkút, Hungary. Bull Geosci Czech Geol Surv 79:1 53–61
Polgári M, Szabó-Drubina M, Tóth M, Szabó Z, Abonyi Tóth Zs (2003a) Submarine primary Sr-rich Mn-oxide mineralization in the Jurassic Transdanubian Range (Hungary). In: DG Eliopoulos et al. (eds) Proc 7th Biennial SGA Meet Athens, Greece, Millpress Rotterdam pp 1233–1236
Polgári M, Tazaki K, Watanabe H, Vigh T, Gucsik A (2006a) Geochemical aspect of chemolithoautotrophic bacterial activity in the role of black shale hosted Mn mineralization, Jurassic age, Hungary, Europe. Clay Sci 12(Suppl 2):233–239
Reeder R (1983) Crystal chemistry of the rhombohedral carbonates. In: Carbonates. Mineralogy and chemistry. Miner Soc Am Rev Mineral 11:1–47
Reynolds RC Jr (1989) Diffraction by Small and Disordered Crystals. In: Bish DL, Post JE (eds) Modern powder diffraction. Mineral Soc Am Rev Miner Washington DC 20:145–182
Richter DK, Götte T, Götze J, Neuser RD (2003) Progress in application of cathodoluminescence (CL) in sedimentary petrology. Mineral Petrol 79:127–166
Roy S (1981) Manganese deposits. Academic Press, London
Sara M, Sleytr UB (2000) S-layer proteins. J Bacteriol 182:859–868
Sunda WG, Huntsman SA (1987) Microbial oxidation of manganese in a North-Carolina Estuary. Limnol Oceanogr 32:3 552–564.
Sung W, Morgan JJ (1981) Oxidative removal of Mn(II) from solution catalyzed by the γ-FeOOH (lepidocrocite) surface. Geochim Cosmochim Acta 45:2377–2383
Szabó Z, Grasselly Gy, Cseh Németh J (1981) Some conceptual questions regarding the origin of manganese in the Úrkút Deposit, Hungary. Chem Geol 34: 19–29
Szabó-Drubina M (1959) Manganese deposits of Hungary. Econ Geol 54:1078–1093
Tashiro Y, Tazaki K (1999) The primitive stage of microbial mats comprising iron hydroxides. Earth Sci 53: 27–35
Tazaki K (1997) Biomineralization of layer silicates and hydrated Fe/Mn oxides in microbial mats: An electron microscopical study. Clays and Clay Miner 45:203–212
Tazaki K (2000) Formation of banded iron-manganese structures by natural microbial communities. Clays Clay Miner 48:511–520

Tebo BM (1991) Manganese(II) oxidation in the suboxic zone of the Black-Sea. Deep Sea Res A. Oceanograph Res Papers Suppl 2 38:S883–S905

Tebo BM, Bargar JR, Clement BG, Dick GJ, Murray KJ, Parker D, Verity R, Webb SM (2004) Manganese biooxides: properties and mechanisms of formation. Ann Rev Earth Planet Sci 32:287–328

Tebo BM, Ghiorse WC, Van Waasbergen LGV, Siering PL, Caspi R (1997) Bacterially mediated mineral formation: Insights into manganese (II) Oxidation from molecular genetic and biochemical studies. In: Nealson KH, Banfield JF (eds) Geomicrobiology: Interactions between microbes and minerals. Miner Soc Am Washington DC 35: pp 225–266

Tebo BM, Nealson KH, Emerson S, Jacobs L (1984) Microbial mediation of Mn(II) and Co(II) precipitation at the O2/H2S interfaces in 2 anoxic fjords. Limnol Oceanogr 29(6):1247–1258

Tebo BM, Nealson KH, Rosson RA (1988) Occurrence and mechanisms of microbial oxidation of mangane. Adv Appl Microbiol 33:279–318

Theng BKG, Orchard VA (1995) Interactions of clays with microorganisms and bacterial survival in soil: A physicochemical perspective. In: Huang PM, Berthelin J, Bollag JM, McGill WB, Page AL (eds) Environmental impact of soil component interactions. CRC Press, Florida, 3:123–139

Tipping E, Hetherington NB, Hilton J, Thompson DW, Bowles E, Hamilton Taylor J (1985) Artifacts in the use of selective chemical-extraction to determine distributions of metals between oxides of manganese and iron. Anal Chem 57(9): 1944–1946

Ueshima U, Mogi K, Tazaki K (2000) Microbes associated with bentonite. Clay Sci 39:171–183

Villalobos M, Toner B, Bargar J, Sposito G (2003) Characterization of the manganese oxide produced by Pseudomonas putida strain MnB1. Geochim Cosmochim Acta 67:2649–2662

Vörös A, Galácz A (1998) Jurassic palaeogeography of the Transdanubian Central Range (Hungary). Rivista Italiana di Paleontol Stratigr 104:69–84

Walker G, Abumere OE, Kamaluddin B (1989) Luminescence spectroscopy of Mn2+ centres in rockforming carbonates. Miner Mag 53:201–211

Webb SM, Bargar JR, Dick GJ, Johnson HA, McCarthy JK, Tebo BM (2004) Insights into the mechanism of enzymatic manganese(II) oxidation by diverse bacterial species. Symposium on Bacterially Mediated Mn and Fe Oxidation in the Biosphere. Geochemistry Division Abstr 227th ACS National Meeting Am Chem Soc Anaheim, California, p 62

Webb SM, Dick GJ, Bargar JR, Tebo BM (2005a) Evidence for the presence of Mn(III) intermediates in the bacterial oxidation of Mn(II). Microbiol 102(15):5558–5563

Webb SM, Tebo BM, Bargar JR (2005b) Structural characterization of biogenic Mn oxides produced in seawater by the marine bacillus sp. strain SG-1. Am Mineral 90(8–9):1342–1357

Weiszburg TG, Tóth E, Beran A (2004) Celadonite, the 10-A green clay mineral of the manganese carbonate ore, Úrkút, Hungary. Acta Miner Petr Szeged 45:1 65–80

Wilson DE (1980) Surface and complexation effects on the rate of Mn(II) oxidation in natural waters. Geochim Cosmochim Acta 44:1311–1317

Index